

Calibration and Analysis of the GCT Camera for the Cherenkov Telescope Array

Jason J. Watson

Brasenose College
University of Oxford

*A thesis submitted for the degree of
Doctor of Philosophy*

Trinity 2018
Abstract

The interaction of very-high-energy astrophysical gamma rays with the Earth's atmosphere produces extensive electromagnetic particle cascades. These showers of particles travel faster than the speed of light in air, and consequently emit photons of blue wavelength, known as Cherenkov radiation. The Imaging Atmospheric Cherenkov Telescope (IACT) technique enables the probing of the universe at TeV energies through the detection of these Cherenkov showers. The Cherenkov Telescope Array (CTA) will represent the next leap forward in gamma-ray astronomy, improving on the sensitivity of current IACTs by a factor of 10, encompassing energies from 20 GeV to 300 TeV, and operating as the first open observatory in this field. A major component of CTA are the Small-Sized Telescopes (SSTs), a necessary ingredient in exploring beyond the present energy frontier in gamma-ray astronomy.

One of three proposed designs for the SST is the Gamma-ray Cherenkov Telescope (GCT). Utilising a dual-mirror Schwarzschild-Couder optical design, GCT enables a 9° Field of View (FoV) for a compact camera design. The camera developed for GCT is the Compact High Energy Camera (CHEC). Two prototypes for CHEC have been built, each utilising different compact photosensor technology. CHEC-M features Multi-Anode Photomultiplier Tubes (MAPMTs), a pixelised extension of the Photomultiplier Tube (PMT) technology extensively used by IACTs. CHEC-S features Silicon Photomultipliers (SiPMs), novel photosensors which utilise semiconductor technology for high-resolution photon counting over a large dynamic range. To fully utilise the signal output from these photosensors, and allow the opportunity for future data analysis procedures to be exploited, the signal received from these photosensors are digitised into waveforms following a trigger. These waveforms have a length of 96 samples with nanosecond precision.

In this thesis, the full calibration and signal-extraction pipeline currently adopted by CHEC to reliably extract the Cherenkov signal from the waveforms is presented. The resulting performance of these procedures, and of the camera designs, is explored with respect to the requirements specified by the CTA Observatory. Potential improvements to the camera and calibration implementations are identified, and simulations of CHEC are utilised to demonstrate the performance increase these proposals provide. Consequently, an improvement to the photosensor that would allow the CHEC-S prototype design to comfortably meet the CTA requirements is specified. Testing of these improvements is anticipated to commence in early 2019. Finally, the results of the second on-telescope campaign for the CHEC-M prototype are presented, during which observations of Cherenkov showers and optical measurements of Jupiter were conducted.

Calibration and Analysis of the GCT Camera for the Cherenkov Telescope Array



Jason J. Watson
Brasenose College
University of Oxford

A thesis submitted for the degree of
Doctor of Philosophy
Trinity 2018

Acknowledgements

First and foremost, I would like to thank my supervisor, Prof Garret Cotter, for the immense amount of opportunities you have given me during my DPhil. I am eternally grateful for the support you have given me, while simultaneously letting me find my own route to develop into an independent researcher.

A major amount of thanks goes to Dr Richard White, for all the assistance you have provided me in the last four+ years, and for all the helpful and interesting discussions, even at odd times of the day. I really appreciate all the time you have invested in me, and all the patience you have shown me. It has all helped me improve and develop myself into a contributing, invested, and hopefully valuable member of the team.

I would like to thank Prof Jim Hinton for introducing me to CHEC and CTA, through the multiple summer placements you offered me while I studied for my MPhys degree at the University of Leicester. Those placements sparked my love for programming, and have led me down this prosperous academic path. Furthermore, I am grateful for the host at the Max-Planck-Institut für Kernphysik during 9 months of my DPhil. I make no secret about how much I loved my time there, and it truly advanced my proficiency as a researcher. I look forward to my continued interaction with MPIK.

A big thanks to all the GCT members, past and present, who enriched not only my work, but also my personal life. Specifically, I would like to thank Andrea De Franco, Tom Armstrong, and Heide Costantini. You three have been some of the biggest help I have from an early point in my DPhil. Furthermore, a big thanks to all those who took the time to proofread my thesis - Tom, Connor, Christoph, Paul, Rich and Garret. You were all a huge help and seriously reduced the stress I was under.

During my journey through undergrad, I met some amazing people who continue to give me immense amounts of happiness and support. Thank you Magda, Ben, Vili, and Viki.

Mum and Dad, you have always believed in me, and you have always encouraged me to be my best. Thank you Mum for all the times we sat together revising for my exams, and thank you Dad for the incessant reminders to keep on top of my homework.

Wiebke, you have been my biggest support during the writing of my thesis. I am so grateful for everything you do. Thank you so much for sacrificing so much of your time to proofread this work. Your advice and reassurances were probably the most valuable thing I received during the past few months. Thank you for being the best partner I could possibly ask for.

Declaration

The material contained within this thesis has not previously been submitted in support of another degree, diploma or other qualification at the University of Oxford, or any other university. The research reported within this thesis was conducted by myself except where otherwise stated. My research was funded by the Science and Technology Facilities Council.

Abstract

The interaction of very-high-energy astrophysical gamma rays with the Earth's atmosphere produces extensive electromagnetic particle cascades. These showers of particles travel faster than the speed of light in air, and consequently emit photons of blue wavelength, known as Cherenkov radiation. The Imaging Atmospheric Cherenkov Telescope (IACT) technique enables the probing of the universe at TeV energies through the detection of these Cherenkov showers. The Cherenkov Telescope Array (CTA) will represent the next leap forward in gamma-ray astronomy, improving on the sensitivity of current IACTs by a factor of 10, encompassing energies from 20 GeV to 300 TeV, and operating as the first open observatory in this field. A major component of CTA are the Small-Sized Telescopes (SSTs), a necessary ingredient in exploring beyond the present energy frontier in gamma-ray astronomy.

One of three proposed designs for the SST is the Gamma-ray Cherenkov Telescope (GCT). Utilising a dual-mirror Schwarzschild-Couder optical design, GCT enables a 9° Field of View (FoV) for a compact camera design. The camera developed for GCT is the Compact High Energy Camera (CHEC). Two prototypes for CHEC have been built, each utilising different compact photosensor technology. CHEC-M features Multi-Anode Photomultiplier Tubes (MAPMTs), a pixelised extension of the Photomultiplier Tube (PMT) technology extensively used by IACTs. CHEC-S features Silicon Photomultipliers (SiPMs), novel photosensors which utilise semiconductor technology for high-resolution photon counting over a large dynamic range. To fully utilise the signal output from these photosensors, and allow the opportunity for future data analysis procedures to be exploited, the signal received from these photosensors are digitised into waveforms following a trigger. These waveforms have a length of 96 samples with nanosecond precision.

In this thesis, the full calibration and signal-extraction pipeline currently adopted by CHEC to reliably extract the Cherenkov signal from the waveforms is presented. The resulting performance of these procedures, and of the camera designs, is explored with respect to the requirements specified by the CTA Observatory. Potential improvements to the camera and calibration implementations are identified, and simulations of CHEC are utilised to demonstrate the performance increase these proposals provide. Consequently, an improvement to the photosensor that would allow the CHEC-S prototype design to comfortably meet the CTA requirements is specified. Testing of these improvements is anticipated to commence in early 2019. Finally, the results of the second on-telescope campaign for the CHEC-M prototype are presented, during which observations of Cherenkov showers and optical measurements of Jupiter were conducted.

Contents

List of Figures	ix
Abbreviations	xiii
Glossary	xvi
1 Introduction	1
1.1 Cherenkov Radiation	1
1.2 Atmospheric Cherenkov Showers	3
1.3 Imaging Atmospheric Cherenkov Telescopes	5
1.4 The Cherenkov Telescope Array	9
1.5 Small-Sized Telescopes	10
1.6 Science with the SSTs	12
2 The Compact High Energy Camera	14
2.1 Introduction	14
2.2 Photosensors	15
2.2.1 Photomultiplier Tubes	16
2.2.2 Multi-Anode Photomultiplier Tubes	18
2.2.3 Silicon Photomultipliers	20
2.2.4 Performance Parameters of SiPMs	22
2.2.5 Excess Noise Factor (ENF)	26
2.2.6 Future	27
2.3 Camera Electronics	28
2.3.1 Front-End Electronics (FEE)	29
2.3.2 Back-End Electronics (BEE)	32
2.3.3 LED Flashers	33
2.4 Signal Digitisation	33
2.4.1 Sampling	33
2.4.2 Triggering	34
2.4.3 Digitisation and Readout	35

3 The CTA System Architecture	37
3.1 Introduction	37
3.2 Requirements	38
3.2.1 B-TEL-1010 Charge Resolution	40
3.2.2 B-TEL-1030 Time Resolution	43
3.2.3 B-TEL-1295 Pixel Availability	44
3.3 Data Level and Flow Model	44
4 Software	49
4.1 Introduction	49
4.2 TARGET Libraries	50
4.2.1 TargetDriver	50
4.2.2 TargetIO	51
4.2.3 TargetCalib	53
4.3 Monte Carlo Software	54
4.3.1 CORSIKA	55
4.3.2 sim_telarray	56
4.4 Reduction Tools	56
4.4.1 ctapipe	58
4.4.2 CHECLabPy	63
4.5 Science Tools	64
4.5.1 Gammapy	65
4.5.2 ctools	66
5 Calibration	67
5.1 Introduction	67
5.2 TARGET Calibration	68
5.2.1 Electronic Pedestal Subtraction	68
5.2.2 Transfer Function	73
5.3 Photosensor Calibration	78
5.3.1 Gain Matching	80
5.3.2 SPE Fitting	82
5.3.3 Flat-Field Coefficients	83
5.3.4 Dead Pixels	87
5.4 Saturation Recovery	87
5.5 Timing Corrections	88
5.6 Future	89

6 Waveform Processing	91
6.1 Introduction	91
6.2 Charge Extraction Methods	92
6.2.1 Peak Finding	94
6.2.2 Integration	97
6.2.3 Approaches Adopted by Other IACTs	99
6.2.4 Performance Assessment	102
6.3 Shower Reconstruction	102
6.3.1 Image Parametrisation	102
6.3.2 Direction Reconstruction	103
6.3.3 Energy Reconstruction	104
6.3.4 Gamma-Hadron Discrimination	105
7 Camera Performance	107
7.1 Introduction	107
7.2 CHEC-S Monte Carlo Model	108
7.3 CHEC-S Charge Resolution	110
7.3.1 Procedure and Datasets	110
7.3.2 Lab Results	112
7.3.3 Lab versus Monte Carlo	115
7.3.4 Night Sky Background	118
7.3.5 Optical Crosstalk	120
7.3.6 Analytical Description	123
7.3.7 Conclusion	124
7.4 CHEC-S Pulse Shape	125
7.5 CHEC-S Time Resolution	127
7.6 CHEC-M	128
8 On-Sky Observations	131
8.1 Introduction	131
8.2 Cherenkov Shower Images	133
8.3 Jupiter Observations	136
8.4 Conclusion	139
8.5 Future	139
9 Summary	140
9.0.1 Outlook	143
Appendices	

A The Silicon Photomultiplier	146
A.1 Introduction	146
A.2 The P-N Junction	146
A.3 Avalanche PhotoDiode (APD)	148
A.4 Geiger-mode Avalanche PhotoDiode (G-APD)	150
A.5 Silicon Photomultiplier (SiPM)	151
B Laboratory Characterisation	153
B.1 Introduction	153
B.2 Filter Wheel	154
B.2.1 Reference SiPMT	155
B.2.2 Camera Correction	156
B.3 Illumination Profile	157
B.3.1 Laser Profile	157
B.3.2 Camera Geometry	158
B.3.3 Total Correction	159
B.4 Absolute Illumination	160
B.5 Average Expected Charge	162
B.6 Consideration of Errors and Uncertainty	163
C SPE Fitting	164
C.1 Introduction	164
C.2 Software	166
C.3 Multi-Anode Photomultiplier Tubes	166
C.4 Silicon Photomultipliers	168
D Transfer Function Investigations	169
D.1 Introduction	169
D.2 TF Generation Approaches	170
D.3 Charge Resolution	171
D.4 Sampling Cell versus Storage Cell	172
D.5 Conclusion	173
E Charge Extractor Investigations	174
E.1 Introduction	174
E.2 Integration Window	174
E.2.1 Optimal Integration Window Parameters	175
E.2.2 Comparison with <i>Cross Correlation</i>	177
E.2.3 Conclusion	180
References	182

List of Figures

1.1	Polarisation produced in a dielectric medium due to the presence of a charged particle.	2
1.2	Geometry of the wavefronts involved in Cherenkov radiation production.	2
1.3	Production of a extended electromagnetic particle cascade.	3
1.4	Comparison of Cherenkov and NSB spectrum.	6
1.5	Photos of modern IACTs.	7
1.6	Differential sensitivity of CTA.	8
1.7	Differential sensitivity of the different CTA telescope types.	9
1.8	The southern-hemisphere Cherenkov Telescope Array.	10
1.9	The three SST designs.	11
2.1	Diagram of a Photomultiplier Tube.	16
2.2	Photomultiplier Tube timing characteristics.	18
2.3	Internals of a Multi-anode Photomultiplier Tube.	19
2.4	Multi-Anode Photomultiplier Tube crosstalk.	19
2.5	Performance characteristics for the SiPMs used in CHEC-S.	22
2.6	Example of the SiPM's PDE dependence on overvoltage.	23
2.7	Illustration of the possible ways optical crosstalk is produced.	24
2.8	Comparison of the single photoelectron multiplication response between CHEC-M and CHEC-S.	27
2.9	Characteristic performance of future CHEC-S SiPMs.	28
2.10	Image of the CHEC-M focal surface.	29
2.11	Image of the CHEC-S focal surface.	30
2.12	Image of the MAPMT and FEE for CHEC-M.	31
2.13	Image of the SiPM and FEE for CHEC-S.	31
2.14	Functional block diagram of the TARGET 5 ASIC.	34
3.1	Charge resolution requirement.	40
3.2	High-level data model hierarchy.	45
3.3	Simplified camera data flow.	46
4.1	Data-flow overview for waveform samples within the TARGET libraries.	51
4.2	CORSIKA extensive air shower simulations.	55
4.3	Contents of the DataContainer object.	59
4.4	Functional block diagram of the EventSource class.	60

4.5	Functional block diagram of the EventSourceFactory class.	61
4.6	Functional block diagram of the <code>ctapipe</code> low-level calibration classes.	63
5.1	Raw waveform.	69
5.2	Comparison of pedestal-subtracted waveform with raw waveform. .	69
5.3	Comparison of calibration stages with a Cherenkov shower image. .	70
5.4	Storage-cell-amplitude dependence on position in the waveform. .	71
5.5	Spread of electronic-pedestal values before and after the pedestal subtraction.	72
5.6	Transfer Function generation waveforms.	74
5.7	Transfer Function lookup tables.	74
5.8	Fit of the waveform in order to extract samples to generate the Alternating Current (AC) Transfer Function.	76
5.9	Gain-Matching Residuals	80
5.10	Comparison of SPE spectra between CHEC-M and CHEC-S.	82
5.11	Flat-field calibration	83
5.12	Flat-field Coefficients	84
5.13	Flat-field residuals.	85
5.14	Flat-field residuals at other illuminations.	85
5.15	Saturation Recovery.	88
5.16	Pulse timing correction for each pixel.	89
6.1	Annotated waveform.	93
6.2	Bright Cherenkov shower image.	95
6.3	Photon arrival time in each pixel for a bright Cherenkov shower. .	96
6.4	Cross correlation stages.	98
6.5	Hillas Parametrisation Schematic.	103
6.6	Shower source location reconstruction.	104
6.7	Shower core location reconstruction.	104
6.8	Discriminating between images of gamma-ray and hadron induced showers.	105
6.9	Hillas width and length from CHEC-S simulations.	106
7.1	Comparison of the SPE spectra between lab measurements and simulations.	109
7.2	CHEC-S measured charge versus average expected charge.	113
7.3	CHEC-S average measured charge versus average expected charge. .	113
7.4	<i>Charge Resolution</i> of the Lab dataset in default units.	114
7.5	<i>Charge Resolution</i> of the Lab dataset with respect to the requirement.	114
7.6	Comparison of the different <i>Charge Resolution</i> procedures.	116

7.7	Comparison of the <i>Charge Resolution</i> at different NSBs.	118
7.8	Comparison of the <i>Charge Resolution</i> at different NSBs using the <i>MCLabTrue</i> procedure.	119
7.9	Comparison of the <i>Charge Resolution</i> at two different NSBs when observing Cherenkov showers (via the <i>MConsky</i> procedure).	119
7.10	Comparison of the <i>Charge Resolution</i> at different values of optical crosstalk.	120
7.11	Comparison of the <i>Lab Charge Resolution</i> with different bias voltages applied to the SiPM pixel.	121
7.12	Analytical fit of the <i>Lab Charge Resolution</i>	124
7.13	Pulse shape versus average expected charge for CHEC-S.	125
7.14	Pulse shape versus average expected charge for a CHEC-S simulation.	126
7.15	CHEC-S <i>Time Resolution</i>	127
7.16	CHEC-M average measured charge versus average expected charge. .	129
7.17	<i>Charge Resolution</i> of CHEC-M.	130
8.1	Photo of CHEC-M installed on the GCT telescope structure.	132
8.2	Photo of the reflection of CHEC-M in the secondary mirror.	133
8.3	<i>Hillas</i> length versus width for an on-sky observation run with CHEC-M.	134
8.4	Selection of on-sky images.	135
8.5	Camera image of the excess baseline RMS for observations of Jupiter.	137
8.6	Camera slices of the Jupiter observations.	137
8.7	Zoom of the Jupiter camera image.	138
A.1	A typical illustration of a P-N Junction.	147
A.2	Illustration of the silicon bandgap.	148
A.3	Diagram of an Avalanche PhotoDiode.	149
A.4	G-APD reverse bias voltage cycle.	150
A.5	Simplified equivalent circuit of an SiPM detector.	151
B.1	Filter-wheel position calibration.	155
B.2	Measured charge versus transmission.	156
B.3	Secondary filter-wheel calibration.	157
B.4	Camera geometry correction schematic.	158
B.5	Illumination profile correction images.	160
B.6	Obtaining relationship between filter-wheel transmission and average illumination.	161
B.7	Calibration from filter-wheel transmission to expected charge. . . .	162
C.1	(Repeated) Comparison of SPE spectra between CHEC-M and CHEC-S.	165

D.1	Comparison of the <i>Poly</i> and <i>Direct</i> Transfer Function lookup tables.	170
D.2	Comparison of the <i>Charge Resolution</i> resulting from each of the Transfer Function generation approaches.	171
D.3	Comparison of the <i>Charge Resolution</i> from the “per sampling cell” versus “per storage cell”.	173
E.1	Definition of integration window on a waveform.	175
E.2	Optimal integration-window parameters.	176
E.3	<i>Charge Resolution</i> comparison between <i>Cross Correlation</i> and <i>Window Integration</i> for <i>Lab</i> data.	178
E.4	<i>Charge Resolution</i> comparison between <i>Cross Correlation</i> and <i>Window Integration</i> for <i>MCLab</i> data with an optical crosstalk of 40 %. .	178
E.5	<i>Charge Resolution</i> comparison between <i>Cross Correlation</i> and <i>Window Integration</i> for <i>MCLab</i> data with an optical crosstalk of 20 %. .	179
E.6	<i>Charge Resolution</i> comparison between <i>Cross Correlation</i> and <i>Window Integration</i> for <i>MCLab</i> data with a high amount of electronic noise.	179

Abbreviations

AC Alternating Current

ADC Analogue-to-Digital Converter

AERIE Analysis and Event Reconstruction Integrated Environment

AGN Active Galactic Nuclei

APD Avalanche PhotoDiode

ASIC Application-Specific-Integrated Circuit

ASTRI Astrofisica con Specchi a Tecnologia Replicante Italiana

BEE Back-End Electronics

CHEC Compact High Energy Camera

CITIROC Cherenkov Imaging Telescope Integrated Read Out Chip

CORSIKA COsmic Ray SImulations for KAscade

CTA Cherenkov Telescope Array

DAC Digital-to-Analogue Converter

DACQ Data-Acquisition

DC Direct Current

DCR Dark-Count Rate

DPPS Data Processing and Preservation System

ENF Excess Noise Factor

FACT First G-APD Cherenkov Telescope

FEE Front-End Electronics

FITS Flexible Image Transport System

FoV Field of View

FPGA Field-Programmable Gate Array

G-APD Geiger-mode Avalanche PhotoDiode

GCT Gamma-ray Cherenkov Telescope

H.E.S.S. High Energy Stereoscopic System

HAWC High-Altitude Water Cherenkov

HV High Voltage

IACT Imaging Atmospheric Cherenkov Telescope

IRF Instrument Response Function

KASCADE KArlsruhe Shower Core and Array DEtector

LST Large-Sized Telescope

MAGIC Major Atmospheric Gamma Imaging Cherenkov Telescopes

MAPMT Multi-Anode Photomultiplier Tube

MST Medium-Sized Telescope

NSB Night-Sky Background

OES Observation Execution System

PDE Photon Detection Efficiency

PMT Photomultiplier Tube

PSF Point Spread Function

QE Quantum Efficiency

RMS Root-Mean-Square

SCT Schwarzschild-Couder Telescope

SiPM Silicon Photomultiplier

SNR Supernova Remnant

SPE Single PhotoElectron

SST Small-Sized Telescope

SUSS Science User Support System

SWIG Simplified Wrapper and Interface Generator

TARGET TeV Array Readout with GSa/s sampling and Event Trigger

UDP User Datagram Protocol

VERITAS Very Energetic Radiation Imaging Telescope Array System

VHE Very High Energy

Glossary

CHEC-M CHEC utilising MAPMTs as the photosensor.

CHEC-S CHEC utilising SiPMs as the photosensor.

FWHM The full width of a pulse (or distribution) at half of its maximum.

Superpixel Group of four neighbouring pixels used for triggering (see Section 2.4.2).

T5TEA ASIC chip used alongside TARGET-C for the trigger handling.

TARGET-5 Version 5 of the TARGET ASIC.

TARGET-C Version C of the TARGET ASIC.

TIO Custom FITS file format defined by TargetIO used for storing waveform data from TARGET-based cameras.

V_{ped} Reference pedestal voltage input into the TARGET ASIC to provide a modest amount of common-mode noise rejection.

1

Introduction

Contents

1.1	Cherenkov Radiation	1
1.2	Atmospheric Cherenkov Showers	3
1.3	Imaging Atmospheric Cherenkov Telescopes	5
1.4	The Cherenkov Telescope Array	9
1.5	Small-Sized Telescopes	10
1.6	Science with the SSTs	12

1.1 Cherenkov Radiation

When a charged particle moves slowly through a dielectric medium, the electric field of the particle distorts the nearby atoms. Momentarily, these atoms are transformed into elementary dipoles where the charged particles that constitute the atom are arranged with respect to the electric field of the travelling particle (Figure 1.1a). Due to the complete symmetry of this polarisation around the travelling particle, no net field is produced by the dielectric medium. However, if instead the velocity of the charged particle is faster than the speed light travels in that medium, an asymmetry along the particle trajectory is formed in the polarisation of the surrounding atoms (Figure 1.1b), resulting in a net dipole field. As the particle continues through the medium, elements of the polarised medium will release a brief burst of electromagnetic radiation. Generally these electromagnetic waves interfere destructively, except inside in the forward direction along the particles trajectory

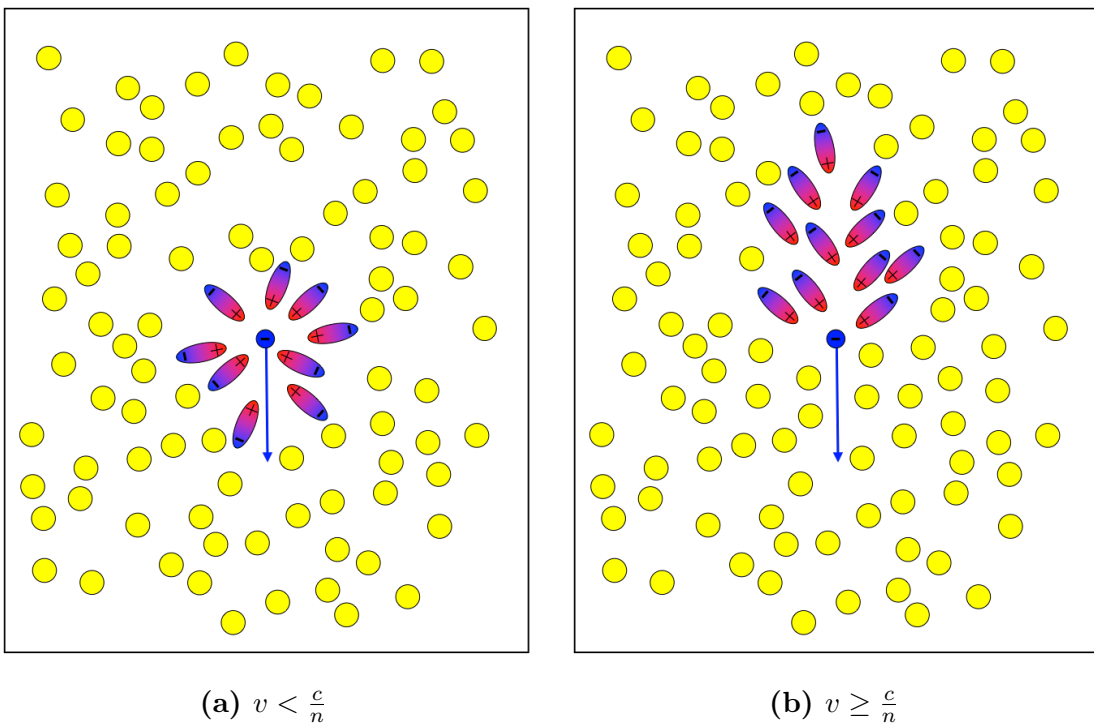


Figure 1.1: Polarisation produced in a dielectric medium due to the presence of a charged particle, for the cases of a non-relativistic and relativistic particle.

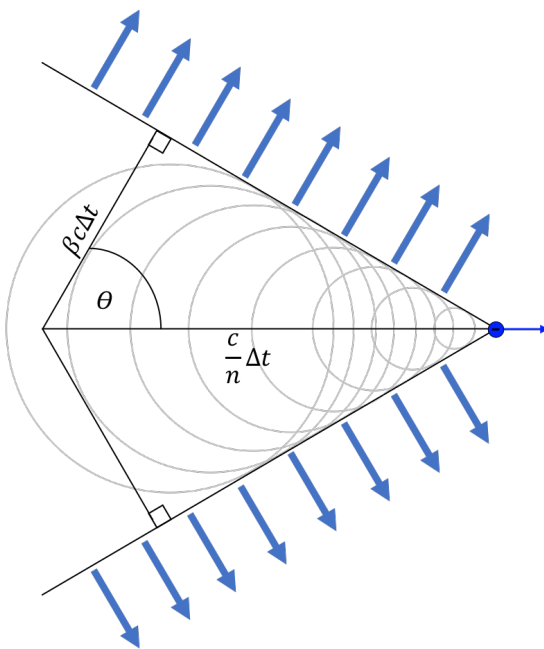


Figure 1.2: Geometry of the wavefronts involved in Cherenkov radiation production. The particle travels at a greater speed than the wavefronts propagate.

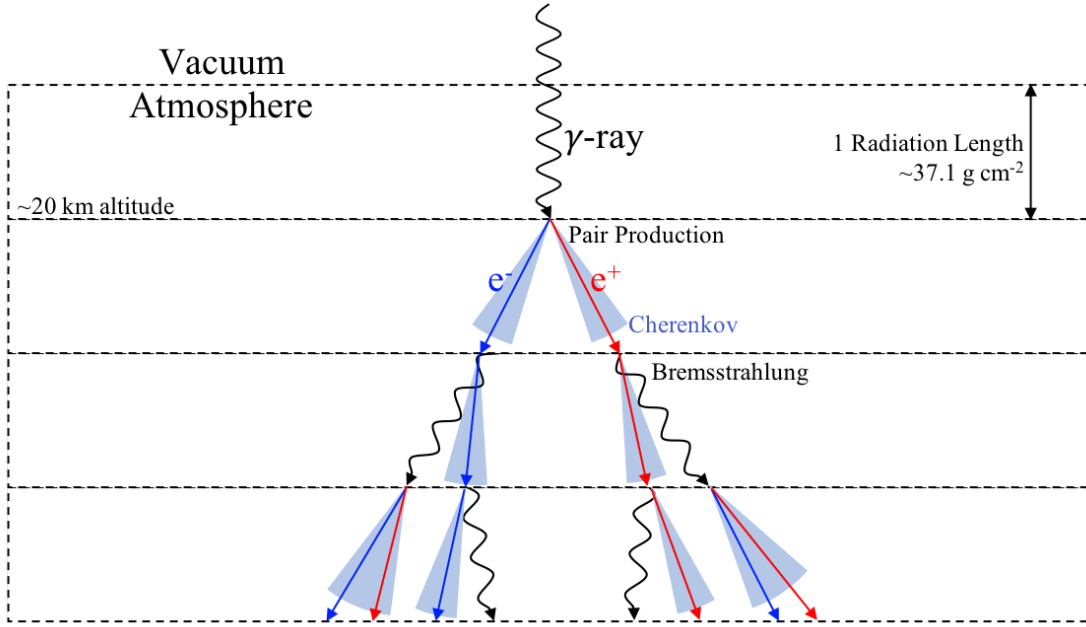


Figure 1.3: Production of an extended electromagnetic particle cascade, demonstrating the different components and interactions.

in an opening angle θ . Although the full characterisation of this relativistic effect is complex, a simple consideration of the geometry involved, shown in Figure 1.2, can be used to describe θ [1]. In a time Δt a particle travels a distance $\beta c \Delta t$ where $\beta = \frac{v}{c}$, while the emitted light will travel a distance $\frac{c}{n} \Delta t$ in a medium with refractive index n . This results in the relation:

$$\cos \theta = \frac{vn}{c}. \quad (1.1)$$

The blue light emitted in this constrained opening angle, via this phenomena, is known as Cherenkov radiation.

1.2 Atmospheric Cherenkov Showers

The Earth's atmosphere is effectively opaque to photon energies above 10 eV [2]. To conduct astronomical observations at higher energies, one must usually leave the Earth's atmosphere, as was done by the Fermi Gamma-ray Space Telescope. However, at energies above $\geq 10 \text{ GeV}$, a “gamma-ray window” in the atmosphere exists where the pursuit of gamma-ray observations can be performed using the

Cherenkov radiation produced by the cascade of particles resulting from the interaction between the gamma ray and the atmosphere.

Two electromagnetic interactions are responsible for the creation of this cascade:

Pair Production The conversion of a photon into an electron-positron pair in the presence of an atom (such as an atmospheric particle). The energy of the photon must exceed the sum of the rest masses of an electron and positron (1.022 MeV). The electron-positron pair share the energy of the progenitor photon, and continue on a similar trajectory. This is the dominating interaction process for photons above ≥ 10 MeV [2].

Bremsstrahlung radiation The emission of a photon due to the interaction of a charged particle with the electric field on an atom (such as an atmospheric particle). This process allows further gamma rays to be produced.

The interplay between these two processes, occurring after each transversal of a radiation length, produces the extensive cascade of energetic electromagnetic particles. This is illustrated in Figure 1.3. The charged particles produced by the pair production in this cascade are responsible for the generation of the Cherenkov light. This cascade is often known as a “Cherenkov shower”.

This cascade continues until the ionisation energy losses are equal to the radiation losses. The number of remaining particles after this point, known as the “shower maximum”, begins to diminish. For a 1 TeV shower this occurs at ~ 8.4 km altitude [2]. The produced Cherenkov light is collimated along the progenitor gamma ray trajectory, and produces a pool of blue light on the ground, with a radius of ~ 120 m [3]. If the direction of the Cherenkov shower is extrapolated back to the cosmic sphere, the location of the source that produced the gamma ray can be inferred. Although the amount of energy that goes into Cherenkov photon production is a tiny fraction of the total energy, the atmosphere acts as a consistent calorimeter, therefore allowing an accurate reconstruction of the progenitors energy from the amount of Cherenkov photons produced.

A further characteristic of the Cherenkov shower is the time profile. The entire shower typically lasts ~ 5 ns. Therefore, despite the abundance of showers in the sky, and the visible wavelength of the Cherenkov light, they are imperceptible by the human eye. Furthermore, due to the faster-than-light velocities of the particles inside the cascade, the last Cherenkov photons produced at the end of the shower reach the ground before the first Cherenkov photons produced at the start of the shower. With different sections of the showers arriving at different times, the Cherenkov shower measurements display a time gradient across the image.

1.3 Imaging Atmospheric Cherenkov Telescopes

A primary issue in Very High Energy (VHE) astronomy is the low flux (~ 0.2 per m^2 per year [4]), requiring a collection area that is not feasible for space telescopes. If instead the Cherenkov showers are used to detect the gamma rays, large arrays of optical telescopes can be built to provide stereoscopic imaging of the Cherenkov showers. These telescopes are known as Imaging Atmospheric Cherenkov Telescopes (IACTs). The multiple stereoscopic views of individual showers provided by arrays of IACTs allow accurate reconstruction of the properties of the shower, such as direction and energy. The topic of reconstruction is discussed in Chapter 6.

As the IACT technique involves imaging the Cherenkov showers, which are much larger than typical astronomy targets, IACTs do not require the resolving power of typical optical telescopes. Instead the priorities of an IACT optical system are to maximise:

- Mirror collection area, such that more photons can be collected. This enables fainter showers to be detected, thereby lowering the energy threshold.
- Field of View (FoV), which improves the surveying capabilities and eases the study of extended sources.

Furthermore, the large collection area provided by the light pool of the Cherenkov shower enables a modest telescope to still make a large amount of gamma ray detections, enabling this technique to be viable despite the small flux.

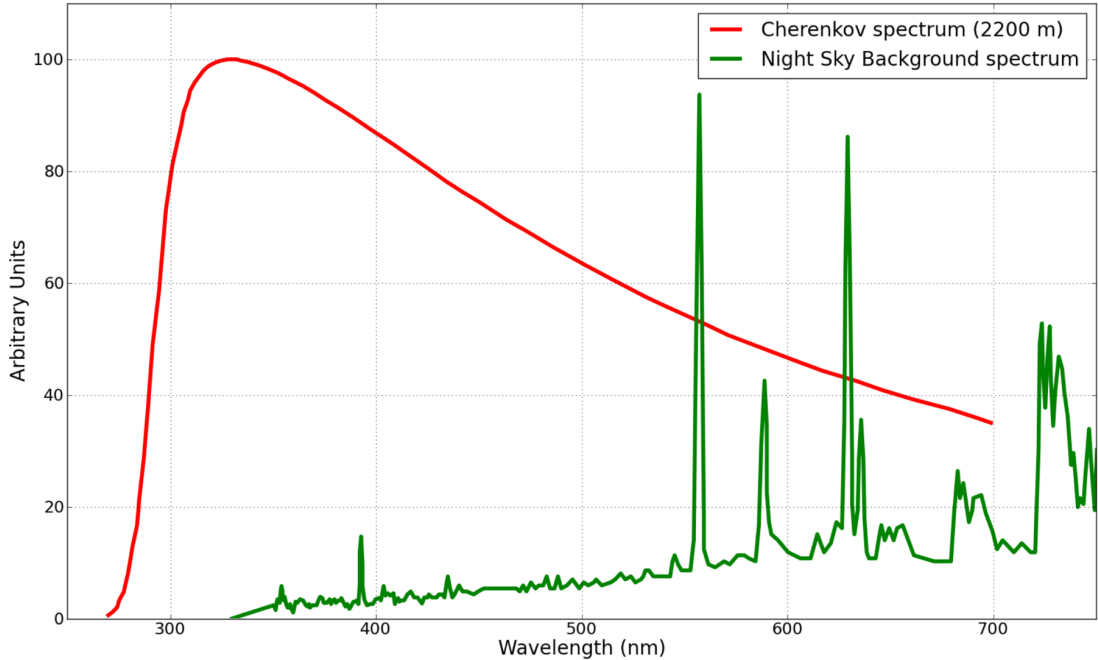


Figure 1.4: Comparison of Cherenkov and NSB spectrum. The Cherenkov spectrum shown is expected at an altitude of 2200 m. The NSB spectrum shown was measured at La Palma [5].

Two major background components need to be accounted for in IACTs:

Cosmic Ray Background Protons (and heavier hadronic nuclei) are also capable of producing Cherenkov showers that are not entirely dissimilar to electromagnetic showers. As these particles are charged, they have been deflected by interstellar magnetic fields on their journey from their source, and therefore cannot be used to reconstruct the location of its source on the sky. Therefore, these showers provide an isotropic background which is 1,000 times as numerous than the shower rate received from the discreet gamma-ray sources. However, a hadronic shower exhibits a morphology that is broader and less symmetric than that obtained from gamma-ray showers. Additionally, distinct features such as “muon rings”, produced by highly penetrating muons reaching low altitudes such that the full Cherenkov cone is visible in a single telescope, accompany hadronic showers. Parametrisations of the Cherenkov shower image therefore enable the discrimination of the hadronic showers (see Chapter 6).

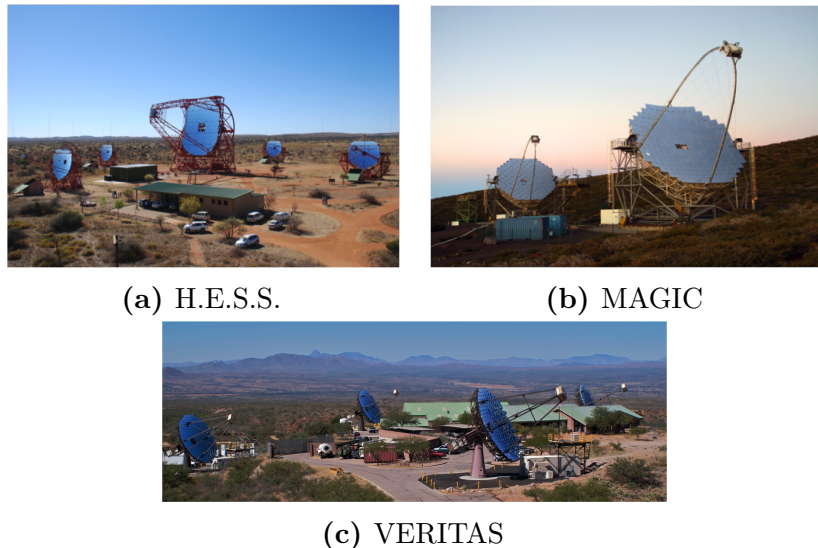


Figure 1.5: Photos of modern IACTs.

Night Sky Background Due to the optical sensitivity of the cameras used by IACTs, the measurements taken are susceptible to starlight, moonlight, and artificial light pollution. The Night-Sky Background (NSB) spectrum for La Palma, compared to the expected Cherenkov spectrum at an altitude of 2200 m, is displayed in Figure 1.4. This background is excluded in two ways. Firstly, smart trigger logic and strict thresholds (such as the one described in Chapter 2) eliminate the triggering on NSB photons. Secondly, unbiased charge extraction technique (described in Chapter 6) exclude this noise from the signal.

The application of the IACT technique was first attempted in the 1960s, but the first large optical reflector built with the purpose of gamma-ray astronomy was the Whipple 10 m telescope in southern Arizona, 1968. At first, gamma-ray astronomy was polluted with unsubstantial claims of transient signals from a variety of pulsars and binaries, but these signals had marginal statistical significance [2, p. 9]. It wasn't until 20 years later, after further development of the technique, that the Crab Nebula was detected by Whipple in 1989, thus reigniting interest in the development of gamma-ray astronomy.

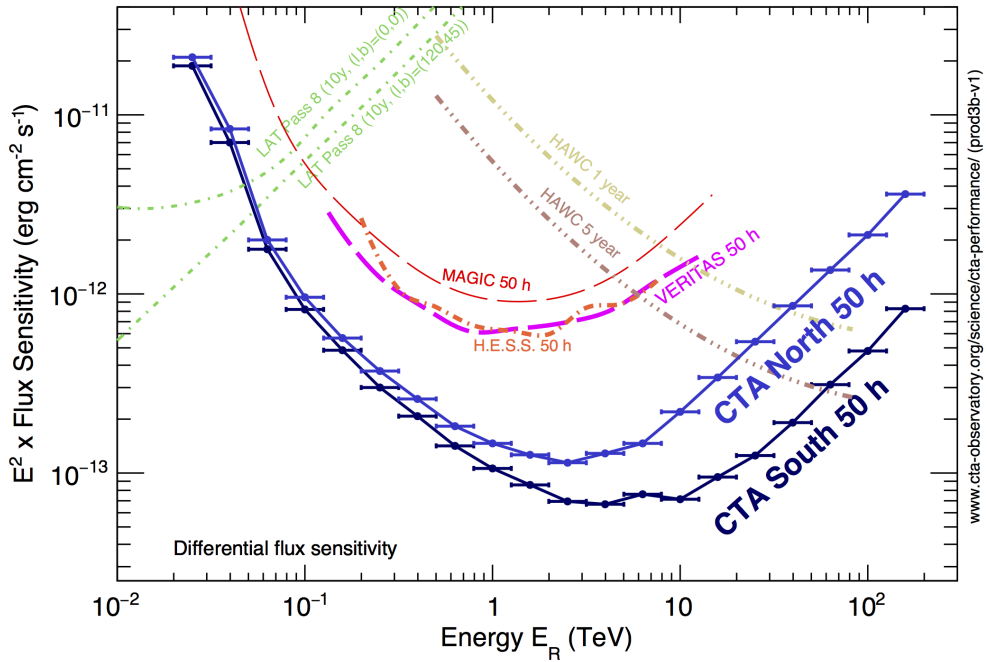


Figure 1.6: Differential sensitivity of CTA predicted by Monte Carlo simulations, compared to the performance of other gamma-ray instruments [6]. The differential sensitivity has been defined as the minimum flux needed by CTA to obtain a 5-standard-deviation detection of a point-like source.

Modern IACTs include MAGIC (Major Atmospheric Gamma Imaging Cherenkov Telescopes), VERITAS (Very Energetic Radiation Imaging Telescope Array System), and the most recent, H.E.S.S. (High Energy Stereoscopic System) (Figure 1.5). All three of these telescope systems operate with the advantage of stereoscopic collaboration. In order to improve on the current IACTs, an array of ~ 100 telescopes was proposed, called the Cherenkov Telescope Array (CTA). This array will have [7]:

- an improved sensitivity of 10 times over previous IACTs (Figure 1.6),
- an observable gamma-ray energy range of 30 GeV to 100 TeV,
- a large ($\sim 8^\circ$) field of view for surveys,
- improved angular and energy resolution,
- and will be the first IACT to operate as an open observatory.

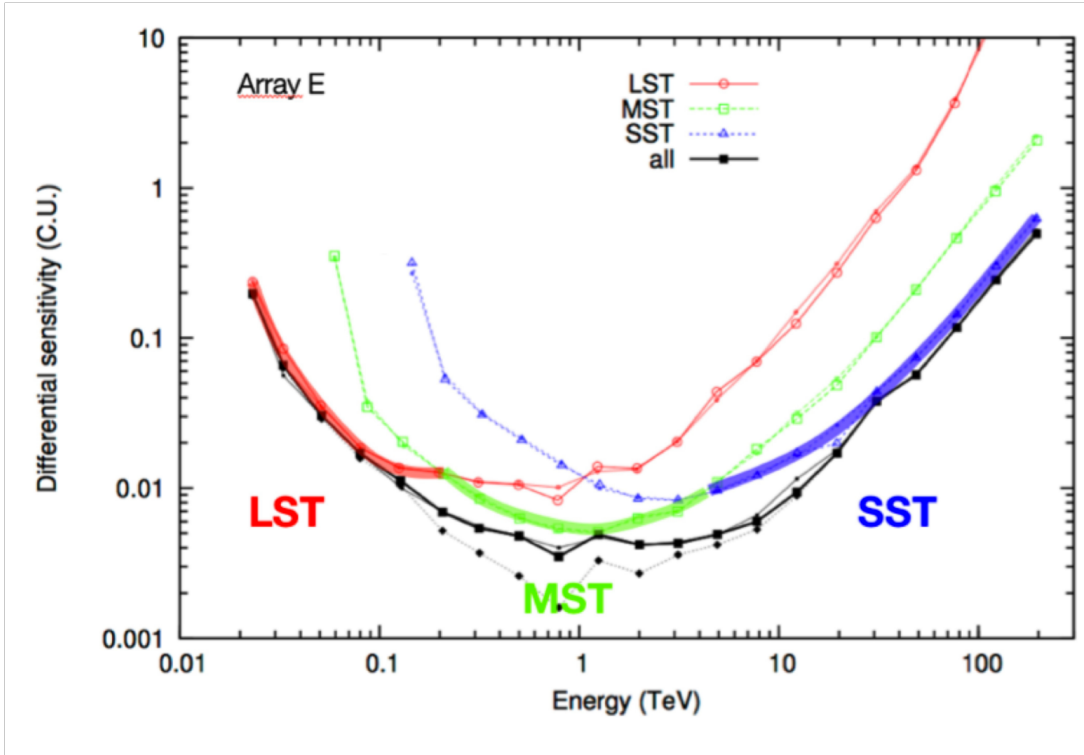


Figure 1.7: Contribution of each telescope type within CTA to the total differential sensitivity [8].

1.4 The Cherenkov Telescope Array

CTA will consist of three different sized telescopes:

- The Large-Sized Telescope (LST), with a mirror diameter of about 23 m to enable the collection of as many photons as possible from the low energy showers (20-150 GeV). Only a few LSTs are needed, as these low-energy showers are relatively frequent.
- The Medium-Sized Telescope (MST), covering the mid-range 0.1-10 TeV with mirror diameters of 12 m.
- The Small-Sized Telescope (SST), monitoring the high energies of 1-300 TeV, with mirror diameters of around 4 m. Only a small mirror area is necessary as the showers at these energies are very bright. However, due to the rarity of higher energy showers, many SSTs need to be spread over an area of several square kilometres, to increase the chance of a detection [7].

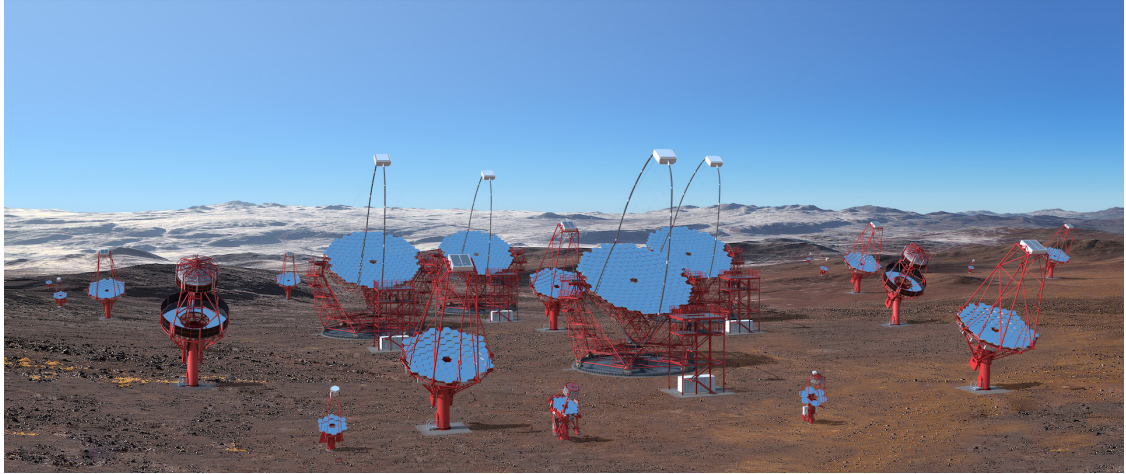


Figure 1.8: Computer-rendered graphic of the southern hemisphere site for the CTA three SST designs: GCT, ASTRI and SST-1M [9].

To illustrate these descriptions, the contributions of each telescope to the sensitivity of CTA is demonstrated in Figure 1.7.

Two CTA sites will exist. A northern hemisphere site for extragalactic observations will be built at La Palma, and is planned to contain 4 LSTs and 16 MSTs. As this site will focus on the energy range from 20 GeV to 20 TeV, no SSTs are included on the northern site. A southern hemisphere site will provide observations of the galactic plane, spanning the full energy range of CTA. Planned to be built nearby the Paranal Observatory in the Atacama Desert in Chile, the southern array is intended to feature 4 LSTs, 15 MSTs, and 70 SSTs, spread over 4 km². A visualisation of the CTA southern array is shown in Figure 1.8.

1.5 Small-Sized Telescopes

Three designs for an SST have been proposed:

- The SST-1M design, a single-mirror Davies-Cotton telescope developed in the collaboration between the Czech Republic, Ireland, Poland, Switzerland and Ukraine. The prototype structure was installed at the Institute of Nuclear Physics in Kraków, Poland in November 2013.

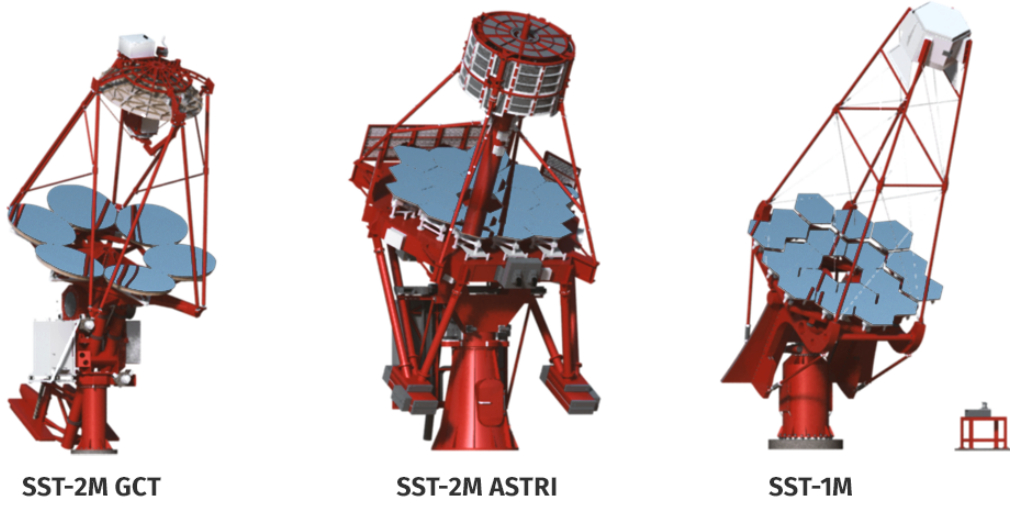


Figure 1.9: Computer-rendered graphics of the three SST designs: GCT, ASTRI and SST-1M [9].

- The ASTRI (Astrofisica con Specchi a Tecnologia Replicante Italiana) design features a dual-mirror Schwarzschild-Couder telescope structure. ASTRI is predominantly developed by Italy, however contributions were provided from Brazil and South Africa [9]. The ASTRI prototype completed construction on Mt. Etna, Italy in 2014.
- The Gamma-ray Cherenkov Telescope (GCT) design also features a dual-mirror Schwarzschild-Couder telescope structure. GCT is being developed through collaboration between Australia, France, Germany, Japan, the Netherlands and the United Kingdom. The prototype telescope structure was inaugurated at the Observatoire de Paris-Meudon, France in November 2015. GCT is the telescope I have been associated with during my DPhil.

Visuals of all three telescopes are shown in Figure 1.9.

The Schwarzschild-Couder optical design was first proposed by German astrophysicist Karl Schwarzschild to eliminate optical aberrations across the FoV. This optical design has since gone through many iterations, however it was never utilised for a reflector telescope due to the complexity and cost required to construct

the mirrors [10]. However, interest in the optical design was recently revitalised by Vassiliev, Fegan, and Brousseau [11], especially as it enables the utilisation of novel compact photosensors. Due to the same adoption of Schwarzschild-Couder optics, the telescopes of ASTRI and GCT have been specifically designed to accommodate the cameras from both SSTs. This increases the possibilities for the final SST design for CTA.

1.6 Science with the SSTs

As shown in Figures 1.6 and 1.7, the SSTs are responsible for exploring beyond the current energy frontier in gamma-ray astronomy. Within 50 hours, the SSTs will be able provide the same sensitivity as five years of observations with the HAWC (High-Altitude Water Cherenkov) observatory [12]. This enables CTA to provide insights into the most energetic processes in the universe, and address prevalent topics of debate in VHE astronomy and particle physics.

The high energy science cases of CTA are mostly concerned with the acceleration mechanisms that produce high energy cosmic rays. This has been an active topic of discussion in the past 100 years since their initial detection. It is therefore hoped that the CTA SSTs can provide new insights into these mechanisms. The different investigations related to this topic can be loosely consolidated into the following categories:

Supernova Remnants It is known that the galactic population of Supernova Remnants (SNRs) play an important role in the acceleration of cosmic rays to high energies. The detection of TeV photons from SNRs (suggesting an efficient acceleration mechanism), and the description of the diffusive shock acceleration mechanism, both corroborate with the detection of high-energy cosmic rays in the Earth’s atmosphere [13]. However, the detection of TeV photons from SNRs could instead be explained by the inverse-Compton scattering between accelerated electrons and the ambient photon background. Therefore, the debate between a leptonic or hadronic origin is still ongoing

[7]. While studies of individual SNRs have improved our understanding of the acceleration mechanisms, a population wide study may help constrain the parameters involved [13]. The probe into higher energies with the SSTs will provide further information about the spectral energy distribution of the currently known SNRs, and the enhanced sensitivity of CTA will increase the population of SNRs known to emit at these energies.

Origin of Cosmic Rays Another important question regarding the locally measured flux of high-energy cosmic rays is their origin [14]. As just described, SNRs do appear to be a dominant source for these particles, but are they the only major contributor to the galactic cosmic rays? Expanding on the discovered VHE galactic source population is the key to answering this question.

Pevatrons A further capability of CTA (provided by the SSTs) is the detection of extreme accelerators that power particles up to the PeV scale. As a result of the acceleration of hadronic cosmic rays to these energies, gamma rays with energies of 100 TeV should be detectable from the accelerator. However, as the cross-section for inverse-Compton electron-photon interactions decreases very quickly above a few tens of TeV [12], the absence of 100 TeV gamma rays from these accelerators would suggest a leptonic origin. The identification of even one Pevatron accelerator would therefore provide a huge breakthrough in the investigations into the origins of VHE gamma rays.

2

The Compact High Energy Camera

Contents

2.1	Introduction	14
2.2	Photosensors	15
2.2.1	Photomultiplier Tubes	16
2.2.2	Multi-Anode Photomultiplier Tubes	18
2.2.3	Silicon Photomultipliers	20
2.2.4	Performance Parameters of SiPMs	22
2.2.5	Excess Noise Factor (ENF)	26
2.2.6	Future	27
2.3	Camera Electronics	28
2.3.1	Front-End Electronics (FEE)	29
2.3.2	Back-End Electronics (BEE)	32
2.3.3	LED Flashers	33
2.4	Signal Digitisation	33
2.4.1	Sampling	33
2.4.2	Triggering	34
2.4.3	Digitisation and Readout	35

2.1 Introduction

Due to the design of GCT as a dual-mirror Schwarzschild-Couder telescope, it is capable of a 9° FoV while simultaneously reducing the plate scale by a factor of ∼3 compared to single-telescope designs. The resulting plate scale value for the GCT design is ∼39.6 mm/° [15]. This large reduction in plate scale allows for a much more compact camera, for which novel opportunities in photosensor technology exist [11].

The appropriate photosensor angular pixel size for an IACT, in order to be less than the FWHM of a typical 1 TeV gamma-ray image, is $\sim 0.2^\circ$. Correspondingly, the GCT camera requires a pixel less than ~ 8 mm. The camera that has been developed for GCT is appropriately known as the Compact High Energy Camera (CHEC).

Two designs have been implemented for CHEC, each featuring a different multi-pixel photon-counting sensor technology. A Multi-Anode Photomultiplier Tube (MAPMT) based camera known as CHEC-M was the first to be commissioned, and received its inauguration on the GCT telescope structure at the Observatoire de Paris-Meudon in November 2015 [16]. A second camera, known as CHEC-S, is currently undergoing commissioning at the Max-Planck-Institut für Kernphysik in Heidelberg, Germany. This camera utilises Silicon Photomultipliers (SiPMs) as its photosensors. CHEC-S also features upgrades to the digitisation chain that were developed since the commissioning of CHEC-M.

This chapter will describe the components of CHEC, covering the photosensor, Front-End Electronics (FEE), and Back-End Electronics (BEE). These descriptions will be focussed on the factors contributed by the components that have a significant influence on the low-level calibration and performance investigations covered in this thesis. Furthermore, the external components and laboratory set-up will be described. Finally, the data output of the camera is described, with specific focus on the characteristics of the waveform readout. The calibration and analysis of these waveforms obtained from the full camera electronics chain is the primary focus of this thesis.

2.2 Photosensors

For a photosensor to be useful to IACTs, it must be:

1. Sensitive to Cherenkov (UV-blue) light.
2. Fast in its response to a signal, which is required to detect the prompt (a few nanosecond) Cherenkov shower flashes.

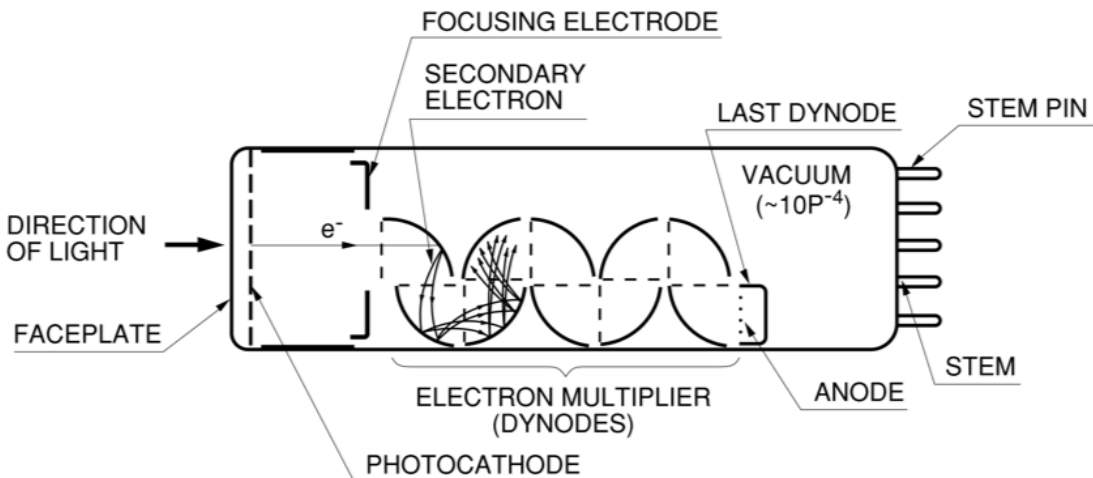


Figure 2.1: Common diagram of a Photomultiplier Tube (box-and-grid type) [17].

3. Cheap, allowing large arrays of them to be combined to fill the full plate scale of the telescope and provide high spatial resolution of the shower.

2.2.1 Photomultiplier Tubes

Since the inception of the Imaging Atmospheric Cherenkov Technique, the photo-sensors used for IACT cameras have almost exclusively been Photomultiplier Tubes (PMTs) [2]. These detectors operate as photon counting devices, where the charge produced by a single photon is amplified into a large current signal that can be read out. The components of a PMT are as follows (using Figure 2.1 for reference):

Photocathode Produces electrons from incident photons via the photoelectric effect. These electrons are often referred to as “photoelectrons”. Associated with a photocathode is its wavelength-dependant probability that a photon will be converted into a photoelectron. This is known as its Quantum Efficiency (QE), and is determined by the compound it is made of. The photocathodes in PMTs are typically sensitive to visible light, with a QE that peaks at $\sim 30\%$ for ~ 400 nm (for the best photocathodes) [17].

Focusing Electrode Ensures that photoelectrons produced at the edges of the photocathode are focussed onto the first dynode.

Electron Multiplier Multiplies the photoelectron into an avalanche of charge.

The High Voltage (HV) across the PMT accelerates the photoelectrons to the first dynode. Upon the impact, the dynode will release a further amount of electrons, the number of which is proportional to the kinetic energy of the incident electron. These secondary electrons are then accelerated to the next dynode, which has a higher voltage than the previous dynode.

Anode Collects the avalanche of charge to produce a measurable current.

The total result of the dynode chain is a proportional amplification from the initial photocathode current I_c to the output anode current I_a . The proportionality factor is known as the gain of the photomultiplier. The gain G depends on the number of dynode stages n , and the value of high voltage applied V [17]:

$$G = \frac{I_a}{I_c} = kV^{\alpha n}, \quad (2.1)$$

where k is a constant that depends on the photomultiplier design, and α is a coefficient determined by the dynode material and geometric structure (typically has values around 0.7 to 0.8).

Due to their wide usage across many fields, PMTs are available at a very reasonable cost. The timing response of PMTs faithfully reproduce the incident light pulse, however the anode's pulse rise time property does modify the response slightly [17]. Additionally, there is a delay in signal due to the electron transit time along the dynode chain. This transit time has an associated “transit time spread” due to the different paths the electrons may take in the dynode chain. These time response characteristics are dependant on the dynode structure and applied voltage. Examples of the typical timing response values are shown in Figure 2.2.

Beyond their low QE, a second disadvantage of a PMT is its high voltage (on the order of 1000 V) requirement [2]. Furthermore, since PMTs generally have ~ 10 dynode stages, Equation 2.1 dictates that a small change in voltage will result in a large variation in gain. The high voltage supply therefore needs to be extremely stable [17]. This is particularly unfavourable for the application

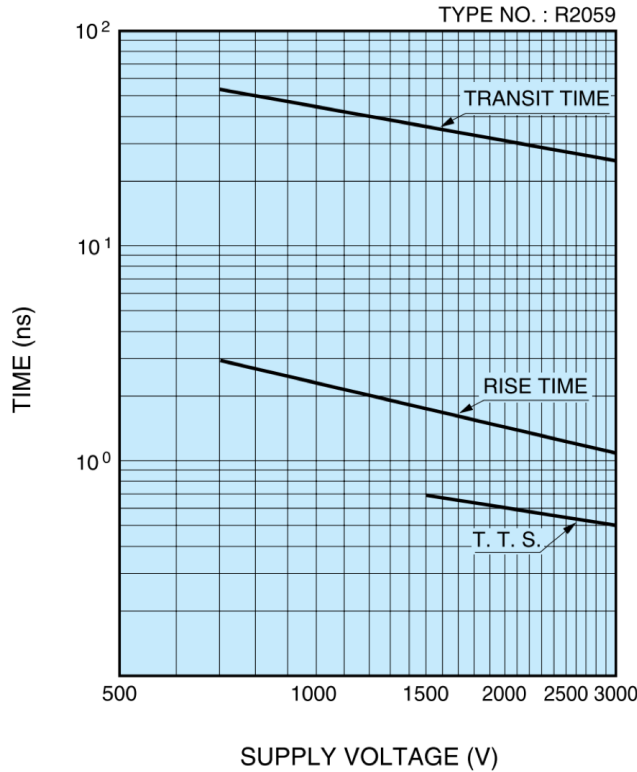


Figure 2.2: Typical values for the timing response of a Photomultiplier Tube [17].

of PMTs in IACTs, due to the typical remoteness of the telescopes. A third disadvantage is the robustness of a PMT, as they are very sensitive to light and can be permanently damaged if exposed to bright sources. This limits the amount of observation time that is safe for IACTs, and considerations such as the moon's location in the sky need to be considered [18].

2.2.2 Multi-Anode Photomultiplier Tubes

In order to be compatible with the reduced plate scale of the telescope, more compact options than PMTs must be found. An extension to the PMT technology is the MAPMT. This photosensor consists of many PMTs arranged in a compact grid to provide position-sensitive detection of light. A diagram of the internal dynode structure for MAPMTs is shown in Figure 2.3. The chosen MAPMT model for CHEC-M is the Hamamatsu H10966B. This flat panel type MAPMT features an 8×8 multianode, resulting in 64 pixels per MAPMT. The entire module's diameter is 49 mm, while each pixel has a diameter of ~ 6 mm. It provides a QE of $\sim 30\%$

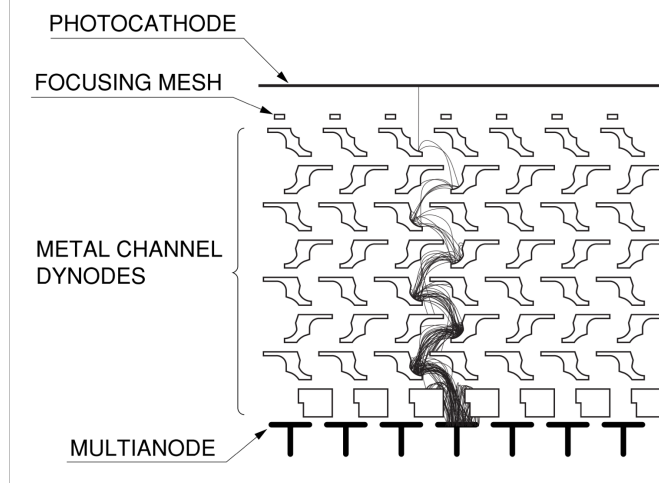


Figure 2.3: Electrode structure of a Multi-anode Photomultiplier Tube, demonstrating an example electron multiplication trajectory [19].

	P1	P2	P3	P4	P5	P6	P7	P8	P8
P1	100	1.3	—	—	—	—	—	—	P16
P9	1.4	0.3	—	—	—	—	—	—	P24
P17	—	—	0.1	0.8	0.2	—	0.2	1.2	P32
P25	—	—	0.5	100	0.7	—	0.7	100	P40
P33	—	—	0.1	0.9	0.2	—	0.2	1.2	P48
P41	—	—	—	—	—	—	—	—	P56
P49	—	—	—	0.3	1.3	0.3	—	—	P64
P57	—	—	—	2.0	100	2.0	—	—	
	P57	P58	P59	P60	P61	P62	P63	P64	

Figure 2.4: Example of the crosstalk present in an MAPMT, measured by using a fibre [20]. The values in each pixel are the relative measured-signal percentage.

at 400 nm wavelength, a typical gain of 3.3×10^5 , and a typical anode rise time and transit time of 0.4 ns and 4 ns, respectively [20].

An important concern when using an MAPMT is the crosstalk. This is the measure of how accurately the signal readout retains its positional information. It is hampered by the broadening of the electron flow in the photocathode and dynode chain. The crosstalk characteristics presented in the technical document

for Hamamatsu H10966B are shown in Figure 2.4.

2.2.3 Silicon Photomultipliers

For a photosensor to be considered as a replacement for the tried-and-trusted PMT technology within IACT astronomy, it must deliver a higher QE for a comparable cost. SiPMs, or its solid state single photon detector precursors, have been actively developed since the 1960s [21]. They have recently matured into a feasible replacement for traditional PMT technology, causing a transitioning trend in the majority of fields that previously relied on PMTs. This trend has been aided by the recent reduction in SiPM cost, offering a modern alternative to MAPMTs for a similar price. The physics behind SiPM technology is more complicated than that of PMTs, therefore a full description of their inner workings is reserved for Appendix A.

As a short summary, an SiPMs microcell consists of a single Avalanche Photo-Diode (APD), operated in Geiger mode (i.e. with a reverse bias voltage past the breakdown voltage). The breakdown voltage is the voltage beyond which the gain of an APD tends to infinity. Therefore, an incident photon (or thermal excitation, i.e. “dark count”) which produces an electron-hole pair in the silicon will consequently cause an avalanche of excess charge carriers, turning the silicon conductive and producing a macroscopic current. As the charge produced in this avalanche is essentially limited by the quenching resistor, the same charge is read out irrespective of the number of incident photons. The APD operated in Geiger mode is therefore referred to as a binary device. By arranging an array of up to 10,000 of these microcells per mm² to form an SiPM pixel, a high resolution photon counting sensor can be produced with a large dynamic range.

The major factors that contribute to the appeal of modern iterations of SiPM technology as a replacement for PMTs are outlined by Ghassemi, Sato, and Kobayashi [22]:

- The transition probability of a photoelectron from a silicon crystal’s valence band to its conduction band is higher than the emission probability achievable

in an alkali-based photocathode. This factor results in a higher attainable QE.

- The semiconductor properties of silicon enable a high collection efficiency of photoelectron charge, resulting in a reduced spread in the amplification of a single photoelectron in comparison to PMTs (in the absence of optical crosstalk considerations, see Section 2.2.5).
- The high electrical conductance of doped silicon enables the low-voltage (of the order of 10-100 V) operation of an SiPM.
- The high fill factor of SiPM pixels and the compactness of the tiles allow a reduced dead space.
- The mechanical reliability in terms of its ageing/warm-up considerations is much better than in PMTs, as well as its performance in magnetic fields.

Additionally, as there is no photocathode to degrade, nor possibility chance for a damaging current to be reached (due to the quenching by the resistor), SiPMs are very robust to excess illuminations of light. This provides IACTs the opportunity to continue observing under bright night sky conditions, such as intense moonlight [18, 23].

The first, and only to date, IACT telescope to adopt SiPMs as the photosensor is FACT (First G-APD Cherenkov Telescope). Operational since 2011, and built on the refurbished HEGRA IACT on the Canary Island La Palma, the 1440 pixel SiPM camera is installed in combination with a 9.5 m^2 single mirror. As reported by Biland et al. [24], FACT has proved that SiPM technology is a viable alternative to PMTs for future IACTs. This conclusion was reached even with the first generation of commercially available SiPMs. SiPMs have gone through considerable improvements since the construction of FACT.

The SiPMs currently used in the CHEC-S prototype are the Hamamatsu S12642-1616PA-50 tiles. These tiles have 256 pixels of size $3 \times 3\text{ mm}^2$. These are combined to provide 64 camera pixels of $\sim 6 \times 6\text{ mm}^2$. The performance parameters of this

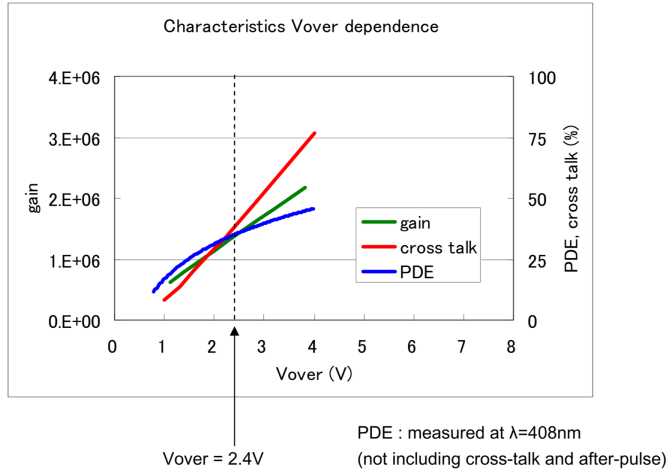


Figure 2.5: Performance characteristics (gain, PDE, optical crosstalk) for the SiPMs used in CHEC-S, copied from the datasheet provided by Hamamatsu [25].

SiPM tile (which are introduced in Section 2.2.4), as measured by Hamamatsu, are displayed in Figure 2.5.

2.2.4 Performance Parameters of SiPMs

For a complete investigation into the performance obtained from the CHEC-S camera, it is important to understand the influence of the characteristic parameters of an SiPM.

Gain

As the charge read out from a SiPM microcell is quantised by the quenching resistor, the gain of an SiPM is characterised with the following simple relation between the capacitance of microcell diode C and the overvoltage ΔV applied [26]:

$$G = \frac{C \Delta V}{e}, \quad (2.2)$$

$$\Delta V = V_{bias} - V_{br}, \quad (2.3)$$

where e is the electron charge, V_{bias} is the bias voltage, and V_{br} is the breakdown voltage. Consequently, the total charge Q , in units of coulombs, output from SiPM pixel is proportional to the number of fired microcells N_{fired} :

$$Q = N_{fired} \times G \times e. \quad (2.4)$$

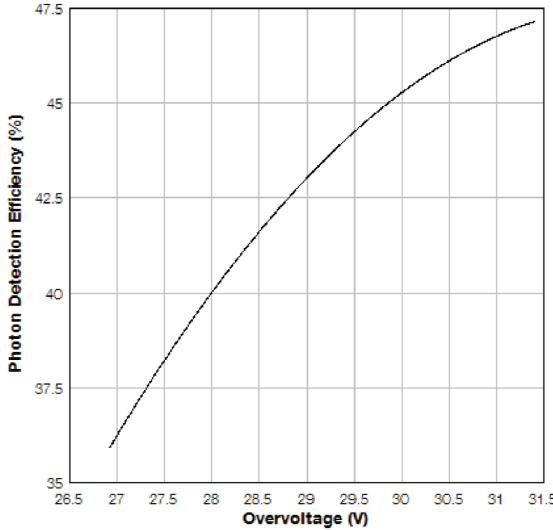


Figure 2.6: Example of the SiPM's PDE dependence on overvoltage [26].

This well-described quantisation of the charge is the reason for the high photon counting resolution of SiPMs.

Photon Detection Efficiency (PDE)

The Photon Detection Efficiency (PDE) of an SiPM is the measure of its wavelength-dependant sensitivity to photons. Due to the microcell structure, this property differs slightly to the QE of a PMT. Qualitatively, it is the statistical probability that an incident photon produces an avalanche. Quantitatively, as shown in the SensL SiPM technical note [26], it is defined as the product between the silicon's:

- Quantum Efficiency $\eta(\lambda)$ - Likelihood of a photon producing an electron-hole pair.
- Avalanche Initiation Probability $\epsilon(V)$ - Probability of a produced excess charge carrier initiating an avalanche.
- Fill Factor F - Ratio of active to inactive area.

Resulting in the equation:

$$PDE(\lambda, V) = \eta(\lambda) \times \epsilon(V) \times F. \quad (2.5)$$

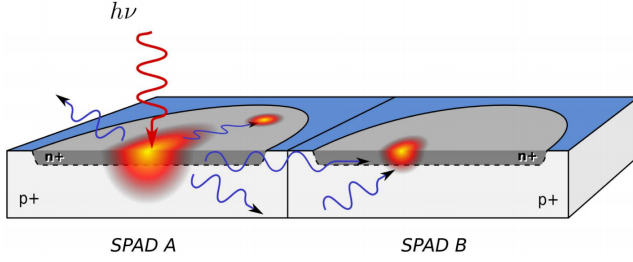


Figure 2.7: Illustration showing the different routes for secondary photon to produce optical crosstalk in adjacent microcells [27].

The dependence of the PDE on its overvoltage is indicated in Equation 2.5 and Figure 2.6. As the overvoltage is increased, $\epsilon(V)$ approaches 1, and the PDE saturates.

Dark Counts

As mentioned in the description of the behaviour of an SiPM microcell, an excess charge carrier can be released from a semiconductor atom through thermal excitation, which then produces an avalanche. This is commonly referred to as a “dark count” (as there was no photon to cause the avalanche), and produces a single photoelectron signal in the SiPM pixel. The Dark-Count Rate (DCR) is the associated measure of this phenomena, quoted in Hz. It is a function of active area, overvoltage and temperature. Although dark counts are also present in PMTs, they are much more prominent in SiPMs.

Optical Crosstalk

During the avalanche process, it is possible for the accelerated charge carriers to produce secondary photons. These photons are able to travel significant distances through the silicon, and could create an electron-hole pair in adjacent microcells. The electron-hole pair for each cell will create an additional avalanche, and possibly create further secondary photons. In Figure 2.7 the various routes a secondary photon can travel to a neighbouring microcell are shown. Not only can secondary photons travel directly to the neighbouring cell, they can possibly be reflected on the boundaries of the silicon, returning to produce an electron-hole pair in the avalanche region [27].

This process happens instantaneously. Therefore, according to Equation 2.4, a single photoelectron/dark-count signal can result in a measured charge N_{fired} times greater than the expected charge of $G \times e$ coulombs. I.e. a single photon may generate a signal equivalent to two or three photons [26]. The value associated with optical crosstalk is its probability that an avalanching microcell will cause an avalanche in a second cell. As with the other parameters discussed so far, the optical crosstalk increases with overvoltage.

Afterpulsing

Another phenomena that can occur as a result of the avalanche is the afterpulsing. This is where an excess charge carrier becomes temporarily trapped in a defect of the silicon, before being released and continuing on their avalanche. The afterpulse probability also increases with overvoltage, however modern SiPMs have severely diminished this probability [22, 26].

Temperature Dependence

Aside from the dark counts, none of the SiPM parameters described in this section have a direct dependence on temperature. However, they do all have a dependence on overvoltage, and consequently, the breakdown voltage. The primary influence of an increase in temperature on an SiPM is a linear increase in the breakdown voltage. The proportionality coefficient for the SiPMs used by CHEC-S is reasonably small, at 60 mV/°C. Nevertheless, a large variation in temperature would result in a change in the SiPM performance parameters.

To keep the temperature controlled and low (to minimise the DCR), the SiPMs in CHEC-S are thermally bonded to a liquid cooled faceplate (Figure 2.11). Furthermore, by changing the bias voltage in response to a change in temperature, the same overvoltage can be maintained, therefore minimising dependence on temperature for the parameters. This process is known as “bias compensation”, and is mentioned again in Section 5.3.

2.2.5 Excess Noise Factor (ENF)

A common expression for the variation in photosensor response to a single photoelectron is its Excess Noise Factor (ENF). This factor encompasses the multiplicative errors in the amplification process for both the MAPMT and SiPM.

The dominating contributions to the ENF in a PMT are the fluctuations in the secondary multiplication factor at each dynode. This is a statistical fluctuation due to cascade multiplication. The multiplication factor can also differ across a dynode, therefore the trajectory of the electron can change the read out amplitude [19]. Conversely, the multiplication of charge in an SiPM is very quantised, due to the microcells being operated in Geiger mode, and therefore functioning as binary device. This would suggest the ENF of an SiPM is very close to 1. However, due to the statistical fluctuations caused by the optical crosstalk and afterpulsing of the device, the ENF is not perfect. Therefore, the ENF of an SiPM has the potential of being worse than that of a PMT, despite the extremely high photoelectron counting resolution [28].

As described by Teich, Matsuo, and Saleh [29], the ENF σ_{ENF} can be expressed in terms of the photomultiplier's average gain μ_G and the gain variance σ_G^2 :

$$\sigma_{ENF} = 1 + \frac{\sigma_G^2}{\mu_G^2}. \quad (2.6)$$

As suggested by Equation 2.6, a perfect photomultiplier with zero multiplication variance would have an ENF of 1. This representation of the ENF can be visualised in terms of the multiplication response/probability of a single photoelectron in the photomultiplier. Figure 2.8 demonstrates this response for the MAPMTs of CHEC-M and the SiPMs of CHEC-S.

Using Equation 2.6, σ_{ENF} is calculated from the mean and variance of the single photoelectron multiplication response for each camera, and displayed in the legend of Figure 2.8. The ENF of the SiPMs is quite large and almost comparable to the ENF of the MAPMTs. The reason for this, as demonstrated in Chapter 7, is the high optical crosstalk (35-40 %) present in this iteration of SiPMs.

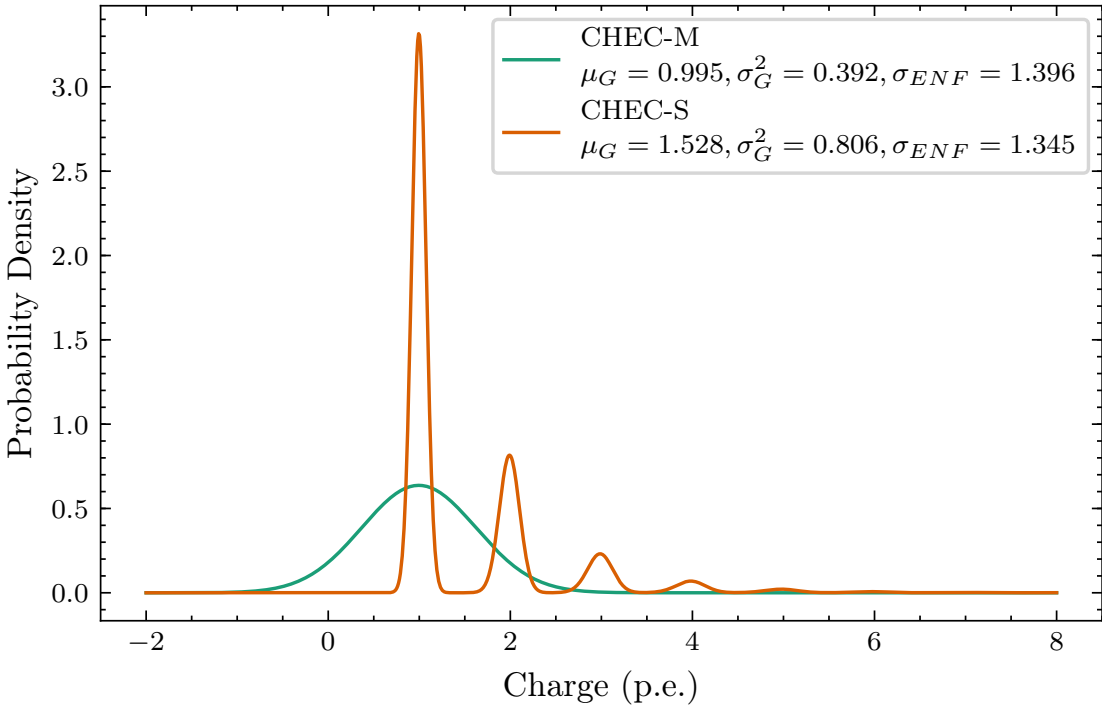


Figure 2.8: Comparison of the single photoelectron multiplication response between CHEC-M and CHEC-S, demonstrating the difference in ENF between the two detector types. The characteristic parameters for the photosensors, used to create this plot, are obtained from the fits described in Appendix C.

The ENF is a key ingredient to the *Charge Resolution* CTA Requirement introduced in Section 3.2.1, and will be further explored in the performance results of the camera in Chapter 7.

2.2.6 Future

It is clear from Figure 2.8 that the main area of improvement to be made in the SiPM chosen for the final design of CHEC is in the optical crosstalk. Producers of SiPMs are actively developing techniques to achieve this with minimal impedance of other characteristics such as the PDE. One simple approach to reduce the optical crosstalk is the inclusion of “trenches” between the cells [30, 31]. This is a form of optical isolation achieved by creating trenches around each cell and filling them with oxide and metal to absorb secondary photons. However, this addition can reduce the fill factor of the SiPM, thereby reducing the PDE via Equation 2.5. Although these trenches stop the majority of secondary photons, which have a direct

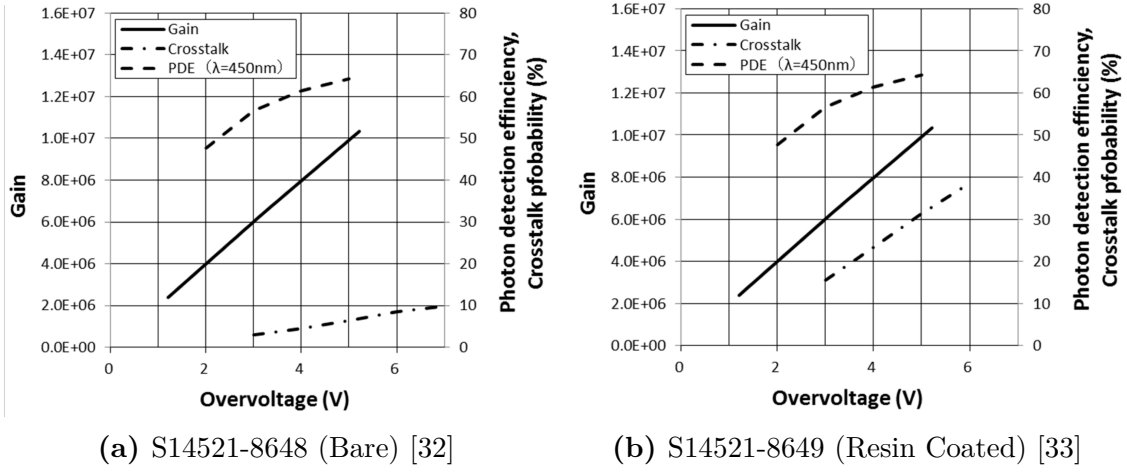


Figure 2.9: Characteristic performance of two potential SiPM productions for the use in future CHEC-S prototypes.

path to the neighbouring microcell (Figure 2.7), they do not affect the photons that take an indirect route via reflection. The trenches therefore reduce optical crosstalk, but does not eliminate it completely.

Two SiPM productions by Hamamatsu are being considered for the next CHEC-S prototype. S14521-8648 exhibits a greatly reduced optical crosstalk, down to <10% (shown in Figure 2.9a). S14521-8649 is the same silicon design, but has a protective resin coating to reduce the chance of damage to the pixels. The optical crosstalk of this second silicon is slightly higher (shown in Figure 2.9b) as the coating allows another surface for secondary photons to reflect into neighbouring microcells. If it is deemed that the protective coating is unnecessary, the former SiPM will be chosen to maximise performance. We expect to be able to begin testing these new SiPM productions in early 2019.

2.3 Camera Electronics

The fully built prototypes of CHEC-M and CHEC-S, including the fitted photosensors, are shown in Figures 2.10 and 2.11. This section will discuss the internal electronics belonging to each of the prototype cameras.

The internal electronics of CHEC can be categorised as either FEE or BEE. The distinction is made in their position in the camera, and the number of photosensors



Figure 2.10: Focal surface of the CHEC-M prototype, annotated with key components. Adapted from Zorn et al. [34].

that are handled by them. A single FEE module is required per photosensor, whereas the BEE handle entire camera, obtaining the data from each of the FEE modules.

2.3.1 Front-End Electronics (FEE)

The FEE of the camera handle the recording of the signal from the photosensors into a digital data stream for storage, calibration, and subsequently the analysis. Images of the FEE modules for the two CHEC prototypes are shown in Figures 2.12 and 2.13.

The first stage in extracting the signal from the photosensors is the amplification and shaping of the analogue signal. The primary reason this is performed is to ensure the signal pulses have the optimal shape for triggering. The optimal pulse is dictated from Monte Carlo simulations to be around 5-10 ns FWHM and a 10-90 % rise time of 2-6 ns [34]. If the pulse shape is faster than this specification, the pulses from individual Cherenkov photons are unable to pile up to produce a trigger due to their intrinsic time gradient (Section 1.2). Conversely, if the pulse is slower, NSB

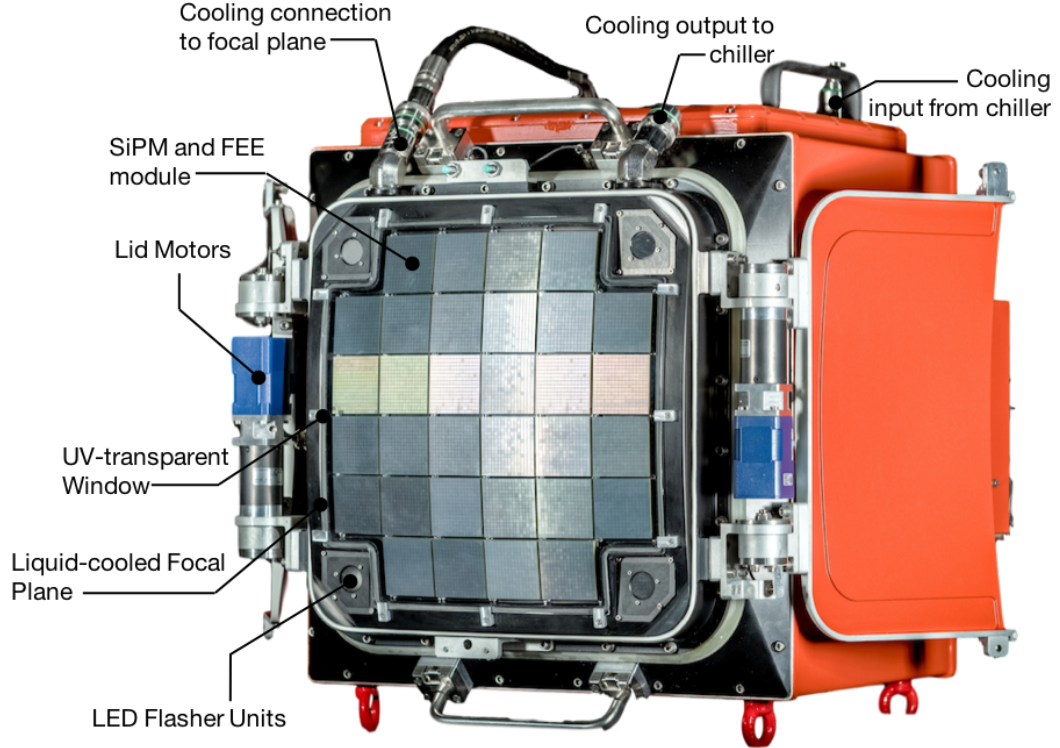


Figure 2.11: Focal surface of the CHEC-S prototype, annotated with key components.

photons are able to produce a trigger. The amplification and shaping is achieved with either the external preamplifier (CHEC-M) or the amplifier and shaper circuits built into the TARGET-C module (CHEC-S).

The second component of the FEE is the TARGET (TeV Array Readout with GSa/s sampling and Event Trigger) module. These modules are composed of [37]:

- the sampling ASIC (Application-Specific-Integrated Circuit),
- the Analogue-to-Digital Converters (ADCs) for digitising,
- the triggering ASIC,
- the Field-Programmable Gate Array (FPGA) to initiate and handle the readout,
- and the internal Digital-to-Analogue Converter (DAC) for setting the operational values for the components.

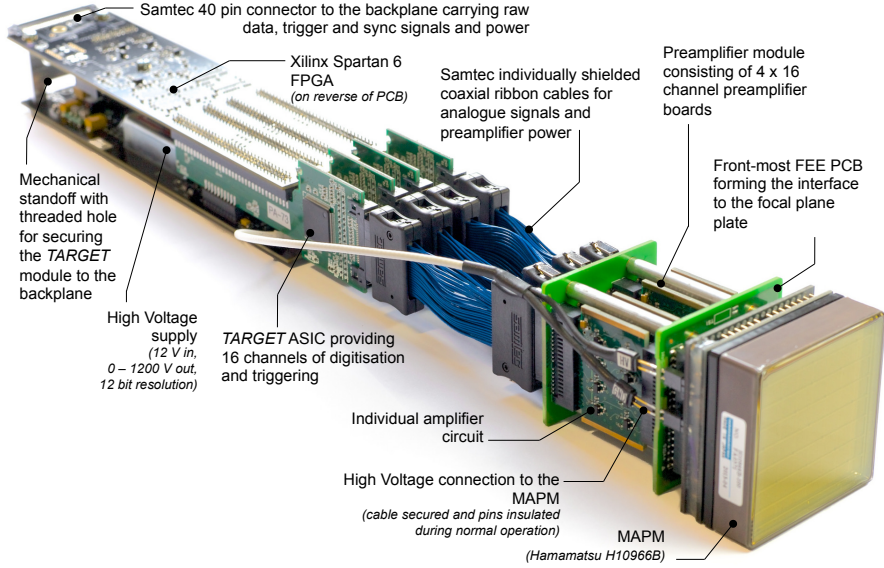


Figure 2.12: Image of the MAPMT connected to the CHEC-M FEE with the components labelled [34, 35].

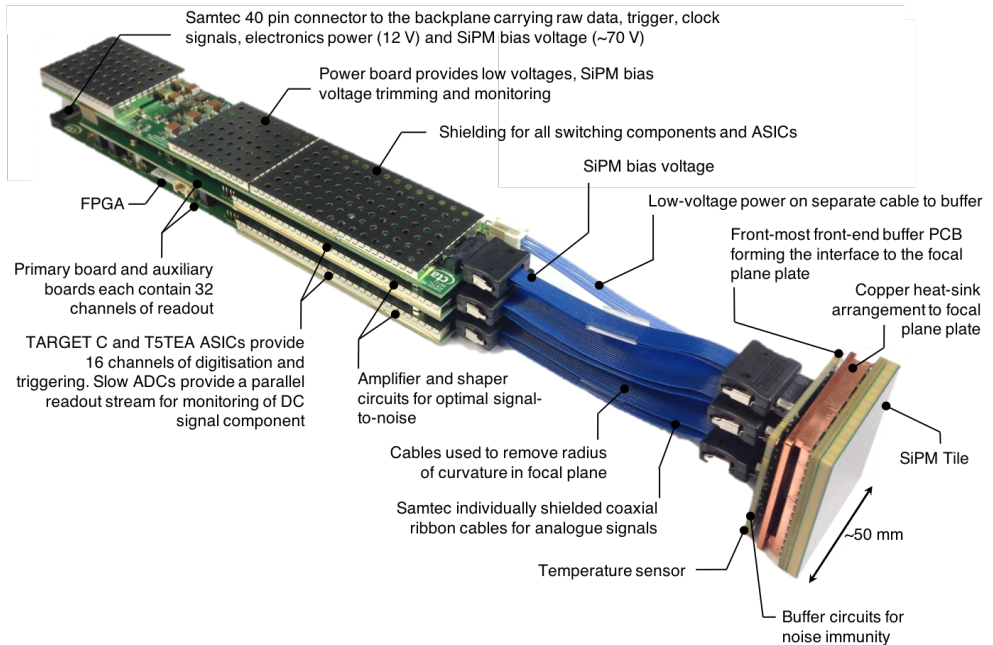


Figure 2.13: Image of the SiPM connected to the CHEC-S FEE with the components labelled [36].

By keeping the TARGET modules limited to this small list of components, they are kept affordable and reliable. Two TARGET modules versions have been integrated into CHEC prototype cameras so far. CHEC-M utilised the TARGET-5 modules (Figure 2.12), named as such due the TARGET-5 ASIC housed in the module. The TARGET-5 ASIC is responsible for both the sampling and the triggering [38]. Meanwhile, CHEC-S uses the latest TARGET module design, often referred to as TARGET-C. This version of the module has split the sampling and triggering between two ASICs to reduce the interference between the two functionalities (thereby improving trigger performance [37]). The sampling and trigger ASICs are known as TARGET-C (hence the module's name) and T5TEA, respectively.

Each ASIC has 16 input channels, associated with 16 photosensor pixels. Therefore, each TARGET module contains four of each ASIC to accommodate all 64 pixels on the photosensors. Both cameras contain a total of 32 FEE modules arranged in a grid, producing the curved focal surface of the camera. This 1 m radius of curvature is required by the Schwarzschild-Couder optics to ensure that the focus of the optics is constant over the field of view (i.e. prevent astigmatism) [11]. The flexibility of the ribbon cables installed between the photosensor and TARGET module allow for this curved alignment, while keeping the module drawers in the camera enclosure simple. The combination of these 32 FEE results in a camera with 2,048 pixels.

Aside from the photosensor, the version of TARGET used in the camera is the only other major differing components between CHEC-M and CHEC-S related to the waveform readout.

2.3.2 Back-End Electronics (BEE)

The BEE also consists of two components [34]:

Backplane Responsible for providing the power, clock and trigger to the FEE modules. It is also responsible for routing the raw waveform data from the FEE to the Data-Acquisition (DACQ) boards.

DACQ Boards Provides a communication link between the camera server PC and the FEE modules. This link is also used for the transfer of raw waveform data. Two boards are used, each connected to 16 FEE modules via 1 Gbps Ethernet links. The connection between a single board and the PC is via two 1 Gbps fibre-optic links. One fibre-optic link is for the downlink, the other for the uplink, ensuring communication with the camera can be maintained during data taking. Data is sent to and from the FEE modules via a custom format over UDP (User Datagram Protocol). To ensure the 1 Gbps uplink is not saturated by the traffic from the 32 1 Gbps links to the FEE, controlled delays between packet sending are utilised.

2.3.3 LED Flashers

An additional component of the camera electronics relevant to this thesis are the LED flashers. Located in each corner of the camera focal surface (Figures 2.10 and 2.11), these units will provide uniform illumination of the camera via reflection in the secondary mirror. The illumination provided by the LED flashes is configurable, and will allow in situ calibration of the camera’s photosensors [39].

2.4 Signal Digitisation

This section will detail the steps of processing the analogue signal received from each photosensor pixel. The description given here is applicable to both CHEC-M and CHEC-S.

2.4.1 Sampling

Designed specifically for the readout of short Cherenkov signal observed with IACT cameras, the TARGET ASIC provides high sampling rates of 1 GSa/s (10^9 samples per second) per channel [37]. The sampling of the ASIC is performed by an array of “sampling cells” and “storage cells”. Each cell physically corresponds to an individual switched capacitor. The sampling array consists of two blocks of 32 cells, corresponding to 64 ns of readout in total. By operating these blocks in a “ping pong”

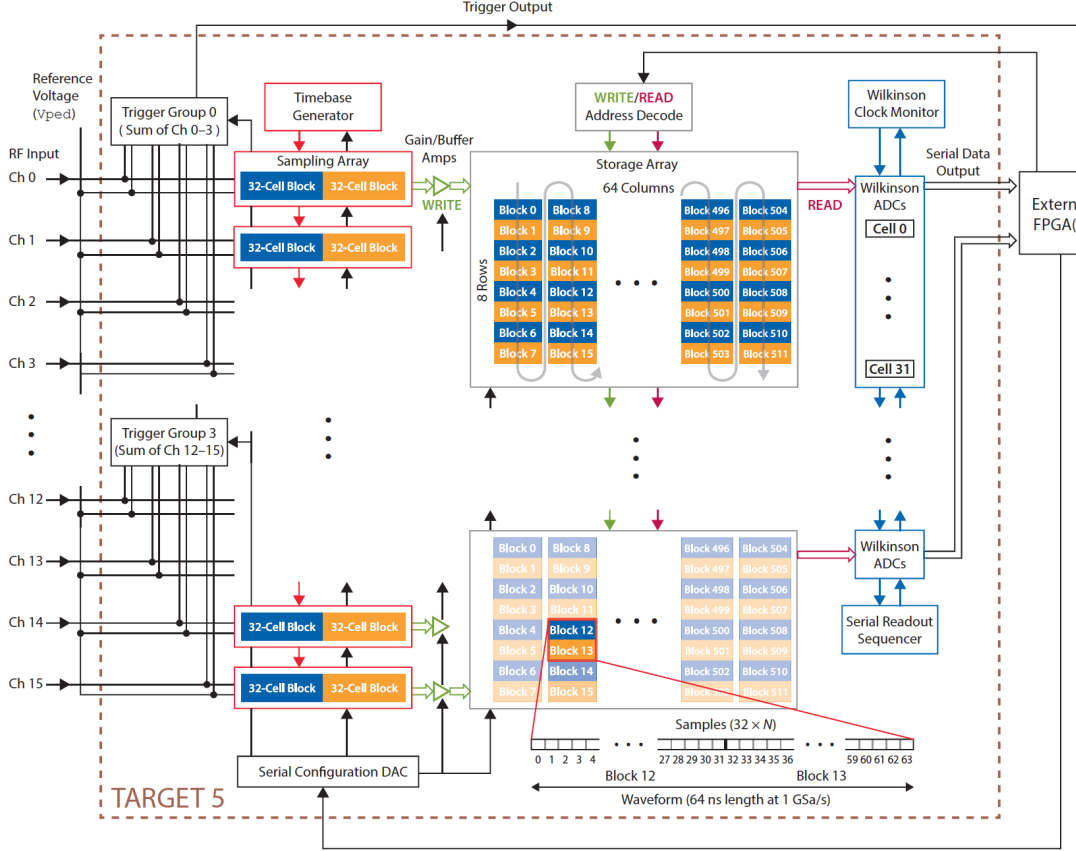


Figure 2.14: Functional block diagram of the TARGET 5 ASIC, demonstrating the sampling, digitisation, and read out processes [38].

mode, the signal from a photosensor pixel can be sampled by one block while the other block is buffered to the storage array. The storage array contains a maximum of $2^{14} = 16,384$ cells, enabling a buffer depth of up to $\sim 16 \mu\text{s}$ [37]. This process is performed in parallel for each of the ASIC channels, and each channel has its own sampling array and storage array. A schematic of the arrays is shown in Figure 2.14.

2.4.2 Triggering

The camera can be either externally triggered (e.g. by using a pulse generator), or internally triggered according to signal generated by the trigger-responsible TARGET ASIC (TARGET-5 or T5TEA). The trigger relies on a two-way communication between the FEE and BEE. The internal trigger operates as follows [34]:

1. The camera pixels are split into square groups of four neighbouring pixels.

These are hereafter referred to as a Superpixel. CHEC therefore has 512 superpixels.

2. The TARGET ASIC responsible for the trigger continuously generates an analogue sum of the photosensor signal on a per superpixel basis.
3. If the analogue sum in a superpixel is greater than a (configurable) threshold, then a digital signal is produced with a (configurable) coincidence time length. A signal is produced per superpixel over the threshold, and sent to the trigger FPGA on the backplane.
4. If there is a coincidence in digital signal between any two neighbouring superpixels then a readout request is sent from the backplane trigger FPGA to all of the TARGET modules.

As this trigger logic requires a simultaneous trigger signal between two neighbouring superpixels, the probability that the camera is triggered from an NSB photon is significantly reduced. In situations where high NSB is present, the threshold may need to be increased, reducing the Cherenkov shower detection rate. The trigger and digitisation rate that CHEC is capable of is 600 Hz, which matches the expected Cherenkov shower rate for gamma rays above 1 TeV [34].

2.4.3 Digitisation and Readout

Included inside the trigger request sent from the backplane is a 64-bit nanosecond counter, known as a TACK. The value of this counter is compared to the counter in the FPGA onboard the TARGET module to determine the look-back time in the ASIC buffer [34]. Starting from the buffer look-back time, the analogue signals stored in the storage capacitors are digitised with the Wilkinson ADC for the user-specified number of cells [37]. The output of this digitisation is a list of 12-bit samples collectively known as the waveform. The number of samples in a waveform corresponds to the number of cells digitised, and must be a multiple of 32. Typically, the number of samples is usually configured to be either 96 or 128 samples per

channel. The units of these raw digitised samples is referred to as “ADC” or analogue-to-digital counts. In addition to the signal from the photosensors, the samples contain electronic noise from the sampling and digitisation chain. Techniques to extract the Cherenkov signal in the presence of this noise, and other noise sources (such as NSB photons and dark counts) are discussed in Chapters 5 and 6.

The waveforms per channel are delivered to the TARGET FPGA, where they are packaged into a UDP packet, and sent to the DACQ boards. The packets from each pixel are then combined, before they are sent to the camera server PC for storage. Sampling continuous on the TARGET ASIC during digitisation, enabling the TARGET module to be dead-time free.

3

The CTA System Architecture

Contents

3.1	Introduction	37
3.2	Requirements	38
3.2.1	B-TEL-1010 Charge Resolution	40
3.2.2	B-TEL-1030 Time Resolution	43
3.2.3	B-TEL-1295 Pixel Availability	44
3.3	Data Level and Flow Model	44

3.1 Introduction

Due to the large scope of CTA, in both its construction and operation, a formal approach towards a system architecture was adopted [40]. One important aspect within this architecture is the distinction between the CTA Consortium and the CTA Observatory. The CTA Consortium is a group of scientists responsible for directing the science goals of the observatory, and for developing software and hardware (including cameras), which are supplied to the observatory as in-kind contributions. The consortium consists of 200 institutes across 31 countries [41]. Conversely, the CTA Observatory is the major astronomical facility that acquires the science data and delivers them to a wide user community as an open observatory. The CTA Observatory gGmbH is the legal entity for CTA in the preparation for the implementation of the CTA Observatory, and works in close cooperation with

the consortium during this process [42].

The purpose of the CTA Architecture is to ensure a coherent view of the functionality and capabilities of CTA. The CTA Architecture can then drive the pre-construction phase to guarantee:

- a coherent development process,
- the seamless integration of the developed units into the final array,
- and that the performance of the final array is capable of meeting its science goals.

During this chapter I will describe two concepts that are connected to the CTA Architecture that are important in the context of this thesis. Firstly, the CTA requirements which all cameras, including CHEC, must meet. Secondly, the descriptions of how data are handled in CTA, including the data flow and data level definitions.

3.2 Requirements

In order to ensure the science goals of CTA are achievable, and that the observatory remains operational for the full 30 year life-time, certain standards must be upheld by all components of the observatory; this is the purpose of the CTA requirements. The requirements cover every aspect of the observatory, including: the survival and operation under different environmental conditions (e.g. **B-ENV-1120 Earthquake collapse prevention (South)**, **B-ENV-0320 Survival humidity**), the time allowed by the analysis pipeline for processing (e.g. **A-OBS-0810 Data Processing Efficiency**), the reliability of telescope components (e.g. **B-TEL-0520 Structure Lifetime**), and the ability to meet the expected performance under different observation conditions (e.g. **PROG-0025 Differential Sensitivity under Low Moonlight - North**). In order for an in-kind contribution to be accepted, it must meet the requirements defined by the observatory. These requirements are therefore the standards against which we compare the performance

of CHEC, and are the primary drivers in my development of the low-level calibration and analysis. However, there exists more than 60 requirements specifically tailored for the cameras. Consequently, the full review of the camera is a large undertaking that extends beyond the scope of this thesis. Instead, only the requirements that have relevance to the topics of this thesis are discussed.

It is important to note that the requirements, located on the CTA Jama website [43], are currently under review and therefore subject to change. A major change that is currently under way at the time of this writing is the redefinition from units of photoelectrons to photons. Originally, a common consolidated PMT was envisioned to be used for all cameras in CTA, motivating the relevant requirements to be expressed in terms of photoelectrons. However, due to the advances in sensor technology and the adoption of SiPMs by cameras such as CHEC-S, this assumption has led to problems with such a definition [44]. While one camera would measure X photoelectrons for a particular number of photons, a different camera (with a different PDE) would measure Y photoelectrons. Additionally, the definition of the requirements in photoelectrons encourages the cameras to be optimised in terms of their ENF, potentially at the cost of its PDE. The measurement in photons is therefore a much more coherent expression of signal for the array, which ensures requirements are stated in terms of the cameras ability to detect the Cherenkov-shower photons, instead of the cameras ability to resolve the number of photoelectrons generated in the photosensor.

As the procedure of converting the requirements from photoelectrons to photons is ongoing, this thesis will contain reference to the photoelectron definition of the requirements. A copy of the requirements relevant to this thesis, in the form they exist in Jama at the time of this writing, are included alongside the discussion in this section. This is to ensure clarity about which version of the requirement definition is being referred to. Future investigations should check the latest requirement definition.

3.2.1 B-TEL-1010 Charge Resolution

Jama Excerpt

The required fractional charge resolution for Cherenkov signals in each Camera pixel for a specified background level of 0.125 photoelectrons/ns is given in the Figure below and Table attached. Charge measurements must be possible for 0-1000 photoelectron signals. The average charge resolution should be calculated for the reference Gamma-Ray Spectrum.

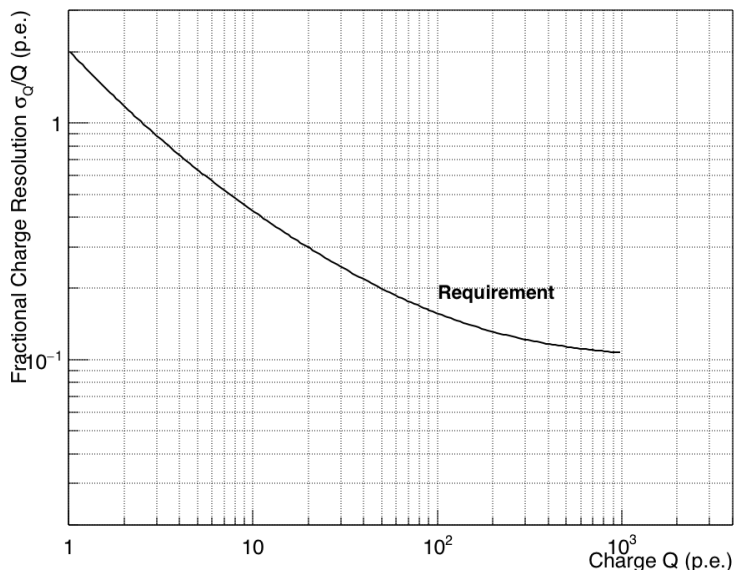


Figure 3.1: Fractional rms charge resolution σ_Q/Q per pixel for different Cherenkov light signal amplitudes, expressed in units of photoelectrons (p.e.). All sources of fluctuations, including Poisson fluctuations in photoelectron number, must be included. The true pixel charge Q is that measured in an ideal detector with the same photon-detection efficiency.

Notes: It is expected that this requirement is verified with reference to:

- Monte Carlo simulation of Cherenkov light from gamma-ray initiated showers (using a verified telescope model),
- Level-C Specification on Laboratory Measured *Charge Resolution*,
- Monte Carlo simulation of the laboratory test set-up (as a means of telescope model verification).

Note that between 1000 p.e. and 2000 p.e., some sensitivity to increasing input signal must exist.

This requirement applies to post-calibration (DL1) data.

Note that this requirement will likely need to be expanded to cover performance at higher NSB levels.

Definition

The standard criterion for the low-level camera performance used in CTA is the *Charge Resolution*. It encompasses both the bias and the standard deviation of the extracted charge versus the expected charge to provide a measure of the waveform, calibration, and charge reconstruction quality. Analogous to the Root-Mean-Square Error, the fractional *Charge Resolution* $\frac{\sigma_Q}{Q_T}$ for a particular “true charge” Q_T (the number of photoelectrons that were produced in sensor, before multiplication) is defined as:

$$\frac{\sigma_Q}{Q_T} = \frac{1}{Q_T} \sqrt{\frac{\sum_{i=0}^N (Q_{M_i} - Q_T)^2}{N}}, \quad (3.1)$$

where N is the total number of measured charges, Q_{M_i} , with that value of Q_T . The associated CTA requirement defines the maximum allowed values of $\frac{\sigma_Q}{Q_T}$ for values of Q_T between 1-1000 p.e., which must be adhered to when resolving the signal for any camera in CTA.

Requirement Derivation

The uncertainty in charge reconstruction can be expressed in the form:

$$\frac{\sigma_Q}{Q} = \frac{1}{Q} \sqrt{\sigma_0^2 + \sigma_{ENF}^2 Q + \sigma_g^2 Q^2}, \quad (3.2)$$

where σ_0 encapsulates noise contributions (electronic and NSB), σ_{ENF} is the *Excess Noise Factor* (a measure of fluctuations in charge amplification, see Section 2.2.5), and σ_g is the multiplicative errors in the calibration (i.e. the miscalibration) of the gain [44][45]. σ_0 can be further expanded in terms of the two primary noise contributions:

$$\sigma_0 = \sqrt{NSB \times t_w + n_e^2}, \quad (3.3)$$

i.e. the *NSB* rate (which includes the DCR for the purpose of this discussion) is coupled with the effective signal readout window size, $t_w = 15$ ns, and summed with the electronic noise, n_e . A contribution from electronic noise of $n_e = 0.87$ p.e. is assumed, combined with a value of $NSB = 0.125$ p.e./ns as defined in the

requirement. A value of $\sigma_g = 0.1$ and $\sigma_{ENF} = 1.2$ is also assumed [44]. The resulting combination of miscalibration and noise factors in Equation 3.2 gives the *Charge Resolution* requirement illustrated in Figure 3.1.

Approach

As it is impossible to know the “true charge” generated by a Cherenkov signal in the field, Monte Carlo simulations must be relied upon in order to prove a camera meets this requirement. The process for achieving this is outlined in the notes to the requirement. It is expected that this requirement is validated in three ways:

1. With lab measurements where the camera is uniformly illuminated with a calibrated light source.
2. With simulations of the previous approach, in order to verify the simulation model of the camera.
3. With Monte Carlo simulations of Cherenkov signal incident on the full telescope model.

The final item is the most important in confirming the requirements are met, as temporally-uniform illuminations do not sufficiently test the ability to find the signal pulse in the waveforms for the case of a Cherenkov-shower illumination. The prior items are important to verify that the *Charge Resolution* result obtained in the final item is applicable to the real camera, i.e. the simulation model of the camera is accurate.

The software package `sim_telarray` (Chapter 4) stores the “true charge” generated in the photosensor for each shower event into the output file. Therefore, with an accurate simulation model of the camera, it is an appropriate package for investigating a camera’s performance against this requirement. However, in order to ensure Poisson fluctuations in photoelectron number are included, as per the requirement, when using the “true charge” stored in the simulation file, the corrected form of Equation 3.1 is

$$\frac{\sigma_Q}{Q_T} = \frac{1}{Q_T} \sqrt{\frac{\sum_{i=0}^N (Q_{M_i} - Q_T)^2}{N} + Q_T}. \quad (3.4)$$

With the form in Equation 3.4, a perfect detector that consistently reads-out a “measured charge” with an equal value to the “true charge” would hit the Poisson limit. This limit ensures realistic conclusions can be reached from the Monte Carlo simulations, as it is not physically possible to know the “true charge” generated inside the photosensor, free from fluctuations.

3.2.2 B-TEL-1030 Time Resolution

Jama Excerpt

The rms difference in the reconstructed signal arrival time for any two simultaneously illuminated pixels in the Camera with amplitudes of five photoelectrons must not exceed 2 ns. This is for a specified background level of 0.125 photoelectrons/ns.

Notes: This requirement should be verified based on laboratory testing of a prototype at the specified background level.

A second important requirement concerning the signal inside the waveforms is the *Time Resolution* requirement. While the capability to accurately locate the signal is already assessed by the *Charge Resolution*, the purpose of this requirement is to instead ensure that the physical camera exhibits sensible behaviour with regards to the relative location of the signal between pixels, per event. One interpretation of the *Time Resolution* σ_T is the standard deviation of the difference in pulse time between every pixel in the camera, per event. This can be expressed as:

$$\sigma_T = \sqrt{\frac{\sum_{i=0}^N (\sum_{j=i+1}^N (T_{i-j} - \bar{T}_{i-j})^2)}{\binom{N}{2} - 1}}, \quad (3.5)$$

$$\bar{T}_{i-j} = \frac{\sum_{i=0}^N (\sum_{j=i+1}^N T_{i-j})}{\binom{N}{2}}, \quad (3.6)$$

where $T_{i-j} = T_i - T_j$, i.e. the difference between the extracted pulse time T_i for pixel i , and extracted pulse time T_j for pixel j . $\binom{N}{2}$ is the binomial coefficient of the number of pixels N “choose” 2, i.e. the total number of unique pixel combinations.

In this definition of *Time Resolution*, σ_T is calculated per event. However, the camera is better characterised by the mean and standard deviation of σ_T over multiple events. In order to meet the requirement, the *Time Resolution* should

be under 2 ns for pixels with measured charges above 5 p.e., in an environment containing an NSB photon rate of at least 0.125 p.e./ns. Any pixel timing corrections (described later in Section 5.5) that are required should be applied to the pulse time extracted from the waveform. Furthermore, the *Time Resolution* does not need to be extracted with the same approach as used in the charge extraction, as long as the approach is justifiable.

3.2.3 B-TEL-1295 Pixel Availability

Jama Excerpt

During observations, at least 95% of all camera pixels must be available and usable for data analysis. In addition, continuous regions of non-functioning pixels must not exceed 2% of all camera pixels. Pixels excluded due to NSB levels beyond those required are not included in this budget.

This requirement sets a limit on the amount of “dead” pixels that a camera is allowed to have before the entire camera is considered to be unavailable. For CHEC, which contains 2048 pixels, this imposes the following possible limitations:

- The camera may only have a maximum of 102 dead pixels. This allows 3 dead pixels per module.
- The amount of continuous pixels that are allowed to be dead is 41, therefore if an entire TARGET module dies (each module containing 64 pixels), the camera’s capabilities become insufficient for the CTA requirements. However, a maximum of two TARGET ASICs (each ASIC containing 16 pixels) are allowed to die.

3.3 Data Level and Flow Model

Further aspects of the CTA Architecture that are relevant to this work are the *Data Processing Level* definitions, and the flow between them. These definitions dictate how the data obtained from the telescopes are handled within the observatory, and are important in ensuring each telescope adopts a similar processing chain to

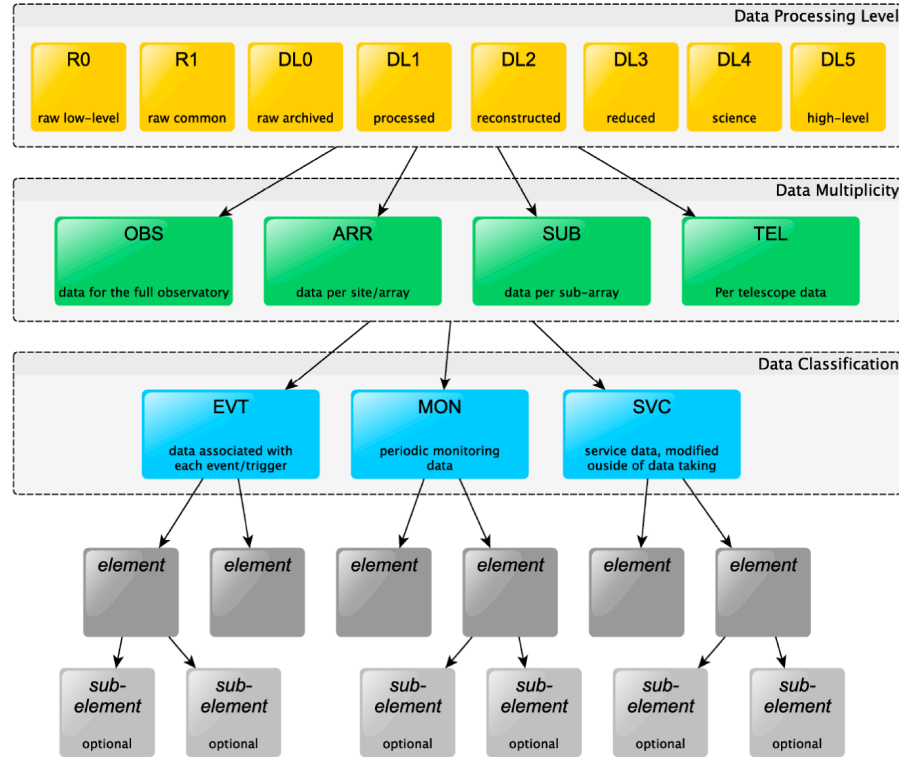


Figure 3.2: Hierarchy of data element names including the data level, the classifications of data (based on their rate), and data elements/groups and sub-elements/groups [46].

guarantee compatibility between themselves and the pipeline framework software. Figure 3.2 shows the full hierarchy for data specification in the observatory. The *Data Processing Level* indicates the progression of the data along the processing chain, the *multiplicity* indicates the scope of the data, and the *classification* designates the type of the data [46]. The levels are also split according to the system responsible for them (Figure 3.3). The Observation Execution System (OES) is responsible for the control and monitoring of the CTA array components, the scheduling of observations, and the online data acquisition and processing. The responsibilities of the Data Processing and Preservation System (DPPS) include processing the observational data into science data products, producing and analysing simulation data, and the long-term preservation of data products. Finally, the Science User Support System (SUSS) will provide access to the high-level CTA data products, along with the corresponding CTA software to analyse them. It also provides a point of access for proposal submission.

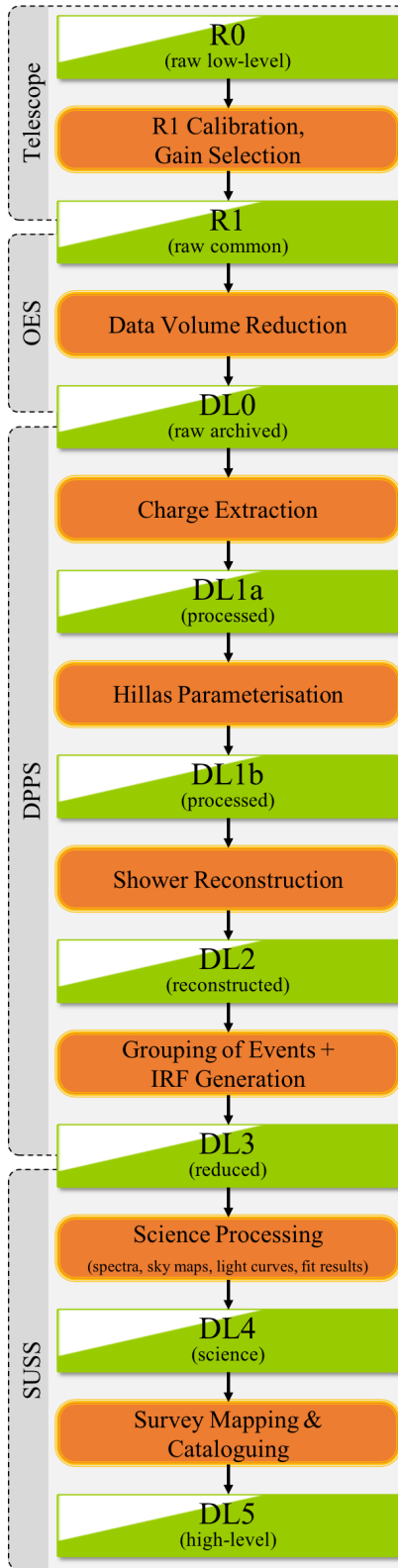


Figure 3.3: Simplified camera data flow, showing the *EVT*-classified data streams (in green) and the processing steps between them (orange). The levels are grouped by the systems responsible for them.

As the primary focus of this thesis is on the waveform data from a single telescope, the rest of this section will be focussed on describing the data levels relevant to the *EVT classification* (Figure 3.2), and the processes used to transition between them. These definitions are still undergoing development within CTA, but the foundations are generally agreed upon.

R0 (*raw low-level*): Raw waveform data, internal to the “Camera Functional Unit” (the official term given to an individual camera).

R1 (*raw common*): Waveform data with *R1 Calibration* applied. This low-level calibration is unique to the camera; the calibration’s purpose is to remove the dependence on the behaviour of its specific electronics, such that *R1* data is in a common format for all telescopes. The CHEC *R1 Calibration* is described in Chapter 5. A selection of gain-channel is also performed for cameras with two channels. The data at this level are serialised to a wire format, i.e. a block of data sent over a network in a common way between the telescopes. This data level is processed by the *Online Analysis* pipeline in order to produce immediate science alerts. The *R1* level therefore has its own set of (relaxed) requirements to adhere to (including its own *Charge Resolution* requirement), ensuring that the minimum standard required for the *Online Analysis* and *Data Volume Reduction* is met. Further (potentially slower) calibration may be applied at a later stage (between *DL0* and *DL1a*) such that the results of the offline pipeline are of optimum quality.

DL0 (*raw archived*): Similar data to the *R1* level, except serialised into files and stored for long-term archival. In order to achieve this with the excessively large data volume produced by CTA, *Data Volume Reduction* must be performed to achieve two orders of magnitude reduction. The simplest form of reduction is known as zero-suppression, where only waveforms of pixels deemed to have signal are kept. This is one of the responsibilities of the OES.

DL1 (*processed*): The signal charge per pixel is extracted from the *DL0* waveform data, and characterised in terms of its *Hillas Parameters*. This process is handled by the DPPS offline data processing pipeline, of which `ctapipe` is a prototype. Further information about `ctapipe` can be found in Chapter 4, and details about the processes involved in this stage are described in Chapter 6.

DL2 (*reconstructed*): The *DL1* products (pixel charges and *Hillas Parameters*) are used to reconstruct shower parameters including energy, direction, and source particle. At this point, the *TEL multiplicity* is dropped, as the information from each telescope has been combined to perform the reconstruction, and the individual telescopes are no longer relevant. The operations involved in this stage are also performed by the DPPS offline pipeline, and are described in Chapter 6.

DL3 (*reduced*): Events are sorted into sets according to their type (e.g. gamma-ray candidates, electron candidates, selected hadron candidates, etc.) alongside their reconstruction parameters. Associated instrumental response characterizations and any technical data needed for science analysis are also included in this level.

DL4 (*science*): The *DL3* data are read into one of the CTA tools within the SUSS designed to support science data analysis. Two prototype tools developed for this purpose are `Gammapy` and `ctools` (Chapter 4). These tools enable the construction of binned data products like spectra, sky maps, or light curves, enabling the analysis of astrophysical sources.

DL5 (*high-level*): *DL4* data is accumulated to generate legacy datasets such as the CTA survey sky maps or the CTA source catalogue.

4

Software

Contents

4.1	Introduction	49
4.2	TARGET Libraries	50
4.2.1	TargetDriver	50
4.2.2	TargetIO	51
4.2.3	TargetCalib	53
4.3	Monte Carlo Software	54
4.3.1	CORSIKA	55
4.3.2	sim_telarray	56
4.4	Reduction Tools	56
4.4.1	ctapipe	58
4.4.2	CHECLabPy	63
4.5	Science Tools	64
4.5.1	Gammapy	65
4.5.2	ctools	66

4.1 Introduction

Arguably, software is one of the most important aspects of modern-day astronomy. This is especially so for the Imaging Atmospheric Cherenkov Technique, due to its reliance on high-speed digitisers, the dependence of its sensitivity on how well one can reconstruct the shower, and the contrast between the rates of VHE gamma rays versus the hadron shower background.

In Chapter 3, the data processing steps required to transition from the digitised waveform data obtain from the cameras to the science data released to the scientific

community are outlined. In order to transition through this chain, a number of software packages were developed, and are to be offered to the CTA Observatory as in-kind contributions. This chapter provides an outline of the software packages involved in the processing pipeline for CTA and the camera commissioning for CHEC. In cases where I have been involved in the development of the software, my contributions are also described.

4.2 TARGET Libraries

A collection of libraries have been created to operate, read-out, and calibrate the cameras containing TARGET modules (i.e. CHEC and the Schwarzschild-Couder Telescope (SCT) camera). Naturally, these are often referred to as the “TARGET Libraries”. These low-level libraries were written in C++ as they prioritise efficiency over flexibility. To enable the use of these libraries from the Python packages used in waveform reduction (described later in this chapter), a Python wrapper for these libraries is automatically generated during compilation through the utilisation of SWIG (Simplified Wrapper and Interface Generator)¹.

These libraries are presently stored on the CTA-SVN version control server, and installation instructions can be found at https://forge.in2p3.fr/projects/gct/wiki/Installing_CHEC_Software, provided you have permissions to the GCT Redmine.

4.2.1 TargetDriver

URL: svn.in2p3.fr/cta/COM/CCC/TargetDriver/trunk
SVN revision: 32311

In order to operate the TARGET modules, the `TargetDriver` library is required. This C++ library configures the TARGET modules, and listens for the UDP packets containing the waveform data.

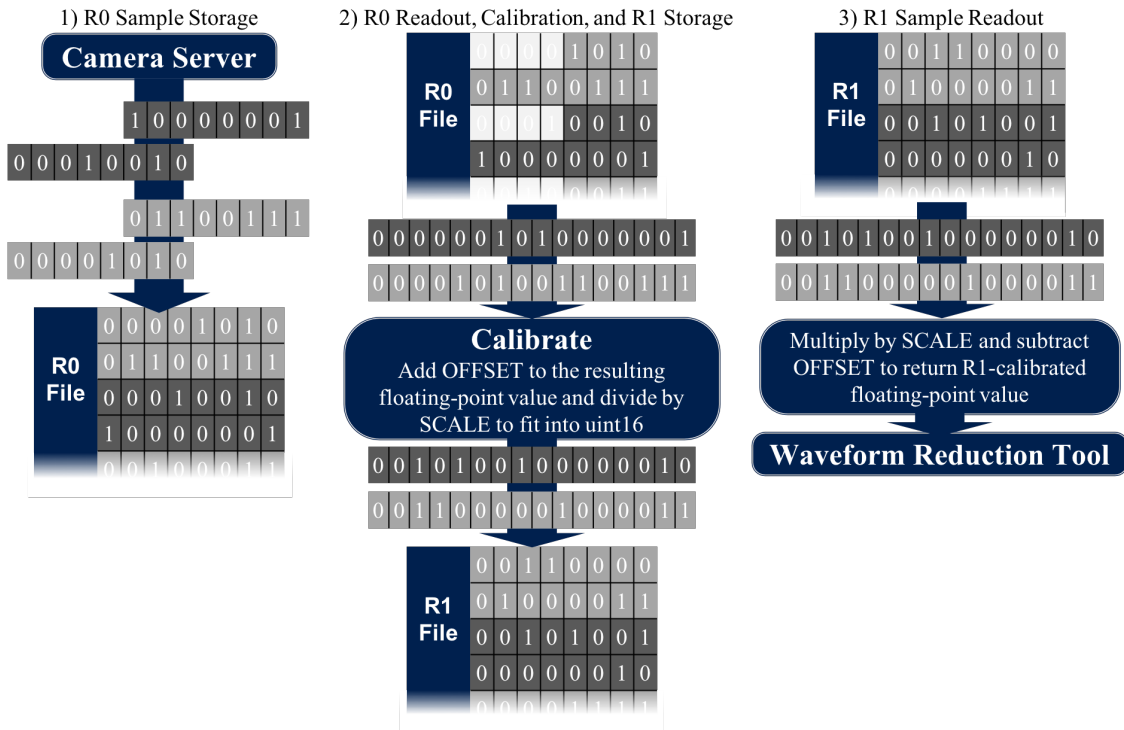


Figure 4.1: Overview of the data-flow for waveform samples within the TARGET libraries. Although only the samples are shown here, all other waveform data is also sent along this stream, including ASIC and Channel number, indicating the start of a new waveform.

4.2.2 TargetIO

URL: svn.in2p3.fr/cta/COM/CCC/TargetIO/trunk
SVN revision: 33028

The file format used to store waveforms from the TARGET modules is the FITS (Flexible Image Transport System) format. A customised binary table, defined by TargetIO, is used to store the waveform data inside of the FITS file. Files containing this TargetIO-defined bin table are hereby referred to as TIO files. This file format was created as a temporary solution as the official CTA format is yet to be defined. FITS was chosen for two reasons:

- It is a well known file format, and uses a convenient library with extensive compatibilities with other programming frameworks/languages.
- As we wished to store the UDP packets with minimal data arranging, the capability to deposit our custom-defined binary table inside the FITS file is

¹<http://www.swig.org/>

pragmatic.

The custom binary table format is complicated to read directly with typical FITS readers, therefore the `TargetTIO` library is always used to read and write waveform and header (information such as observation time) data to and from the TIO file. TIO files can either contain *R0* (uncalibrated) or *R1* (low-level calibrated) waveform data. Each sample in a waveform is stored to file as an unsigned 16-bit integer. The procedure of storing the samples is demonstrated by Figure 4.1:

- 1) 8-bit/char packets are sent from the TARGET FPGA and stored directly to file. The raw waveform digital counts measured by the camera are serialised in an unsigned 12-bit integer format, therefore the first four bits of the first 8-bit sample packet are used to indicate sample order.
- 2) When reading a sample from the *R0* TIO file, the first four bits are ignored, and the remaining twelve bits are combined into an unsigned 16-bit sample. The samples are passed to `TargetCalib` for calibration. The resulting calibrated floating-point sample is scaled and offset to fit into an unsigned 16-bit integer for storage. The OFFSET and SCALE are stored in the header of the FITS file.
- 3) When reading a sample from a *R1* TIO file, the entirety of the two 8-bit packets are kept and combined. The value is returned to floating-point format using the OFFSET and SCALE stored in the file header.

To ensure the full efficiency of the C++ library is exploited via the Python wrapper, I contributed the `WaveformArrayReader` C++ class, which, when passed a contiguous block of memory (such as a `numpy.ndarray`), promptly fills the array with the entire camera's waveform data for that event. For example, to read an *R1* TIO file from Python using `TargetTIO` directly:

```

1 import numpy as np
2 from target_io import WaveformArrayReader
3
4 # Create the reader and get the number of pixels and number of
5 # samples from the header
6 reader = WaveformArrayReader("/path/to/file/Run17473_r1.tio")
7 n_pixels = reader.fNPixels
8 n_samples = reader.fNSamples
9
10 # Generate the memory to be filled in-place
11 waveforms = np.zeros((n_pixels, n_samples), dtype=np.float32)
12
13 # Storage cell id for the first sample of the event per pixel
14 first_cell_ids = np.zeros(n_pixels, dtype=np.uint16)
15
16 # Fill the arrays
17 event_index = 20
18 reader.GetR1Event(event_index, waveforms, first_cell_ids)
19 # 'waveforms' array is now filled with entire event's waveform data

```

4.2.3 TargetCalib

URL: svn.in2p3.fr/cta/COM/CCC/TargetCalib/trunk
 SVN revision: 33028

To correct for the effects of the TARGET electronics on the waveforms, **TargetCalib** was built. I have been responsible for the development of this package for the majority of its lifetime. The calibrations performed by this library are detailed in Chapter 5. This package has also been adopted by SCT recently. The main classes in the library include:

PedestalMaker Generates the Pedestal calibration file.

TfMaker Generates the Transfer Function calibration file.

Calibrator Applies the Pedestal and Transfer Function calibration files to the waveform samples.

Mapping Handles the files containing the camera’s pixel mapping, and provides an interface to the information. This class is necessary due to the non-intuitive mapping between physical pixel position, and order of pixel readout. Most commonly, this class is utilised for the plotting of camera images. The class is compatible with the mapping of any square-pixel telescope, and

customisable to provide the mapping of the pixels in a single module, the mapping of the superpixels, the mapping of the modules, or the neighbours to a pixel/superpixel/module. This class will be deprecated once the central CTA database of telescope configurations exists.

CameraConfiguration Provides an interface to certain camera-version dependant variables. Currently the variables that might change with camera-version (stored in the TIO file header) include number of storage cells, pixel mapping, and reference pulse shape. The correct version of the parameter is returned according to the camera-version provided, allowing for the automated processing of the data of different camera versions. This class will also be replaced by the central CTA database.

Efforts are being made to improve the `TargetCalib`'s (more specifically the `Calibrator` class's) efficiency in terms of both memory and processing time, as it will need to meet the CTA Requirements for *Online Analysis* (Chapter 3). It is possible that in the future there will be two separate `Calibrator` classes for the *Online* and *Offline Analyses* respectively.

4.3 Monte Carlo Software

An important aspect in modern IACT analysis is the utilisation of Monte Carlo simulations. Within CTA they are paramount in both the design of the array, to find the most cost-effective solution that enables the attainment of its scientific goals [47], and as a complement to observational data in order to reconstruct Cherenkov showers from IACT images. Two packages are typically used for the generation of the files containing simulated Cherenkov shower images: `CORSIKA` (`C0smic Ray SImulations for KAscade`) and `sim_telarray`. While I had no involvement in the development of these packages, I had to learn how to use them in order to obtain simulations containing a model of the CHEC camera.

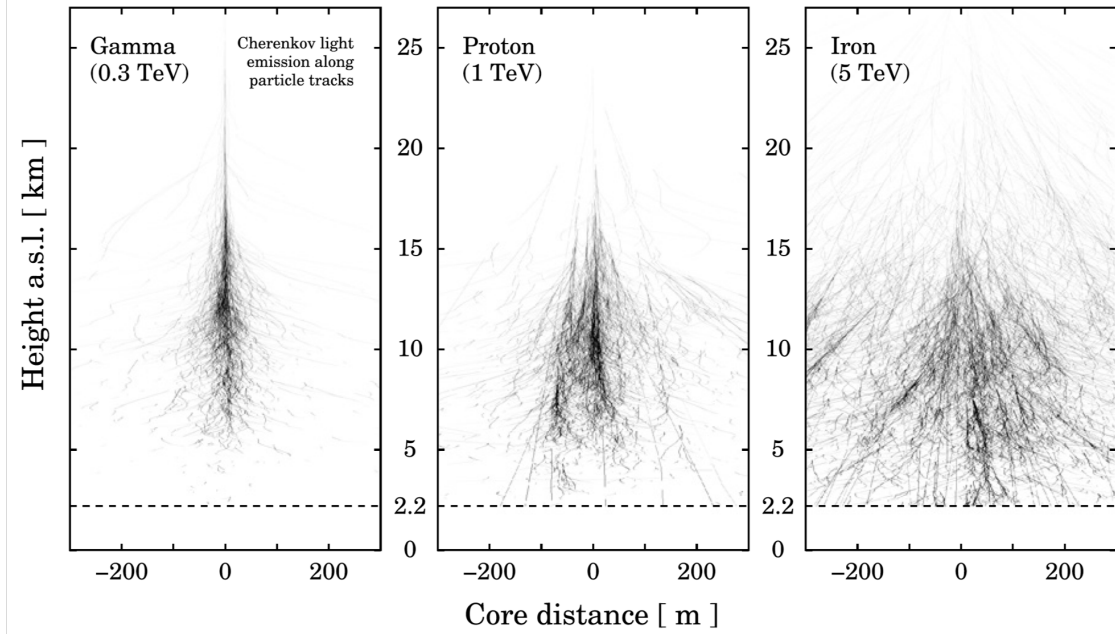


Figure 4.2: Cherenkov light production simulation from extensive air showers simulated by CORSIKA, for different primary particles for a site at 2200 m altitude. Darkness of the particle tracks shown increases with increasing emission of Cherenkov light [48].

4.3.1 CORSIKA

URL: <https://www.ikp.kit.edu/corsika/>
Version: 6.99

Originally developed for the KASCADE (KARlsruhe Shower Core and Array DEtector) cosmic-ray experiment, the CORSIKA package is “a program for detailed simulation of extensive air showers initiated by high energy cosmic ray particles” [49, p. i]. Given a specified astrophysical primary particle (protons, light nuclei, photons), the simulation tracks the particle, its interaction products, and its secondary decay products through the atmosphere, using the latest hadronic and leptonic interaction models. It can also simulate the Cherenkov photon production produced by the superluminal products. In combination with the IACT extension package written by Bernlöhr [48], these Cherenkov photons are tracked to a “fiducial sphere” surrounding the telescope, while including atmospheric refraction and absorption effects (Figure 4.2). Photons emitted at angles away from the telescope can be ignored to reduce the computational cost of this tracking. Photons are also simulated in bunches as opposed to individually to aid efficiency. The philosophy behind the development of CORSIKA is to provide an evolving package which accumulates the

expertise from various experiments with connections to high energy and air shower physics. Due to the complexity involved in simulating extensive air showers, this is an attractive approach to minimise effort and errors, and ease the comparison of simulation results between experiments. As a result, **CORSIKA** is the most extensively used air shower simulation package in VHE astrophysics. Experiments other than CTA that utilise **CORSIKA** include (but are not limited to) H.E.S.S., VERITAS, MAGIC, and HAWC.

4.3.2 **sim_telarray**

URL: <https://www.mpi-hd.mpg.de/hfm/CTA/MC/Software/>
 Version: 2018-06-12_testing

The second component in simulating the CTA observations of air showers is the simulation of the instrument’s response to the Cherenkov photons resulting from the **CORSIKA** output. This includes the optical ray-tracing of the Cherenkov photons from where they impacted the “fiducial sphere” in **COSIKA** through the telescope’s optics, the conversion of the photon into a photoelectron by the sensors, the activation of the camera’s trigger, and the digitisation of the resulting signal. The **sim_telarray** package, developed by Bernlöhr [48] for H.E.S.S., has been adopted and developed to reproduce the CTA telescopes response to Cherenkov light in the Monte Carlo simulation chain.

Also included within the **sim_telarray** package is the **light_emission** package. This simple simulator produces **CORSIKA** output files for simple illumination cases. For example, one can simulate the uniform illumination of the camera focal plane. Therefore, using this **CORSIKA** output file as input to **sim_telarray** will reproduce the illumination profiles often used in lab tests during the camera commissioning phase. This is especially useful in the Monte Carlo verification and validation process, discussed in Chapter 7.

4.4 Reduction Tools

Tools used to process the waveforms in order to either characterise the camera or progress down the data-level chain (Figure 3.3) are often referred to as “reduction

tools”. Within the CHEC group we utilise Python for all of our waveform reduction. We made this choice due to its high popularity for data science and signal processing and its extensive library of statistical and numerical packages. The most important examples of these packages include:

NumPy² Enables the efficient processing of numerical data. This is accomplished using their powerful N-dimensional array object known as a `numpy.ndarray` [50]. At the lowest level, a `numpy.ndarray` is a contiguous block of memory much like an array in C. However, NumPy defines many methods which utilise optimised low-level C and Fortran operations to process the contained data in the most efficient way possible, often performing better than handwritten C or Fortran.

SciPy³ Expands on the operations one can perform on the `numpy.ndarray` object, providing an extensive amount of functionality useful for scientific computing, including statistical operations, interpolation, and signal processing.

Astropy⁴ Developed by the astronomy community to consolidate various common astronomy procedures into a single package.

Pandas⁵ Provides high-performance, easy-to-use, table-like data structures known as a `pandas.DataFrame`. Each column in the table can be processed as a `numpy.ndarray`.

Matplotlib⁶ Supplies extensive 2D plotting capabilities for Python, and is compatible with `numpy.ndarray` objects.

Different reduction packages may be designed with different purposes, but each can potentially import methods from another, which is especially simple to do when developing in Python. Although many other CTA groups have also adopted Python for their waveform reduction software, it is not a standard across CTA.

²<http://www.numpy.org/>

³<https://www.scipy.org/>

⁴<http://www.astropy.org/>

⁵<https://pandas.pydata.org/>

⁶<https://matplotlib.org/>

4.4.1 `ctapipe`

URL: <https://github.com/cta-observatory/ctapipe>
 Version: 0.6.0

Waveform data from each CTA telescope must be processed and the results combined using standardised approaches, such that the data at each processing stage is compatible with the next, and the resulting reduced data and shower reconstruction is of optimum quality. This was the motivation behind the design of the *Data Processing Level* architecture (Section 3.3). The most reliable way to ensure this architecture is adhered to was to create a single data processing pipeline with the capability to transform *DL0* waveforms into *DL2* reduced shower parameters. The prototype that has been developed among members of the CTA Consortium for this purpose is `ctapipe`.

The majority of pipeline frameworks in VHE astronomy utilise what we refer to as a “bottom-up” approach, where the algorithms are written in low-level languages such as C or C++, and perhaps interfaced with a high-level language such as Python. Examples of this include the software written for H.E.S.S. (including their Data Acquisition system [51]), and the AERIE (Analysis and Event Reconstruction Integrated Environment) framework written for HAWC [52]. Contrary to this, the `ctapipe` framework utilises a “top-down” approach, where algorithms are first written in Python. Through the utilisation of `NumPy`, the majority of these Python algorithms will process data efficiently, removing the need to write complex low-level code. Additionally, as mentioned previously, there exists a wide scientific-computing community in the world of Python, contributing their collective knowledge into open-source packages. Within `ctapipe` we utilise this rich resource and benefit from the open-source model: reducing time wasted to re-implement existing methods, and limiting the potential for bugs to go undiscovered. However, in some complicated applications which perform very specific tasks, it is not possible to implement an algorithm with `NumPy` expressions efficiently. As `ctapipe` utilises `numpy.ndarray` for the storage of data wherever it is possible or logical (including the camera waveforms and images), the following additional options are available for processing the data efficiently:

```
ctapipe.io.containers.DataContainer:
    r0.*: Raw Data
    r1.*: R1 Calibrated Data
    dl0.*: DL0 Data Volume Reduced Data
    dl1.*: DL1 Calibrated image
    dl2.*: Reconstructed Shower Information
    mc.*: Monte-Carlo data
    mcheader.*: Monte-Carlo run header data
    trig.*: Central trigger information
    count: Number of events processed
    inst.*: Instrumental information (deprecated)
    pointing[*]: Telescope pointing positions
```

Figure 4.3: Print result of a `ctapipe.io.containers.DataContainer` object, showing its contents.

Numba A Python compiler, either prior to runtime, or “just-in-time”. Allows for the optimisation of array-oriented and maths-heavy Python code without the need to switch to a different language.

Cython Converts Python code into C code, which can then be compiled for easy optimisation. Also enables the easy importing of external C or C++ code into Python.

C/C++ The algorithm could instead be completely written in C or C++. The code can be included into Python in a variety of ways. One way is the use of **Cython**. A second possibility is the utilisation of **SWIG**, as we have done for the TARGET libraries.

In the remainder of this subsection, I will describe the most important areas of `ctapipe` to which I have contributed.

DataContainer

As `ctapipe` must be capable of processing the data from any camera indiscriminately, one of the most important classes in `ctapipe` is the `ctapipe.io.containers.DataContainer`. This class can be filled from any data source, thereby allowing the same operations to be performed on the data irrespective of camera type. One

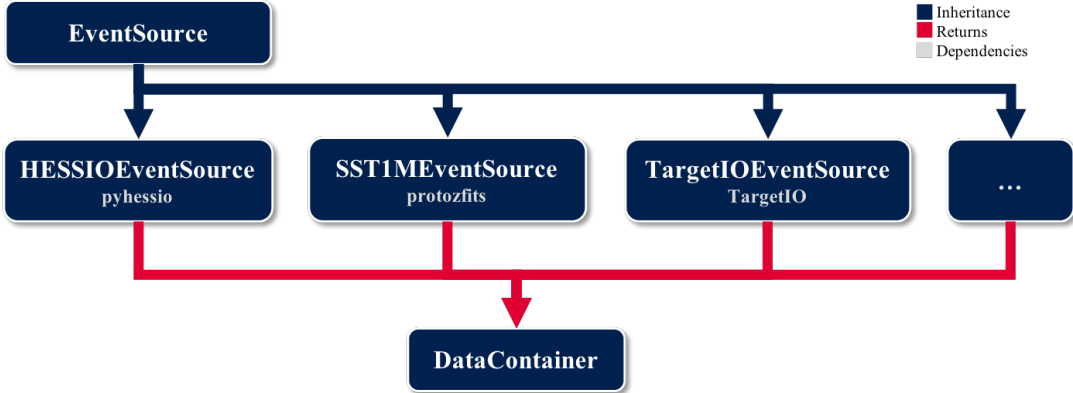


Figure 4.4: Functional block diagram of the `ctapipe.io.eventsource.EventSource` class, showing the inheritance, dependencies, and object returned for a selection of the existing `EventSource` classes.

of my contributions to `ctapipe` was to suggest that it would be logical for the contents of this class to closely follow the CTA data-level definitions (Section 3.3), as demonstrated in Figure 4.3. Therefore, in each stage of the data processing, the correct data level is read, and the following data level is filled. This also easily allows for different data levels to be saved to file, and to be read at a later time for further processing along the chain.

EventSource

Presently in the development of CTA, a common file format has not yet been defined. Therefore, each camera currently uses their own data format for camera prototyping, such as the TIO format within CHEC. Additionally, `sim_telarray` stores the telescope simulation files in its own compressed data format, called HESSIO (for legacy reasons). In order for `ctapipe` to be fully prototyped, it must therefore be capable of reading in each of these file formats. One of my major contributions to `ctapipe` was the development of the `ctapipe.io.eventsource`.`EventSource` class. This class provides a base from which a new `EventSource` class can be created in order to add a file format to `ctapipe`'s compatibility list. For example, I also created the `ctapipe.io.hessioeventsources`.`HESSIOEventSource` and `ctapipe.io.targetioeventsources`.`TargetIOEventSource`. To create a new `EventSource` class,

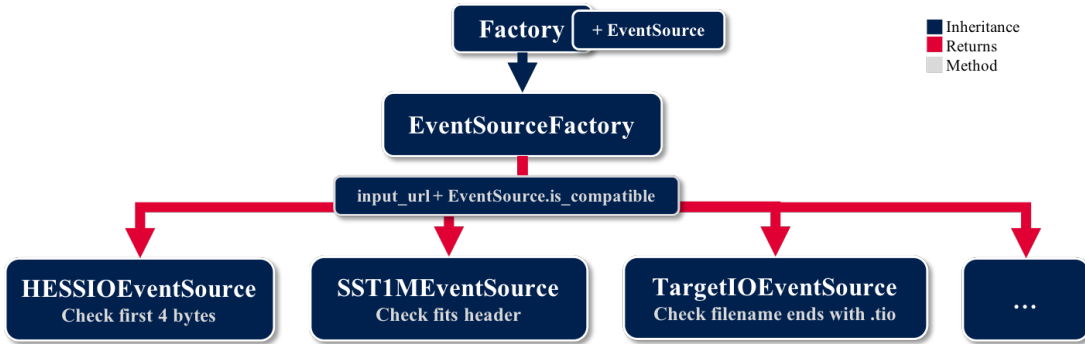


Figure 4.5: Functional block diagram of the `ctapipe.io.eventsourcefactory`.
EventSourceFactory class, showing the inheritance, the potential `EventSource` classes that
could be returned, and the methods used to assess the compatibility of the input URL
with the `EventSource`.

one simply has to define how the data is read from the file, into the `ctapipe.io.containers.DataContainer`. A dependency on the external custom camera software may exist for the reading of the file format. One must also create an `is_compatible` method for checking if the file supplied is compatible with the `EventSource`. The functional block diagram for the `EventSource` class is shown in Figure 4.4.

Factory

Alongside the variety of file formats, there also exists a variety among IACT analysis techniques that are applicable to CTA, such as different charge extraction techniques or shower parametrisation approaches (Chapter 6). Early in my involvement with `ctapipe` I identified the need for a design pattern that could enable the configuration of the processing chain at runtime, depending on user and file inputs. This approach needed to be clean and modular, otherwise such approaches can get very confusing and hard to maintain. As Python is a very flexible language, this problem was potentially easier to solve than if `ctapipe` was designed in a different language. The accepted solution, which I proposed and implemented, was to generate the `ctapipe.core.factory.Factory` class, which operates according to the “factory method pattern” [53]. By inheriting from the `Factory` class, one can design a factory that, when given a particular input, returns the corresponding class. The

input can be designed to be anything, from a file path to a user’s input on the command line. One example of a Factory is the `ctapipe.io.eventsourcefactory`.`EventSourceFactory` class (Figure 4.5). Given an input URL, every `EventSource` is looped through, and the corresponding `is_compatible` static method is called. When `is_compatible` returns True, that `EventSource` is returned and used to read the file into the `DataContainer`. This functionality design makes reading any compatible file format into `ctapipe` extremely simple. The code snippet below demonstrates how to read a file and print the `event_id` for each event. It uses the helper function `ctapipe.io.eventsourcefactory.event_source` which internally handles the creation of an `EventSourceFactory` object. This snippet also demonstrates the simple functionality provided by the `EventSource` to easily loop through the events inside the file, irrespective of the file format.

```

1 from ctapipe.io.eventsourcefactory import event_source
2 with event_source(url) as source:
3     for event in source:
4         print(event.r0.event_id)

```

Calibration and Waveform Reduction in `ctapipe`

Another major contribution of mine has been the development and maintenance of the calibration and waveform reduction pipeline within `ctapipe`. As with the `DataContainer`, each stage is split according to the data levels. Although the *R1 Calibration* is a responsibility of the Camera Functional Unit (Section 3.3) and not the DPPS, it was concluded that it may be useful to be able to call *R1 Calibration* methods from `ctapipe` during the prototyping phase. As shown in Figure 4.6, the `ctapipe.image.charge_extractors.ChargeExtractor` classes are included within this scheme. The different charge extraction methods (Chapter 6) are each selectable via the `ctapipe.image.charge_extractors.ChargeExtractorFactory`. An example of importing C code via Cython can be found for the `NeighbourPeakIntegrator`, as the loop over neighbouring pixels within a camera was too complex to optimally execute using NumPy.

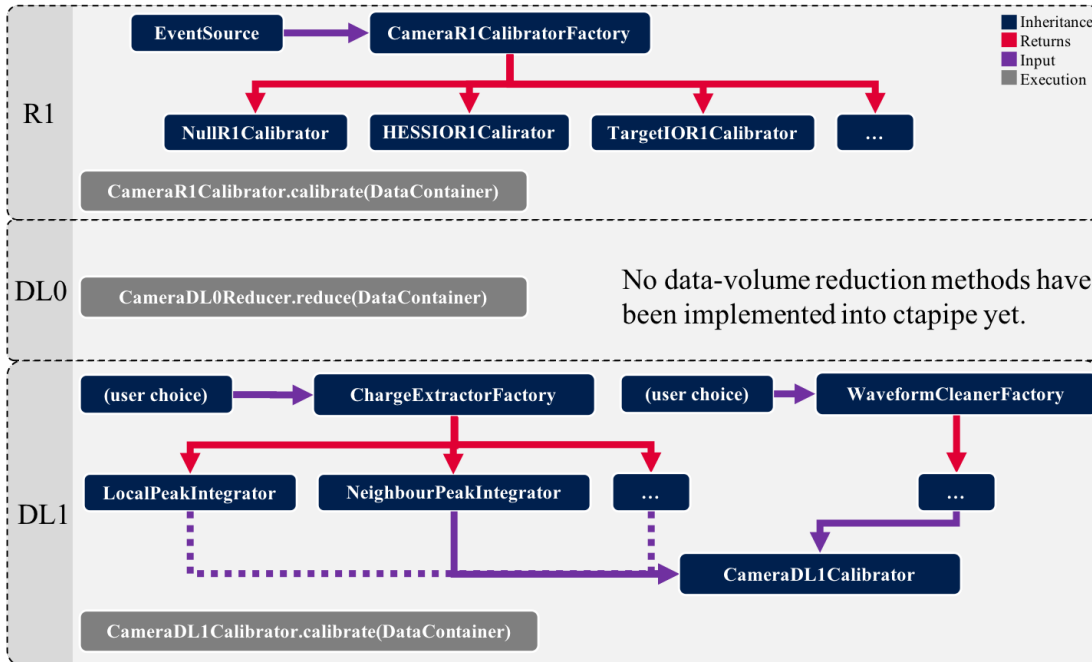


Figure 4.6: Functional block diagram of the `ctaapipe` low-level calibration and waveform reduction classes (*R1*, *DL0*, and *DL1*).

The development of `ctaapipe` is ongoing, but it now contains implementations of many of the common procedures used in the Imaging Atmospheric Cherenkov Technique, described in Chapter 6. It also contains some of the more complex procedures, such as the latest version of the ImPACT shower reconstruction technique developed by [54]. `ctaapipe` has reached a level of maturity where people are able to utilise it for the processing of the waveform data from their prototype cameras. I have used `ctaapipe` extensively for this purpose during my DPhil to analyse waveform and image data from CHEC, especially for the Cherenkov showers images obtained during the GCT on-telescope campaigns (Chapter 8). Additionally, CTA members have began to produce their own Instrument Response Functions (IRFs) using `ctaapipe`. An official implementation of IRF production is intended to be included in `ctaapipe` soon.

4.4.2 CHECLabPy

URL: <https://github.com/cta-chec/CHECLabPy>
 Version: Thesis-JW (commit 785068a)

It was decided within CHEC that we need our own waveform reduction pipeline for camera commissioning and algorithm prototyping. The purpose of creating

this package was to unify the analysis code in CHEC, and supply a common method for file IO, thereby simplifying the reading of TIO files. A second primary motivation for this package was to provide an executable that would reduce the waveforms from TIO files into its signal, noise, and timing parameters, and store it into an accessible data format with no dependencies on the TARGET libraries or `ctapipe`. This therefore allows anyone within CHEC to easily and immediately perform investigations on a dataset.

To meet these needs, I created the `CHECLabPy` Python package. `CHECLabPy` has been designed with a similar coding style to `ctapipe`. It operates on the same principle of a “top-down” approach, and utilises common scientific computing Python packages. Due to this similarity, algorithms that are deemed useful to transfer to `ctapipe`, such as the charge extraction approach we choose to use for CHEC, can easily be integrated into `ctapipe` in the future. The primary executable for reducing waveform data from TIO files is called `extract_d11.py`, which allows a selection of `WaveformReducer` from the command-line using a similar factory method to the one I designed for `ctapipe`. The reduced parameters from the waveforms are then stored into a `pandas.DataFrame` object, which is then saved to disk in the HDF5⁷ file format.

4.5 Science Tools

Although not used in within this thesis, the science tools are important components to the CTA processing pipeline that are worthy of mention in this chapter. They will be provided to the scientific community, along with the *DL3* data, by the SUSS to support the science data analysis. This is an important aspect of the “open-observatory” operation of CTA. The purpose of the science tools is to perform the following tasks (as described by Deil et al. [55, p. 4]):

- selection of a data cube (energy and positions) around a sky position from all event lists,

⁷<https://support.hdfgroup.org/HDF5/>

- computation of the corresponding exposure,
- estimation the background directly from the data (e.g. with a ring background model [56]) or from a model (e.g. templates built from real data beforehand),
- creation of sky images (signal, background, significance, etc) and morphology fitting,
- spectrum measurement with a 1D analysis or with a 3D analysis by adjusting both spectral and spatial shape of gamma-ray sources,
- computation of light-curves and phasograms, search for transient signals,
- derivation of a catalog of excess peaks (or a source catalog).

As previous IACT experiments all built their own internal analysis tools, no common tools exist within the gamma-ray astronomy field. Therefore, two independently-developed tools have been proposed for this purpose: **Gammapy** and **ctools**. Both packages intend to improve on the sharing-of-tools aspect of gamma-ray astronomy, through enabling the analysis of observational data from other experiments, and encouraging the standardisation of the data format used (FITS). Although the tools were developed to perform very similar operations, such as the construction of binned data products (including spectra, sky maps, and light curves) they have opposing design philosophies.

4.5.1 Gammapy

URL: <https://github.com/gammapy/gammapy>

A package known as PyFACT was developed in 2011/2012 which explored the possibility of using the open-source Python model for VHE data analysis, utilising the common scientific computing packages, NumPy and SciPy [55]. Although PyFACT was never adopted in any official capacity, it did demonstrate that such an approach could be useful in the VHE astronomy field. From the inspiration by PyFACT, and due to the amalgamation of the Python astronomy community to create **Astropy**, it was decided to create **Gammapy** as an **Astropy** affiliated package. This means that wherever possible, it uses functionality from **Astropy**, thereby benefiting from

the entire Python astronomy community. This design philosophy is the same approach adopted by `ctapipe`.

4.5.2 `ctools`

URL: <http://cta.irap.omp.eu/ctools/index.html>

Conversely, the design philosophy of `ctools` is to strictly minimise dependencies as much as possible. The only dependency of `ctools` is the adjacently developed `GammaLib` C++ shared library, which contains “all the classes, support functions, and some global variables that are needed to analyse gamma-ray event data” [57, p. 2]. The advantage of this design lies in the complete independence from the maintenance of other libraries. If a dependency is no longer maintained in the future, many problems can arise in the form of incompatibilities, such those regarding operating systems or the updates inside the software package itself. However, the disadvantage of this design is the larger initial development effort required, and necessity to reimplement common methods from scratch. Much like other science analysis frameworks in high-energy astronomy (e.g. Fermi Science Tools), `ctools` is a collection of tools that each perform a single, well-defined analysis step. These tools are written in C++, but can also be called directly from Python via the SWIG-generated interface. However, no standard interface exists for conversion between `numpy.ndarray` and `ctools` objects, forcing the reliance on the `GammaLib` library for any efficient analysis.

5

Calibration

Contents

5.1	Introduction	67
5.2	TARGET Calibration	68
5.2.1	Electronic Pedestal Subtraction	68
5.2.2	Transfer Function	73
5.3	Photosensor Calibration	78
5.3.1	Gain Matching	80
5.3.2	SPE Fitting	82
5.3.3	Flat-Field Coefficients	83
5.3.4	Dead Pixels	87
5.4	Saturation Recovery	87
5.5	Timing Corrections	88
5.6	Future	89

5.1 Introduction

In order to obtain meaningful and reliable results from the camera, a number of calibrations must be applied to the waveform readout. A primary objective of my DPhil was to investigate the most optimal and efficient approaches for these calibrations (in accordance with the CTA requirements described in Chapter 3), and to determine if additional calibrations are required.

When I joined the CHEC development, the calibration discussion was still in its infancy. Some approaches had been tested in a laboratory environment [58], but there had been little discussion on how exactly the calibrations could be applied

efficiently in an analysis pipeline, where one might not be able to use the same detailed calibration due to limited resources (such as memory and processing time). A major contribution of my DPhil was to prototype the calibration procedures, develop an approach for a calibration pipeline, write the software to perform such a pipeline, and finally assess its performance. This was an iterative process, the development of which is still ongoing. However, a procedure now exists that allows us to obtain meaningful results from the waveform data, a capability that is of paramount importance in the commissioning of the camera.

In this chapter I will outline each of the calibration steps that are presently adopted for CHEC. They are introduced in the general order that they are applied, and split into the categories of TARGET ASIC, photosensor, and "other" calibrations.

5.2 TARGET Calibration

The calibrations described in this section relate to the TARGET module. As detailed in Chapter 2, the TARGET ASIC is responsible for the sampling, digitisation and readout of the waveform data. As a result, there are two calibrations that are solely related to the TARGET ASIC: electronic pedestal subtraction and the linearity correction via the transfer function.

The functional block diagram of the TARGET ASIC in Figure 2.14 outlines the electronics that require calibration, and can be used as a reference in the following descriptions.

As the calibrations in this section are very low-level, and related to CHEC's specific FEE, they are handled by the TargetCalib library (Chapter 4).

5.2.1 Electronic Pedestal Subtraction

The most important, but also the simplest, waveform data calibration to apply is the subtraction of the electronic pedestal. Each cell in the storage array of the ASIC is a unique capacitor. For a specific V_{ped} , each capacitor has its own resulting electronic pedestal value. As each sample of the waveform corresponds to a single storage cell, each sample therefore has a unique pedestal value to be subtracted. This is apparent

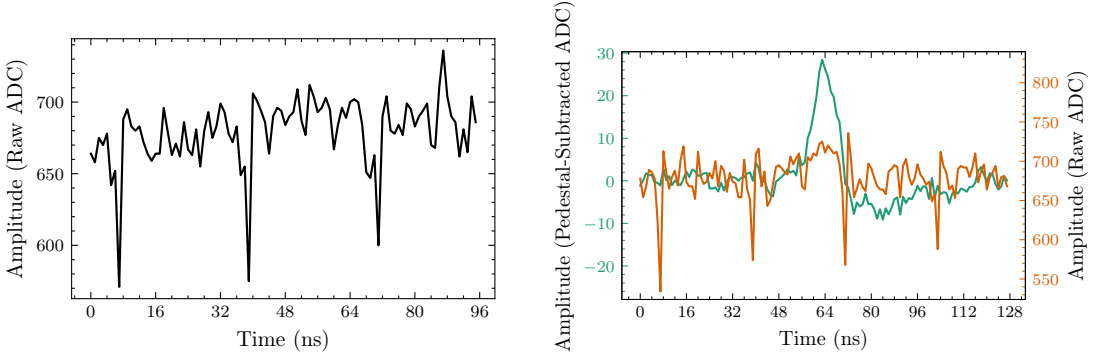


Figure 5.1: TARGET-C waveform as read out from CHEC-S, showing the electronic pedestal in the absence of any other input, before any calibration is applied.

Figure 5.2: CHEC-S waveform containing a 5 p.e. pulse, before and after pedestal subtraction.

in Figures 5.1 and 5.2 where the variation from sample-to-sample is very large in the raw waveform, and the low-amplitude pulses are almost indistinguishable. The fluctuations in the raw waveforms between pixels is also significant, to the point where low-amplitude Cherenkov showers are undetectable in the camera (Figure 5.3a). However, the dominating variations are between ASICs. As a result, the outlines of the ASICs are the dominating feature in camera images containing raw samples, such as Figure 5.3a. With a pedestal-subtraction calibration alone, the waveforms are transformed into a state in which a moderate amount of Cherenkov shower assessment can be performed, as demonstrated in Figure 5.3b.

There are $2^{14} = 16,384$ storage cells per channel (for CHEC-M, $2^{12} = 4096$ for CHEC-S), therefore one could naively conclude that there are $32(\text{Modules}) \times 64(\text{Channels}) \times 16,384(\text{Cells})$ pedestal values to keep record of. However, an additional characteristic of the TARGET ASIC is that the pedestal amplitude depends on the position in the waveform. The source of this characteristic is due to the fact that the storage cell blocks are not entirely decoupled from each other; the discharge of one block affects adjacent blocks. This effect is apparent in Figure 5.4, where the pedestal amplitude of a single cell changes depending on the position of its parent block in the waveform. Consequently, an extra dimension of “position in waveform” must be considered in the waveform lookup table.

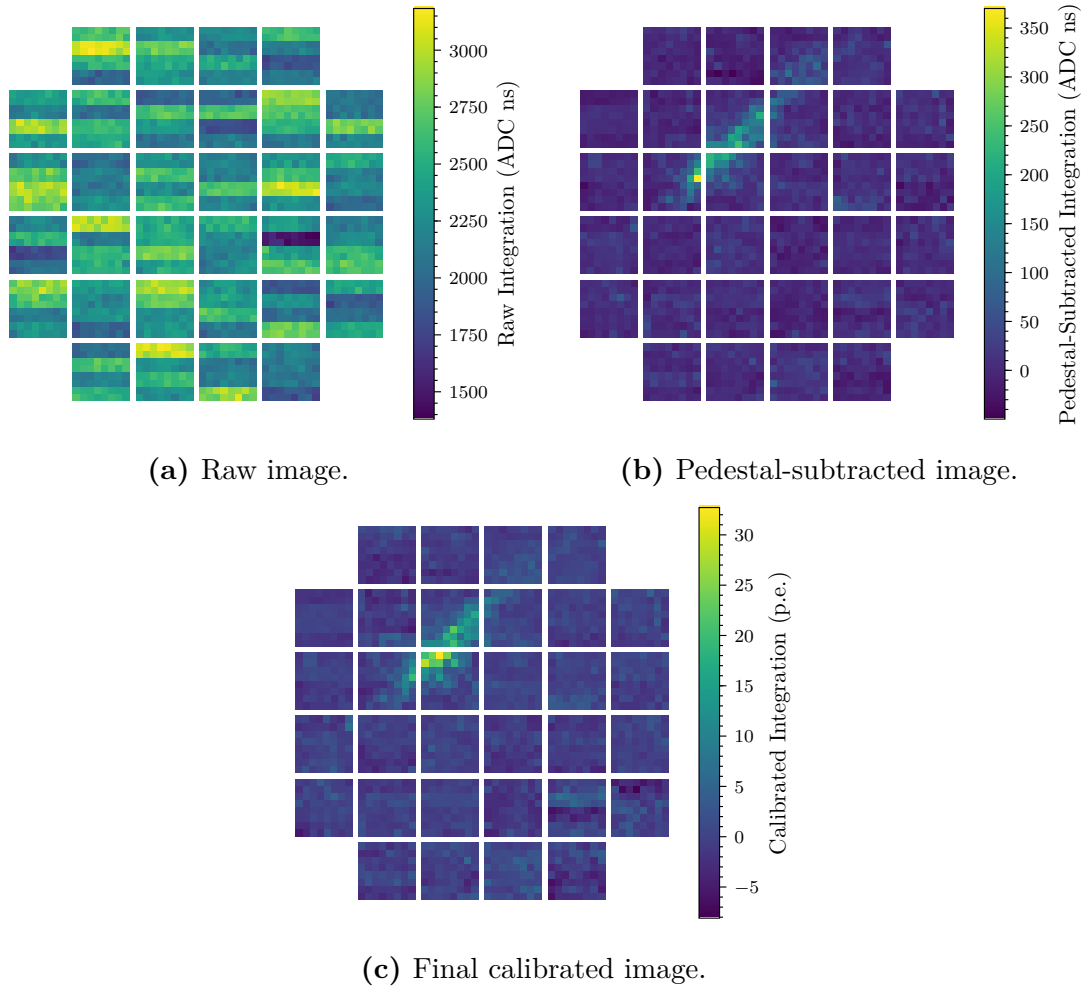


Figure 5.3: The same image of a Cherenkov shower taken with CHEC-M, but at different stages of calibration: (a) An image of the sample values taken at a timeslice corresponding to the shower maximum. (b) The same timeslice, but after the pedestal subtraction calibration has been applied to the samples. (c) The final image, after charge extraction (Chapter 6) and calibration into units of photoelectrons. The value of the samples An integration window was chosen using the *Neighbour Peak Finding* technique (Chapter 6) on the p.e. calibrated waveforms. The same samples were then integrated for each of the calibration stages.

Generation

In order to perform the pedestal subtraction, one must first generate a lookup table of pedestal values. This can be easily obtained with a calibration run where the voltages across the photosensor are disabled, and forcing the camera to trigger (with either an external pulse generator, or internally via software) to obtain a large amount of waveform data. Typically around 30,000 events provide enough samples

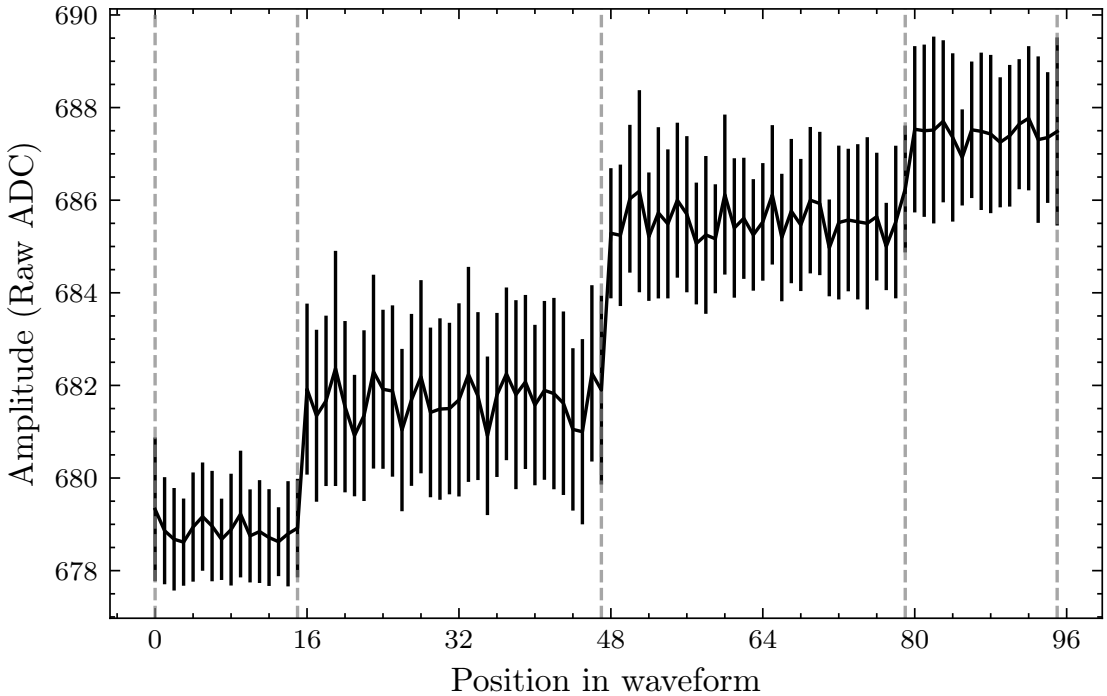


Figure 5.4: Average amplitude of the electronic pedestal for a single storage cell in a TARGET-C ASIC, at different positions in the waveform. Error bars indicate the standard deviation of the amplitudes. The grey dashed lines indicate the position of the block edges in the waveform for this cell. The average of the values inside each block segment equals the pedestal value stored in the lookup table for that cell, in each of those block positions.

for every storage cell, in every waveform position, to have at least 10 entries. The samples are then collected as a running average with the dimensions:

$$[Module, Channel, StartingBlock, Blockphase + Sample_i], \quad (5.1)$$

where the *StartingBlock* is the storage block that the first sample in the waveform belongs to, *Blockphase* is the cell index within the storage block that the waveform begins on, and *Sample_i* is the index of each sample in the waveform.

The TargetCalib library handles the pedestal lookup table generation, and stores it into a FITS file. A new pedestal file is typically generated at the start of each new dataset, as the dependencies on temperature and evolution with time are still being investigated.

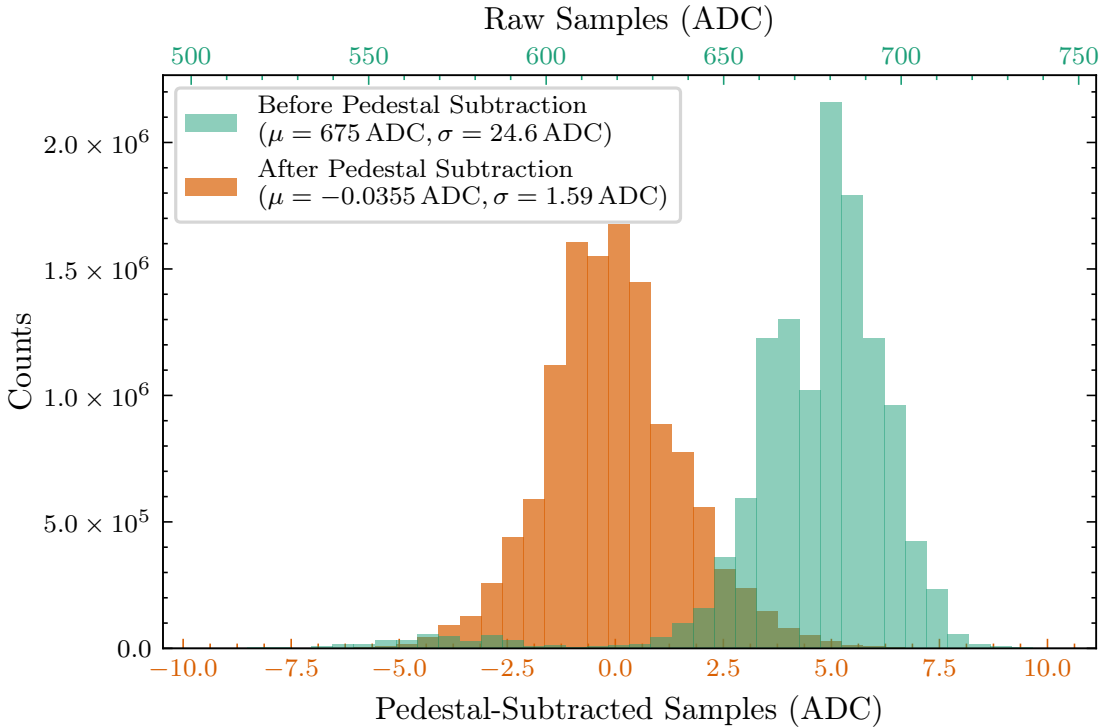


Figure 5.5: Spread of electronic-pedestal values before and after the pedestal subtraction for a single TARGET-C channel. The waveforms used to create the pedestal lookup table are from a different dataset to those used in these histograms. The mean μ and the standard deviation σ of each distribution are also shown.

Application

To apply the pedestal, the entry within the lookup table that corresponds to each sample is subtracted from the waveform. The result of the subtraction can be seen in Figures 5.2 and 5.3b.

Performance

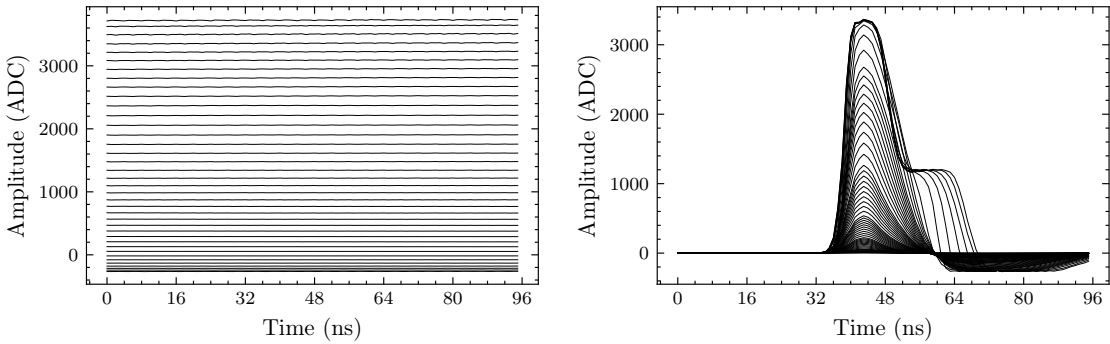
The primary quantification of this calibration's performance is the standard deviation of electronic-pedestal samples that have had separately-created pedestal values subtracted from them. Figure 5.5 demonstrates the performance of the pedestal subtraction for a TARGET-C channel, achieving a residual variation of 1.59 ADC (approximately 0.286 p.e.).

5.2.2 Transfer Function

The other calibration related to the sampling and digitisation inside the TARGET ASIC is caused by the non-linearities in the storing and reading of the analogue signal, to and from the storage cells (i.e. the charge and discharge of the switched capacitors). With reference to Figure 2.14, this means the non-linearity occurs in the steps between the sampling and storage array, and between the storage array and the Wilkinson ADCs. The non-linearity of these components is propagated to the sample readout - a sample with twice the amplitude input into TARGET will have less than twice the amplitude when readout.

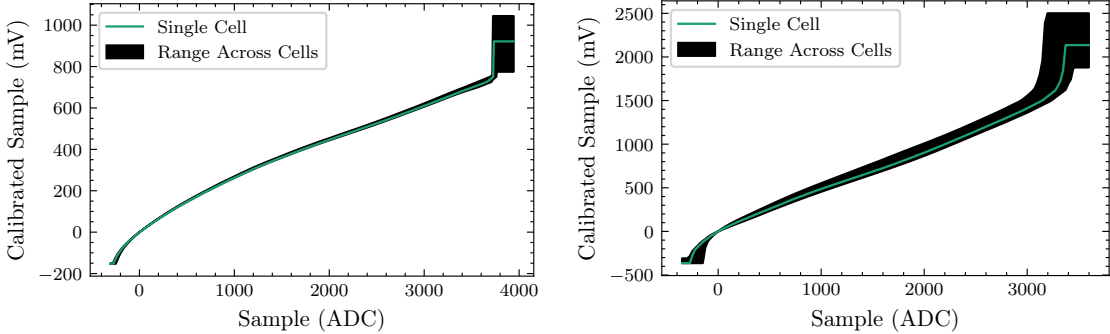
To correct for this non-linearity, a look-up table is generated to convert from the sample amplitude that is read out from the ASIC (in ADC) to the sample amplitude that is input into the ASIC (in mV). This look-up table is known as the Transfer Function. As one might expect, each sampling cell has its own linear response to account for, and therefore a look-up table is typically required at least per channel and per sampling cell, however measurements conducted by other CHEC members noticed an improvement in the calibration when considering a Transfer Function per storage cell. However, my own investigation using the *Charge Resolution*, shown in Appendix D, was unable to confirm this.

There are two forms of Transfer Function that have been considered for CHEC, distinguished by the type of input used to generate them. A Direct Current (DC) Transfer Function is created by applying a constant DC input of known voltage into the module, and iterating over the full dynamic range by varying the voltage. An AC Transfer Function is generated by inputting a pulse of a known amplitude with a shape expected from the photosensor, and iterating as with the DC approach. During previous investigations of the TARGET module, where sinusoidal signals were input into the module, a dependence on the signal frequency and input amplitude was observed that acts to further reduce the output amplitude [38, 58]. The source of this dependence was deemed to be due to the amplifiers, which cannot slew fast enough to keep up with the input signal if the frequency and amplitude are large.



(a) DC Transfer Function input, measured with TARGET-5. (b) AC Transfer Function input, measured with TARGET-C.

Figure 5.6: Multiple average waveforms, increasing in amplitude. Each average contains 1000 waveforms from the same single channel. These waveforms cover the full dynamic range of the TARGET ASIC, and are used as inputs to generate the DC and AC Transfer Functions, respectively. The saturation behaviour of the TARGET-C ASIC can be seen in the high amplitude waveforms in (b).



(a) DC Transfer Function lookup table, measured with TARGET-5. Contains 64 Transfer Functions, one for each Sampling Cell. (b) AC Transfer Function lookup table, measured with TARGET-C. Contains 4,096 Transfer Functions, one for each Storage Cell.

Figure 5.7: The Transfer Function lookup tables for a single channel.

Due to the use of a pulse to generate the AC Transfer Functions, the result inherently includes the correction required for the frequency that the pulses correspond to.

Generation (DC Transfer Function)

During the commissioning of CHEC-M, a DC Transfer Function was used with no AC corrections. To generate this Transfer Function, the internal input pedestal voltage (V_{ped}) setting is used to apply a DC voltage offset to the sampling ASIC. This pedestal voltage is provided by a commercially obtained DAC, installed on

the TARGET-5 module. This DAC has been characterised by the supplier, so the voltage amplitude obtained for each setting is known.

By repeating the process for V_{ped} values from 500 mV to 1700 mV, in steps of 25 mV, the full dynamic range of the module is explored, covering the range –250 ADC to 3700 ADC (Figure 5.6a). The running averages of the ADC samples are grouped and monitored according to:

$$[Module, Channel, Sampling Cell, Input Amplitude], \quad (5.2)$$

utilising every sample in the waveform. Around 1,000 events are required to provide sufficient statistics.

The second step in the generation of the DC Transfer Function is to linearly interpolate the running averages at the ADC points defined by the user. This provides a lookup table of mV values with dimensions:

$$[Module, Channel, Sampling Cell, ADC Value], \quad (5.3)$$

that can be used to provide a calibrated value for a measured ADC value. The lookup table for a single channel is illustrated in Figure 5.7a. This table is saved to a FITS file, ready for application. A fresh DC Transfer Function lookup table was typically created once a day during the CHEC-M commissioning.

Generation (AC Transfer Function)

When the upgrade from the TARGET-5 module to TARGET-C was made, the commercially provided DAC for the setting of V_{ped} was removed, and instead T5TEA generates a V_{ped} internally itself. Contrary to the commercial DAC, the V_{ped} provided by T5TEA is uncalibrated. Furthermore, the voltage applied is individual per channel, complicating the procedure to calibrate in. As a result, the approach of using the internal V_{ped} setting to generate a DC Transfer Function was abandoned. Instead, the decision was made to transition to an AC Transfer Function that uses the expected pulse shape as an input. This approach therefore corrects for the AC effect with the appropriate frequency. However, in order

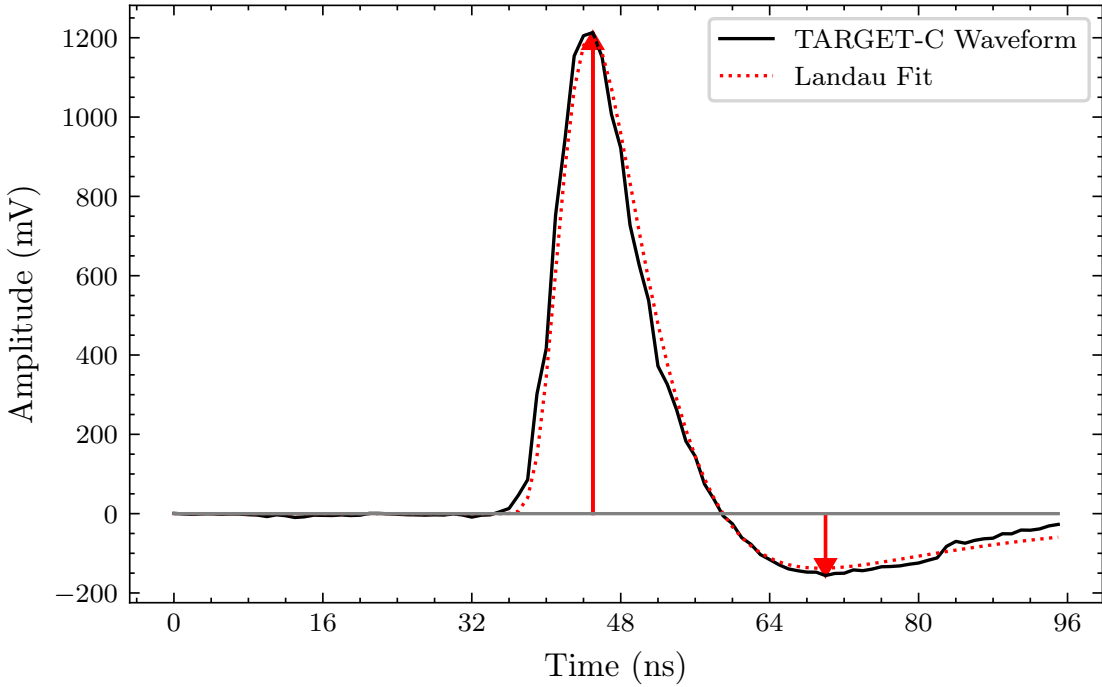


Figure 5.8: An example of the amplitude extraction used for generating the AC Transfer Function. The waveform is fit with two Landau functions (red curve). The samples of the waveform that occur at the time of the minimum and maximum of the fit (red arrows) are used as the inputs to the AC Transfer Function.

to externally input pulses from a pulse generator the module must be removed from the camera. Therefore, the AC Transfer Function is only generated once in the present calibration pipeline.

The full dynamic range is once again probed, by injecting pulses of varying amplitude. In order to extract the values that correspond to negative amplitudes in this method, the amplitude of the input undershoot is also monitored. Only the samples that correspond to the maximum of the input pulse (and minimum of the undershoot) has a “true” amplitude of the input amplitude. Therefore, to extract the correct samples, each waveform is fitted with two Landau functions, a fair approximation to the pulse shape (Figure 5.8). Consequently, only two samples are extracted per waveform, requiring a much larger population of events ($\sim 200,000$) in order to generate a reliable running average grouped according to:

$$[Module, Channel, StorageCell, InputAmplitude]. \quad (5.4)$$

It is important to note that a Transfer Function per storage cell was adopted for TARGET-C, as it was found to significantly improve the residuals (see Appendix D for further discussion).

The second step in the generation of the AC Transfer Function is identical to that in the DC case. The resulting lookup table for a single channel can be seen in Figure 5.7b.

Application

Irrespective of the Transfer Function type, the lookup tables are stored in a format which enables them to be applied identically. When calibrating an ADC sample, the relevant lookup table is obtained according to the channel and cell of the sample, and is linearly interpolated to provide the calibrated mV value for the specified ADC value.

Performance

Due to its complexity and variety of approaches, the Transfer Function is still one of the most actively discussed aspects of the CHEC calibration. Some possibilities for improvement include:

- An improved sample extraction method for the AC Transfer Function Waveform,
- The possibility for a DC approach for TARGET-C,
- Returning to the approach described in earlier TARGET studies where the pedestal is included inside the Transfer Function [38],
- Alternatives to linear interpolation, such as Piecewise Cubic Hermite Interpolating Polynomial (PCHIP),
- Exchanging the lookup table for a parametrised regression characterisation of the Transfer Function (such as a high-order polynomial),
- Deciding between "per storage cell" or "per sampling cell",

- Inclusion of temperature corrections.

Assessing the performance of the Transfer Functions is a more complicated task than for the pedestals. We are no longer comparing to a null signal, and instead comparing to an input amplitude which contains its own uncertainty, and could potentially be incorrect. So while the performance results may indicate that the residuals of the Transfer Function are small, this does not necessarily mean the calibration is accurate. Therefore, the most decisive performance indicator should be one that provides an independent measurement on the “correct” amplitude. The most obvious scheme fitting this requirement is the *Charge Resolution*, described in Chapter 3, the results of which are explored in Appendix D.

5.3 Photosensor Calibration

The other primary component in the detector chain that requires calibration is the photosensor itself. As photosensors are a much more common instrument used in a variety of experiments, the calibration procedures required are already well known in the academic community. It is therefore mostly a simple case of adapting existing approaches to fit our requirements.

The typical procedure in Cherenkov camera waveform analysis includes extracting the signal/charge from the waveform of each pixel. This procedure, and the different methods to achieve it, is described in Chapter 6. The value extracted is typically in digitisation counts (ADC) or units of voltage, multiplied by time if the charge extraction approach is an integral over the waveform. For example, the units of the extracted charge from CHEC-S using the *Cross-Correlation* method (see Section 6.2.2) is mVns. Once extracted, this charge must be corrected for the relative efficiency of its pixel compared to the mean of the camera in order to achieve a uniform response (“flat-fielding”), and then converted into a counting unit that is common among the telescopes in the array (such as photons or photoelectrons), thereby simplifying the processing of array data [59]. This

procedure is characterised in the equation:

$$I_i = \frac{A_{Qi} - A_{0i}}{\gamma_Q} \times \gamma_{FFi}, \quad (5.5)$$

where

- A_{Qi} is the charge extracted in units of mVns for pixel i , proportional to the number of photoelectrons,
- A_{0i} is the baseline in the absence of a signal for pixel i . It should be obtained using the same charge extraction approach used for the signal,
- γ_Q is the nominal conversion value from mVns to photoelectrons/photons for the entire camera,
- γ_{FFi} is the flat-field coefficient for the pixel i ,
- and I_i is the resulting calibrated signal in photoelectrons/photons.

In the final calibration design of CTA, A_{0i} is intended to be supplied by the telescope alongside the waveforms at regular intervals. The regular updating of this value ensures that any changes to the baseline due to electronic noise, NSB rate, or temperature variations (which can also increase DCR, see Section 2.2.4) are accounted for. However, this parameter was set to zero for the content of this thesis, and was not investigated. Instead, a less effective but simpler baseline subtraction was performed by monitoring the running average of the first 16 samples of the past 50 waveforms for each pixel. This running average was subtracted from each waveform before charge extraction. The remainder of this section will describe how to obtain the other calibration values, γ_Q and γ_{FFi} , and the other procedures related to the photosensor calibration.

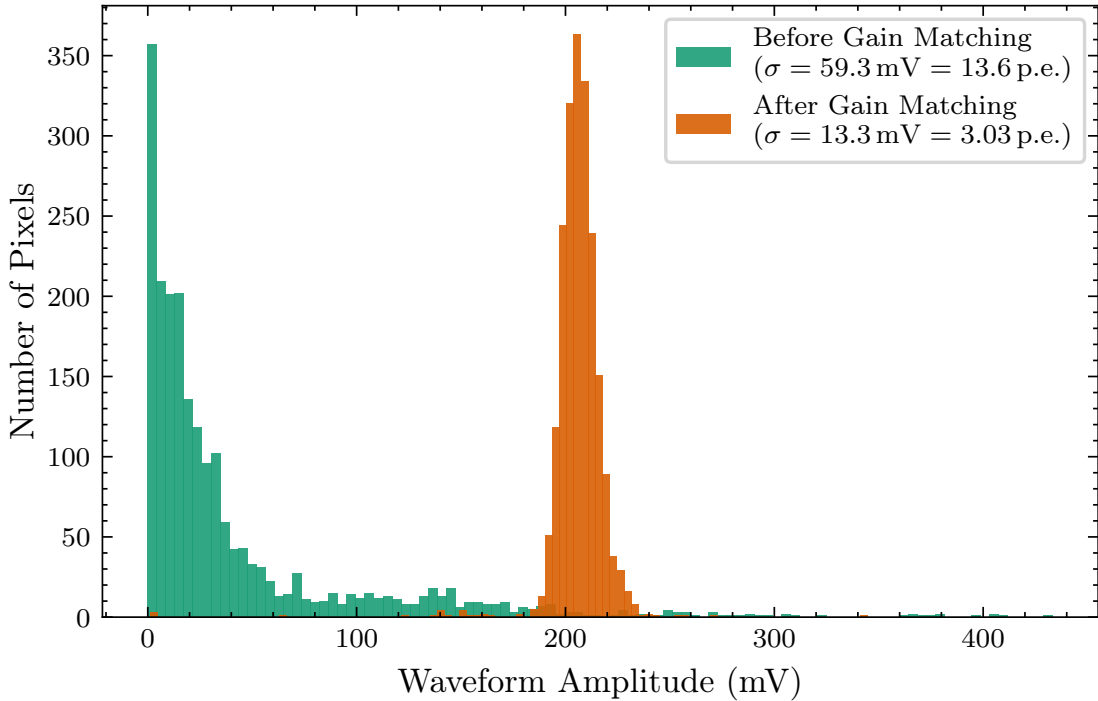


Figure 5.9: Comparison between the spread in the average signal amplitude per pixel before and after gain matching with CHEC-S, for a dataset with approximately 50 p.e. average illumination. In the “before” case the DAC value in every superpixel was set to 100. Every pixel in the camera was included in the histogram. The mean μ and the standard deviation σ of each distribution are also shown.

5.3.1 Gain Matching

The flat-field coefficients, γ_{FF_i} , provide an offline compensation for the photosensor parameters which alter the signal response in the waveform. While this is typically only the gain in the case of MAPMTs, these parameters are more numerous for SiPMs, and are described in Section 2.2.4. However, these parameters also have a dependence on the voltages across the photosensor, which is a controllable value. The dependence of the CHEC-S SiPM parameters on voltage is shown in Figure 2.5. With the CHEC-M MAPMTs it is only possible to change the voltage value for an entire module, whereas with the CHEC-S SiPMs the voltages can be configured per superpixel (group of four pixels). Therefore, voltage values can be selected before data-taking which result in a more uniform signal response between photosensor pixels. This is referred as “Gain Matching”, however the name is slightly misleading, as it is the signal that is being matched, not the gain. It is performed by specifying

the amplitude (in mV) that every pixel should be matched to, and then performing the following iterative procedure:

1. The camera is uniformly illuminated with approximately 50 p.e..
2. The waveforms are readout, calibrated, and averaged per superpixel/module (excluding any dead pixels).
3. The peak amplitudes of the average waveforms are extracted.
4. Each module/superpixel is categorised as being above or below the requested amplitude.
5. Depending on their category, the voltage setting is increased or reduced by steps of 5 (in arbitrary DAC units), such that it increments closer to the requested amplitude. If the amplitude has been overstepped in the previous measurement, a smaller step value is used. The minimum DAC step value available is 1, which corresponds to $\frac{10}{256}$ V. If the amplitude is not responding to changes in voltage, the pixel is classified as “dead”, and excluded from the average waveforms.
6. The new voltage settings are applied and the process is repeated.

In the future, this iterative technique will be replaced with a set of lookup tables for different requested amplitudes. These lookup tables will contain the final voltage settings resulting from this iterative technique. Additionally in the future, the requested signal will not be specified in terms of peak amplitude, but in terms of the *Cross Correlation* charge extraction approach. The resulting spread in signal response for CHEC-S as a result of the gain matching is shown in Figure 5.9.

The additional benefit of the gain matching is that it provides a convenient part in the data-taking chain to apply the bias compensation for temperature dependences (introduced in Section 2.2.4). This is achieved using the monitored temperature value per module (included in the data stream from the FEE modules) and a lookup table of the appropriate corrections to the voltages, such that a constant signal

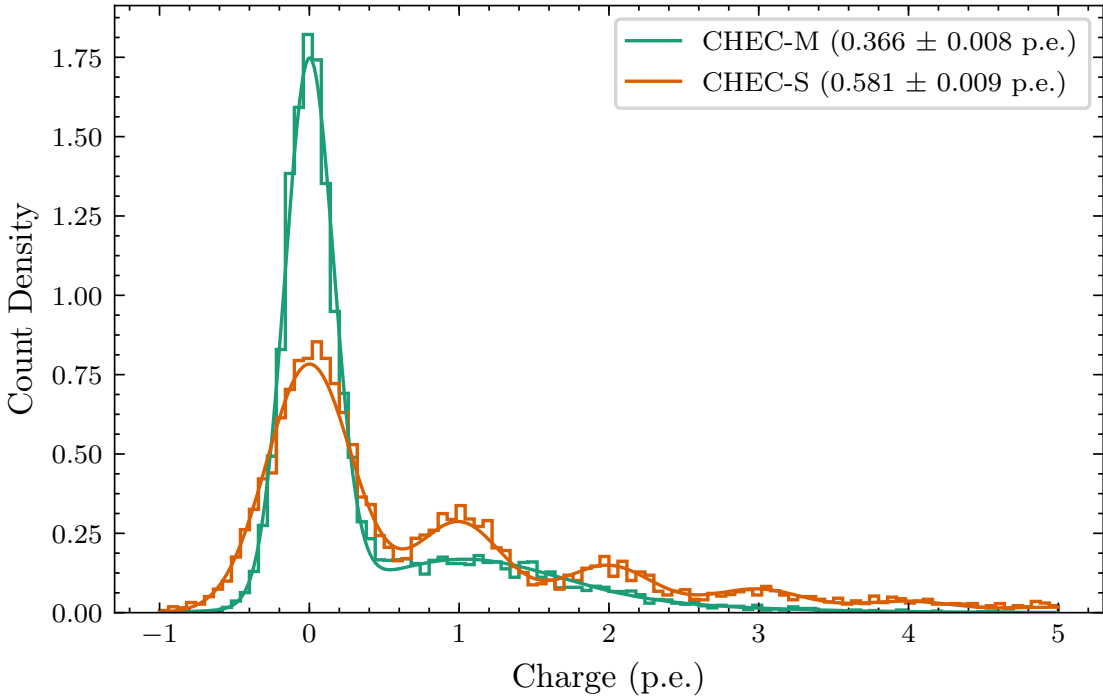


Figure 5.10: Comparison of SPE spectra between CHEC-M and CHEC-S for a single pixel, along with their corresponding fit function.

response is kept across the camera. This particular in-situ calibration has not yet been implemented, but is intended for the future.

5.3.2 SPE Fitting

Due to the photon-counting nature of MAPMTs and SiPMs, when the signal extracted from a pixel, illuminated with a low light-level (~ 1 p.e.), is accumulated into a histogram, the resulting spectra (Figure 5.10) show peaks at regular intervals corresponding to the baseline (zeroth peak), 1 p.e. (first peak), 2 p.e. (second peak), etc. As explained in Section 2.2.4, the single photoelectron resolution of SiPMs is very high, much higher than is observed with MAPMTs. This accounts for the difference between the two photosensors in Figure 5.10. These spectra are referred to as “Single PhotoElectron (SPE) Spectra”. The physical processes that result in these spectra are well understood for MAPMTs and SiPMs, and therefore analytical formulae exist describing the spectra. When these formulae are fit to the histogram, they can be used to extract certain parameters of the photosensor, including the

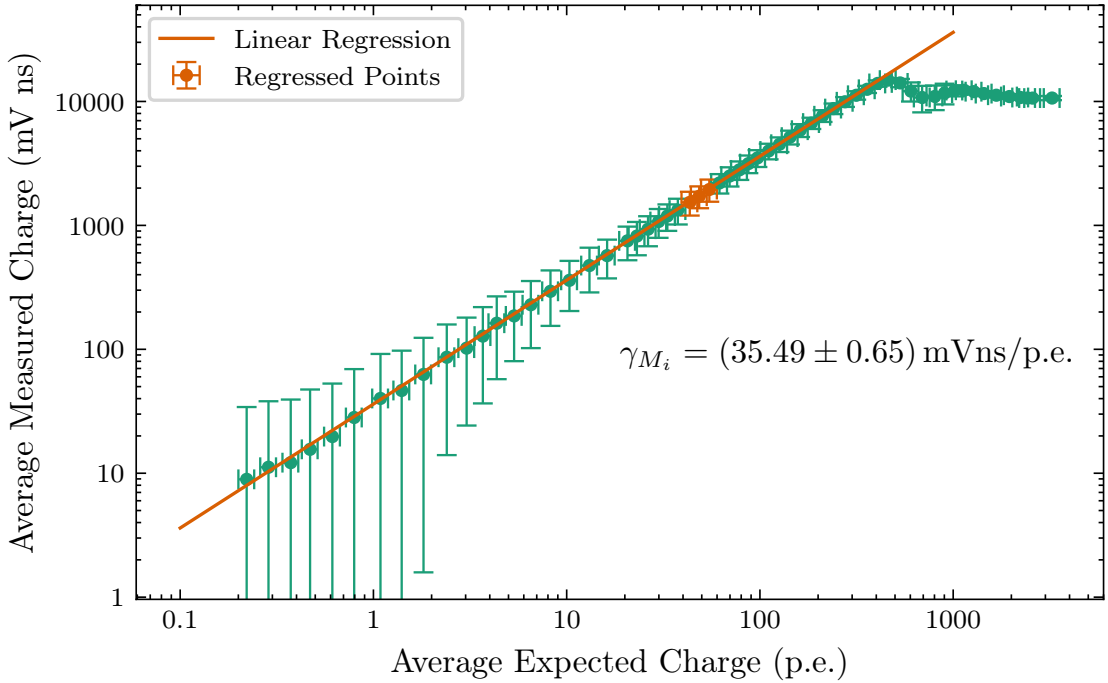


Figure 5.11: The average measured charge per illumination for a single pixel. The Y error bars are the standard deviations of the charges for each illumination for a single pixel. The X error bars are the uncertainties on the average expected charge calibration (Section B.6). The orange points were used in a linear regression through the origin to determine the flat-field coefficients for each pixel. The resulting gradient for the pixel (γ_{M_i}) is annotated.

average incident illumination λ , in units of photoelectrons. As λ provides an absolute illumination value, it allows for the full calibration of average expected charge for each filter-wheel position, for each pixel (conducted in Appendix B). This is the first step required in obtaining the flat-field coefficients. For more details on this fitting procedure, and the formulae used to describe the SPE spectra, refer to Appendix C.

5.3.3 Flat-Field Coefficients

Once the “average expected charge” dependence on filter-wheel position/transmission is characterised (Appendix B), we can calculate the coefficients, γ_{M_i} , required to convert the average measured charge (in mVns) into the charge we expect (in photoelectrons/photon). The application of these coefficients to the extracted/measured charge has two effects:

- The signal response between pixels is homogenised - the same average amount

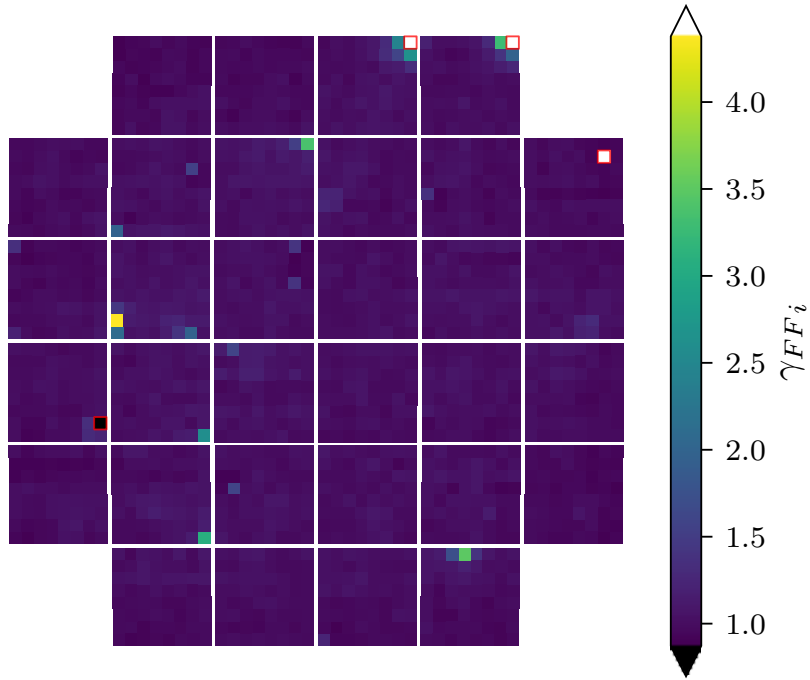


Figure 5.12: Camera image of the flat-field coefficient value, γ_{FF_i} , per pixel. Pixels that were designated “dead” or misbehaving are outlined in red, and exist beyond the colour-scale range.

of charge will be extracted for any pixel illuminated with an average of N photons.

- The signal response is converted into the common telescope-array units of photoelectrons or photons.

Therefore:

$$\gamma_{M_i} = \frac{\gamma_Q}{\gamma_{FF_i}}. \quad (5.6)$$

To obtain γ_{M_i} per pixel i in the lab, datasets with around 50 p.e. average expected charge per pixel were produced. For each pixel, the average measured charge (in mVns) was linearly regressed, while forcing the fit through the origin. This regression is shown for a single pixel in Figure 5.11. The resulting gradient of the regression is equal to γ_{M_i} , which was combined with Equations 5.5 and 5.6 for the calibration of measured charge into photoelectrons. The nominal conversion value from mVns to photoelectrons for CHEC-S was calculated to be $\gamma_Q = (35.555 \pm 3.041)$ mVns/p.e.,

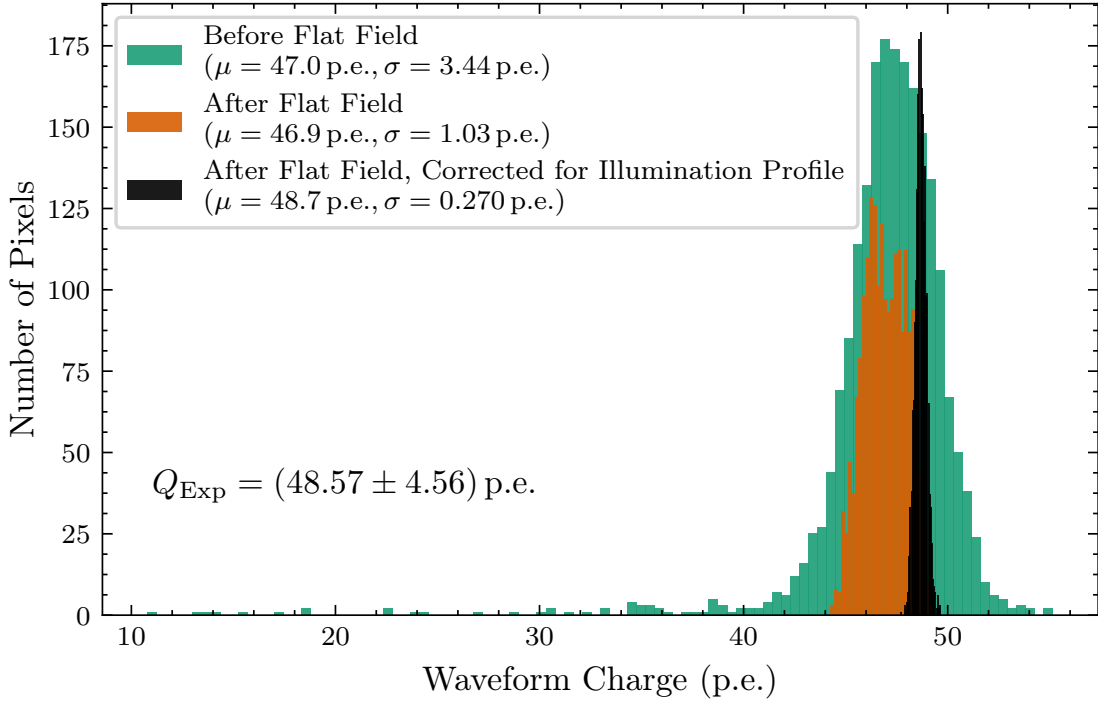


Figure 5.13: Comparison between the spread in the average signal amplitude per pixel before (blue) and after (orange) the flat-fielding calibration. The charges were extracted from a dataset where a theoretical pixel located at the centre of the camera would be expected to have a charge of $Q_{\text{Exp}} \approx 50 \text{ p.e.}$. The black histogram contains the charges after the difference in the illumination profile (Section B.3) between the pixels was considered, i.e. they contain the charge that would be measured if every pixel was located at the camera centre. Every pixel in the camera, excluding the “dead” pixels, was included in the histograms. The mean μ and the standard deviation σ of each distribution are also shown.

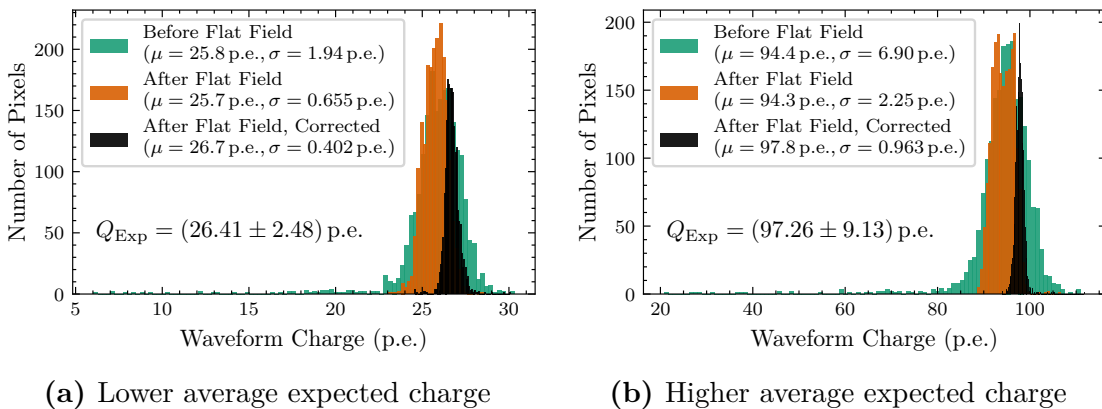


Figure 5.14: Same as Figure 5.13, but with a higher and lower average expected charge (Q_{Exp}).

and the spread of γ_{FF_i} across the camera is shown in Figure 5.12. The value for γ_Q can be converted into its equivalent single mV sample (i.e. peak-height) equivalent using the reference pulse from the *Cross Correlation* extraction method (Chapter 6), resulting in a conversion value of (4.373 ± 0.374) mV/p.e..

The resulting residual spread in signal response between pixels at an average expected charge of (47.67 ± 3.79) p.e. is shown in Figure 5.13. The final variation in signal response between pixels at this illumination was measured to be 0.5%. Figures 5.14a and 5.14b show the improvement of the average charge spread between pixels for a higher and a lower illumination.

As the flat-field coefficients have been calculated in a manner in which they are unfolded from the illumination profile (by calculating the average expected charge individually for each pixel), they are applicable to any environment the camera is used in. Any deviations that are measured in the signal between pixels are then due to the illumination profile present in the environment, and not due to the characteristics of the photosensor. Once the camera is on the telescope, the flat-field coefficients are intended to be routinely updated using the reflection of the LED flashers (Section 2.3.3) in the secondary mirror. This calibration will require an updated illumination profile in order to be performed.

Consideration of Errors and Uncertainty

The standard error on the estimate of the gradient per pixel, $\sigma_{\gamma_{M_i}}$, that arises from a standard linear regression can be calculated with the relation derived by Taylor [60]:

$$\sigma_{\gamma_{M_i}} = \sigma_r \sqrt{\frac{N}{N \sum Q_{\text{Exp}_i}^2 - (\sum Q_{\text{Exp}_i})^2}}, \quad i = 0, 1, 2, \dots, N, \quad (5.7)$$

$$\sigma_r = \sqrt{\frac{\sum (A_{Q_i} - A_{Q_f})^2}{N - 1}}, \quad (5.8)$$

where N is the total number of regressed points i , σ_r is the mean square error of the regression, the dependant variable A_{Q_i} is the average measured charge at the average expected charge Q_{Exp_i} , and A_{Q_f} is the value that results from the regression at that same value of Q_{Exp} . The denominator in Equation 5.8 is $N - 1$ as we constrained the regression through the origin, therefore there was only one free parameter.

The error on γ_{M_i} is used as weights when calculating the average to obtain γ_Q . Therefore the uncertainty on γ_Q is quoted from the weighted standard deviation across the values of γ_{M_i} for each pixel.

5.3.4 Dead Pixels

Figure 5.12 shows that some of the photosensor pixels contained either no signal or an odd signal, resulting in an extreme flat-field coefficient. This was likely due to damage to the pixel during handling, or due to water ingress. However, the four pixels constitute to 0.2 % of the camera, therefore the camera is still well within the **B-TEL-1295 Pixel Availability** CTA requirement (Section 3.2.3). These pixels were excluded from any calculations involving multiple pixels, including the expected-charge calibration and the charge-resolution across the camera.

5.4 Saturation Recovery

As evident in Figure 5.11, high illumination measurements (greater than ~ 200 p.e.) are affected by saturation of the detector. The saturation shown is due to the TARGET ASIC, which saturates before the photosensor. However, while the height of the pulse increased no further, the excess charge caused the pulse to extend further (Figure 5.6b). Therefore, it could be possible to perform a simple correction for the saturation recovery by utilising this waveform behaviour. A simple, initial investigation into saturation recovery is shown in Figure 5.15, where the waveform was integrated in a window that started just before the pulse maximum, and extended to the end of the waveform. This resulted in an extracted charge that continued to increase with illumination, apart from in the region immediately after saturation. More investigation is required for this calibration.

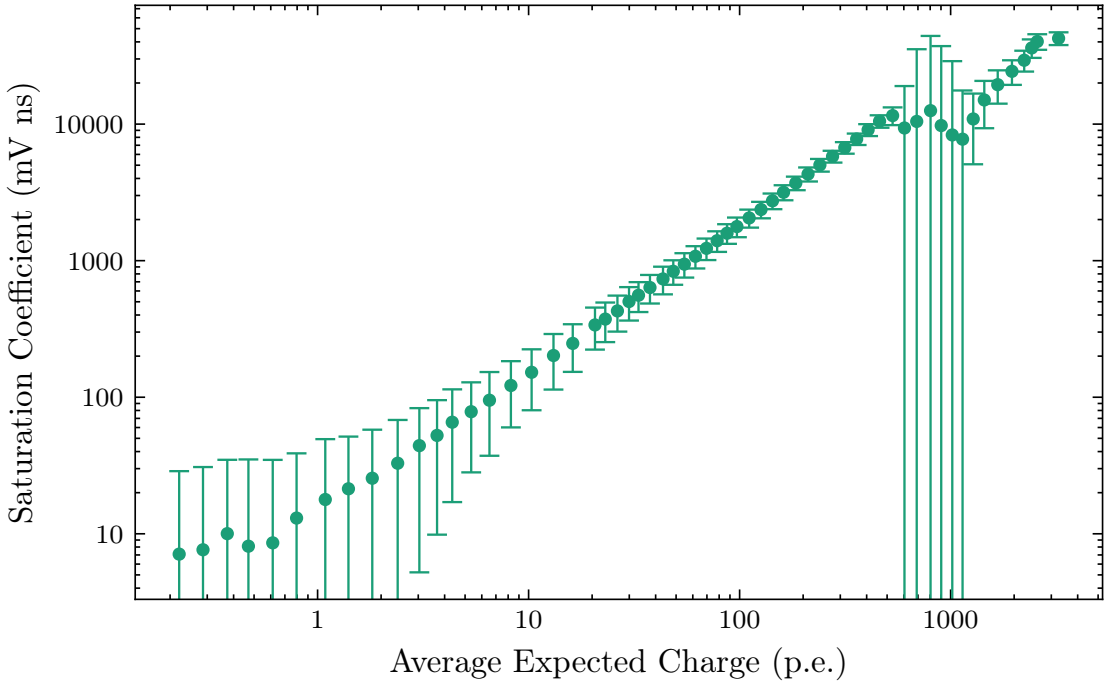


Figure 5.15: Initial investigation into recovering charge from a saturated waveform for the same pixel as shown in Figure 5.11. The saturation coefficient is the integral from just before the pulse maximum, to the end of the waveform readout.

5.5 Timing Corrections

Due to the routing of the electronics in the front-end, the electrical signal path is slightly different per channel, causing a small difference in apparent arrival of the pulse in the waveform. The relative arrival time per pixel for CHEC-S is shown in Figure 5.16. This is measured by extracting the average arrival time per pixel over 1000 events at an average illumination of ~ 100 p.e., and subtracting each pixels value by the average across the camera. It is clear that in every module, there is one particular ASIC slot, corresponding to a 16-pixel corner of the module, that has a longer electrical signal path.

Not only does the timing correction need to be taken into consideration when investigating the timing performance, it also can have a significant impact on the charge extraction performance. This is because the charge extraction approaches typically rely on other pixels (neighbouring or entire camera, see Chapter 6) sharing a compatible pulse time. A charge extraction routine that incorrectly extracts the

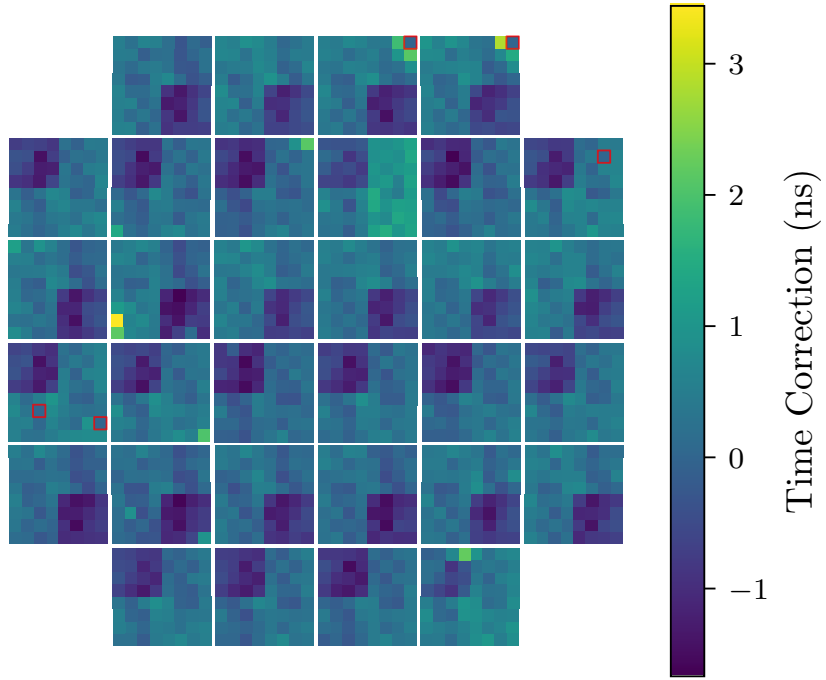


Figure 5.16: A camera image of CHEC-S showing the timing correction for each pixel. The “dead” pixels are outlined in red, and have a zero timing correction.

charge by 1 ns can have a negative impact on the *Charge Resolution*. Discussions are ongoing on how to best include the timing corrections in the charge extraction.

5.6 Future

During the long development of CHEC, the calibration procedure has evolved significantly. Multiple iterations of the procedures have occurred to:

- Accommodate the changes required in the upgrades of hardware (such as from TARGET-5 to TARGET-C).
- Simplify the calibration to save on computing resources.
- Account for additional factors, thereby improving the calibration (such as the AC contribution to the Transfer Functions).

Therefore, while each iteration improves in one aspect, it may be at the expense of the others. As a result, the TARGET calibration procedure described in this

chapter appears quite complicated compared to the approaches detailed by Bechtol et al. [58] and Albert et al. [38]. The next step in the calibration development for CHEC is therefore to review the procedure used, with the aim of producing an approach that is simpler, includes aspects such as temperature dependence, and meets the requirements and processing rates required by CTA.

6

Waveform Processing

Contents

6.1	Introduction	91
6.2	Charge Extraction Methods	92
6.2.1	Peak Finding	94
6.2.2	Integration	97
6.2.3	Approaches Adopted by Other IACTs	99
6.2.4	Performance Assessment	102
6.3	Shower Reconstruction	102
6.3.1	Image Parametrisation	102
6.3.2	Direction Reconstruction	103
6.3.3	Energy Reconstruction	104
6.3.4	Gamma-Hadron Discrimination	105

6.1 Introduction

Methods for retrieving information about the Cherenkov shower have been a primary component of the Imaging Atmospheric Cherenkov Technique since its inception. Early techniques such as those used in the first observation of TeV Gamma rays from the Crab nebula [61] are still utilised in modern IACTs. These techniques are also applicable to CTA telescopes, and as CTA is a large consortium which consists of the worldwide IACT community, the developers of advanced waveform reduction and shower reconstruction approaches used by previous IACTs have prepared them for use within CTA (for example, the ImPACT shower reconstruction technique

developed by [54]. However, as:

- (a) CTA will consist of the most advanced IACTs to date, with higher shower imaging resolution and telescope multiplicity than has previously been available,
- (b) the capabilities of digital signal processing have significantly increased in the past decade,

the opportunity for more advanced and more successful algorithms exists for CTA. Some efforts have already been made to develop novel approaches, for example, the utilisation of convolutional neural networks to reconstruct the shower’s direction [62]. However, it is an aspect that is expected to constantly evolve and improve during the lifetime of CTA. In this chapter I will provide insight into the existing and in-development reduction techniques utilised to extract the Cherenkov shower signal from the waveforms, and my involvement in designing a charge-extraction technique for CHEC-S. I will also provide a brief overview of the shower reconstruction methods typically used with IACTs. With regards to the CTA data levels (Figure 3.3), this chapter is mostly concerned with the steps from *DL0* to *DL2*.

6.2 Charge Extraction Methods

The immediate step after the waveform calibration is the extraction of signal (also sometimes referred to as charge) from the waveforms provided by the individual cameras. As a result of the low-level calibration detailed in Chapter 5, the waveforms from each CTA camera exist in a common state, with no remaining dependencies on the electronics they were produced by. Therefore, the extraction techniques are typically applicable to all CTA cameras.

The extraction of signal from a waveform is a very generic problem, allowing for the utilisation of common signal processing techniques that are not unique to Cherenkov shower analysis. The goal is to extract the majority of signal from the pulse created by the Cherenkov shower light, while simultaneously limiting the inclusion of noise factors. Figure 6.1 shows a CHEC-S waveform which contains

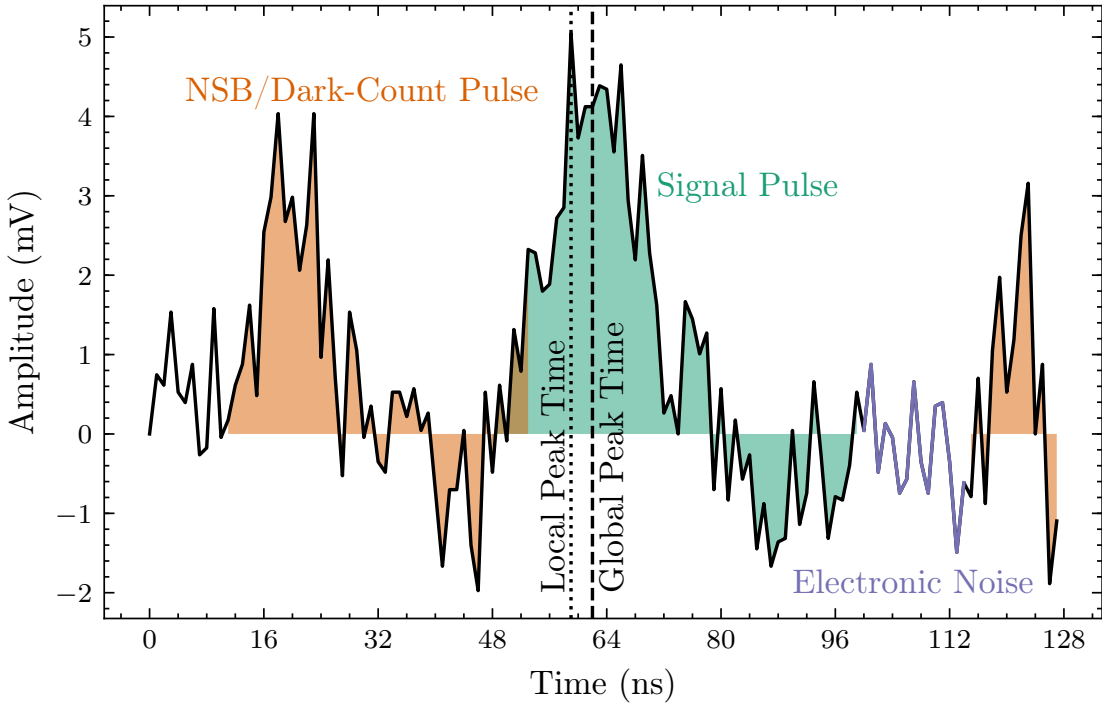


Figure 6.1: A waveform from CHEC-S lab data, illuminated by the laser with the filter wheel set to give an average expected charge of 3 p.e.. The waveform is annotated with the different components that contribute to the charge extraction. Although the electronic noise is only highlighted at one section, it affects every sample.

both signal and noise. Two quantities are extracted in this stage: the signal charge in each pixel, and the signal arrival time per pixel.

The total signal charge in a pixel, i.e. the total number of photo-electrons released from the PMT's photocathode or the number of electron-hole pairs generated in an SiPM, is proportional to the total area below the pulse corresponding to the Cherenkov photons (blue area of Figure 6.1). If the waveforms were completely free of noise, and the readout window was large enough to capture the full Cherenkov signal, a simple integration of the entire readout would be a satisfactory approach for obtaining the signal charge. However, as we do not have the luxury of perfect waveforms, more complex methods are required. Charge extraction algorithms typically consist of two aspects: how the signal pulse is found, and how the pulse is integrated.

6.2.1 Peak Finding

Two factors must be considered when finding the signal pulse of a Cherenkov shower. Firstly, the majority of camera pixels will not contain any Cherenkov signal while still containing noise. A peak finding technique that assumes a signal exists in the readout will be biased, as it will mistake the noise for a signal. Secondly, due to the nature of Cherenkov showers (Section 1.2), the Cherenkov signal will have different arrival times between pixels due to the time evolution of the Cherenkov image. This time gradient across the image is especially apparent for high-energy showers at a large core distance from the telescope. The most successful peak-finding technique is one that best accounts for those two factors. Some simple techniques used to define a peak time from a waveform include:

- **Local Peak Finding:** Each waveform is treated independently from the others. The maximum point in the waveform is treated as the peak/arrival time. This approach is intrinsically biased to assume every waveform contains a signal; therefore, in the absence of a Cherenkov signal, the largest noise pulse will be extracted, resulting in a higher total charge than should be obtained.
- **Global Peak Finding:** The waveforms from each pixel are combined into an average waveform, from which the maximum sample is treated as the peak time for every pixel. This technique is only useful if a large portion of the camera is simultaneously illuminated, such as by a laser in the case of lab commissioning and calibration runs.
- **Neighbour Peak Finding:** The waveforms from neighbouring pixels to the pixel-of-interest are combined into an average waveform. The maximum sample in the average waveform is treated as the peak time for the pixel-of-interest. This technique is often preferred for Cherenkov images as it has a reduced charge bias (especially if the pixel-of-interest’s waveform is not included in the average); pixels with Cherenkov signal typically have

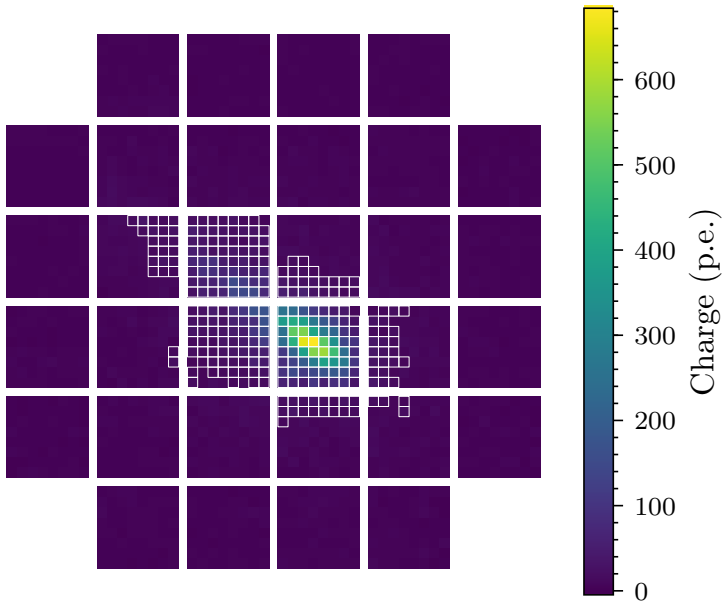


Figure 6.2: Camera image showing the charge extracted in each pixel, using the *Neighbour Peak Finding* technique and a simple waveform integration. The white-outlined pixels are those that survived the (17, 8) tailcuts (Section 6.3.1). This image corresponds to a bright Cherenkov shower observed during the second on-telescope campaign for CHEC-M (Chapter 8).

neighbours that also contain Cherenkov signal at a correlated time, while the neighbours of empty pixels only contain random noise, and therefore a peak time that is uncorrelated to the noise is chosen.

- **Fixed Peak Value:** Due to a reliable definition of the camera trigger and subsequent electronic chain, the position of the pulse in the waveform could consistently be known a priori, allowing for a fixed peak time. However, this method requires a larger integration window size in order to capture the full pulse in the tail of the Cherenkov shower, which occur at a later time than the initial photons which trigger the camera. As a result, a larger amount of noise will be included in the integration window. However, this technique usually contains the least bias, as no signal is assumed to exist.

A more complex peak-finding technique is the *Gradient Peak Finding* approach. This approach was designed for the VERITAS telescope [63][64][65], but is applicable to any IACT telescope that allows the dynamic specification of an integration

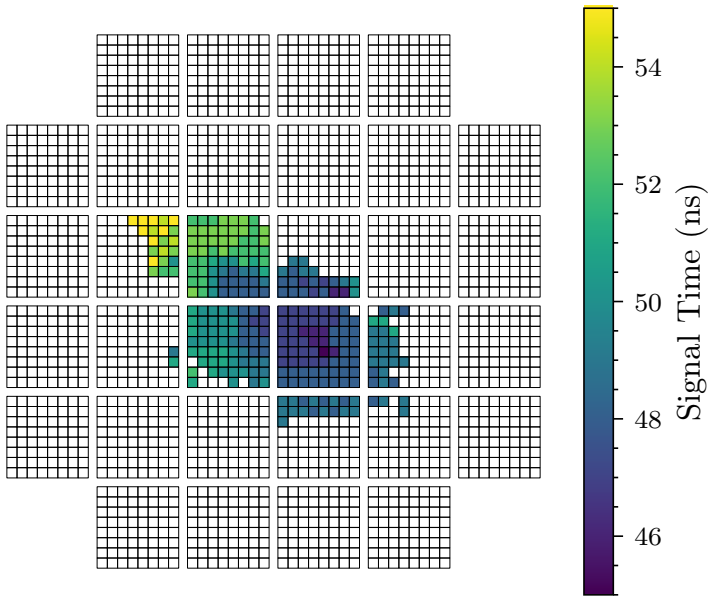


Figure 6.3: Camera image showing the pulse time in each pixel, extracted with the *Neighbour Peak Finding* technique, and cleaned using the tailcuts (Section 6.3.1). This image corresponds to the same event shown in Figure 6.3.

window. *Gradient Peak Finding* utilises the gradient profile of the photon arrival time for gamma-induced Cherenkov showers, described in Section 1.2. The time gradient for a bright Cherenkov shower (Figure 6.2) is illustrated in Figure 6.3. This peak-finding technique is a two-pass approach performed by first extracting the signal using one of the other methods. The pulse-timing information contained within the pixels that survive the image cleaning (Section 6.3.1) can then be used to obtain a relation between “distance along primary image axis”, D_{ax} , and the pulse time, T_0 . Using the obtained relation between D_{ax} and T_0 , an unbiased pulse time is obtained for each pixel depending on its position along the image axis.

These peak-finding methods have been described in relation to the maximum of the signal pulse, however they may instead use other characteristic positions of the pulse, such as the half-maximum time on the rising edge, or the centre of gravity of the pulse. Additionally, more advanced peak-finding techniques may up-sample (possibly by zero-padding in the frequency domain via a Fourier transform) or interpolate the signal to obtain a more precise peak time [64, 65], or even apply low-pass filters in order to remove low frequency baseline noise.

The peak finding should be done in conjunction with any timing corrections (Section 5.5) that may be required.

6.2.2 Integration

Once the peak time has been obtained, the simplest approach to extract the signal is to define an integration window centred about this time. The size of the window needs to be large enough to capture sufficient signal from the pulse, but small enough that not too much noise (NSB, dark counts, afterpulsing) is included within the window, thereby maximising the signal-to-noise. Additionally, the camera’s pulse shape may not be symmetric, so a better signal-to-noise may be achieved by shifting the window a few samples with respect to the peak time. The optimal integration window size and shift for the CHEC-S waveforms is found to be 5 samples and 2 samples (i.e. 5 ns and 2 ns), respectively, according to the investigations performed in Appendix E.

Beyond the simple “boxcar” integrator method (where every sample integrated has a weight of 1), other more advanced strategies may be used to extract the charge. One example is the fitting of the waveform in order to extract the signal pulse, either with an analytical description of the expected pulse or with a more unconstrained description, such as a cubic spline. A second advanced approach is the use of digital filters, which can be used in combination with knowledge of the pulse shape to robustly extract the signal even in the presence of high frequency noise with a large amplitude. Such a technique has been designed and adopted for GCT, referred to as the *Cross-Correlation* method.

Cross Correlation

Cross-correlation is a common signal processing technique used as a measure of the similarity between two signals as a function of the displacement in time applied to one of the signals. Given a continuous function $f(t)$ defined between $0 \leq t \leq T$ and a second continuous function $g(t)$, the cross-correlation between

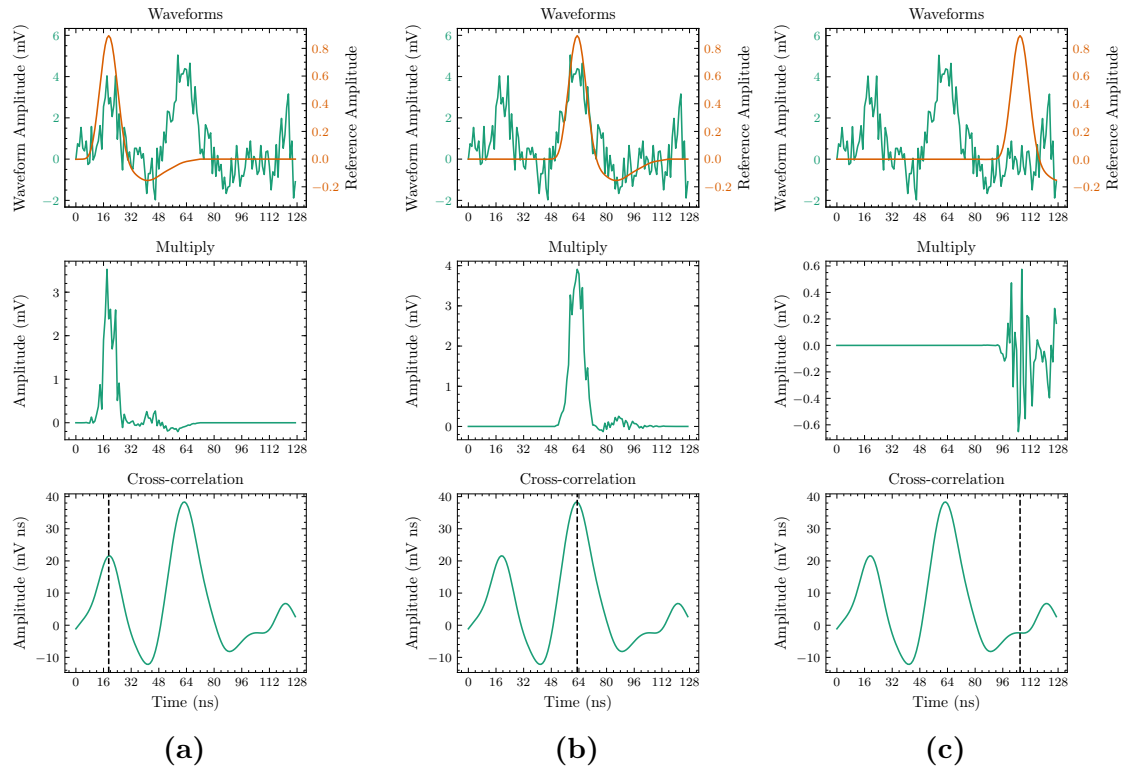


Figure 6.4: The three stages involved in obtaining the cross Correlation of a waveform with the reference pulse. The waveform investigated is the same one shown in Figure 6.1. The stages are shown for three time displacements (Equation 6.1): on an NSB/dark-count pulse before the signal (a), at the time of the signal (b), and at a time where there is only the baseline (c). The top panels show the waveform and the reference pulse shifted by the time displacement. The middle panels show the multiplication of the two traces in the first panel. The bottom panel shows the cross correlation for all time displacements. The value of the cross correlation at the time displacement shown by the red line is obtained by summing all the samples from the trace in the middle panel.

the two functions $(f \star g)$ is defined as

$$(f \star g)(\tau) = \int_0^T \bar{f}(t)g(t + \tau)dt, \quad (6.1)$$

where $\bar{f}(t)$ is the complex conjugate of $f(t)$ and τ is the time displacement (also referred to as the “lag”) between the two functions [66]. In descriptive terms, as τ increases, $g(t + \tau)$ will slide past $f(t)$. The cross-correlation for a value of τ_1 is then the integral across t of the product between $f(t)$ and $g(t + \tau_1)$. For a discrete function that is real-valued, such as a sampled waveform, Equation 6.1 can instead be defined as

$$(f \star g)[n] = \sum_{m=0}^N f[m]g[m+n], \quad (6.2)$$

where N is the total number of samples in the waveform and n is the sample displacement from sample m .

Through utilising a template of the expected pulse shape in the absence of noise (hereafter referred to as the “reference pulse”), features inside the waveform that are correlated with the reference pulse shape are emphasized, while features that are not, such as the electronic noise, are suppressed. Therefore, the peaks in the cross correlation correspond to the displacements where the signals match best, and the values of the peaks correspond to an weighted integral of the entire waveform, and can be used as an extracted charge value. An illustration of the *cross-correlation* technique being applied on a CHEC-S waveform is shown in Figure 6.4.

The reference pulse we use for the cross correlation was obtained via probing the input analogue signal on the TARGET module and averaged on an oscilloscope. It was then normalised such that cross-correlation between it, and the reference pulse normalised to have an integral of 1, has a maximum value of 1. This normalisation ensures that the cross-correlation result of a 1 p.e. signal, contained in a waveform with units of mV, gives the conversion value from mVns to p.e.. The relative conversion into mV for “peak-height” investigations is also possible using the reference pulse. An optimised implementation of cross-correlation exists in `scipy.ndimage.correlate1d` [67], where the waveforms for every pixel are processed in parallel.

6.2.3 Approaches Adopted by Other IACTs

Some examples of charge-extraction approaches adopted by other IACTs are outlined below.

MAGIC

Members of the MAGIC telescope, Albert et al. [68], performed a study comparing the techniques proposed for their signal reconstruction. Four approaches were compared: *fixed-window*, *sliding-window* with amplitude-weighted time, *cubic spline fit* with integral or amplitude extraction, and *digital filter*. It was concluded that

the digital filter, which relies on knowledge of the signal shape to minimise the noise contributions, provided a charge reconstruction with acceptable bias and minimal variance, while remaining stable in the occurrence of small variations in pulse shape and position.

VERITAS

Similar to the aforementioned study for the MAGIC telescope, comparisons of charge extraction approaches were also performed for VERITAS [63–65]. Specifically, the extraction methods compared included:

- a *simple-window* integration using a priori knowledge of the Cherenkov pulse time in the trace,
- a *dynamic-window* integration which slides across the trace to find the Cherenkov pulse,
- a *trace-fit* evaluator with fits the trace with two exponential functions which respectively describe the rise and fall time of the pulse,
- a *matched-filter* which “uses a digital filter based on the assumed shape of the FADC pulse to integrate the charge” [65, p. 2],
- and finally an implementation of the *Gradient Peak Finding* approach described earlier in this chapter.

At first glance, some of these approaches bear resemblance to those used by MAGIC, however there are slight differences:

- In the VERITAS pulse fitting technique, an attempt to describe the pulse analytically was made whereas the MAGIC approach used a more loosely defined spline.
- The filter used by VERITAS is a cross-correlation in Fourier space, whereas the filter used by MAGIC is generated using their knowledge of the noise auto-correlation matrix.

Either as a result of these differences, or due to the difference in the instruments themselves, the VERITAS *matched-filter* appears to result in a worse reconstruction than one would expect from the conclusion reached by MAGIC. The study performed by Cogan and Collaboration [65] for VERITAS concludes that the *matched-filter* "holds promise" for reconstructing low-amplitude signals, whereas while the *trace-fit* performs extremely poorly for the low-amplitude signals (as expected), it performs the best for amplitudes greater than 4 photoelectrons.

H.E.S.S.

The standard mode of charge extraction for the H.E.S.S. telescopes is to integrate N samples with respect to a fixed, but regularly verified, signal time [59]. H.E.S.S. camera electronics underwent an upgrade in 2015/2016, subsequently allowing for the update of the standard extraction mode to also output time-of-maximum and time-over-threshold, and also allowed for full sample readout enabling the utilisation of more complex charge extraction techniques [69][70].

ASTRI

Contrary to the other techniques described in this section, ASTRI took the alternative direction of a hardware-implemented charge extraction, utilising their CITIROC (Cherenkov Imaging Telescope Integrated Read Out Chip) ASIC. The pulse from their SiPM is amplified and shaped (with both a high-gain and low-gain channel) with a constant shaping time of 37.5 ns. The maximum of the shaped peak-height is then converted into an integrated charge, achieving no more than 1% introduced systematic error [71]. The *DL0* and *DL1* formats are therefore identical in ASTRI's case as the charge-extracted value is provided in place of waveforms. However, while this charge-extraction technique is optimised for the ASTRI electronics, it removes the flexibility of being able to dynamically select a charge-extraction technique within the software, and adopting new software-based techniques that may be designed in the future.

6.2.4 Performance Assessment

Deciding on which charge extraction method to use is not trivial - as shown in the above discussion, different cameras may perform better with different algorithms. This is anticipated in `ctapipe` (Section 4.4.1), where different ChargeExtractors can easily be selected at runtime depending on the camera source.

The assessment technique typically used for charge extractors in the context of CTA is the *Charge Resolution* (Section 3.2.1). A performance assessment of charge extraction techniques for CHEC-S can be found in Appendix E.

6.3 Shower Reconstruction

The resulting images of the extracted signal per triggered telescope is only the first stage of many to retrieve the properties of the Cherenkov-shower progenitor particle: direction, energy, and class. The direction is necessary to retrieve in order to obtain the source's position and spatial morphology. The energy is desired for studies of the source's spectrum. The class of the progenitor particle (gamma-ray, electron, or cosmic-ray hadron) is required in order to identify the gamma-rays among the hadronic background. All the information required to obtain these progenitor particle properties is contained within the image of extracted charge. As the focus of this thesis is on the low-level performance of the GCT cameras, this section will only include a brief overview of the simplest methods used in shower reconstruction. This information is supplied as context for the results described in Chapter 8.

6.3.1 Image Parametrisation

Pixels containing signal from the Cherenkov shower are identified by an image cleaning method such as the tailcuts approach: any pixels above a certain signal threshold are kept, and any neighbouring pixels (to those that survive the first threshold) that are above a lower signal threshold are also kept. The thresholds are optimised per telescope using Monte Carlo simulations. The resulting pixels are then parametrised in terms of their second moments. This parametrisation

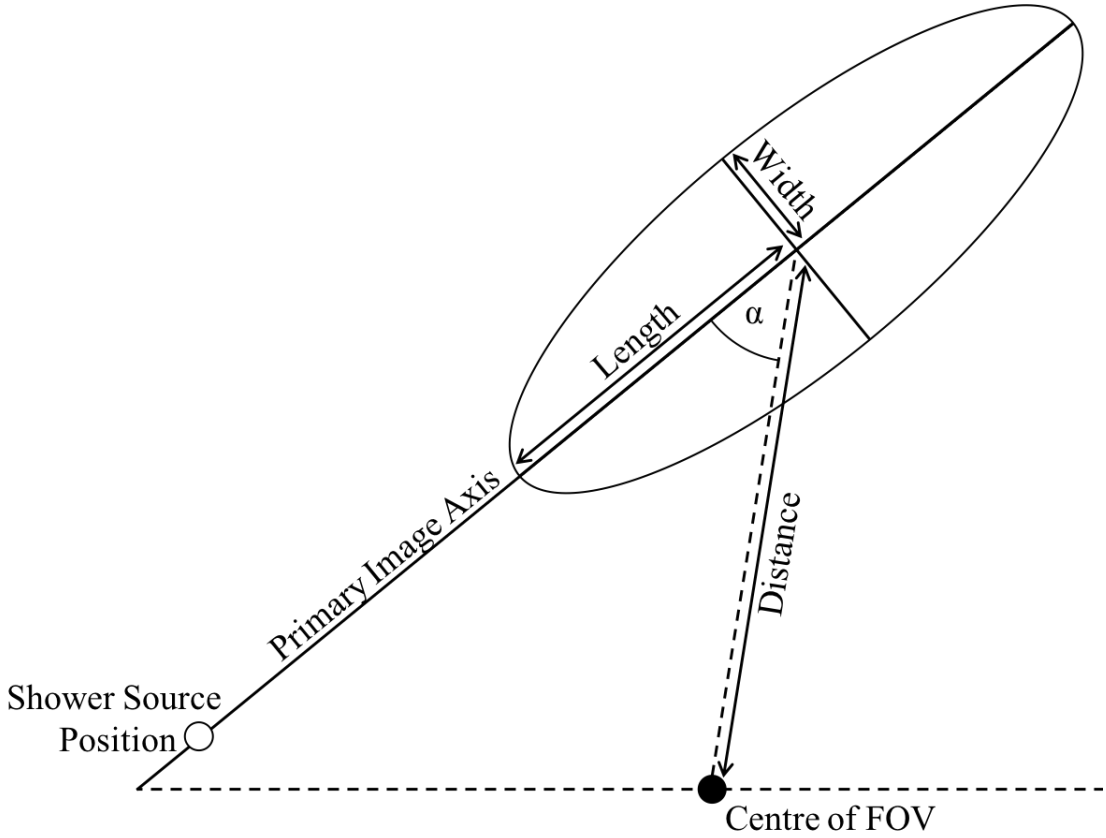


Figure 6.5: Schematic of the *Hillas Parameters* used to describe the Cherenkov shower image ellipse.

is a predominant IACT analysis technique that has been utilised in the majority of IACT experiments. It was first formalised by Hillas [72] and has subsequently been known as the *Hillas Parametrisation*. This technique exploits the elliptical shape of the gamma-induced shower images, and provides values for the centre of gravity of the ellipse, its primary axis position and orientation, its width, and its length (Figures 6.5). The `ctapipe` implementation of the *Hillas Parametrisation* is defined by Reynolds et al. [73].

6.3.2 Direction Reconstruction

Through utilising the primary image axis that results from the *Hillas Parametrisation*, the positional information about the shower can be obtained [64, 74, 75]. By superimposing the ellipses from different telescopes onto a single image (Figure 6.6), the stereoscopic combination allows for the source position of the shower to be

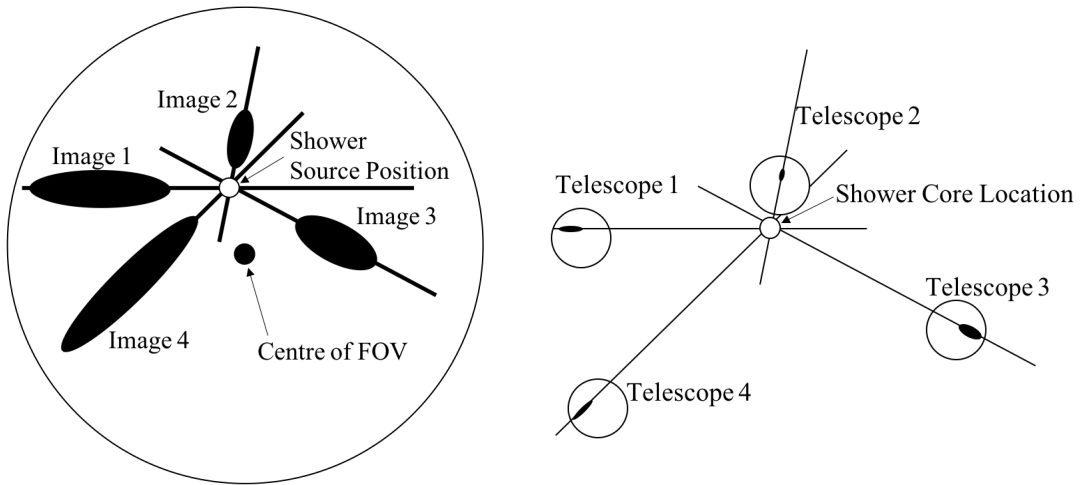


Figure 6.6: Reconstruction of the source location on the sky for the shower, achieved by superimposing the different views of the showers from different telescopes.

Figure 6.7: Reconstruction of the location of the shower core on the ground, achieved by combining the primary image axes at the relative telescope separations.

retrieved with simple geometry. This corresponds to the astrophysical-source position on the sky for a gamma-ray shower. If, instead, the primary image axes are combined with the relative positional view of the telescopes (Figure 6.7), the core location of the shower in terms of ground coordinates may be obtained. For obtaining the intersections of the axes in both applications, the weighted-mean-direction of the intersections is typically calculated [47, 76]. While the extraction of the directional information is much more reliable through the use of the stereoscopic combination of the images, it is not impossible to estimate the direction of the source when only a single telescope is available. The primary challenge when performing this operation with a single telescope is the degeneracy in determining which direction along the primary image axis the source exists in. This is overcome with the *disp* method developed by Lessard et al. [77].

6.3.3 Energy Reconstruction

As aptly described by Dickinson [75, p. 16], “determining of the energy of the progenitor of a particular air shower relies on a form of electromagnetic calorimetry”. Once the distance from the telescopes to the shower is known (from the core

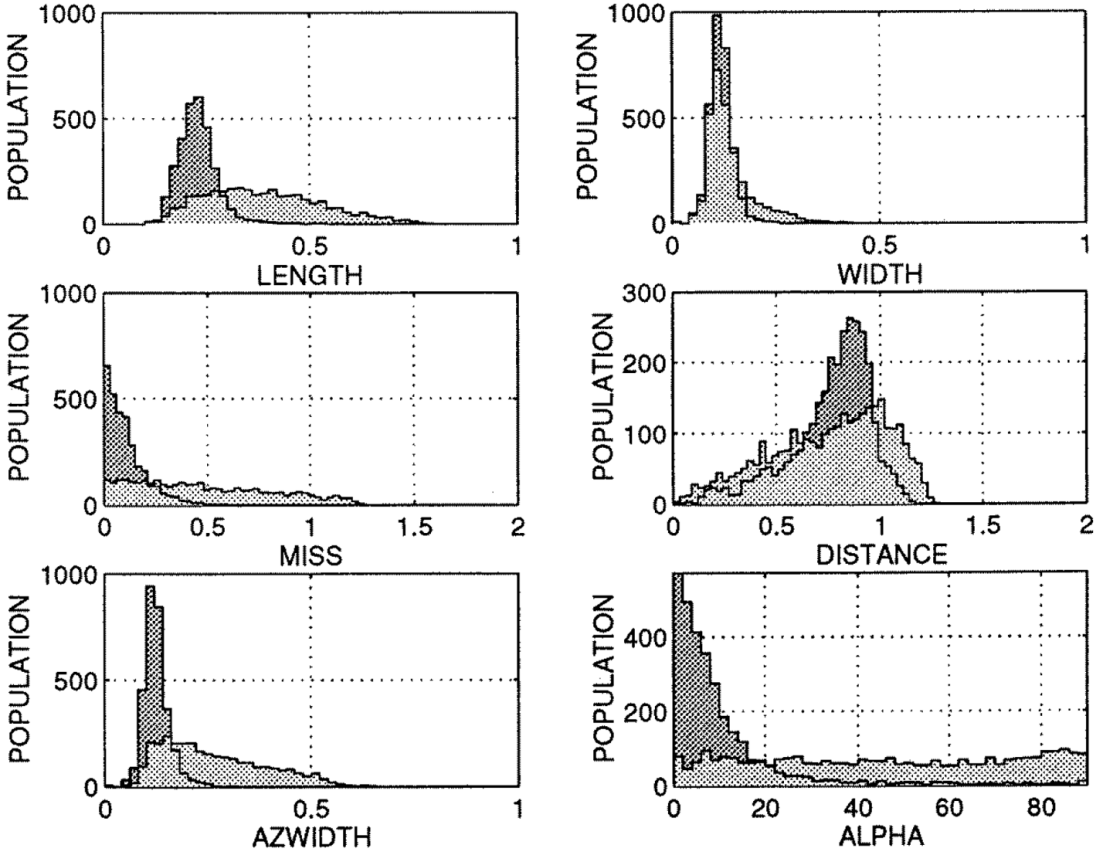


Figure 6.8: Example of the differences in the distributions of *Hillas Parameters* between simulated gamma-ray-induced showers (dark) and real hadronic-induced showers (light) for the Whipple 10 m reflector [78].

position), it can be coupled with the *image size* (the total amount of integrated signal obtained from the Cherenkov shower) to obtain total energy released as Cherenkov light [47, 64]. This is a proportional measure of the energy of the shower progenitor particle (Section 1.2).

6.3.4 Gamma-Hadron Discrimination

One of the primary disadvantages of the Imaging Atmospheric Cherenkov Technique is the extremely large hadronic shower background. The sensitivity of an IACT is heavily influenced by its ability to exclude this background. A property that is traditionally relied upon in this background rejection process is the differences in morphology between gamma-ray and hadronic shower images. This is further described in Chapter 1. In traditional IACT analysis, the morphology of the showers

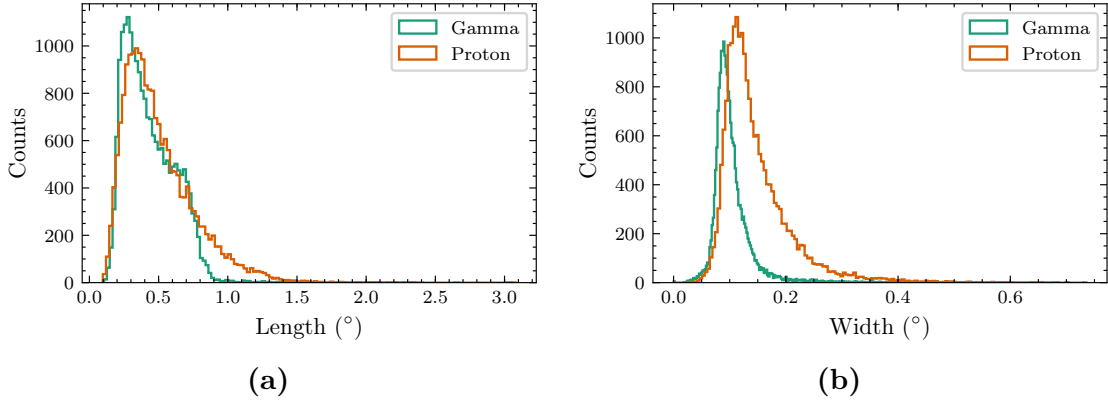


Figure 6.9: The *Hillas* width and length parameters I have extracted during my investigations of the Monte Carlo simulations of CHEC-S on the ASTRI telescope structure, for both gamma-ray and proton induced showers. The energy ranges simulated were 2-330 TeV for the gamma rays and 6-600 TeV for the protons. Each histogram contains approximately 20,000 shower images.

are quantified by the *Hillas Parameters*. Gamma-ray showers typically exist within a narrow range of the parameters, while hadronic showers typically exhibit a broader spectrum of parameter values, as illustrated in Figure 6.8. By creating an acceptance range for the *Hillas Parameters*, the hadronic background can be excluded in a very simple way [3, 75, 78]. However, the higher the energy of the hadron shower is, the more it begins to resemble a gamma-ray shower, making it harder to discriminate using simple cuts on the *Hillas Parameters*. This is especially a problem for the SSTs, which are designed to operate within the gamma-ray energy range of 1-300 TeV. The distributions of the *Hillas* width and length from simulations of CHEC-S on the ASTRI telescope structure are shown in Figure 6.9. More advanced techniques, such as the use of *Boosted Decision Trees* [79], provide a much more effective background reduction, and therefore can considerably improve the sensitivity.

7

Camera Performance

Contents

7.1	Introduction	107
7.2	CHEC-S Monte Carlo Model	108
7.3	CHEC-S Charge Resolution	110
7.3.1	Procedure and Datasets	110
7.3.2	Lab Results	112
7.3.3	Lab versus Monte Carlo	115
7.3.4	Night Sky Background	118
7.3.5	Optical Crosstalk	120
7.3.6	Analytical Description	123
7.3.7	Conclusion	124
7.4	CHEC-S Pulse Shape	125
7.5	CHEC-S Time Resolution	127
7.6	CHEC-M	128

7.1 Introduction

As discussed in Chapter 3, it is important that the CHEC camera meets certain criteria in order for it to be accepted as an in-kind contribution to CTA. One important subset of the criteria is the camera’s performance. The requirements that must be fulfilled are driven by the science goals of CTA. If a camera does not meet the requirements laid out by the CTA observatory, then it will be refused as a contribution in its current state, lest the science goals of CTA are not achieved.

This chapter will cover many of the primary standards used to assess a CTA

camera's performance. The results shown in this chapter are all my own, and are obtained using the procedures defined in the preceding chapters. Two important aspects of the camera's performance which are not included in this chapter are the trigger efficiency and absolute photon detection efficiency. The investigations into these parameters are ongoing, and I have not had direct involvement with these as part of my DPhil.

7.2 CHEC-S Monte Carlo Model

An important preface to reporting on the performance of CHEC is the description of the efforts in generating an accurate model of the camera for use inside the Monte Carlo simulations performed by `sim_telarray` (Chapter 4). These simulations allow us to explore the parameter space related to our camera performance more widely, and identify potential issues that cause the real camera to drift away from ideal operation. It is also a necessary step in investigating the on-sky performance of the telescope, as:

- One does not have prior knowledge of the properties of the light incident on the pixels in the real world.
- The camera is still being tested in the lab. An on-sky campaign for CHEC-S on the ASTRI telescope structure is planned for later this year.

Contained within the lab data are the parameters required for the Monte Carlo validation process. Important parameters include:

- Pixel position on the focal surface,
- Pulse shape of a single photoelectron,
- Trigger discrimination behaviour,
- Quantum efficiency (or PDE),
- Variation of quantum efficiency between pixels,

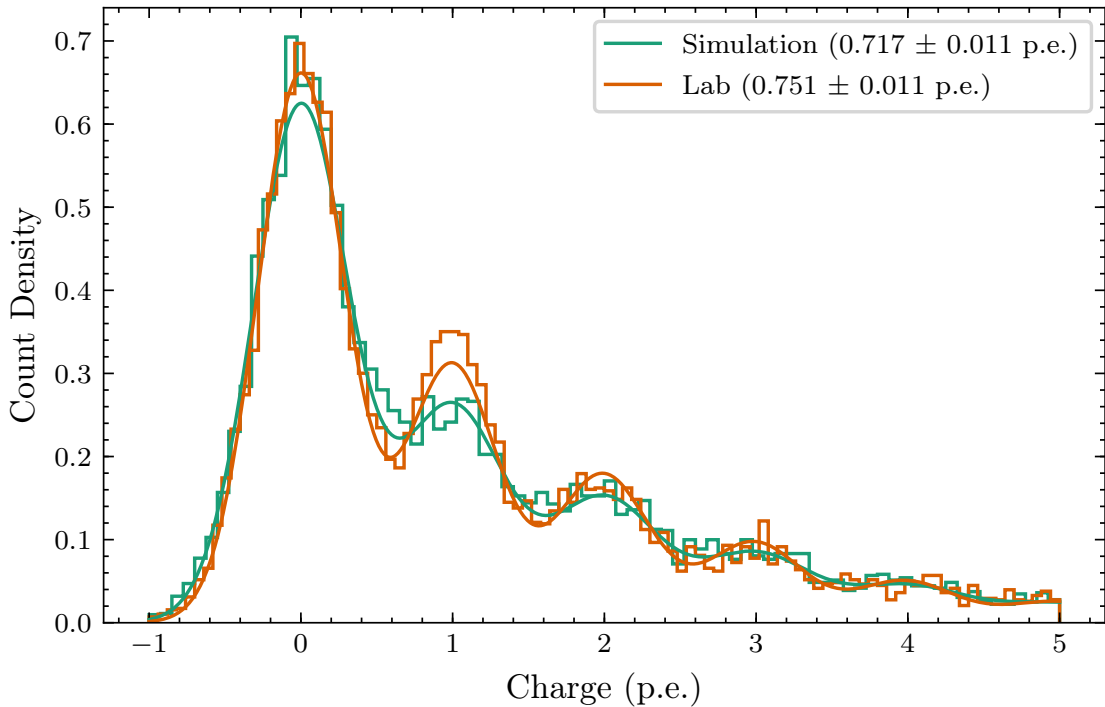


Figure 7.1: Comparison of the SPE spectra for a single pixel between lab measurements and simulations after an initial attempt towards a more accurate Monte Carlo model. The SPE spectra were identically constructed in both cases, using the *Cross Correlation* charge extraction method. Each spectra histogram was then fit using the procedure described in Appendix C. Three illuminations were simultaneously fit, however just a single illumination is displayed here. Both spectra are normalised in the x direction by their respective single-photoelectron value, and in the y direction such that their integral is 1.

- Electronic baseline variation,
- Photosensor gain,
- Variation of gain between pixels,
- Single photoelectron multiplication response (Figure 2.8).

For the simulation results presented in this thesis, an updated value was obtained for as many of the relevant `sim_telarray` parameters as possible. Figure 7.1 displays the resulting differences in terms of the SPE spectra between lab and simulation. The differences in the parameter values resulting from the fits to the two SPE spectra are shown in Table 7.1, and are deemed to be close enough for the investigations in this thesis. Further details about the fit procedure for SPE

Fit Parameter		Simulation	Lab
Average Illumination	[p.e.]	0.717 ± 0.011	0.751 ± 0.011
Pedestal Deviation	[p.e.]	0.314 ± 0.003	0.286 ± 0.002
Gain Deviation	[p.e.]	0.109 ± 0.009	0.078 ± 0.007
Optical Crosstalk		0.387 ± 0.007	0.350 ± 0.006

Table 7.1: Parameter values resulting from the fit to the spectra in Figure 7.1. The 1σ parabolic errors obtained from the covariance matrix of the fit parameters are also quoted.

spectra can be found in Appendix C. The differences between lab and simulation in other factors and at higher amplitudes are explored through *Charge Resolution* comparisons, investigated later in this chapter.

7.3 CHEC-S Charge Resolution

The *Charge Resolution* is the principle criterion used within CTA to express how well the camera can resolve a signal. The concept of *Charge Resolution* is introduced in Section 3.2.1, alongside the CTA requirement **B-TEL-1010 Charge Resolution**. It not only measures the quality of the camera’s photosensor and electronics, but also the aptitude of the calibration and signal extraction. Consequently, obtaining a *Charge Resolution* of the camera that meets this requirement has been the underlying driver behind my efforts in developing the techniques described in this thesis.

7.3.1 Procedure and Datasets

As directed in the **B-TEL-1010 Charge Resolution** requirement, one must simulate the response of the camera to Cherenkov shower illumination to verify the requirement is met. However, this result must be supported by evidence that the *Charge Resolution* appropriately resembles the behaviour of the real camera. To achieve this, I display the *Charge Resolution* with four different procedures. Each procedure bridges the gap between the *Charge Resolution* I obtained with Cherenkov shower simulations, and the *Charge Resolution* I obtained from lab measurements. The procedures, and their associated names for the purpose of this thesis, are:

Lab Utilises uniform illumination datasets taken in the lab that cover the full dynamic range of the camera, with 1000 events at each illumination. The average expected charge per pixel (in photoelectrons) for each illumination is calibrated by the procedure detailed in Appendix B. Using the calibration procedures detailed in Chapter 5 and the *Cross Correlation* charge extraction technique (Chapter 6), a value of measured charge in photoelectrons is obtained for every waveform. As the average expected charge includes the Poisson fluctuations, it is appropriate to use Equation 3.1 for calculating the *Charge Resolution*, with the measured charge per waveform used for Q_{M_i} and the average expected charge for Q_T . It is important to note that these datasets are taken with no NSB contribution, and are therefore not a completely appropriate measure against the CTA requirement (defined for an NSB photon rate per pixel of 0.125 p.e./ns = 125 MHz). However, a DCR of ~ 5 MHz is assumed to be present in the SiPM.

MCLab Simulations of the dynamic range datasets from the lab are obtained with the updated `sim_telarray` camera model. Using the identical method used for the lab data (excluding the TARGET calibration) the charge is extracted and calibrated from the waveforms. The average expected charge for each illumination per pixel is also obtained in the same way as the previous procedure. However, the simulations contain perfect laser uniformity across the camera face (though the geometry corrections shown in Section B.3 are still applicable, as the simulations contain a point source ~ 1.5 m from the camera). This dataset then fully represents the same measurements, but with the Monte Carlo model of the camera instead of the physical camera. With an accurate model of the camera, the *Charge Resolution* result should be the same as from the lab measurements. Equation 3.1 is also used in this procedure for calculating the *Charge Resolution*.

MCLabTrue Utilises the same dataset as the previous procedure, but instead of using the average expected charge, the true number of photoelectrons that

were incident on the pixel for each waveform are extracted from the simulation file. The linear fit between the average measured charge and the “true charge” is used to calibrate the extracted charge into corresponding units. As the unique value of “true charge” per waveform is now used as Q_T , Equation 3.4 must be used to account for the lack of Poisson fluctuations in Q_T . The *Charge Resolution* resulting from this procedure demonstrates the change in transitioning from “average expected charge” to “true charge”, which is important for interpreting the results from the next procedure.

MCOnsky Produced using a dataset containing Monte Carlo simulations of gamma-ray-induced air shower observations is created using **CORSIKA** and **sim_telarray**. A model of CHEC-S on the ASTRI telescope structure is used in the simulation. The *Charge Resolution* is then calculated with the same procedure as in *MCLabTrue*. As only a small section of the camera is illuminated by the Cherenkov shower, this procedure is dependant on the peak-finding methods described in Chapter 6. The *Local Peak Finding* technique is used for this investigation. This *Charge Resolution* procedure is the definitive approach for assessment of *Charge Resolution*, as defined in the requirement. The previous procedures exist to support the claim that this result is applicable to the real camera.

7.3.2 Lab Results

To begin, the different representations of the *Charge Resolution* are first explained in terms of the *Lab* procedure and dataset. Figure 7.2 demonstrates the charge extracted for the entire dynamic range dataset, post calibration. It is the purpose of the *Charge Resolution* to consolidate the spread and bias of these measured charges (from the average expected charge) into a single value per average expected charge (or “true charge” where appropriate). The average measured charges in Figure 7.3 seem to strongly follow a one-to-one relation with the average expected charge (in the non-saturated region), attesting to the success of the extracted charge calibration. However, to fully explore the performance of the camera, we

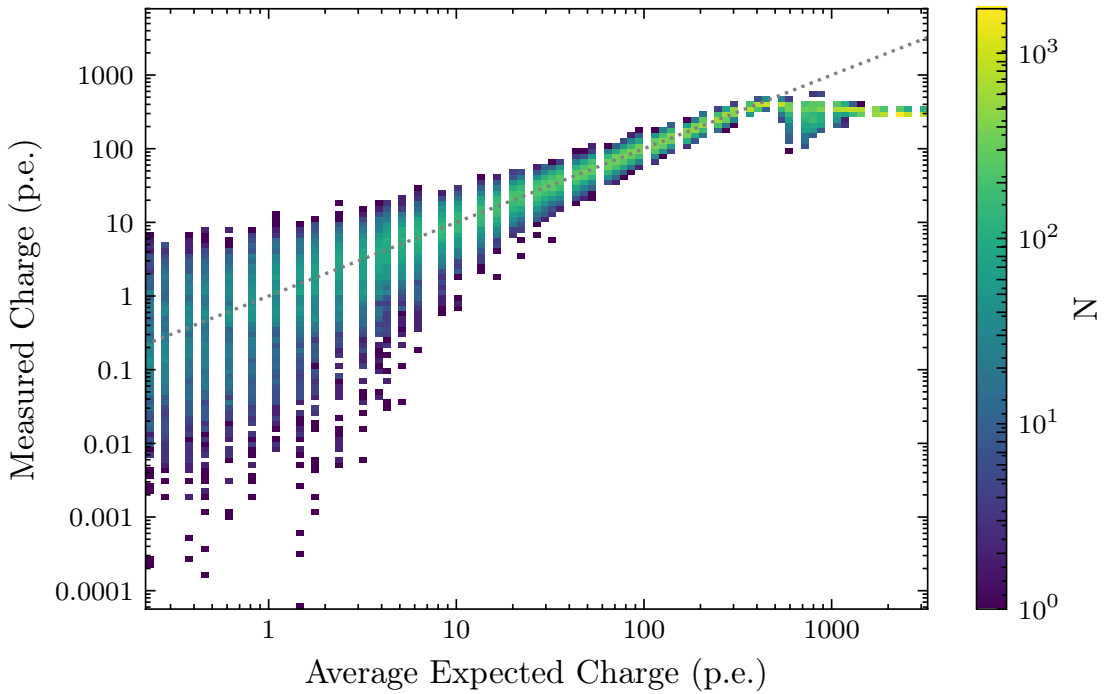


Figure 7.2: Two-dimensional histogram showing every measured charge for a single CHEC-S pixel, covering the full dynamic range. This dataset matches the one described in the *Lab* procedure in Section 7.3.1. The grey dotted line represents a one-to-one relation between the axes.

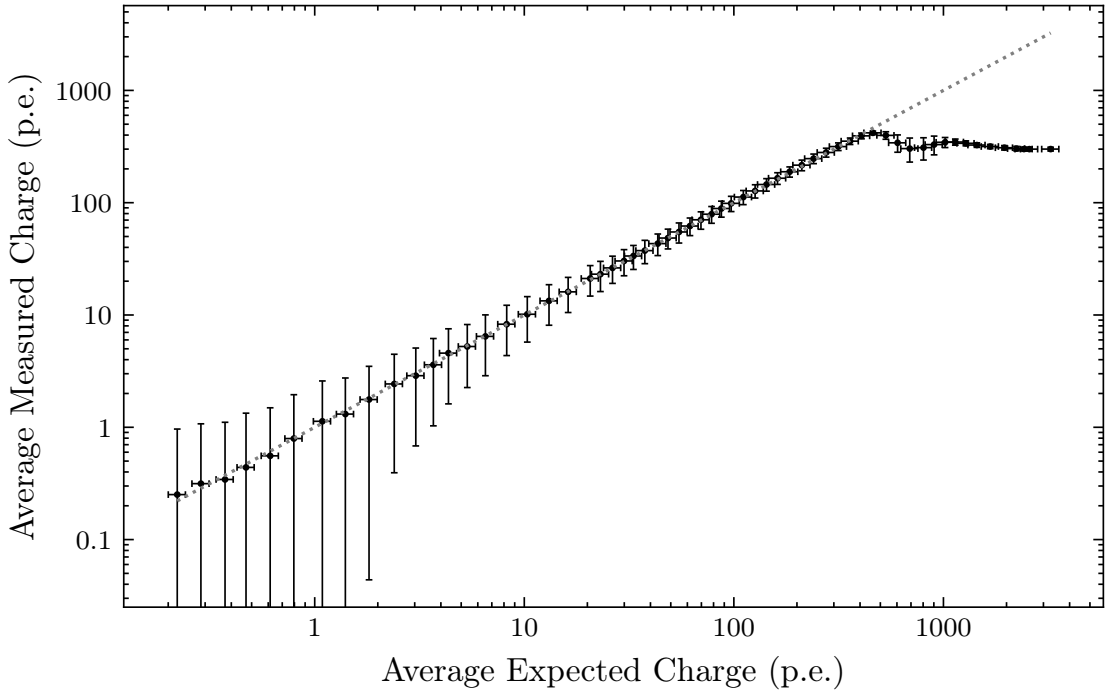


Figure 7.3: Similar to Figure 7.2, but summarising the entries in terms of their averages and standard deviation for each illumination. The X error bars represent the uncertainty in the filter-wheel calibration into units of p.e. (Section B.6).

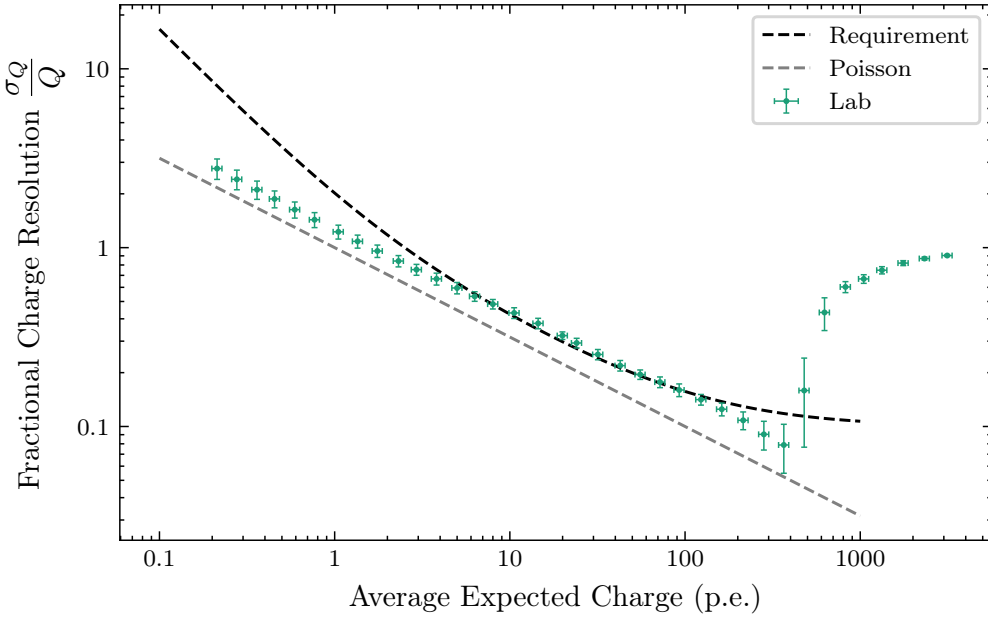


Figure 7.4: Average *Charge Resolution* across CHEC-S (excluding “dead” pixels) for the same Lab dynamic range dataset Figure 7.2 uses. The Y error bars represent the standard deviation of the *Charge Resolution* values across the camera. The X error bars represent the uncertainty in the filter-wheel calibration into units of p.e. (Section B.6). The points are binned to improve visibility. The presentation of the *Charge Resolution* in this form matches Figure 3.1.

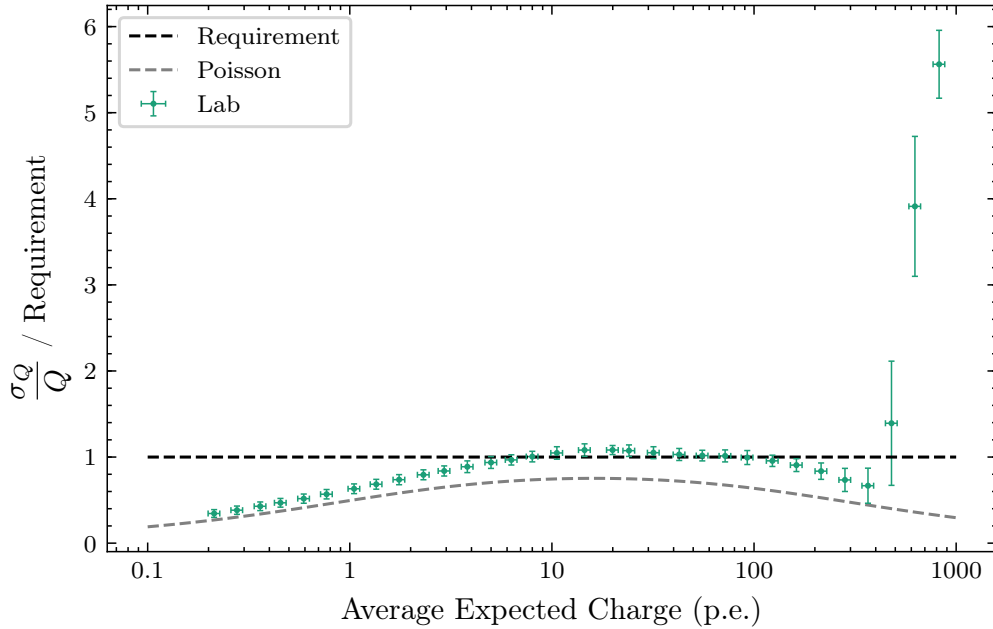


Figure 7.5: Same result shown in Figure 7.4, but with respect to the requirement curve to emphasise the separation between it and the points.

continue on to the *Charge Resolution* shown in Figure 7.4. It is immediately obvious that in the saturated region (>300 p.e.), the camera fails the *Charge Resolution* requirement. This is expected, as we make no attempt to recover saturated signals in this investigation. Methods to account for the saturation are briefly described in Section 5.4, and will be fully explored in a future investigation.

To investigate other less obvious features in the *Charge Resolution*, I display the *Charge Resolution* in terms of its deviation from the requirement curve. This is achieved by dividing the *Charge Resolution* curve by the requirement curve. Figure 7.5 expresses the *Charge Resolution* from Figure 7.4 in this format. This is how the *Charge Resolution* is visualised elsewhere in this thesis, as it shows how close the points are to the requirement, and emphasises features that cause the results to fail the requirement. In the region of $10 < Q_{\text{Exp}} < 100$ p.e., the *Charge Resolution* of the *Lab* dataset is above the requirement curve, and therefore fails the requirement. By comparing this *Charge Resolution* to those resulting from different Monte Carlo simulations that explore the contributing parameter space, we are able to identify the primary factors resulting in a failure to meet the requirement.

7.3.3 Lab versus Monte Carlo

As a preface to the simulated *Charge Resolution* investigations, the differences in the results of the procedures described in Section 7.3.1 are illustrated in Figure 7.6. The earlier descriptions of each procedure indicate the following expected differences between their *Charge Resolutions*:

- With a perfect Monte Carlo model of the camera, there should be no differences between the *Charge Resolution* of *Lab* and *MCLab*. Any deviations arise from a misunderstanding in the camera’s behaviour, or from an unaccounted noise contribution.
- The difference between *MCLab* and *MCLabTrue* demonstrates the expected change when transitioning from the average expected charge, to the “true charge” that was detected in the pixel.

- As they are the same camera model, and the same *Charge Resolution* calculation approach, there should be very little difference between *MCLabTrue* and *MCOnsky*. The only factor to contribute to differences between the two procedures is the peak-finding that is necessary for the *MCOnsky* datasets.

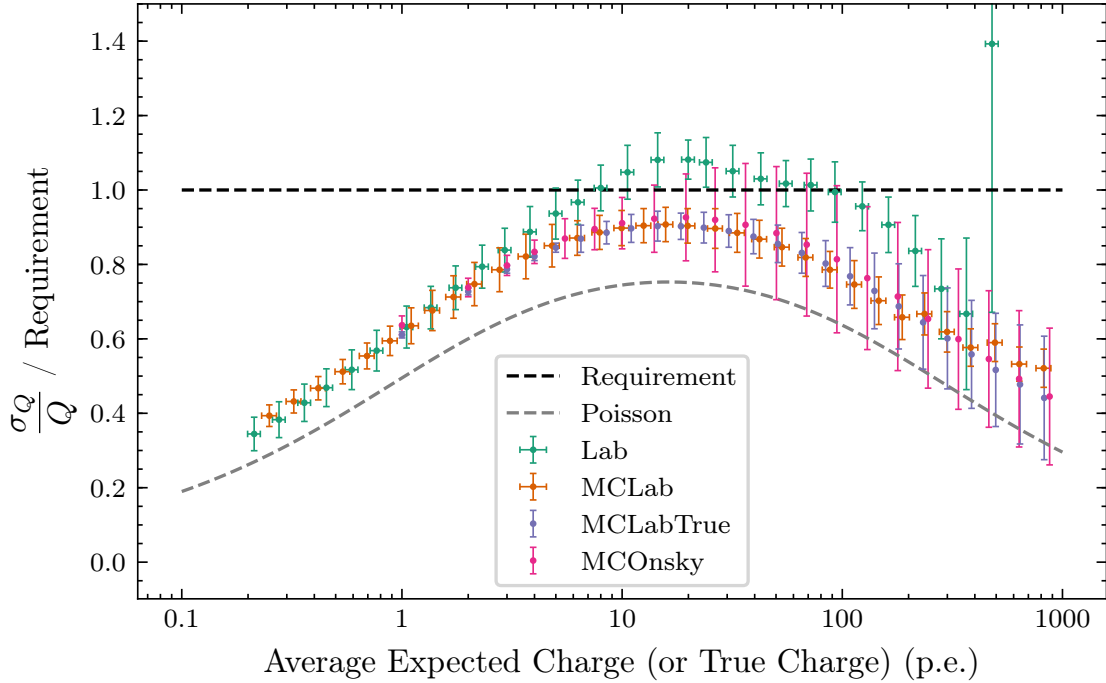


Figure 7.6: Comparison of the *Charge Resolutions* resulting from the different procedures described in Section 7.3.1. A background photon rate of 5 MHz is simulated in the Monte Carlo datasets to represent the DCR we expect inside the datasets produced from lab measurements. The saturated points from the *Lab* measurements are outside of the figure's range.

It is therefore apparent in Figure 7.6 that our simulation model is not a perfect representation of CHEC-S. The lack of saturation in the simulated datasets is expected, and that is a feature we will include in future investigations. However, from the simulated datasets we can conclude that in the absence of additional NSB photons, the *Charge Resolution* of our camera before the saturated region should be below the requirement. As we do not observe this in the non-simulated dataset, there must be a noise contribution we have not appropriately accounted for. Further work is required to fully diagnose this noise contribution. However, possible options include:

Transfer Functions The simulations do not fully simulate the CHEC-S electronics. They contain no resemblance of the digitising behaviour of TARGET ASICs, and therefore no variations in amplitude response exists from sample-to-sample. Inaccuracies in the Transfer Function calibration (Chapter 5) could manifest themselves as differences between the *Charge Resolutions* of lab and simulated data.

Timing As mentioned in Section 5.5, the variations in signal arrival time between pixels could degrade the *Charge Resolution*. This contribution is not included in the simulation.

Electrical Crosstalk Inside the simulation, each pixel is considered independently. Due to electronic coupling, this is unfortunately not the case in reality. Interference between pixels, especially if a large amplitude is measured, can occur via faults in the electronic design, for example “ground bounce”.

Optical Crosstalk A simplified form of optical crosstalk is used in the simulation, via the input SPE spectra shape. This may not fully characterise the full behaviour of the optical crosstalk.

Reference Pulse Shape Another major difference between simulation and reality is the behaviour of the pulse shape. In simulations, the pulse shape at all illuminations is constructed by the superposition of the individual photo-electron pulses. If that description was appropriate for the real camera, the pulse shape dependency with amplitude would not be seen in Section 7.4. As we use the *Cross Correlation* charge extraction method, the measured charge is sensitive to changes in pulse shape. This could, in theory, result in discrepancies between the *Charge Resolutions* of lab and simulated data. However, the investigations in Appendix E seem to suggest this factor is not significant.

Identifying the cause of this noise contribution is of paramount importance in the commissioning of CHEC-S. However, the remainder of this section will explore the

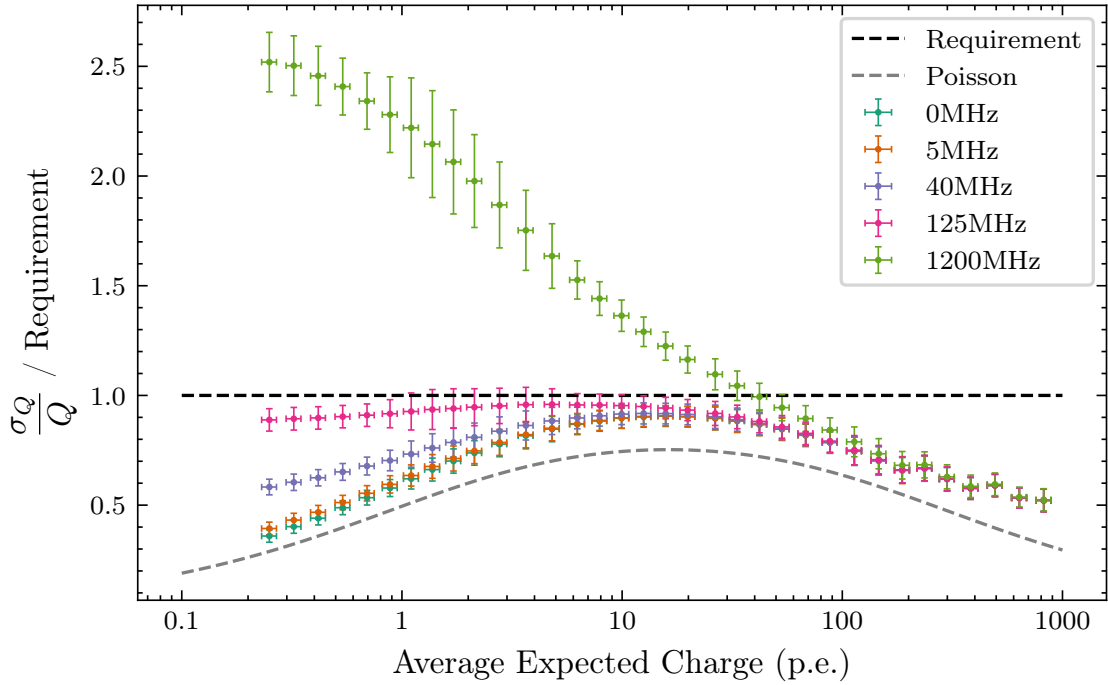


Figure 7.7: Comparison of the *Charge Resolutions* obtained from the *MCLab* procedure when simulating different Night Sky Background (NSB) photon rates.

possibility of meeting the *Charge Resolution* even in the presence of this unknown noise contribution. This procedure may give insight into the source of the noise.

7.3.4 Night Sky Background

As the NSB photon rate increases, we expect more noise to be included in the charge extraction. This results in a higher charge than expected, and increases the variation in signal measured for the same average illumination. Figure 7.7 illustrates the degradation in charge resolution caused by an increase in NSB rate. The effects are most pronounced at the lower values of average expected charge, where an increase in NSB has a larger impact on the signal-to-noise ratio. We can conclude from this figure that even if the unknown noise contribution in the *Lab* datasets is corrected for, the current design of CHEC-S could potentially fail to meet the CTA requirement at the specified NSB of 125 MHz.

A similar dependence on NSB is observed with the *MCLabTrue* procedure in Figure 7.8, however the *Charge Resolutions* demonstrate an overall improved performance over the *MCLab* representation (Figure 7.7).

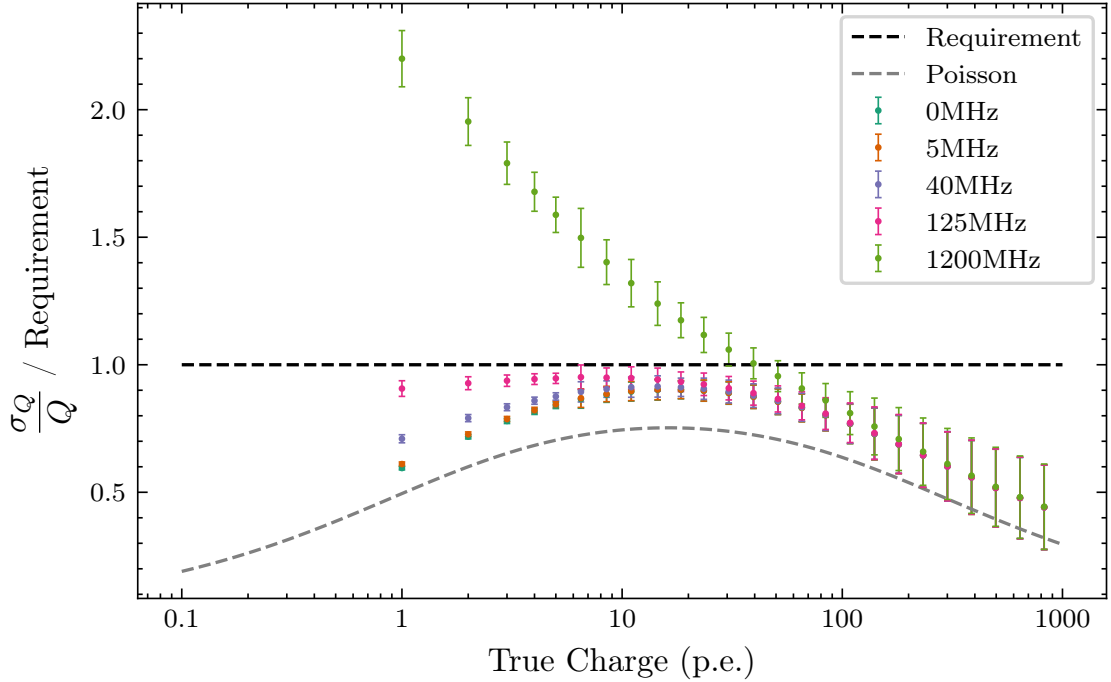


Figure 7.8: Comparison of the *Charge Resolutions* obtained from the *MCLabTrue* procedure when simulating different values of NSB.

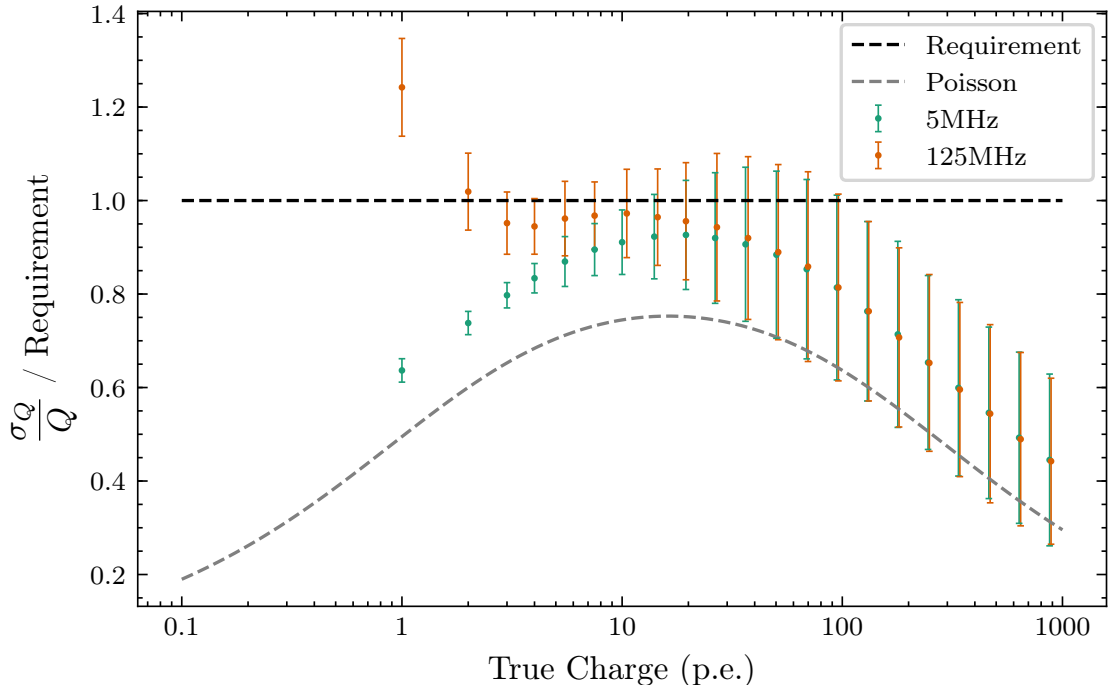


Figure 7.9: Comparison of the *Charge Resolutions* obtained from simulated observations of Cherenkov showers (via the *MCOnsky* procedure), when simulating different values of NSB. The signal inside each waveform is found with the *Local Peak Finding* approach.

Despite the improved performance achieved when using the “true charge”, a second consequence of higher NSB is the increased difficulty of finding the signal pulse among the noise pulses. As shown in Figure 7.9, this causes the current model of CHEC-S to fail the *Charge Resolution* requirement when observing Cherenkov showers. An alternative to the *Local Peak Finding* approach could improve on this bias to noise pulses, and therefore enable the requirement to be met.

7.3.5 Optical Crosstalk

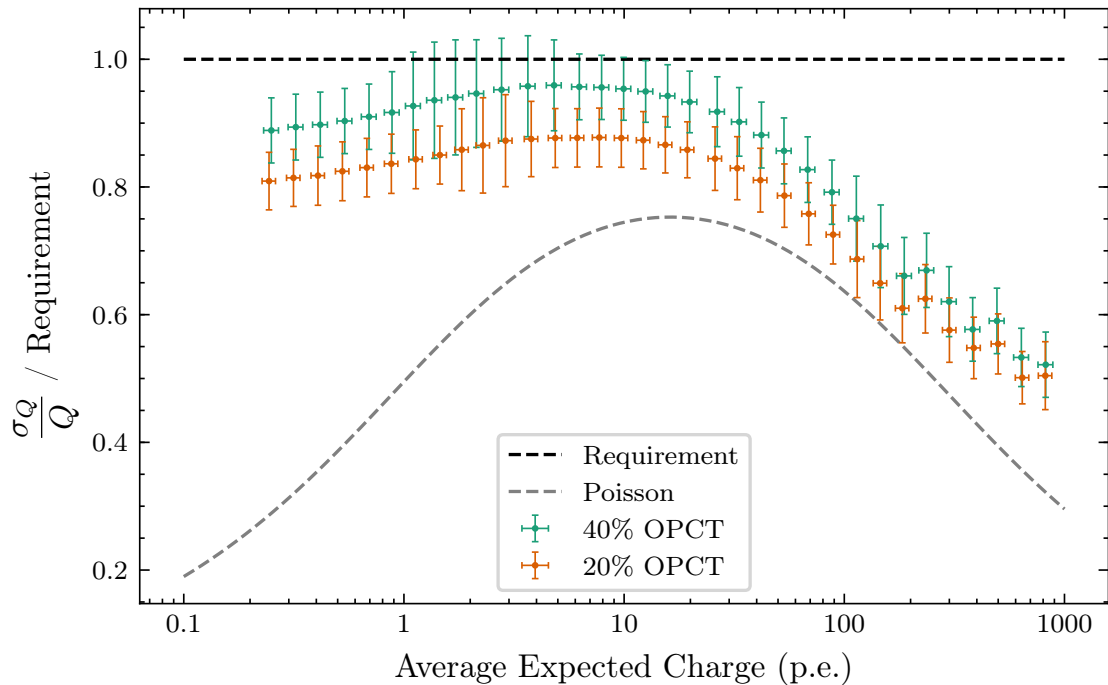


Figure 7.10: Comparison of the *Charge Resolutions* obtained from the *MCLab* procedure when simulating different values of optical crosstalk (abbreviated here as OPCT). An NSB rate of 125 MHz was included in these simulations.

As described in the discussion of ENF in Section 2.2.5, a major contributing factor that could degrade the *Charge Resolution* for an SiPMs-based camera is the optical crosstalk. This is especially anticipated to be significant in the CHEC-S prototype, due to the high (35-40 %) optical crosstalk exhibited by the installed SiPMs. This value range of optical crosstalk is obtained from the SPE fit parameters to the camera pixels (the values for a single pixel are shown in Table 7.1). The optical crosstalk contributes to the extracted charge in two ways:

- The measured charge is consistently higher. This factor is accounted for in the flat-fielding calibration (Section 5.3).
- The spread in charge that results from a particular amount of photons is larger. This is therefore expressed as an increase in the ENF (see Section 2.2.5).

Monte Carlo

Figure 7.10 demonstrates the *MCLab Charge Resolution* for a simulation of the CHEC-S model, but with 20 % optical crosstalk. This is compared to the original model with 40 % optical crosstalk. The effect of a reduced optical crosstalk in the simulation is an improvement in the *Charge Resolution* for all illuminations.

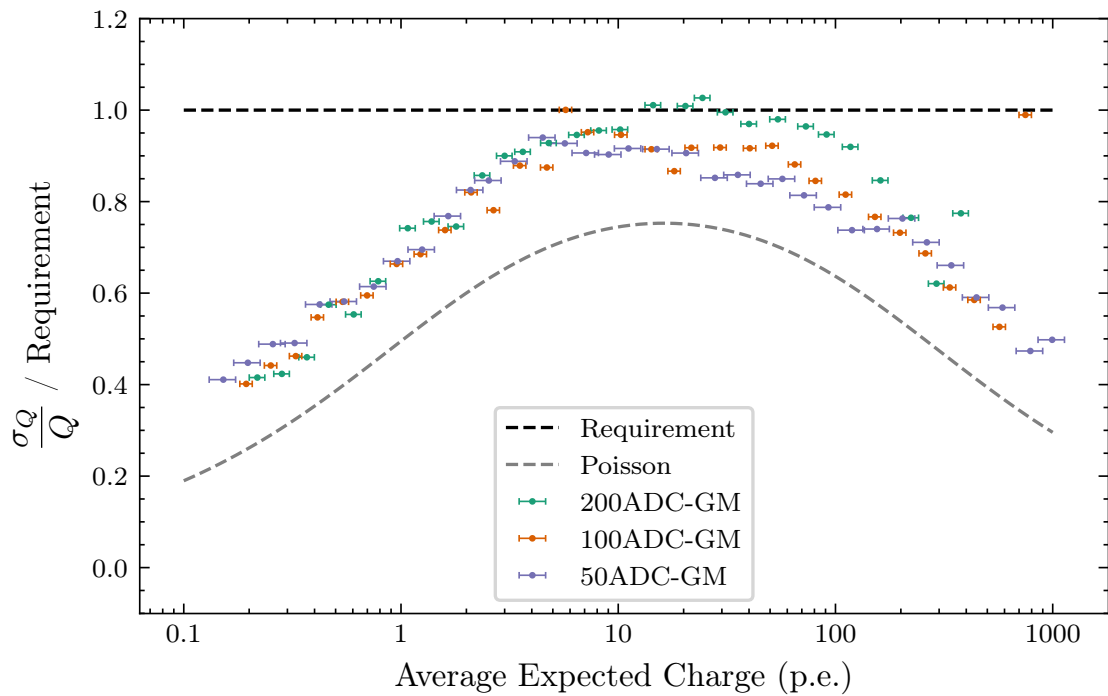


Figure 7.11: Comparison of the *Charge Resolutions* obtained from different *Lab* datasets. Each dataset is gain-matched to a different ADC value. By gain matching to different ADC values, a different bias voltage is applied to the SiPM pixel. As this dataset was gain-matched in units of ADC, the spread between pixels is large. Therefore, only a single pixel's *Charge Resolution* is shown.

Changing Bias Voltage

Due to the dependence of the optical crosstalk on the overvoltage across the SiPM (described in Section 2.2.4), it is possible to investigate the impact a reduced optical

Fit Parameter		200 ADC	100 ADC	50 ADC
Average Illumination 1	[p.e.]	1.061 ± 0.014	0.903 ± 0.023	0.550 ± 0.009
Average Illumination 2	[p.e.]	0.793 ± 0.012	0.688 ± 0.021	0.394 ± 0.008
Average Illumination 3	[p.e.]	0.625 ± 0.010	0.535 ± 0.014	0.301 ± 0.007
Pedestal Deviation	[mVns]	6.047 ± 0.043	5.668 ± 0.049	5.913 ± 0.039
Gain	[mVns]	21.33 ± 0.073	16.06 ± 0.108	12.10 ± 0.094
Gain Deviation	[mVns]	1.684 ± 0.159	0.005 ± 15.03	0.003 ± 11.05
Optical Crosstalk		0.339 ± 0.006	0.242 ± 0.011	0.100 ± 0.006

Table 7.2: Parameter values resulting from the fit to the SPE spectra of the different gain-matched datasets for a single pixel. Three illuminations were simultaneously fit. These three illuminations are identical in terms of filter-wheel transmission (and therefore average photons) between the three gain-matched datasets.

crosstalk has on *Charge Resolution* using *Lab* data that is taken with different bias voltages. Three datasets were generated, each gain-matched to a different ADC value (the Transfer Functions were not included in the gain matching procedure at the time). The 200 ADC gain-matched dataset is at a similar bias voltage to the the dataset in Figure 7.5. The 100 ADC and 50 ADC gain-matched datasets are produced by reducing the bias voltage. The effect of a reduced bias voltage on the SiPM characteristics is quantified in the parameters extracted from the fit to the SPE spectra, shown in Table 7.2. In total, the optical crosstalk is reduced by a factor of 3 to 10 % in going from a gain matching of 200 ADC to 50 ADC.

Figure 7.11 shows the improvement in *Charge Resolution* with reduced bias voltage, bringing the result below the requirement. Additionally, by reducing the bias voltage, the unexplained noise component that was identified in the comparison between the *Lab* and *MCLab* datasets (Figure 7.6) appears to diminish, suggesting it is possibly related to the optical crosstalk.

However, it is important to note that by reducing the bias voltage, we also decrease the PDE of the SiPM (Figure 2.5). This effect is evident in the average illumination values quoted in Table 7.2. The result of a lower PDE is a reduction in the camera’s ability to detect Cherenkov shower photons. This contradiction between improving *Charge Resolution*, but reducing Cherenkov shower resolution,

is one of the primary reasons the CTA requirements are being redefined to be in terms of photons, as described in Chapter 3.

7.3.6 Analytical Description

One further way to characterise the camera's *Charge Resolution* is to use the analytical description of the *Charge Resolution* provided by Equation 3.2. However, to fully interpret this function, we must understand the contribution of optical crosstalk to the σ_{ENF} parameter. If we assume that optical crosstalk is the dominant contributor to σ_{ENF} for an SiPM (a reasonable assumption due to the high photoelectron resolution, as shown in Figure 2.8), the following equations derived by Vinogradov [28] can be used to express the σ_{ENF} in terms of the optical crosstalk probability P_{optc} :

$$\sigma_{ENF} \approx 1 + P_{\text{optc}}, \quad (7.1)$$

$$\sigma_{ENF} \approx 1 + P_{\text{optc}} + \frac{3}{2}P_{\text{optc}}^2, \quad (7.2)$$

where the former equation is applicable in a geometric chain model of the optical crosstalk behaviour (each single electron response is capable of only producing 1 or 0 further electron responses) and the latter equation is applicable in a branching Poisson model (each single electron response produces a Poisson distributed random number of further electron responses). The P_{optc}^3 term from the equation derived by Vinogradov [28] is assumed to be negligible.

Fit Parameter		Values
Background Noise	σ_0	0.000 ± 0.316
Excess Noise Factor	σ_{ENF}	1.338 ± 0.003
Miscalibration	σ_g	0.067 ± 0.001

Table 7.3: Parameter values resulting from the fit to the *Lab Charge Resolution* (Figure 7.12) using Equation 3.2.

Shown in Figure 7.12 is the result from fitting Equation 3.2 to the *Lab Charge Resolution* from Figure 7.5. The resulting parameters, shown in Table 7.3, indicate that σ_0 was poorly constrained by the data points, however σ_{ENF} and σ_g are well characterised. The first conclusion provided by the fit is the miscalibration is very low, and is potentially still overestimated due to the lack of high charge

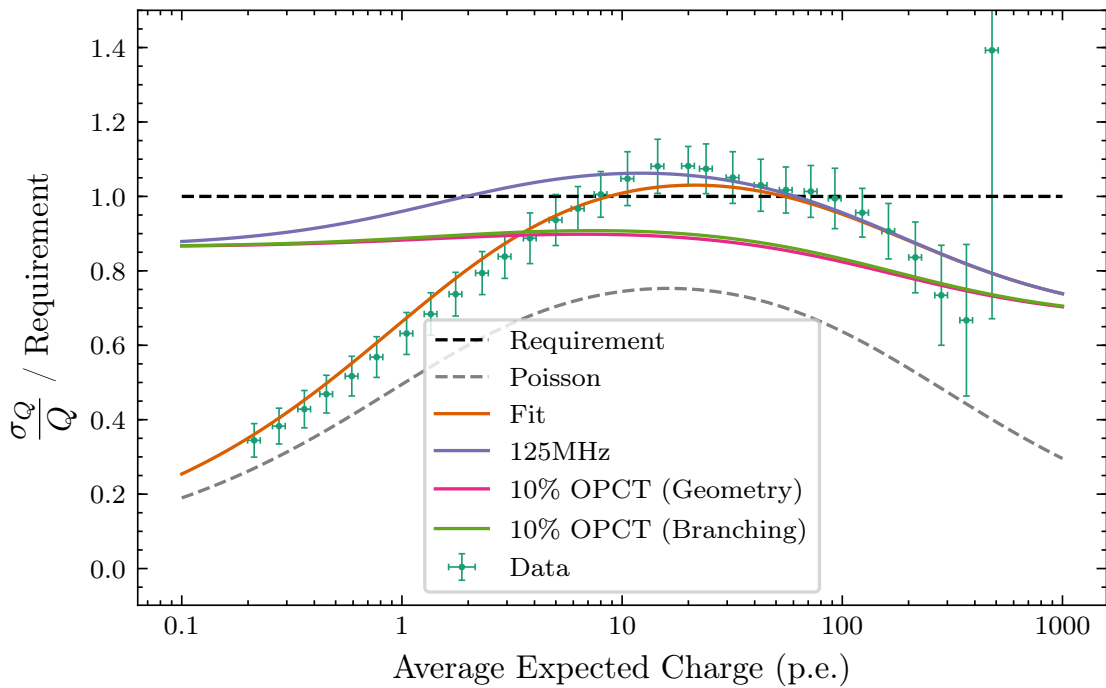


Figure 7.12: Analytical fit of the *Lab Charge Resolution* using Equation 3.2. All “non-dead” pixels are included in the fit to give an average characterisation of the whole camera. The fit result is used to predict the *Lab Charge Resolution* at 125 MHz NSB, and then with 10 % optical crosstalk in the presence of 125 MHz NSB. The possible relationships between ENF and optical crosstalk are shown in Equations 7.1 and 7.2.

measurements (values above the saturation point were excluded). Secondly, the value extracted for σ_{ENF} in this fit is compatible with that obtained from the consideration of the single photoelectron multiplication response in Section 2.2.5. Thirdly, using Equations 7.1 and 7.2, the measured ENF suggests either an optical crosstalk of 34 % (geometric) or 25 % (branching Poisson) for the camera. If the same parameters are used in combination with a value for σ_0 calculated using Equation 3.3 and values $NSB = 125 \text{ MHz}$, $t_w = 15 \text{ ns}$, and $n_e = 0.3$, we can once again conclude that the *Charge Resolution* requirement is failed by the current CHEC-S design. The curve resulting from this extrapolation is shown in Figure 7.12 labelled as “125 MHz”.

7.3.7 Conclusion

The results of these *Charge Resolution* investigations seem to suggest the optical crosstalk is the dominating factor in the degradation of the *Charge Resolution* performance for CHEC-S. They also show that a reduction in optical crosstalk could

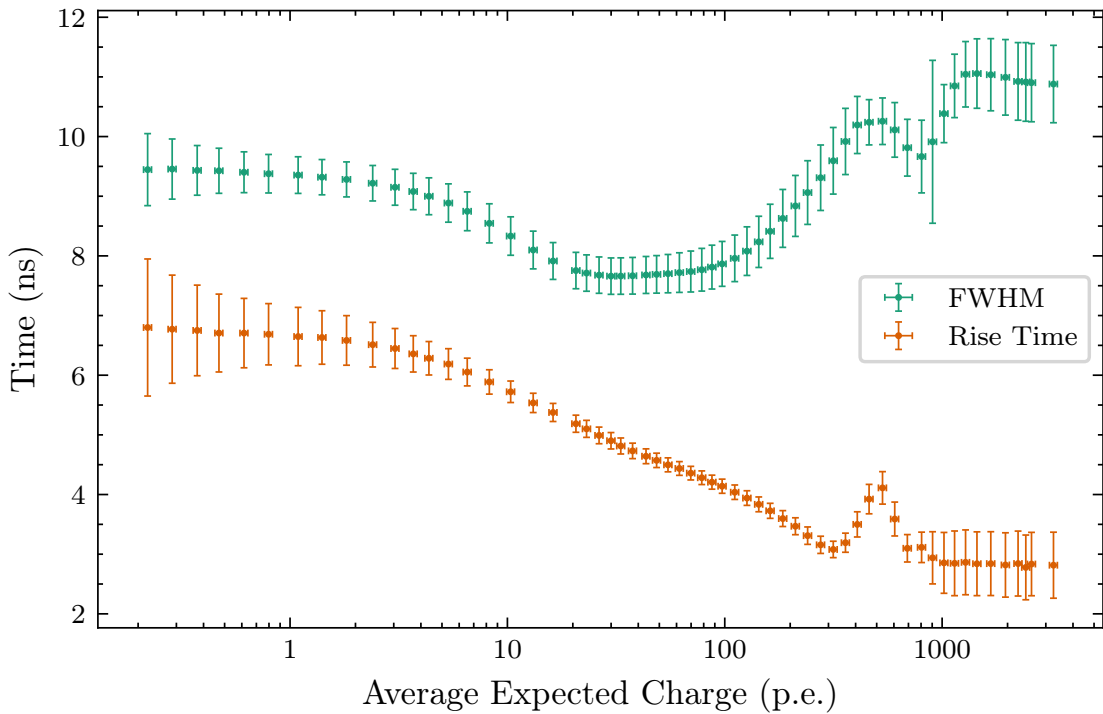


Figure 7.13: The average pulse shape across CHEC-S as a function of average expected charge (i.e. illumination). The Y errors are the standard deviation of the pulse shape parameters across the camera. The “dead” pixels are excluded from the calculation.

ensure CHEC-S is able to meet the *Charge Resolution* requirement. Such a reduction is possible with newer SiPMs, which use techniques such as “trenching” to reduce the optical crosstalk between microcells. This is discussed in more detail in Section 2.2.6. The testing of the latest production of SiPMs, which are reported to have an optical crosstalk of $\sim 10\%$ (Figure 2.9a). If we once again use the result of the fit from Figure 7.12, we can predict the *Charge Resolution* performance of a CHEC-S camera with this new silicon installed, under 125 MHz NSB. This is shown in the curves “10 % OPCT (Geometry)” and “10 % OPCT (Branching)”, and concludes that such a camera will comfortably meet the *Charge Resolution* requirement.

7.4 CHEC-S Pulse Shape

Although there is no CTA requirement attached directly to it, the pulse shape of the camera is important to understand. The pulse shape behaviour influences the performance of the charge extraction, especially when using methods that utilise the

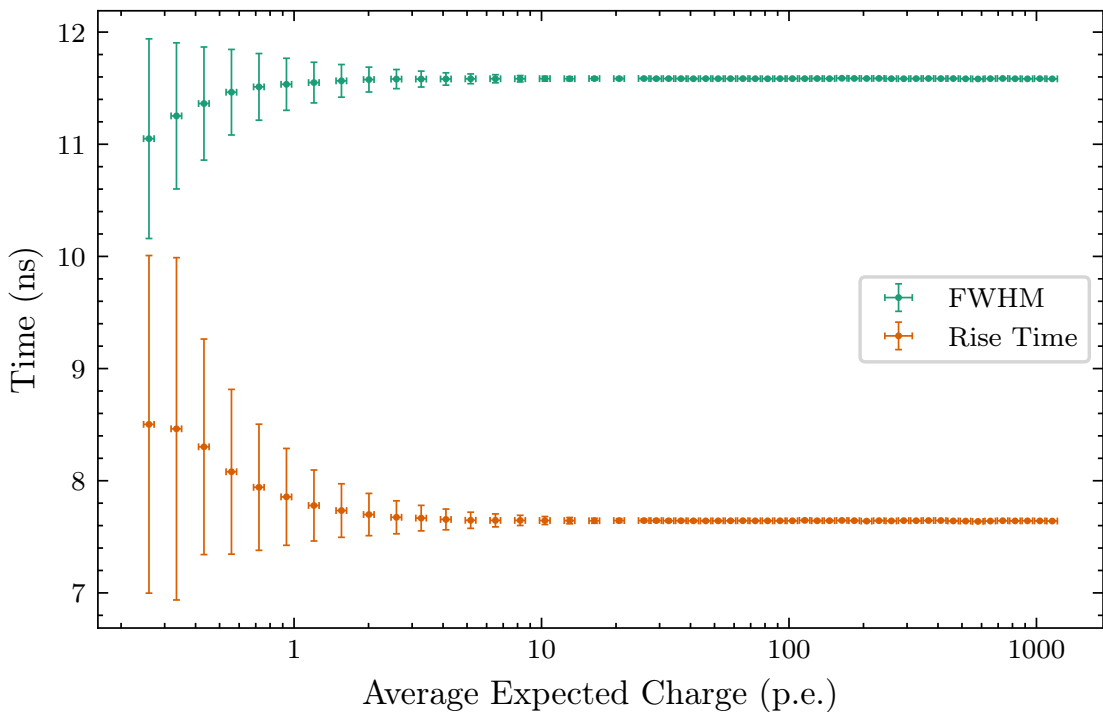


Figure 7.14: The average pulse shape extracted using data obtained from simulations of CHEC-S. The processing and representation is identical to those used in Figure 7.13. An NSB photon rate of 5 MHz is included to imitate the expected DCR contained in the measurements from the real camera.

expected shape of the pulse, such as a fitting technique, or the *Cross Correlation* method. Figure 7.13 displays the average pulse shape of CHEC-S in terms of the pulse’s FWHM and rise time. The FWHM is defined as the width of the pulse at half of its maximum. The rise time is the time between 10 % of the pulse maximum, to 90 %. A perfect detector should have a consistent pulse shape at all illuminations, as shown with the simulation dataset in Figure 7.14. The only deviations from a constant pulse shape in the simulation dataset is at low illuminations, where the noise makes it harder to characterise the pulse.

It is suspect that the region in which the FWHM appears to drop in Figure 7.13 coincides with the same region where we see the discrepancy between the *Lab* and *MCLab Charge Resolutions* (Figure 7.6). This suggests the two factors could be correlated. Further investigation into the pulse shape behaviour is required, possibly by probing at different points in the FEE to observe each components effect on the pulse shape.

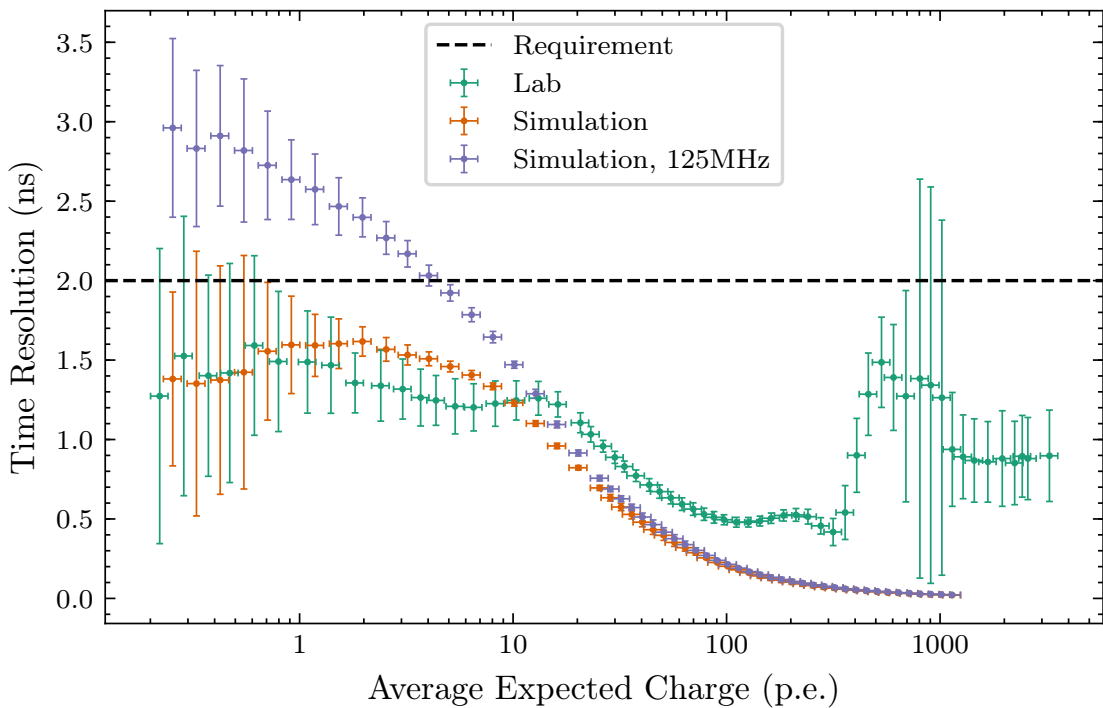


Figure 7.15: The *Time Resolution* of the CHEC-S prototype, compared against the *Time Resolution* from simulations of CHEC-S. The points represent the average *Time Resolution* across 100 events, while the Y error bars indicate the standard deviation across 100 events. The X error bars are the uncertainty in the average expected charge.

7.5 CHEC-S Time Resolution

A further criterion for assessing a camera’s behaviour within CTA is the *Time Resolution*. Introduced in Section 3.2.2, the *Time Resolution* is a measure of how the pulse time varies between pixels. After applying the timing corrections for each pixel (Section 5.5), the *Time Resolution* σ_T for an event is calculated using Equation 3.5. Only pixels with a measured charge greater than 5 p.e. are included in the calculation. The mean and standard deviation of σ_T across multiple events is then expressed against the average expected charge as shown in Figure 7.15. In order to meet the CTA requirement, the *Time Resolution* must remain below the requirement at all values of average expected charge.

While the curve for the real CHEC-S prototype appears to meet the requirement in Figure 7.15, the dataset used contained no NSB photons (only an assumed DCR of 5 MHz). Therefore, for extrapolation purposes, the *Time Resolution* extracted

from a simulation at an NSB photon rate of 5 MHz, and a second simulation at a rate of 125 MHz, was included alongside the result from the real camera.

The pulse time extraction method used in this investigation was to select the maximum sample within a 14 ns window around the maximum of the average waveform across all pixels. This technique is very simple and highly influenced by to sample-to-sample variations. It is therefore no surprise that the camera appears to fail the *Time Resolution* requirement at high NSB photon rates. As outlined in the requirement, the method used to extract the pulse time for the calculation of *Time Resolution* does not need to be the same method used for charge extraction. Therefore a more advanced method, such as fitting the pulse, could be used to improve the resolution, and meet the requirement.

A further conclusion that may be drawn from Figure 7.15 is that the real “Lab” camera does exhibit some additional time variations from pixel-to-pixel due to the electronics, which are not present in the simulation. This is the cause of the discrepancy between the “Lab” and “Simulation” *Time Resolution* curves at high illuminations. At lower illuminations however, the sample-to-sample noise is the dominating factor, resulting in a more similar behaviour between the two curves.

7.6 CHEC-M

Earlier studies of mine, that were concerned with the performance of CHEC-M, have previously been included in a publication on CHEC-M by Zorn et al. [34]. However, the calibration procedures have improved since that publication (hereafter referred to as the “CHEC-M paper”), and an investigation into the *Charge Resolution* was not previously performed. A brief update regarding the performance of CHEC-M is therefore included here, using the same techniques developed for CHEC-S, while relying on the same dataset used to produce the figures in the CHEC-M paper.

Firstly, an updated version of the dynamic range plot (Figure 15 in the CHEC-M paper) is shown in Figure 7.16. By utilising similar techniques described in Appendix B, the understanding of the filter wheel’s behaviour (as it existed at the time this data was taken) was improved. This is reflected in the new positions

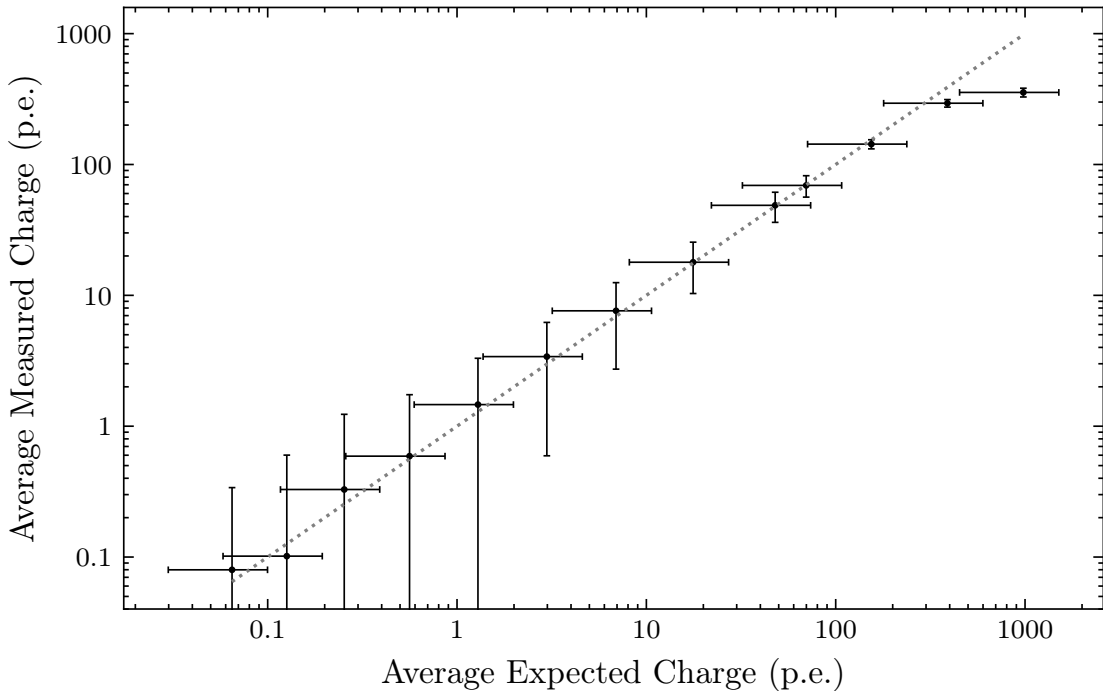


Figure 7.16: The dynamic range for a single CHEC-M pixel. Equivalent to Figure 7.3, but for CHEC-M.

of the points on the X axis, and the larger error bars which more appropriately represent the uncertainty in the calibration.

Fit Parameter	Values
Background Noise σ_0	0.814 ± 0.007
Excess Noise Factor σ_{ENF}	1.642 ± 0.008
Miscalibration σ_g	0.073 ± 0.003

Table 7.4: Parameter values resulting from the fit to the CHEC-M *Charge Resolution* (Figure 7.17) using Equation 3.2.

Resulting from the dynamic range measurements, the *Charge Resolution* of CHEC-M can be constructed. This is shown in Figure 7.17, compared against the *Lab Charge Resolution* of CHEC-S, and the fit of Equation 3.2 to the CHEC-M points. The parameters resulting from the fit are shown in Table 7.4. While the MAPMTs of CHEC-M do not suffer from the large optical crosstalk found in the SiPMs of CHEC-S, CHEC-M does seem to still have a larger ENF. This is one justification for the choice of CHEC-S over CHEC-M.

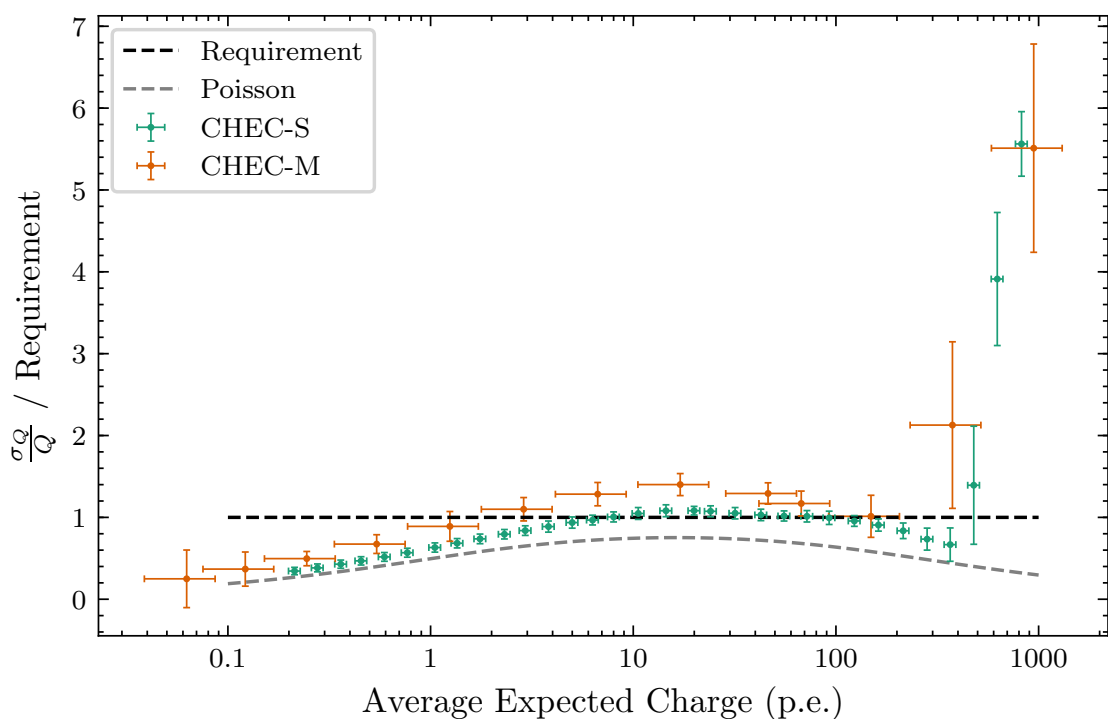


Figure 7.17: Charge Resolution of CHEC-M compared to the Charge Resolution of CHEC-S. The fit to the CHEC-M Charge Resolution using Equation 3.2 is also shown.

8

On-Sky Observations

Contents

8.1	Introduction	131
8.2	Cherenkov Shower Images	133
8.3	Jupiter Observations	136
8.4	Conclusion	139
8.5	Future	139

8.1 Introduction

Testing the operation of the camera on the telescope structure is a very important part of the commissioning procedure. When on-telescope, the camera is in an environment we have very little control over. It is exposed to factors such as weather conditions and excessive NSB from various sources (including moonlight, starlight, and artificial light pollution). The on-telescope campaigns are therefore a useful measure of the robustness of the camera, and the procedures used to operate the the telescope as a whole.

The first on-telescope campaign took place during November 2015, at the location of the GCT prototype telescope structure (Observatoire de Paris-Meudon), just before the inauguration of the GCT prototype. The primary intention of this campaign was to test the integration and operation procedure for CHEC-M on the



Figure 8.1: Photo of CHEC-M installed on the GCT telescope structure, taken during the first on-telescope campaign [80].

telescope structure, however the first detection of Cherenkov light from atmospheric showers by a CTA prototype camera was also achieved [16].

After returning to the lab for further testing and characterisation, CHEC-M was then re-installed on the GCT structure in March 2017 for a second on-telescope campaign. During this second campaign the GCT telescope was pointed towards two VHE gamma-ray sources, Mrk421 and Mrk501. These two sources are blazar objects (Active Galactic Nuclei (AGN) with a relativistic jet directed towards Earth) and were the first extragalactic TeV sources to be discovered [82, 83], testifying to their brightness. However, due to the high NSB background that is present at the Meudon site due to its proximity to Paris (20 to 100 times higher NSB than expected at the final CTA site), the camera had to be operated at a low gain and high trigger threshold [34]. The former setting was used as a precaution to avoid damage to the MAPMTs, and the latter to avoid triggering on the NSB photons. The combination of these operating conditions, and the limited observation time, meant an astrophysical detection was unlikely for this campaign. Nevertheless, Cherenkov showers were detected during the campaign. This chapter will describe the results I have obtained from the camera images taken during the campaign.

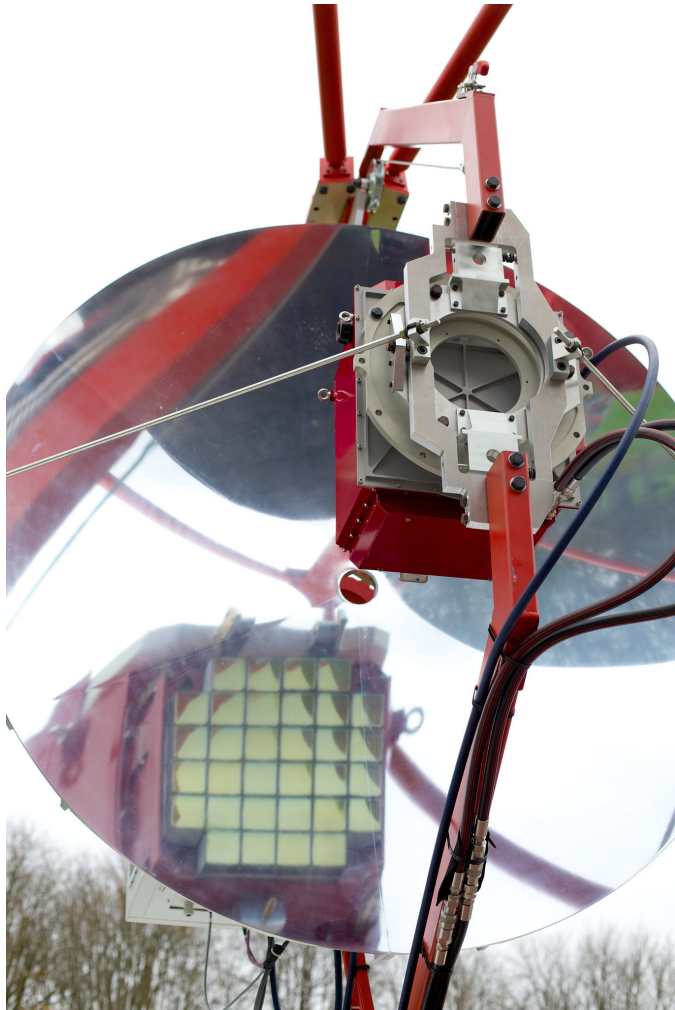


Figure 8.2: Photo of the reflection of CHEC-M in the GCT telescope’s secondary mirror, taken during the first on-telescope campaign [81].

8.2 Cherenkov Shower Images

Utilising the calibration procedure defined in Chapter 5, and a simple integration window combined with the *Neighbour Peak Finding* technique described in Chapter 6, the signal in each pixel was extracted for every trigger event. The results shown in this section originate from a 30-minute-long observation of Mrk501, during which the camera received triggers at a rate of ~ 0.1 Hz.

Figure 8.3 displays the distribution of *Hillas* width and length (Section 6.3.1) for the events that caused a camera trigger. Four events were chosen from the collection, and are marked with a cross on the figure. The images corresponding to each of the selected events are shown in Figure 8.4. These events were manually

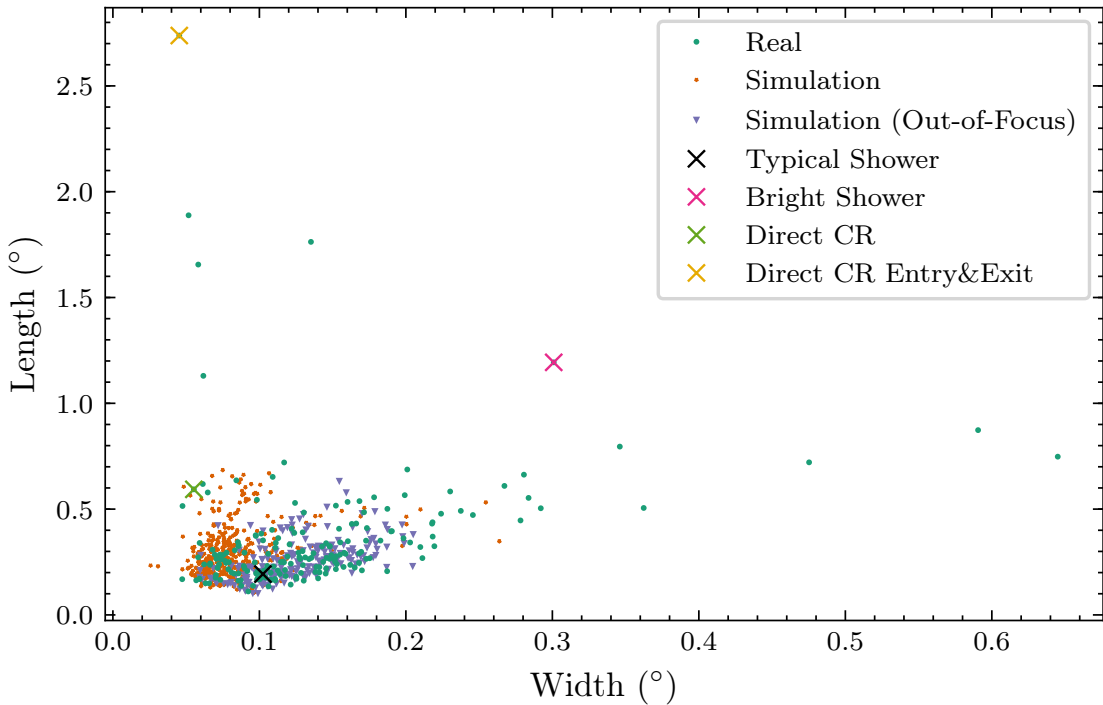


Figure 8.3: The *Hillas* length versus width of each image in a 30-minute-long observation of Mrk501 with CHEC-M on the GCT telescope structure (labelled as “Real”). Simulations of CHEC-M on the GCT telescope are also included for comparison. Four different types of events have been highlighted and assigned a category based on a manual examination of their camera image.

selected as they represent a range of possible event types:

- Figure 8.4a - A typical Cherenkov shower, most likely produced from a hadronic cosmic ray due to their abundance compared to gamma-ray showers. The majority of events fall under this category, and result in a cluster at low values of *Hillas* width and length.
- Figure 8.4b - A bright Cherenkov shower, from a high energy cosmic ray. These events are characterised by their large *Hillas* width and length.
- Figure 8.4c - A direct cosmic ray, grazing along the pixels on the focal surface and producing an electron avalanche in the MAPMTs. As the signal is located along the incident path of the cosmic ray, the ratio of *Hillas* length to width for these events is large. Due to their locality to a single telescope, these events are ignored in an IACT array, as only a single telescope triggers.

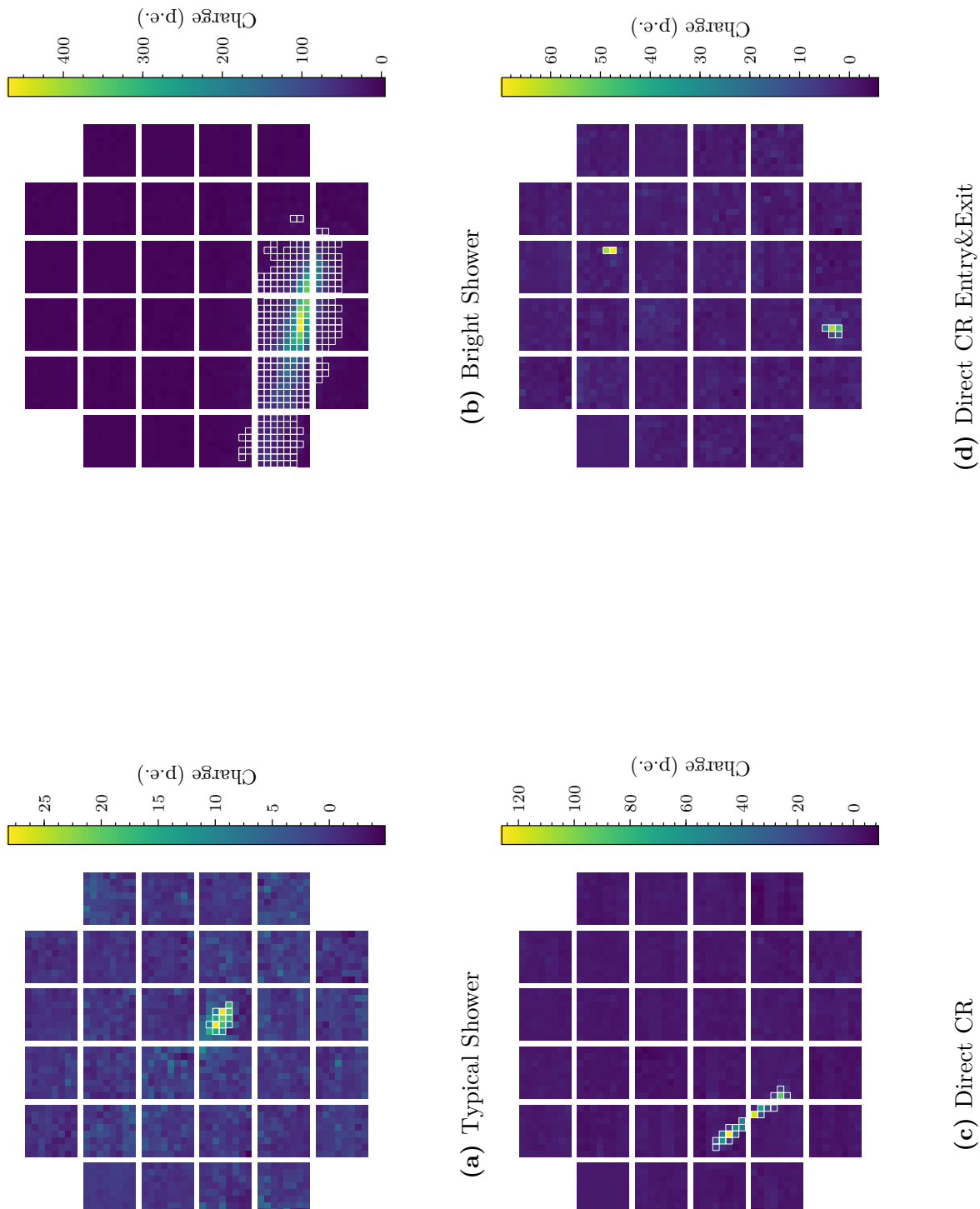


Figure 8.4: A selection of images taken by CHEC-M during its second on-telescope campaign. The images chosen correspond to the individually highlighted events in Figure 8.3. The white-outlined pixels are those that survived the (17, 8) tailcuts.

- Figure 8.4d - Another cosmic ray. Due to the curved focal surface of CHEC-M, it is possible for a cosmic ray to enter and exit the focal surface at opposite sides. These events are characterised by very large ratios of *Hillas* length to width.

A Monte Carlo simulation of proton-induced Cherenkov showers, combined with a model of CHEC-M on the GCT telescope structure, was produced for a comparison against the real results. The signal and Hillas parameters were extracted from the simulated waveforms, with the identical procedures used for the real data. The distribution of *Hillas* width and length are also shown in Figure 8.3, under the label “Simulation”. It is immediately apparent that the distribution of *Hillas* width is a lot tighter in the simulation. An explanation for this is supplied later in Section 8.4.

8.3 Jupiter Observations

It has been considered within CTA that the pointing calibration for the telescopes may be performed using the change in pixel current as a star crosses a pixel’s boundary [84]. As one of the primary effects of a higher NSB (such as that from starlight) is the increased variation of the waveform’s baseline, it may be possible to achieve a pointing calibration using this information instead of the currents. An initial investigation into this possibility was explored during the second on-telescope campaign using Jupiter as a source.

Two runs were taken: an “ON” axis observation, and an “OFF” axis observation. The ON observation was pointed at (and tracked) Jupiter, however intentionally slightly off axis to avoid it being located in the gap at the centre of the camera. The OFF observation was taken without Jupiter, or any other optically bright star in the FoV. The camera was triggered externally triggered at a rate of 300 Hz for approximately 5 minutes. This resulted in approximately 80,000 waveforms per pixel for each of the observations. The Root-Mean-Square (RMS) of the waveforms was extracted for each waveform, and averaged over all events. The average RMS

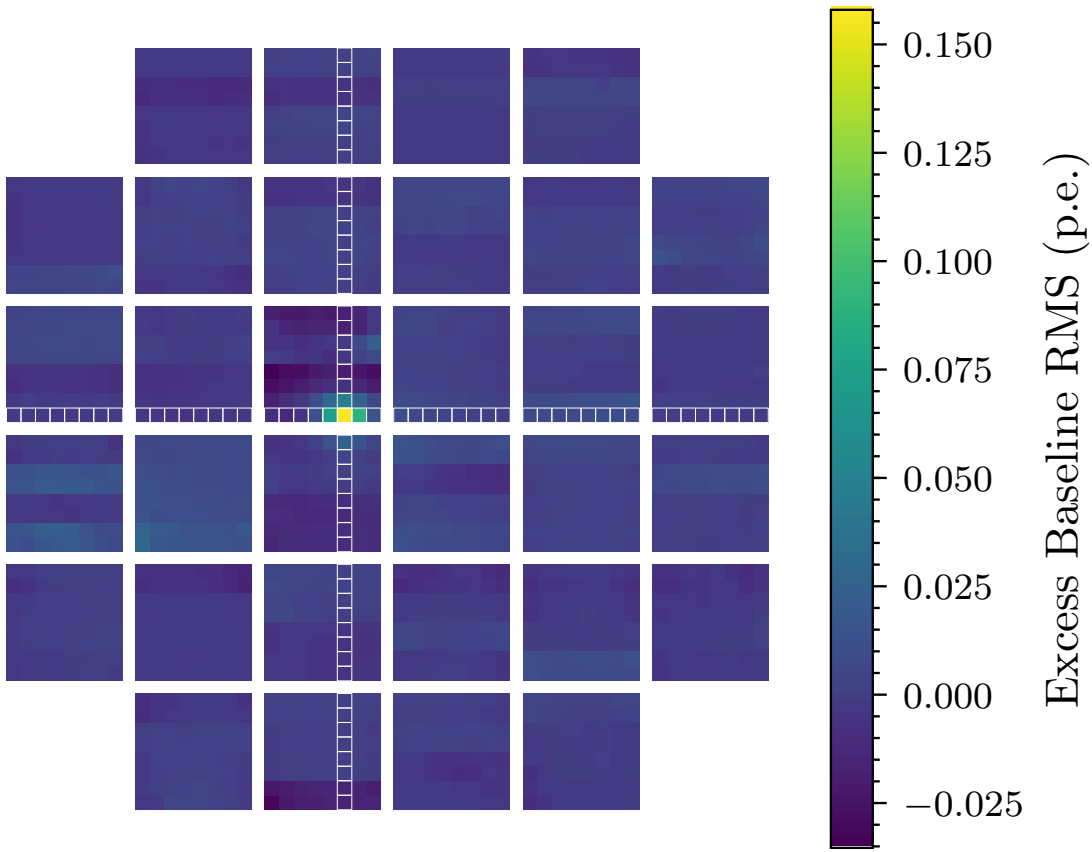


Figure 8.5: Camera image of the excess baseline RMS for observations of Jupiter taken during the second on-telescope campaign for CHEC-M.

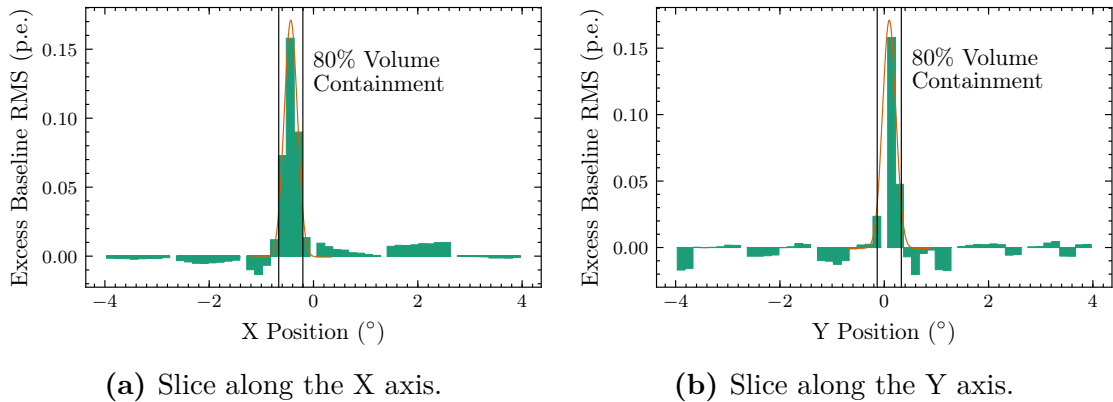


Figure 8.6: Slices of the camera image from Figure 8.5, along the white-highlighted pixels, showing the excess baseline RMS from each pixel in the slice. A slice of the 2D Gaussian fit to the PSF resulting from observing Jupiter is also shown, along with the corresponding 80 % volume containment radius.

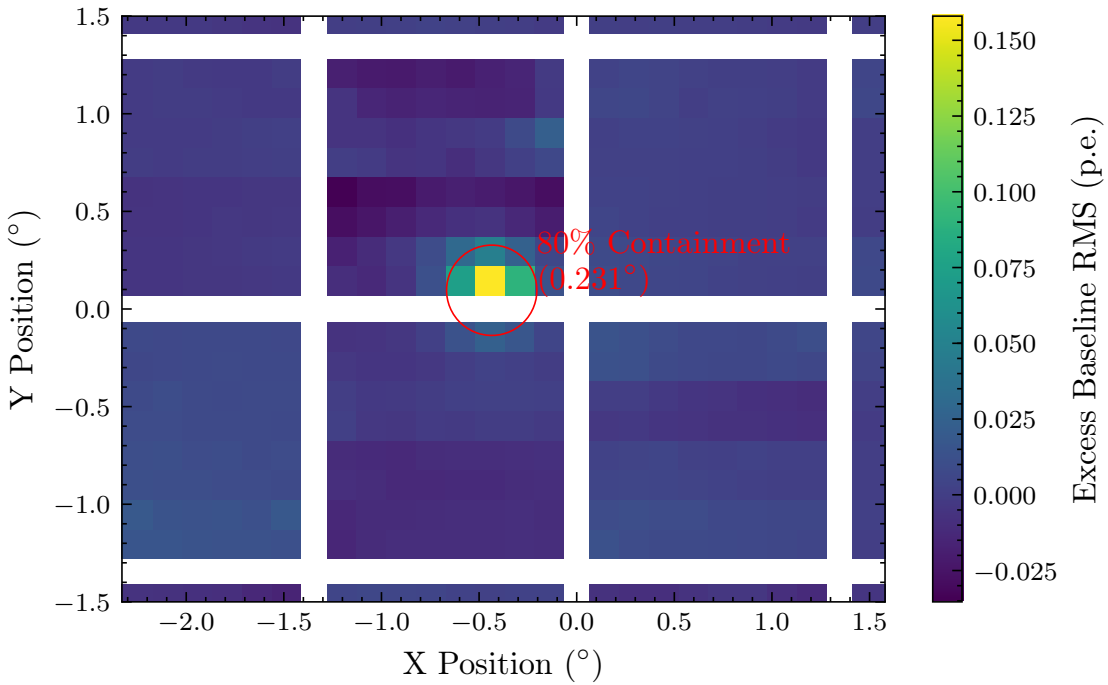


Figure 8.7: Zoom of Figure 8.5, showing the result of the 2D Gaussian fit to the PSF resulting from observing Jupiter, and the corresponding 80 % containment radius.

per pixel for the OFF observations were then subtracted from the ON observations. This removed any contributions from the camera electronics.

The resulting camera image of the excess RMS per pixel is shown in Figure 8.5. This profile of Jupiter in the camera is a measure of the Point Spread Function (PSF) of the telescope. The value that is used in CTA to characterise the PSF is the 80 % containment radius [15, 85]. To extract this value, a 2D Gaussian was fit to the camera image, using the X and Y coordinates of every pixel and their corresponding value of excess RMS baseline. In Figures 8.6a and 8.6b, a slice of the camera image for each axis is shown, intersecting at the pixel with the maximum excess RMS. Shown alongside the pixels distributions are the corresponding slices of the 2D Gaussian fit, demonstrating the fit’s successful representation of the profile, even with it being on the edge of a module. Figure 8.7 illustrates the 80 % containment radius radius on the camera image, resulting in a value of 0.23° .

8.4 Conclusion

The value extracted for the PSF is a magnitude larger than expected from Monte Carlo simulations, where a value of $\sim 0.02^\circ$ was obtained [85]. This result is compatible with the discrepancy seen in the *Hillas* width between the real observations and simulations in Figure 8.3. One possible source of this discrepancy is the quality of the prototype mirrors. As shown by Rulten et al. [15], an increase in the mirror surface roughness translates into an increase in the PSF. A second potential explanation is an incorrect separation between the camera focal plane. It was concluded by Rulten et al. [15] that an a incorrect separation of just a few millimetres could account for a magnitude increase in the 80 % containment value.

A new simulation was generated with a PSF of 0.28° , to more closely represent the PSF of the telescope prototype. The *Hillas* parameter distribution we obtain from this simulation, labelled as “Simulation (Out-of-Focus)” in Figure 8.3, is in much closer agreement with the *Hillas* parameters obtained during the on-telescope campaign.

8.5 Future

The next on-telescope campaign is planned for November 2018, where CHEC-S will be placed on the ASTRI telescope structure which has been constructed on Mt. Etna, Sicily [86]. This will be the first on-telescope campaign for the CHEC-S prototype, and the first time a CHEC prototype has been installed on the ASTRI telescope structure. This campaign will extend for two weeks, during which priority will be given to the characterisation of the trigger efficiency in the presence of NSB, and the formalisation of the operation procedures. New Cherenkov shower detections will also be obtained during this campaign, however the detection of a astrophysical gamma-ray source is not a priority of the campaign.

9

Summary

CTA is intended to be the most sensitive IACT array to date. This ambitious goal will be attained with the construction of the largest ever IACT array, exploiting the latest developments in optics, photosensors, computational advances, and Cherenkov shower analysis techniques. Observations of the highest energy phenomena in the universe will be facilitated by the SSTs, for which GCT is one of three designs proposed.

The camera designed for the GCT telescope is known as CHEC. During the development of this camera, the decision was made to prototype two novel photosensor technologies. CHEC-M incorporates MAPMTs as their photosensor, while CHEC-S incorporates SiPMs. The factor most likely to impede the performance of the CHEC-M prototype is the poor photoelectron resolution that is apparent in PMT technology. This arises due to the fluctuations in the secondary multiplication factor at each dynode in the chain. Conversely, in the CHEC-S prototype, which features excellent photoelectron resolution due to its SiPM photosensor, the characteristic most likely to limit the performance is the high optical crosstalk of 35-40 %. The phenomena of optical crosstalk occurs when secondary photons (generated during the electron-hole avalanche) cause additional avalanches in neighbouring microcells. These pitfalls of each photosensor are characterised in terms of their ENF. The next production of SiPMs for the CHEC prototypes are expected to have an optical crosstalk of $\sim 10\%$, thereby overcoming this limitation in performance.

The CTA Observatory has defined requirements that must be adhered to for an in-kind contribution to be accepted. These requirements ensure that the science goals of CTA are met. This thesis primarily focussed on the *Charge Resolution* performance criteria, and its associated CTA requirement. The *Charge Resolution* is a measure of how well the Cherenkov shower signal can be reconstructed, thereby quantifying the performance of the calibration, charge extraction, and the camera design into a single value per illumination level.

The packages relevant to the waveform processing, Cherenkov shower reconstruction, and Monte Carlo simulation are outlined in Chapter 4. The `TargetCalib` library is among these packages, and is used to perform the calibration required for waveform data obtained with the TARGET modules. Another important package is `ctapipe`, a Python library developed by CTA consortium members to be utilised as the low-level data processing pipeline. This purpose encapsulates the transformation of calibrated waveform data obtained from the camera, into event lists containing the characteristics of the progenitor particle which created the Cherenkov shower, detected by the array.

A significant proportion of my contributions towards the commissioning of CHEC has been in the development of a calibration pipeline for the digitised waveform data. This includes the correction of samples for the storage cell dependence, induced by the TARGET ASICs; specifically, subtracting the electronic pedestal and rectifying for non-linearities (Transfer Function). It also encompasses the conversion of the photosensor signal into photoelectrons, and the flat-fielding of the signal response across the camera. This ensures that each pixel reports the same charge on average for a certain number of photons. A correction for saturated signals is also required. An initial investigation towards this has been undertaken, however this is an area where further investigation is required.

The step following the calibration of the waveforms is the extraction of the Cherenkov signal embedded within them. This process is typically split into two procedures: peak finding and charge extraction. This signal extraction process is not only a common IACT procedure, but also a generic signal processing exercise.

Consequently, many methods already exist to achieve this. A technique I have implemented for charge extraction utilises a *Cross Correlation* of the waveform. This technique is designed to reliably extract the pulse in the presence of uncorrelated noise. The result of the charge extraction is a single value per pixel, forming the image of a Cherenkov shower, which often appears as an ellipse. The expression of the image in terms of its second moments is the conventional method for parametrisation. These are commonly known as its *Hillas Parameters*. These parameters enable the properties of the progenitor particle to be inferred, including its classification, trajectory, and energy. The first property is used to exclude the prevalent hadronic shower background, while the last two provide information about the astrophysical source that produced the gamma-ray.

To appropriately assess the performance of the CHEC-S prototype, one must do so within context of the CTA Requirements. To fully perform this investigation, an updated simulation model that accurately represents CHEC-S was generated. While the measurements from the constructed CHEC-S prototype do not appear to meet the *Charge Resolution* requirement, even in the absence of NSB, the corresponding simulated lab measurements do suggest it is possible to meet the requirements with the current design. The cause of the discrepancy in results between the real measurements and simulations is currently unknown. However, the *Charge Resolution* obtained when reducing the bias voltage across the SiPM suggest it may be connected to the optical crosstalk, while investigations into the pulse shape suggest it could be correlated with a changing FWHM of the pulse with amplitude. Regardless, an investigation into the improvement of *Charge Resolution* via a reduction in optical crosstalk can be performed. I have conducted such an investigation in three ways: with simulations of a CHEC-S prototype with 20% optical crosstalk; by reducing the bias voltage (and therefore the overvoltage) across the SiPMs; and analytically, using the equation that represents the *Charge Resolution* requirement curve, which encapsulates the contributions from the electronic noise, NSB rate, ENF, and the miscalibration. In all three investigations, it is observed

that the *Charge Resolution* requirement will be comfortably achieved with a CHEC-S prototype that contains SiPMs with the lower optical crosstalk of at least 20 %. A comparison against the *Charge Resolution* performance achieved with CHEC-M shows the improvement one would expect in switching from MAPMTs to SiPMs, due to the reduction of ENF between the respective photosensors.

During the second on-telescope campaign for CHEC-M, observations of Cherenkov showers, and optical measurements of Jupiter (using the increase in the variance of the waveform baseline) were conducted. An inconsistency in the results obtained from each of the observation types, when compared to results obtained from simulations, was identified. These each independently suggested that the telescope prototype does not achieve the PSF that existed in the simulations. An updated simulation, which reflected the true PSF of the camera during the campaign, resulted in Cherenkov shower images that more closely represented those measured by the camera.

9.0.1 Outlook

A full review within the context of the remaining CTA Requirements is necessary to prove CHEC can be accepted as an in-kind contribution to the CTA Observatory. This is a large undertaking, requiring the accumulation of work from the entire CHEC group. An important aspect of this review is the full validation and verification of the Monte Carlo model of the CHEC prototype, which must ensure there are no disparities between the simulations and the data. This process will involve the identification of the additional noise factor observed in the non-simulated dataset.

We shall begin testing the latest production of SiPMs from Hamamatsu, featuring optical crosstalk of <10 %, on the CHEC-S prototype in early 2019. During this testing, the *Charge Resolution* investigation will be revisited to confirm the predictions made by this thesis.

The finalisation of the calibration procedure of CHEC is also intended early 2019. This includes the production of a processing chain that can perform the required operations at rates required by the CTA Observatory. This development will

include the production of a procedure to directly generate *R1* TIO files during data taking (i.e. online calibration), as opposed to generating *R0* TIO and calibrating offline. Furthermore, the Transfer Function calibration could benefit from further development, as better performance at low amplitudes should be achievable (see Appendix D). Finally, the two major factors currently missing from the calibration chain are the consideration of how the corrections change with temperature, and the correction of saturated measurements. These will be a primary focus for future investigations into improving the calibration performance.

The next on-telescope campaign is anticipated for November 2018, when the CHEC-S prototype will be transported to Mt. Etna, Sicily, to be integrated on to the ASTRI telescope structure for two weeks. During this campaign, priority will be given to formalising the operation procedure, and fully characterising the trigger efficiency of the telescope in the presence of NSB.

Appendices

A

The Silicon Photomultiplier

Contents

A.1	Introduction	146
A.2	The P-N Junction	146
A.3	Avalanche PhotoDiode (APD)	148
A.4	Geiger-mode Avalanche PhotoDiode (G-APD)	150
A.5	Silicon Photomultiplier (SiPM)	151

A.1 Introduction

Solid state photon detectors have been an active field of research since the 1960s [21], however the development into a photosensor that is capable of both high resolution photon counting, and a large dynamic range was only achieved in the 1990s [87]. Possibly as a result of their development process, the description of how an SiPM operates can be subdivided into various solid state detectors, which provided the building blocks towards the SiPM design. Due to their complexity compared to PMTs, the full description of SiPMs are reserved for this appendix.

A.2 The P-N Junction

As with all solid state devices, the building blocks of SiPMs are P-N Junctions. A p- and n-type material are created by the addition of impurities to a semiconducting material such as silicon. The impurities added to produce the n-type semiconductor

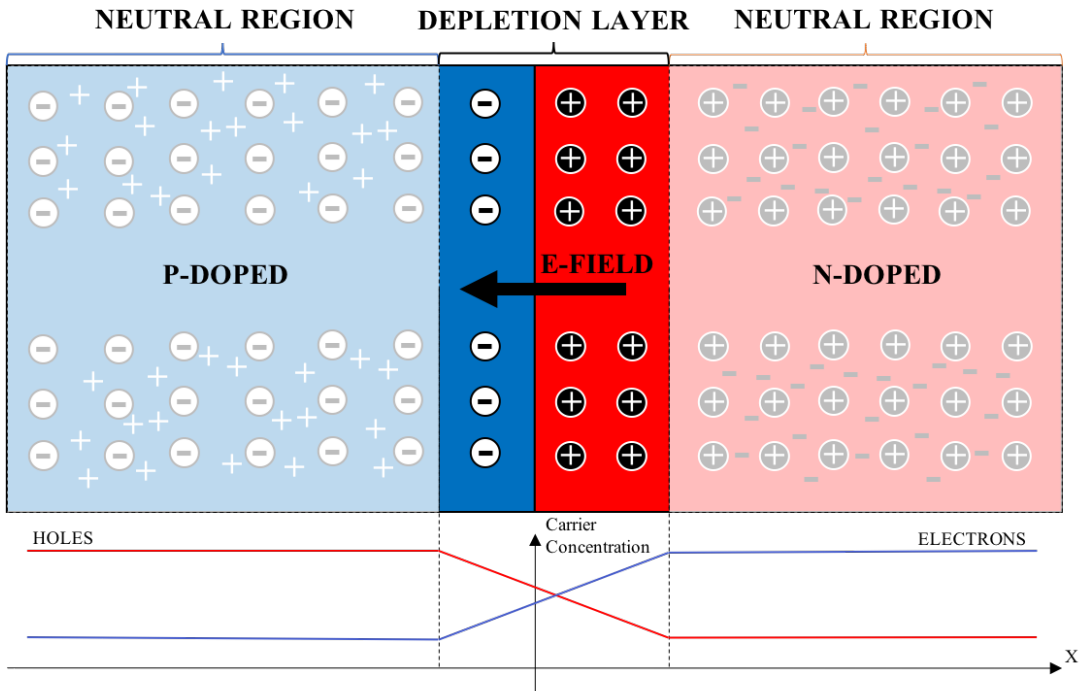


Figure A.1: My own illustration of a P-N Junction, inspired by Ghassemi, Sato, and Kobayashi [22].

increases its number of freely moving electrons, while the impurities added to produce the p-type semiconductor increases its number of freely moving holes. When the two materials are joined, the P-N Junction is formed. As a result of the abundance of charges in each material, a diffusion current forms with electrons moving from the n-type material (leaving behind its immobile positive ions) to combine with the holes in the p-type material. The same occurs vice versa for the excess holes in the p-type material, leaving behind its immobile negative ions. The result is a region adjacent to the junction with no free charges remaining, known as the depletion layer (Figure A.1). The charge difference from the immobile ions produces an electric field inside the depletion layer, that points from its positively charged N side to its negatively charge P side. This electric field opposes the diffusion current and causes an equilibrium to be reached across the junction.

However, this equilibrium can be disturbed by the input of energy into the system, either by thermal excitation (producing what is known as *dark counts*) or by the photoelectric effect. If the energy provided to a bound electron is greater

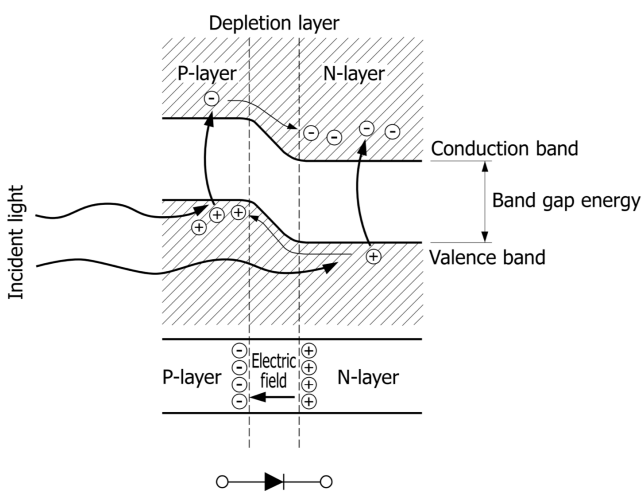


Figure A.2: Illustration of the silicon bandgap, demonstrating a bound electron being exited into an excess charge carrier via the photoelectric effect. The excess charge carrier is then accelerated in the opposite direction of the electric field, resulting in a current [22].

than the band gap energy (inherent to the semiconductor) then it becomes an excess charge carrier, leaving behind a hole. These excess charge carriers are known as an electron-hole pair. If these excess charge carrier are produced in the depletion layer, they will travel along the electric field in the direction according to its charge. For example, an excess electron charge carrier released in the P side of the depletion layer will travel in the opposite direction to the electric field, crossing the P-N Junction to the N side. This is illustrated in Figure A.2. If a connection is formed between the P and N regions, this process will produce a current. If excess charge carriers are freed outside the depletion layer, they are generally short-lived, as there is no significant electric field to accelerate them, and therefore no net current is produced.

A.3 Avalanche PhotoDiode (APD)

In order to maximise the photosensitivity of the semiconductor, the depletion layer depth must be maximised. To achieve this, a reverse bias voltage is applied to the semiconductor. This means biasing the N side (cathode) to a higher electric potential than the P side (anode). The result of this is the freely-mobile holes on the P side, and the freely-mobile electrons on the N side, are pulled away from the

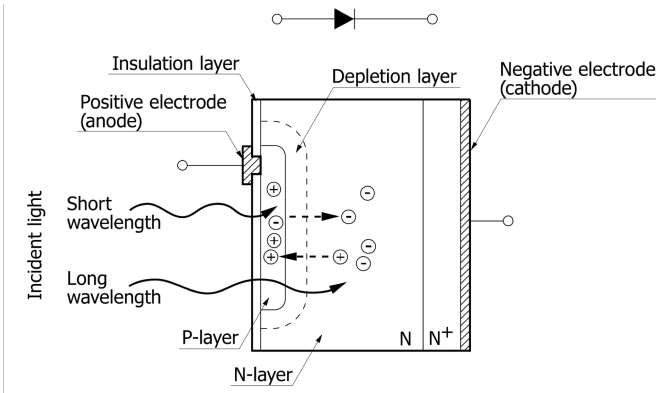


Figure A.3: Diagram of an Avalanche PhotoDiode with a reverse bias voltage applied. The N side of the semiconductor acts as the cathode. Traditionally the cathode is the “negative electrode”, however in reverse bias the N side is connected to the positive terminal. The P side of the semiconductor acts as the anode. Similarly to the N side, although the anode is the name traditionally given to the “positive electrode”, in reverse bias the P side is connected to the negative terminal. The result is the electrons are accelerated to the N side cathode, while holes are accelerated to the P side anode [22].

junction. This leaves behind the charged ions and causes the depth of the depletion region to increase. The anode and cathode is illustrated in Figure A.3.

In addition to an increased depletion layer depth, this reverse bias increases the electric field within the depletion region. Excess charge carriers achieve a higher kinetic energy as a result. If the mean kinetic energy attained between collisions with ions is greater than the band gap energy, additional charge carriers may be released. This impact ionisation effect results in a rapid multiplication of excess charge carriers, and is referred to as an avalanche. Such a device is therefore known as an APD. The ratio of final charge carrier signal that is read out to the initial photo-carriers produced is the gain of the APD, analogous to the gain of a PMT.

The typical operation of a APD is to apply the bias voltage that optimally maintains relatively constant bandwidth and stable noise output, while achieving the highest gain level [22]. This voltage occurs before the *breakdown voltage*, where the gain approach infinity. This operation of the APD is known as “proportional” or “linear” mode [87], as the gain increases proportionally with bias voltage. However, APDs in this mode suffer from limited gain and large variations in their single amplification, and are therefore not useful in single photon counting. To better

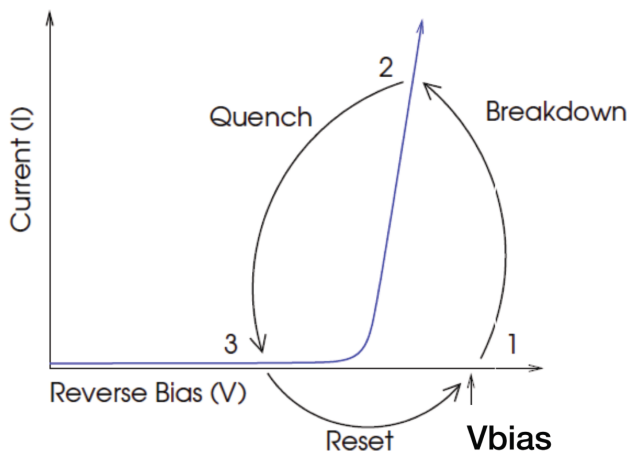


Figure A.4: Diagram of the current created by the avalanche versus reverse bias voltage [26]. The stages in the cycle of the G-APD operation are labelled. 1) The G-APD is set to a reverse bias voltage above the breakdown voltage. No current flows yet. 2) A excess charge carrier is produced by thermal excitation or the photoelectric effect. The carrier causes a Geiger discharge, creating a macroscopic current. 3) The current is quenched by a resistor in series with the diode. The bias voltage across the diode is reduced below the breakdown voltage, and the avalanche ceases. The G-APD then recharges ready for the next avalanche.

utilise APDs we must increase the bias voltage beyond the breakdown voltage, causing the APD to transition into Geiger mode.

A.4 Geiger-mode Avalanche PhotoDiode (G-APD)

In Geiger mode, a single photoelectron produces a self-perpetuating ionisation cascade. This effectively causes the silicon to become conductive, thereby amplifying the original electron-hole pair into a measurable current flow [26]. A “quenching resistor” is used in series with the diode to limit the current drawn during breakdown, thereby lowering the bias voltage across the diode and bringing it below the breakdown voltage. This halts the avalanche and results in a signal shape that can be read out from the voltage across the quenching resistor. The SiPM then undergoes a recovery back to the original “overvoltage” above the breakdown voltage, ready for the next photoelectron avalanche. This operation cycle of the Geiger-mode Avalanche PhotoDiode (G-APD) is shown in Figure A.4.

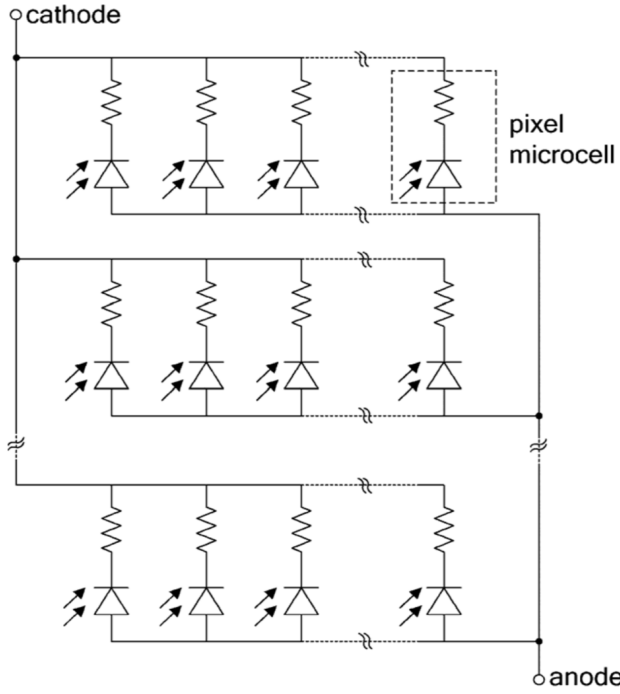


Figure A.5: Simplified equivalent circuit of an SiPM detector, demonstrating the individual microcells connected in parallel [8].

The disadvantage of this mode is that the G-APD is a binary device. All information about the number of generated photoelectrons in the semiconductor is lost. The only knowledge one can have is that there was at least one photoelectron. However, the response that results from this signal, completely independent of the number of initial photoelectrons, is extremely large and well defined, with a gain in the range 10^5 - 10^7 . G-APDs are therefore very useful as single photon counting devices, but are not so useful in operations where a large dynamic range is desired.

A.5 Silicon Photomultiplier (SiPM)

The final transition in this technology chain is to the concept of the SiPM. This device utilises a densely packed array of up to 10,000 G-APDs per mm^2 . Each of these G-APD “microcells” has its own quenching resistor, and all the microcells are connected in parallel to a common bus [87]. Figure A.5 shows a simplification of the equivalent circuit diagram for an SiPM. The result is a detector that can

count multiple photons, with a dynamic range that is essentially the number of microcells. Though, each microcell still operates as a binary sensor, therefore two photons incident on the same cell will only register as one. The superposition of the output current pulses from all the microcells results in the highly quantised measure of the number of photoelectrons produced.

B

Laboratory Characterisation

Contents

B.1	Introduction	153
B.2	Filter Wheel	154
B.2.1	Reference SiPMT	155
B.2.2	Camera Correction	156
B.3	Illumination Profile	157
B.3.1	Laser Profile	157
B.3.2	Camera Geometry	158
B.3.3	Total Correction	159
B.4	Absolute Illumination	160
B.5	Average Expected Charge	162
B.6	Consideration of Errors and Uncertainty	163

B.1 Introduction

At the time of this writing, the CHEC-S prototype is being commissioned at the Max-Planck-Institut für Kernphysik in Heidelberg, Germany. The camera is stored in a dedicated dark room, which in this thesis I refer to as the lab. The CHEC-S test bench consists of:

- an enclosure to further limit the background light that enters the camera,
- a robot arm with an attached reference SiPM,

- a laser combined with a filter wheel containing a continuous neutral density filter,
- and a diffuser to spread the light uniformly onto the camera focal surface.

The latter two are contained within the smaller box attached to the camera enclosure.

In order to fully commission the camera and understand its performance, we must have accurate knowledge of average number of photoelectrons incident on each pixel (i.e. the illumination), for each position setting of the filter wheel. It was therefore necessary to characterise the lab set-up, via the calibration of the laser and filter wheel combination. This was achieved via three stages:

1. Measuring the relationship between filter-wheel position and light transmissivity.
2. Measuring the relative amount of light each pixel received due to its position on the focal surface.
3. Measuring an absolute illumination in photoelectrons for at least one filter-wheel position.

Although I was not personally involved with the initial calibration of the filter-wheel, in this appendix I present my own analysis of the available data in order to achieve a complete lab calibration procedure. The result of this procedure is a conversion factor from filter wheel transmission to expected charge in photoelectrons, which I require for the analysis presented in the other chapters of this thesis.

B.2 Filter Wheel

The calibration of the filter wheel was performed in two stages: an initial measurement with a reference SiPM in order to obtain an approximate handle on the relative illumination, and a secondary correction using the camera at different gain settings.

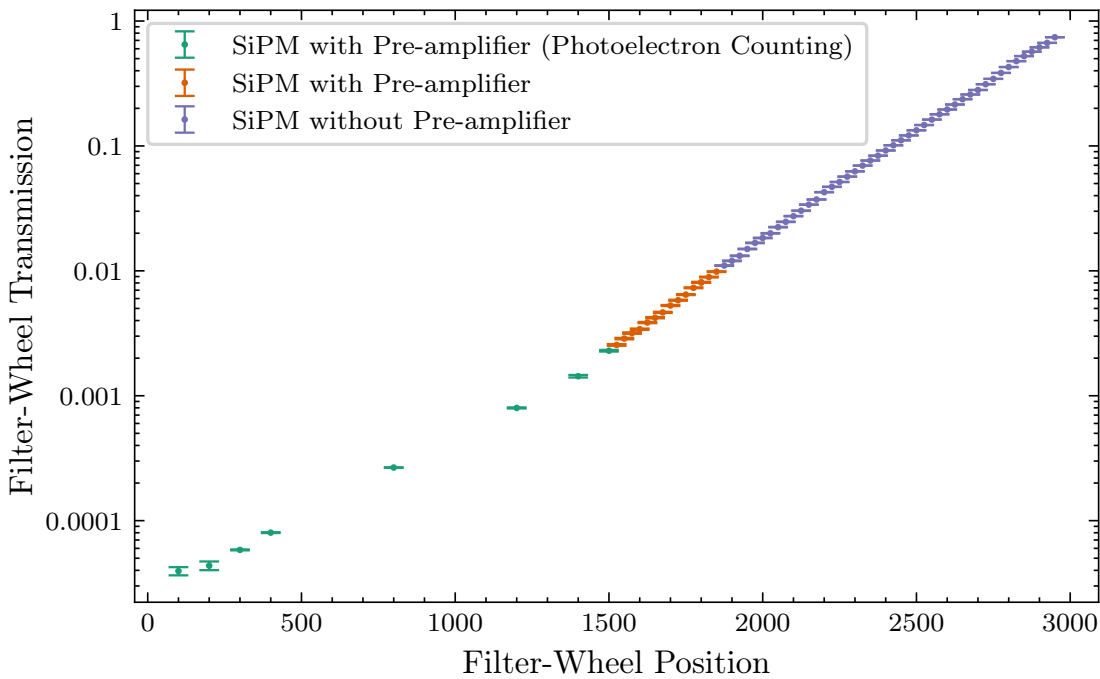


Figure B.1: Logarithm of transmission versus position for the filter wheel. The relationship is fit with a straight line.

B.2.1 Reference SiPMT

Using a single reference silicon photomultiplier pixel connected to an oscilloscope, centred on the camera focal plane, the ratio between the signal with and without the neutral-density filter was calculated for different filter-wheel positions (i.e. different attenuations). As the dynamic range of the reference SiPM was limited, in order to cover the full range of filters attenuations, three approaches were utilised:

1. **Low-range** - Average illumination obtained from SPE spectrum, with a pre-amplifier attached to the SiPM.
2. **Mid-range** - Average pulse area, with a pre-amplifier attached to the SiPM.
3. **High-range** - Average pulse area, with no pre-amplifier attached.

The overlapping values from each method were used to stitch the datasets together. The resulting points, shown in Figure B.1, were then used as a lookup table for the conversion from filter-wheel position to transmission.

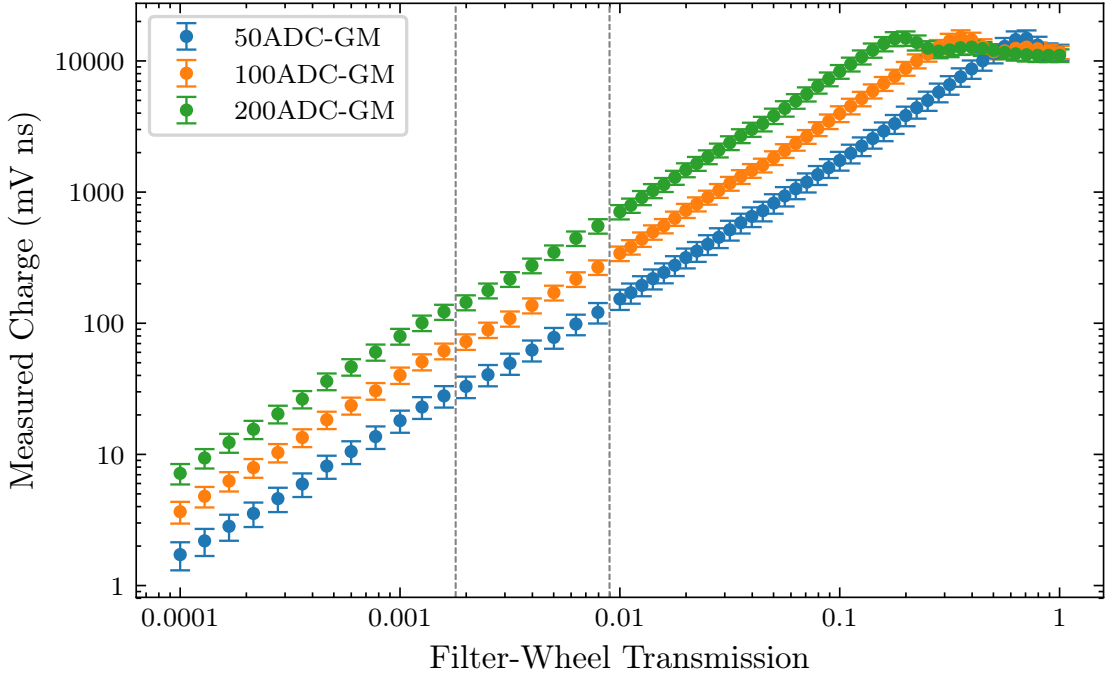


Figure B.2: Average charge across all CHEC-S pixels versus filter-wheel transmission. Three differently-gain-matched datasets are shown (50 ADC, 100 ADC, 200 ADC). Each gain matching results in a different bias voltage across the photosensor, and therefore a different gain, optical crosstalk, and PDE. Features shared between the datasets at a transmission value can only be due to errors in the filter-wheel calibration. Two clear features are highlighted by the vertical grey lines. Features shared at a measured charge value are due to shared properties in the Transfer Function (such as saturation).

B.2.2 Camera Correction

When looking at the average measured charge across the camera as a function of transmission, for three datasets where each has different bias voltages applied to the photosensors, features that share a position on the X axis can only occur from artefacts of the previous filter-wheel calibration. Figure B.2 indicates some of the artefacts which are easy to see. The measured charge was then converted into an “effective transmission” using the relation in Figure B.2. By plotting the “effective transmission” against filter-wheel position, a new conversion from filter-wheel position to transmission was obtained from the fit shown in Figure B.3.

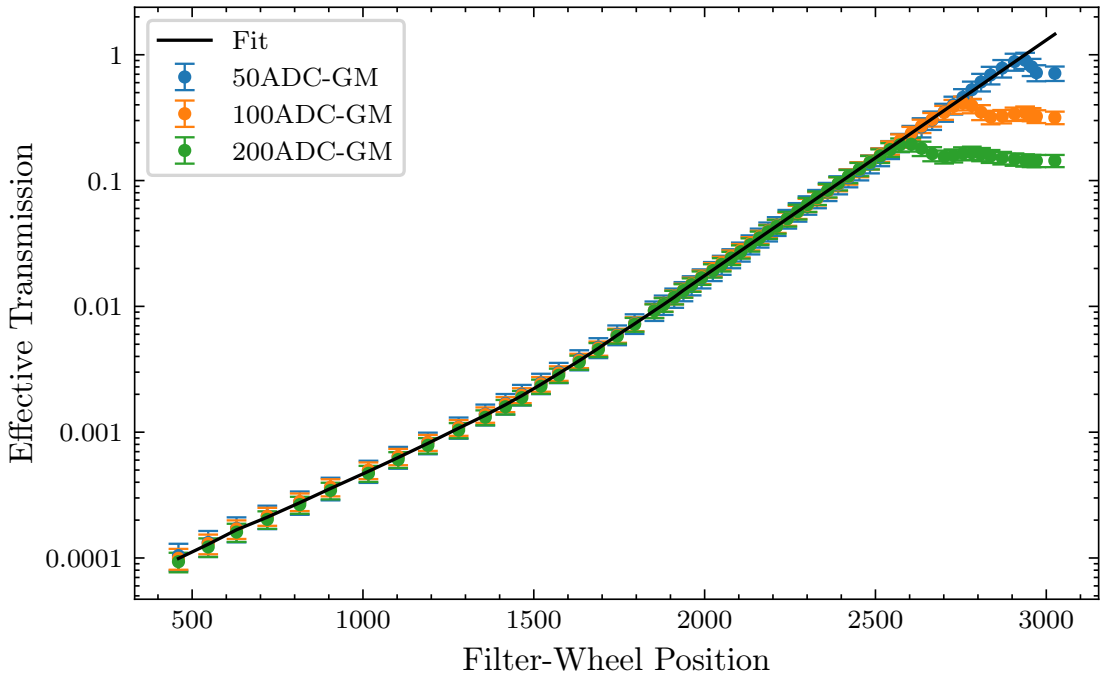


Figure B.3: The measured charges from Figure B.2 converted into an “effective transmission”, providing a filter-wheel calibration that is corrected for artefacts resulting from the first stage of calibration.

B.3 Illumination Profile

Two contributions influence the relative amount of light each pixel receives, depending on its position on the camera focal surface. The first is due to the laser uniformity characteristics, the second is due to the curved focal surface of the camera.

B.3.1 Laser Profile

Despite attempts to homogenise the illumination from the laser-diffuser combination, non-uniformities were still present in the light received at the camera pixels. These non-uniformities needed to be accounted for in the calibration of the laser illumination. A trench in laser illumination across the Y coordinate that could be approximated with a linear gradient was found. This was discovered by attaching a single silicon photomultiplier pixel to a robot arm, and placing it at the camera position in front of the laser. Through the use of a single pixel, the amplitude measured is disentangled from the relative PDE. This pixel was then moved to each x-y position to calculate the ratio in signal amplitude, returning back to the

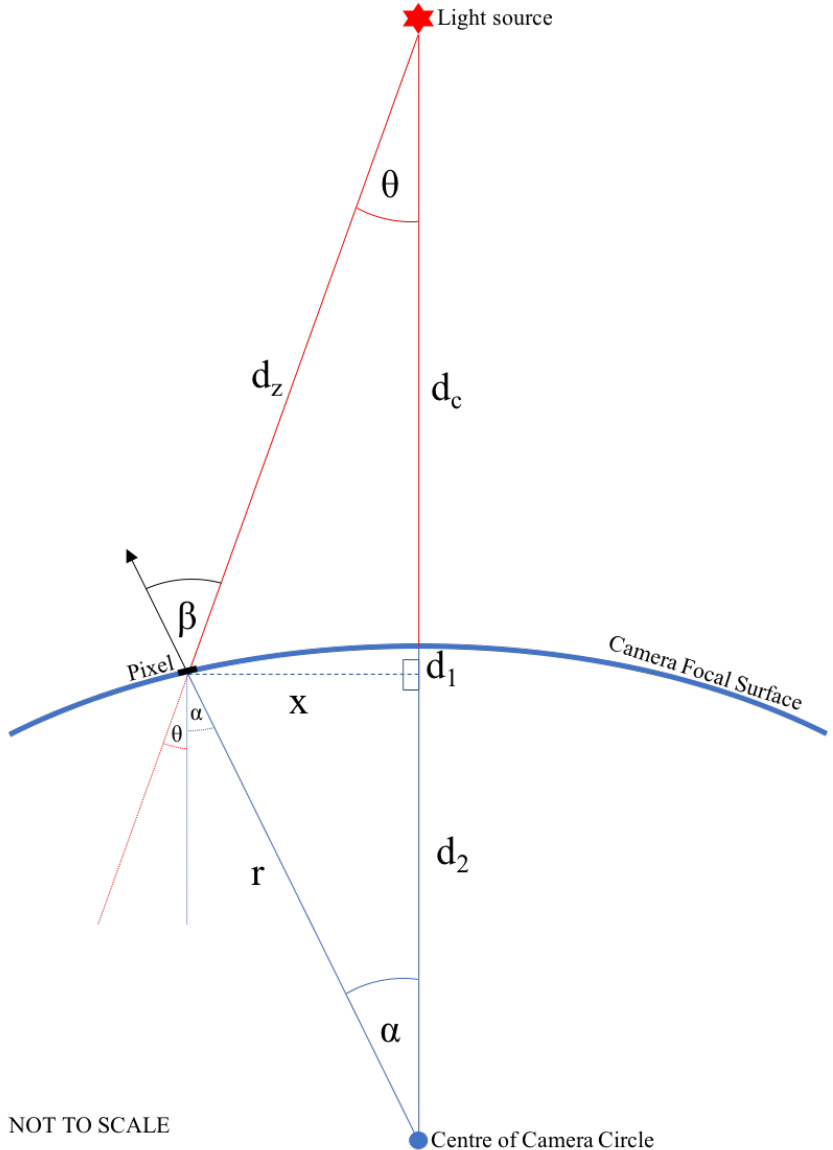


Figure B.4: Two-dimensional geometry schematic of the laboratory set-up for uniform camera illumination, used to calculate the reduction in light level for each pixel depending on its distance from the camera centre.

origin to obtain a fresh value for comparison, thereby correcting for any deviations that may have occurred due to a change in temperature. The resulting linear gradient across the camera is shown in Figure B.5a.

B.3.2 Camera Geometry

Due to the spherical camera focal surface, each pixel is at a different distance d_z from the light-source, and therefore receives a different amount of light depending on

its distance x from the camera centre. Furthermore, at a “viewing angle” β , i.e. the angle between the normal to the pixel and the light-source, the amount of surface area of the pixel A_P visible to the light-source is reduced. The visible surface area is known as the “viewing area” A_V . The combined geometric correction to the light intensity required to compensate for these effects is almost circularly symmetric, and therefore can be analytically approximated by using a two dimensional description of the camera, with a circular focal surface:

$$d_1 = r - d_2 = r - \sqrt{r^2 - x^2}, \quad (\text{B.1})$$

$$d_z = \sqrt{x^2 + (d_c + d_1)^2} = \sqrt{x^2 + (d_c + r - \sqrt{r^2 - x^2})^2}. \quad (\text{B.2})$$

$$\beta = \theta + \alpha = \sin^{-1} \frac{x}{d_z} + \sin^{-1} \frac{x}{r}, \quad (\text{B.3})$$

$$\frac{A_V}{A_P} = \cos \beta, \quad (\text{B.4})$$

$$\frac{I_x}{I_c} = \frac{d_z^2}{d_c^2} \times \cos \beta, \quad (\text{B.5})$$

where A_P is the pixel area, I_x is the intensity measured at the position of the pixel, I_c is the intensity measured at the centre of the camera, and the remaining distances and angles are shown in Figure B.4.

The resulting geometry corrections to the intensity for each pixel, arising from Equation B.5, can be seen in Figure B.5b.

B.3.3 Total Correction

The final illumination profile correction, combining both the laser profile and camera geometry, is shown in Figure B.5c. The description used for this calibration is only an approximation to the lab set-up. The following factors cause deviations from this model:

- The pixels are not precisely aligned on the spherical focal surface; the pixel angle is fixed to its module’s angle. The modules are aligned on the spherical focal surface.

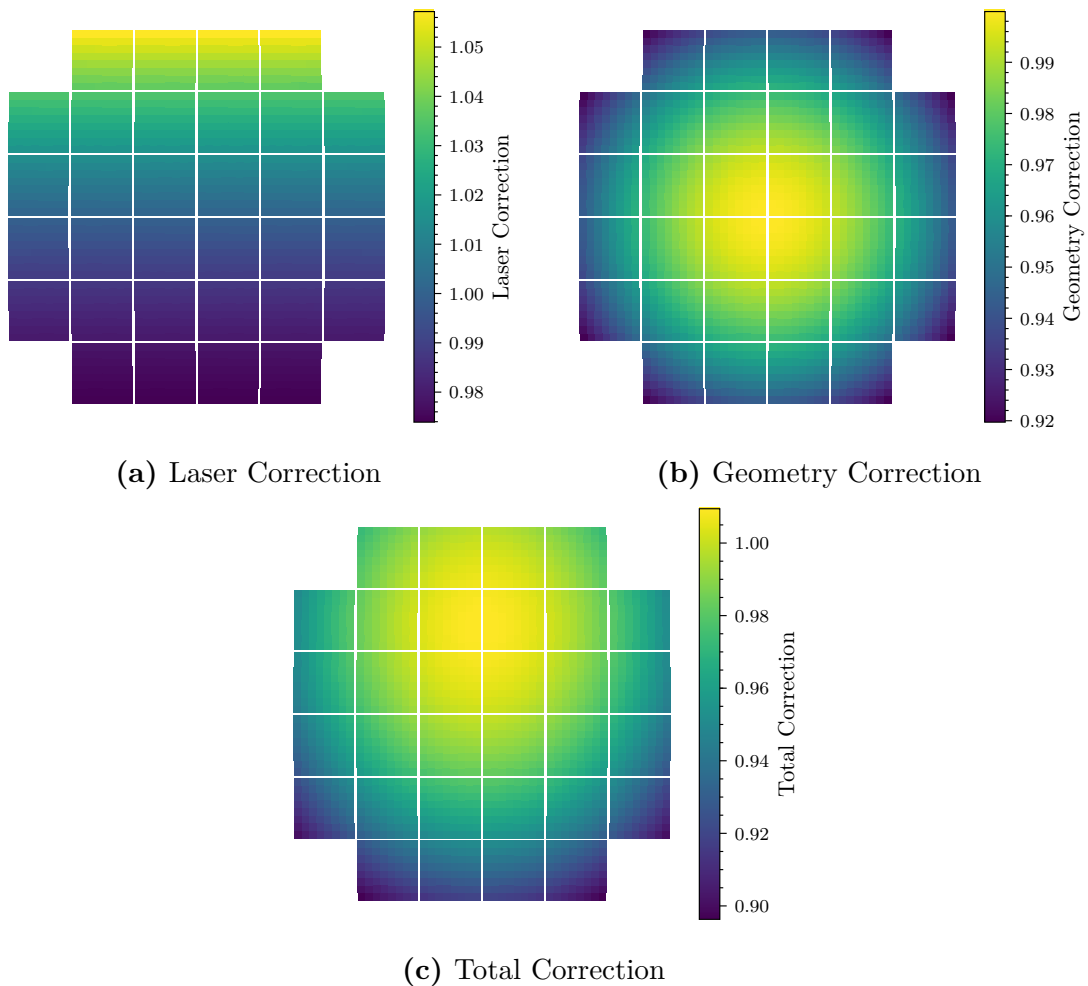


Figure B.5: The correction per pixel for the laser profile, camera geometry, and the combination of the two.

- The light source is not point-like. It produces a diffuse emission, which likely reflects along the walls of the box.

A future study could further improve on the models used for the illumination correction.

B.4 Absolute Illumination

The method adopted to obtain a value for the absolute illumination was to use a fit to the SPE spectrum resulting from low-amplitude illumination of the pixels. Contained within this fit is the average illumination parameter, λ . The concept of the SPE fit is further covered in Chapter 5 and Appendix C.

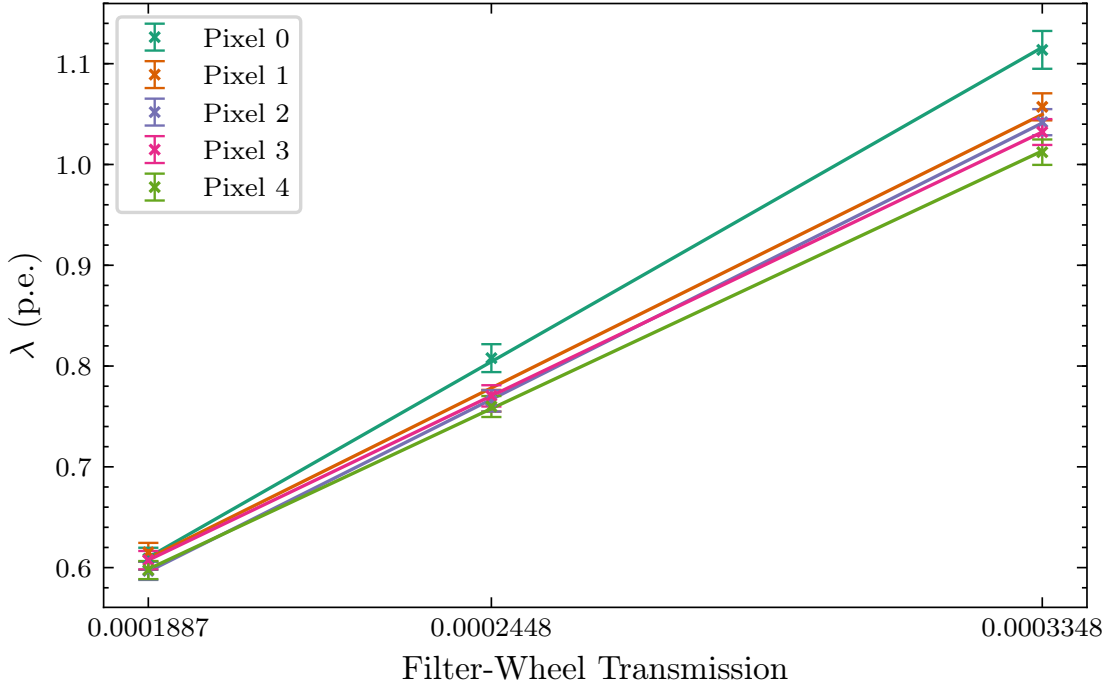


Figure B.6: Example of the linear regression to obtain the relationship between filter-wheel transmission and average illumination in photoelectrons (λ), for 5 pixels. The values of λ are obtained from the simultaneous fits to the SPE spectra (Appendix C). The error bars on the points are the 1σ parabolic errors obtained from the covariance matrix of the fit)

By simultaneously fitting three illuminations, we obtained three values of λ per pixel. With the three filter-wheel transmissions (corresponding to the three illuminations) on the x-axis, these values of λ were linearly regressed (weighted by the 1σ parabolic error of the fit, σ_λ) to obtain the gradient M_λ and y-intercept C_λ per pixel. This linear regression is shown in Figure B.6. The y-intercept represents the value of λ one would get with zero filter-wheel transmission, and therefore indicates the NSB and DCR. The variation in M_λ across the pixels arises from the folding of the illumination profile and the relative PDE. Therefore, the next step was to correct for the illumination profile contribution to the gradient. The resulting spread of M_λ is solely from the relative PDE. The calibration from filter-wheel transmission T_{FW} to the average illumination across the whole camera \bar{I}_{pe} is then obtained by taking the averages of the linear regression coefficients:

$$\bar{I}_{pe} = \bar{M}_\lambda T_{FW} + \bar{C}_\lambda, \quad (\text{B.6})$$

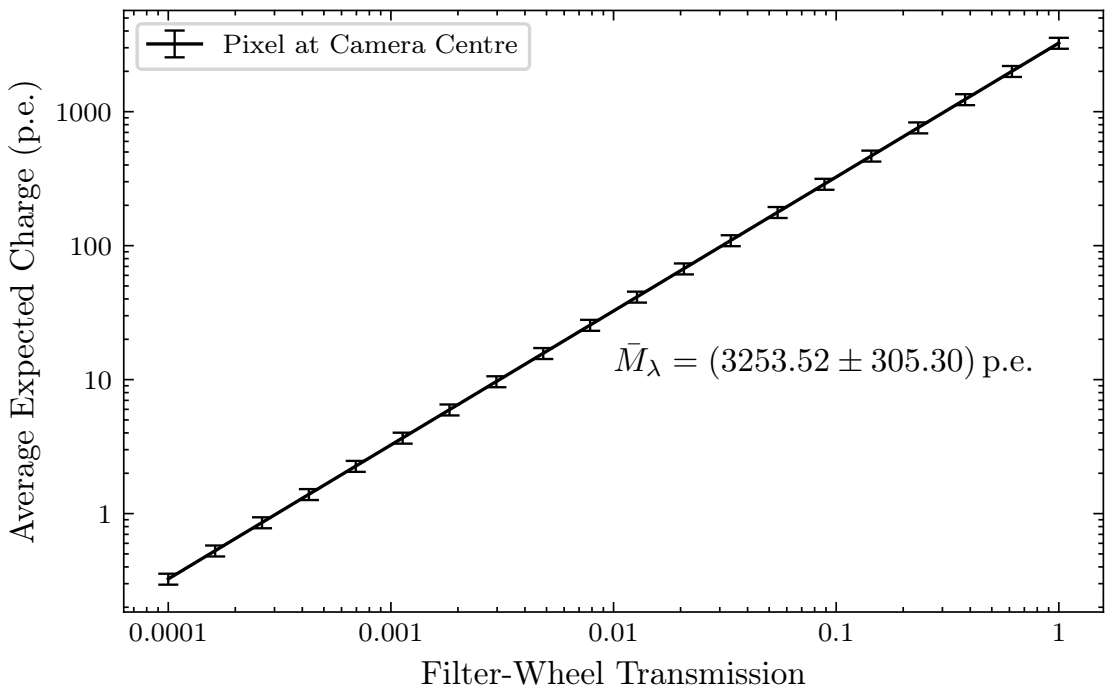


Figure B.7: Relationship between filter-wheel transmission and average expected charge in photoelectrons resulting from the filter-wheel calibration. The black line shows the conversion for a theoretical pixel positioned exactly at the camera centre. The error bars are calculated from the weighted standard deviation of the gradient estimates between the pixels, explained in Section B.6

B.5 Average Expected Charge

As we corrected for the NSB in the extracted signal value (Section 5.3), the NSB contribution to Equation B.6 (\bar{C}_λ) is subtracted to give us the charge we expect when illuminating the camera with a filter-wheel transmission T_{FW} , for a theoretical pixel perfectly positioned at the camera centre. This relation is shown in Figure B.7. To obtain the average expected charge Q_{Exp} for each true camera pixel, this relation must be folded with the illumination profile correction factor F_{pix} :

$$Q_{\text{Exp}} = \bar{M}_\lambda T_{\text{FW}} F_{\text{pix}}. \quad (\text{B.7})$$

This expression is important for the flat-fielding calibration (Chapter 5) and the calculation of the *Charge Resolution* for lab measurements (Chapter 7), as it tells us for a certain pixel and filter-wheel transmission, what charge we should expect to measure on average.

B.6 Consideration of Errors and Uncertainty

When performing the weighted linear regression between λ_i and filter-wheel transmission T_{FW_i} (with weights $w_i = \frac{1}{\sigma_{\lambda_i}^2}$ accounting for the parabolic error in λ_i), the standard error on the estimate of the gradient per pixel, σ_{M_λ} , can be calculated with the relation derived by Taylor [60]:

$$\sigma_{M_\lambda} = \sqrt{\frac{\sum w_i}{\sum w_i \sum w_i T_{FW_i}^2 - (\sum w_i T_{FW_i})^2}}, \quad i = 0, 1, 2, \dots, N. \quad (\text{B.8})$$

During the correction for the illumination profile on the gradient estimates, the illumination correction factors were also applied to the standard error on the gradient estimate.

While calculating the average gradient across the camera, \bar{M}_λ , the individual gradient estimates were weighted by their corresponding standard error. To calculate an uncertainty on the resulting value for \bar{M}_λ , the weighted standard deviation between the gradient estimates were also calculated. This uncertainty is illustrated in the error bars in Figure B.7. The resulting conversion value from filter wheel transmission to expected charge for a theoretical pixel located at the centre of the camera was calculated to be $\bar{M}_\lambda = (3253.76 \pm 305.32)$ p.e..

C

SPE Fitting

Contents

C.1	Introduction	164
C.2	Software	166
C.3	Multi-Anode Photomultiplier Tubes	166
C.4	Silicon Photomultipliers	168

C.1 Introduction

Due to the multiplicative process applied to a photoelectron in both MAPMTs and SiPMs, the resulting charge distribution is quantised according to the number of photoelectrons that were produced before the multiplication.

If an MAPMT or SiPM is illuminated to a very low light level (such that the photosensors perform as individual photon counters), and the resulting signal is accumulated inside a histogram, the distinct peaks corresponding to the detected number of photoelectrons are observed. The resolution of these peaks is determined by the ENF, as detailed in Section 2.2.5. This visualisation is known as the SPE spectrum, and it is a powerful tool utilised in the calibration of these photosensors.

The typical characteristics of the SPE spectrum are Gaussian peaks corresponding to each photoelectron, the height of which follow a Poisson distribution corresponding to the average illumination level that was present when taking the data.

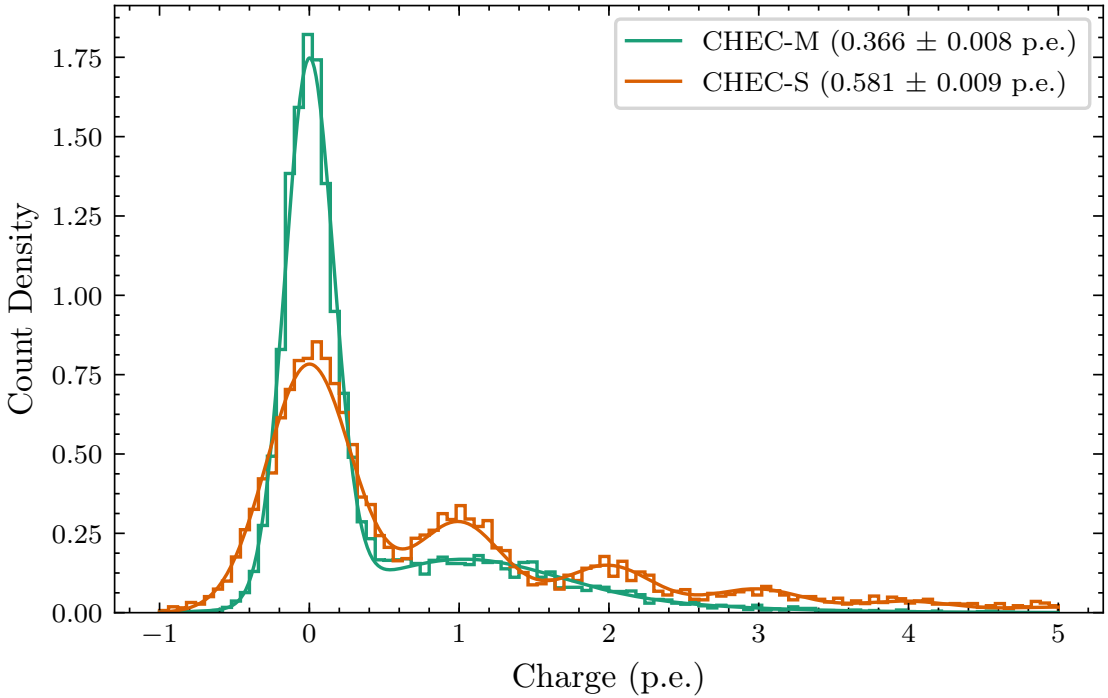


Figure C.1: Repeat of Figure 5.10. Comparison of SPE spectra between CHEC-M (MAPMT) and CHEC-S (SiPM) for a single pixel, along with their corresponding fit function. In both cases, three illuminations are simultaneously fit.

Typically, the following features from the SPE spectra can be extracted with simple approaches:

- The position and width of the pedestal peak, indicating the level of electronic noise.
- The position of the first photoelectron peak, suggesting the gain of the photosensor.
- The average illumination from the ratio of the pedestal to single photoelectron peak.

As is illustrated in Figure C.1, the resolution of the SPE peaks obtained from an MAPMT is much lower than that obtained from an SiPM, making it difficult to characterise the SPE spectrum by eye, or by simple fits using the aforementioned features. Additionally, many factors that contribute the SPE spectrum are hard to entangle. Therefore, an analytical description, that consolidates the contributing

Fit Parameter		CHEC-M	CHEC-S
Average Illumination	[p.e.]	0.366 ± 0.008	0.581 ± 0.009
Pedestal Deviation	[p.e.]	0.163 ± 0.001	0.285 ± 0.002
Gain Deviation	[p.e.]	0.626 ± 0.009	0.078 ± 0.007
Optical Crosstalk			0.350 ± 0.006

Table C.1: Parameter values resulting from the fit to the spectra in Figure C.1. The 1σ parabolic errors obtained from the covariance matrix of the fit parameters are also quoted.

factors of the photosensor to generate the SPE spectrum observed, is used to fit the histogram.

C.2 Software

The `extract_spe.py` script inside `CHECLabPy` allows the correct analytical function corresponding to the dataset to be chosen at runtime. It then utilises the `SpectrumFitter` class to flexibly fit N datasets of different illuminations simultaneously. This simultaneous fit helps to disentangle certain parameters. In the case of the SiPMs the optical crosstalk and average illumination are closely entangled, and a fit to a single illumination can have trouble providing accurate values. However, when increasing the average illumination, the optical crosstalk remains constant. The fit can therefore better constrain the difference each parameter contributes. Furthermore, the `extract_spe.py` script fits each pixel in parallel, considerably reducing the runtime.

C.3 Multi-Anode Photomultiplier Tubes

The behaviour of a PMT (which extends to MAPMTs) is very well understood, and is simple to quantify.

At an average illumination λ , there exists a probability to get either 0, 1, 2, 3... k photoelectrons, defined by the Poisson distribution:

$$P(k) = e^{-\lambda} \frac{\lambda^k}{k!}. \quad (\text{C.1})$$

The distribution of values from Equation C.1 are delta functions at each photoelectron value. This corresponds to the SPE spectrum you would measure for a perfect photosensor, with no electronic noise or ENF.

In the case $k = 0$ (the pedestal peak), the probability to measure a charge q (in mV, mVns, ADC, or p.e., depending on the calibration applied and the charge extraction approach used) is represented as a Gaussian with area $P(0)$, standard deviation σ_0 (representing the variation in electronic noise), and a mean μ_0 (as the baseline of the waveforms may not be corrected):

$$P(q) = e^{-\lambda} \frac{1}{\sqrt{2\pi\sigma_0^2}} e^{-\frac{(q-\mu_0)^2}{2\sigma_0^2}}. \quad (\text{C.2})$$

In the case $k > 0$, the mean and the standard deviation of the Gaussian increases with k . Additionally, the pedestal spread is also present in the $k > 0$ peaks. Therefore, the probability to measure a charge q is expressed as a Gaussian with area $P(k)$. The standard deviation $\sigma(k)$ is expressed as the quadrature sum of the two contributions:

$$\sigma(k) = \sqrt{\sigma_0^2 + k\sigma_1^2}, \quad (\text{C.3})$$

where σ_1 is the standard deviation in the multiplication of a single photoelectron. The mean $\mu(k)$ is the mean of the first photoelectron peak μ_1 multiplied by k . This results in the expression:

$$P(q, k) = P(k) \frac{1}{\sqrt{2\pi\sigma(k)^2}} e^{-\frac{(q-\mu(k))^2}{2\sigma(k)^2}}. \quad (\text{C.4})$$

The sum over each distribution of $P(q)$, for each value of k (I only go up to $k = 10$), gives the probability of getting each value of charge q . Combined with a normalisation factor, this equation can then be used to fit the spectrum of an MAPMT.

C.4 Silicon Photomultipliers

The analytical description for an SiPM is a bit more complicated. The formula we have found to work well is the one described by Gentile, Kuznetsova, and Meddi [88]. It expands on the formula I have described for MAPMTs to include the SiPM optical crosstalk and afterpulsing.

As with MAPMTs, the probability to get k initial photoelectrons (i.e. k initially fired microcells) follows a Poisson distribution. However, to find the probability of getting a total number of fired microcells n , the optical crosstalk probability ϵ , must be included:

$$P(n) = \sum_{k=1}^n P(k)(1 - \epsilon)^k \epsilon^{n-k} \binom{n-1}{k-1}. \quad (\text{C.5})$$

The formula for the probability of obtaining a charge q is also similar to the MAPMT case. However, two additional terms are included to account for two levels of afterpulsing, occurring at a reduced charge of δ_1 and δ_2 from the photoelectron peaks, each with a probability of that level of afterpulsing occurring. Due to the diminished afterpulsing probability in recent SiPM productions (Section 2.2.4), we removed the second level of afterpulsing from the fit, as we already get a very small value from using the first afterpulse level in the fit.

D

Transfer Function Investigations

Contents

D.1	Introduction	169
D.2	TF Generation Approaches	170
D.3	Charge Resolution	171
D.4	Sampling Cell versus Storage Cell	172
D.5	Conclusion	173

D.1 Introduction

In the upgrade from TARGET-5 to TARGET-C, the ability to internally set the Vped to a known voltage was lost. The approach adopted to replace the Transfer Function generation was to input pulses of the correct shape into the module from an external pulse generator. However, this approach can only be done for one module at the time, outside of the camera enclosure. As a result, we must rely on the Transfer Function data already taken for the generation of Transfer Functions for the TARGET modules currently installed in the CHEC-S prototype. However, there are different options for how to approach the second step in the AC Transfer Function generation (Chapter 5). This appendix will explore the performance I obtained with different expressions of the Transfer Function.

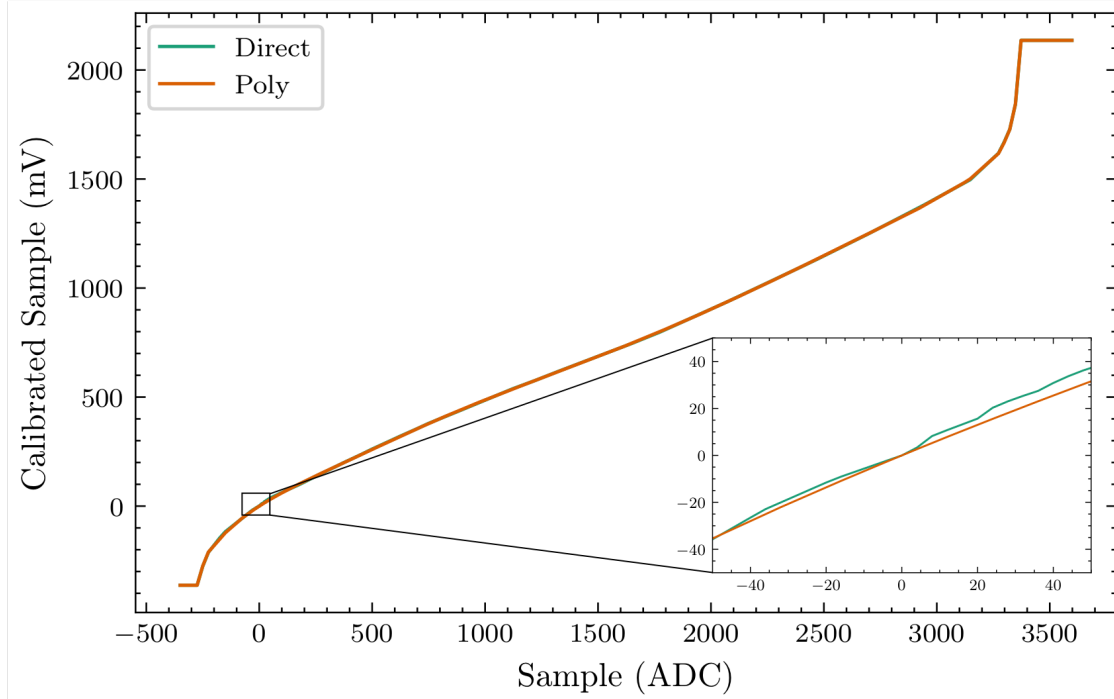


Figure D.1: Comparison of the *Poly* and *Direct* Transfer Function lookup tables, including a zoom at low amplitudes.

D.2 TF Generation Approaches

Four AC Transfer Function generation approaches are considered:

1. *Direct* - The values extracted from the waveforms are directly used, and a linear interpolation is performed to generate the lookup table.
2. *PCHIP* - The low amplitude values are ignored as the waveform fit may not have performed reliably at that level. A Piecewise Cubic Hermite Interpolating Polynomial (PCHIP) is used to generate the lookup table as opposed to a linear interpolation, resulting in a smooth function.
3. *Poly* - The Transfer Function of the *Direct* approach is regressed with a high order polynomial. In this exercise a 14th order polynomial was used, however a much lower polynomial is sufficient if the saturated region is ignored. The difference between the *Poly* and *Direct* Transfer Function lookup tables for a single cell are shown in Figure D.1. The zoom in the figure shows the much smoother function for the *Poly* approach.

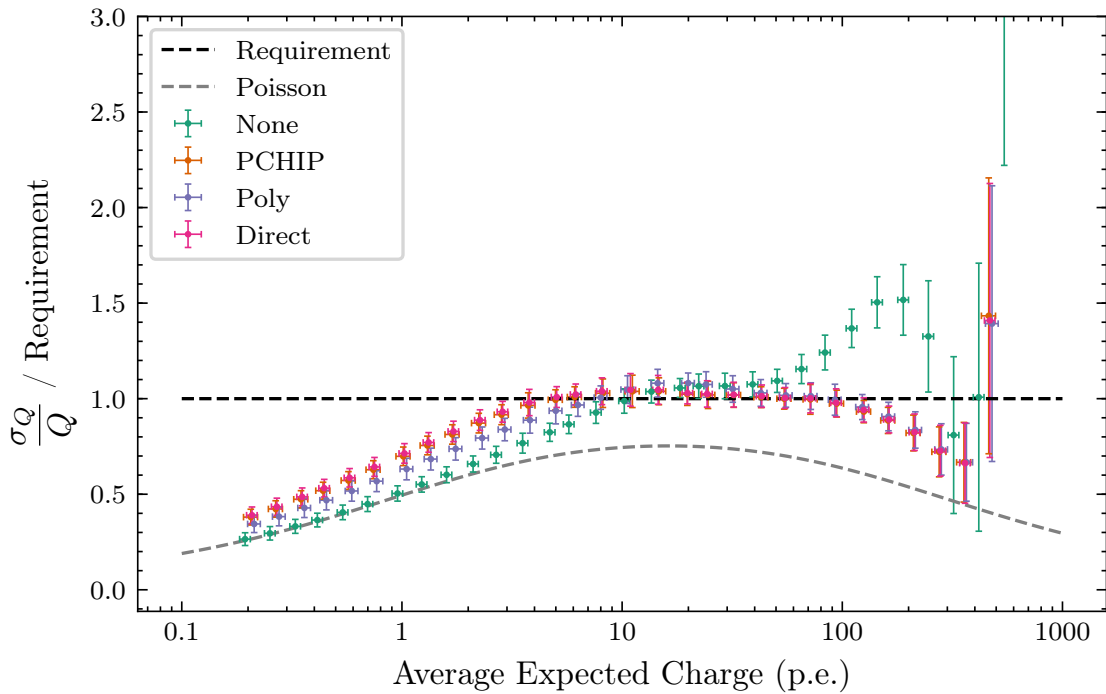


Figure D.2: Comparison of the *Charge Resolution* resulting from each of the Transfer Function generation approaches.

4. *None* - No Transfer Function calibration is applied. The pedestal subtraction calibration is still applied to the waveforms. Technically not a generation approach, but will give a benchmark to compare against.

D.3 Charge Resolution

The same dataset for the lab measurements shown in Chapter 7 is used, but the different Transfer Function lookup tables are applied for the waveform calibration in each case. The filter-wheel calibration, flat-field calibration and charge extraction is also re-performed for each Transfer Function. Figure D.2 compares the *Charge Resolution* result for each approach, allowing the following to be inferred:

- The PCHIP interpolation results in only a minor improvement over the linear interpolation used for the *Direct* approach.
- The use of a polynomial regression to express the Transfer appears to be the most successful Transfer Function approach.

- No significant difference between the generation approaches is observed above an average expected charge of 10 p.e., suggesting the performance above that value is not dominated by the Transfer Function calibration.
- The *Charge Resolution* in the absence of a Transfer Function calibration performs extremely well, approaching the poisson limit, for charges up to 30 p.e.. This result is significantly better than the results observed in all cases where a Transfer Function calibration was applied. This suggests the Transfer Function calibration, in its current form, is introducing an additional noise factor to the baseline.
- The *Charge Resolution* does perform significantly worse above an expected charge of 30 p.e. when no Transfer Function calibration is applied to the waveforms.

An ideal Transfer Function calibration would result in the low amplitude performance currently observed in the absence of the calibration, while retaining its linearity correction at higher amplitudes to maintain the performance. A Transfer Function calibration that only corrects large amplitudes may be a more favourable approach, therefore avoiding additional noise at the low amplitude level.

D.4 Sampling Cell versus Storage Cell

One further comparison approach performed for the Transfer Function calibration was between storing a lookup table per sampling cell or per storage cell. The former would result in 64 Transfer Functions per channel, the latter in 4,096 Transfer Functions per channel (for CHEC-S). The *Charge Resolution* results of this comparison are shown in Figure D.3. In both cases, the *Poly* approach for generating the lookup table was used.

Despite investigations performed by other CHEC members concluding that an improvement is found by considering a Transfer Function per storage cell, I observe no improvement in the *Charge Resolution* results. This discrepancy between

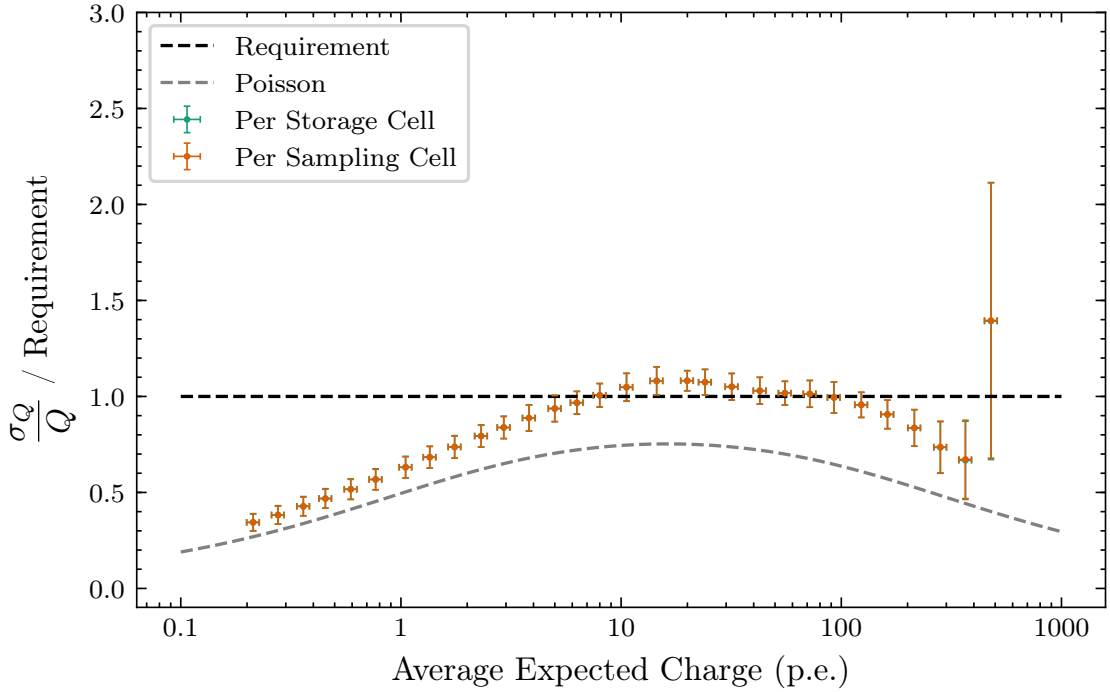


Figure D.3: Comparison of the *Charge Resolution* resulting from a Transfer Function calibration in which each sampling cell has its own lookup table, versus one where each storage cell has a lookup table.

my conclusion and the conclusion obtained by others is likely due to the other more dominating contributions to the *Charge Resolution*. Assuming a cell-level Transfer Function calibration is kept, this investigation should be repeated in future iterations of the CHEC prototype, as the reduction in the other contributions may make the relative difference between “per storage cell” and “per sampling cell” more significant. If no significant distinction is found, the “per sampling cell” should be used due to the less number of lookup tables required.

D.5 Conclusion

It was concluded from these results that the best Transfer Function calibration currently available for CHEC is provided by the *Poly* generation approach, with a lookup table stored per storage cell. Therefore, this was the calibration approach used for this thesis.

E

Charge Extractor Investigations

Contents

E.1	Introduction	174
E.2	Integration Window	174
E.2.1	Optimal Integration Window Parameters	175
E.2.2	Comparison with <i>Cross Correlation</i>	177
E.2.3	Conclusion	180

E.1 Introduction

In Chapter 6, the different algorithms for extracting charge from a waveform are extensively discussed, as well as the important considerations one must be vigilant of when producing a charge-extraction algorithm. The purpose of this appendix is to demonstrate the performance of the *Cross Correlation* charge-extraction method, in contrast a more simpler *Window Integration* approach. I performed this investigation in the context of the CHEC-S prototype.

E.2 Integration Window

As an alternative to the *Cross Correlation* integration approach, one may instead use a simple integration window, defined by the number of samples inside the “window width”, and the number of samples the window is “shifted” from the peak time. In order to investigate the performance of the integration-window approach fairly, one

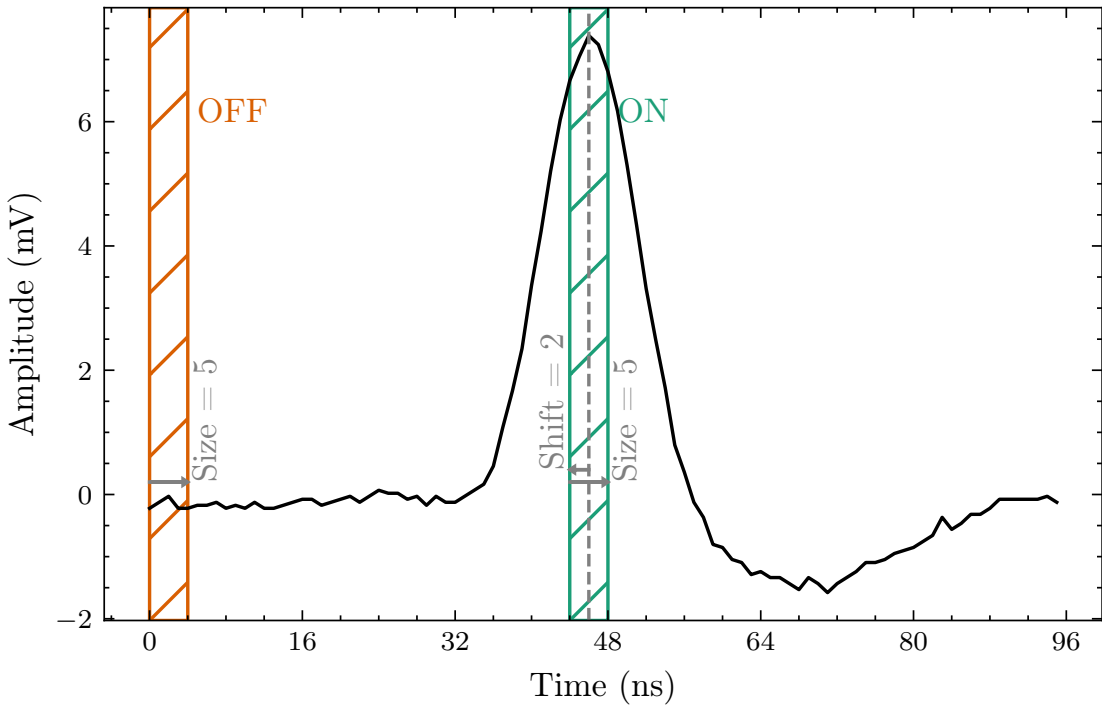


Figure E.1: Example waveform from a Monte Carlo simulation of CHEC-S, containing an approximately 50 p.e. signal. The “on” and “off” regions used to extract the signal-to-noise are illustrated. The window start position is defined as the peak position subtracted by the window shift. The window end position is defined as the window start plus the window size. A window size of 5 corresponds to 5 samples being included in the integration.

must first optimise the values for the width and shift of the window when extracting charge from a CHEC-S waveform. This exercise was performed using a Monte Carlo simulation of the lab set-up, where the camera was uniformly illuminated. The pulse time is consistent in simulations of this nature, therefore the same pulse time is manually chosen for every waveform. This allows the following investigation to be solely on the integration approach, avoiding any dependence on the peak finding.

E.2.1 Optimal Integration Window Parameters

As explained in Chapter 6, the optimal integration window parameters are noise dependant; a larger integration window is likely to include more noise (NSB and DCR). However, a larger window size results in more of the signal being captured. In Figure E.2 the signal-to-noise (S/N) as a function of integration-window parameters is shown for different amplitude and noise values. The S/N investigation was

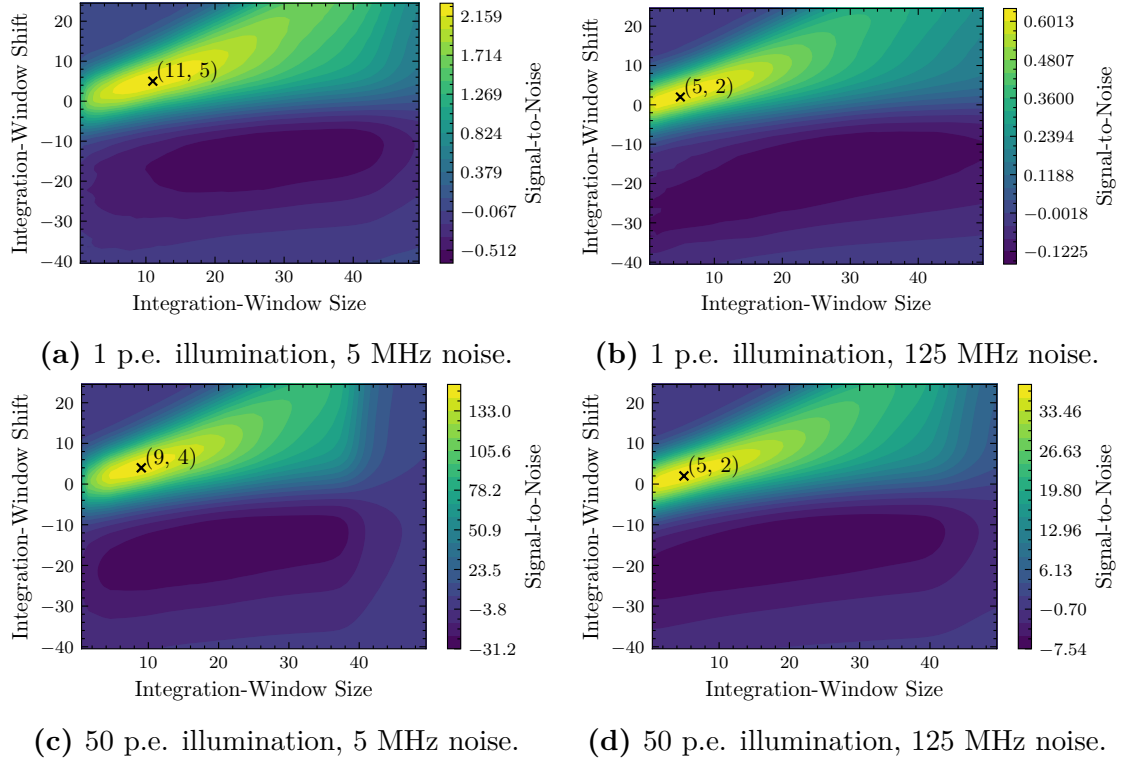


Figure E.2: Contour plot of signal-to-noise as a function of window width and shift, for different amplitudes and noise values. The maximum, annotated with the cross and position, indicates the optimal integration-window parameters when applied to a CHEC-S waveform. The definitions of window and shift are shown in Figure E.1. The contours are split into percentiles of the range; the top 5% of values are contained in the brightest yellow contour. Negative values correspond to an integration window concentrated on the undershoot of the pulse.

performed as follows. Assume an “on” region of the waveform, where the extracted value contains the signal plus the noise, and an “off” region where the extracted value contains solely the noise contributions (Figure E.1). The optimal window for a constant signal on top of a fluctuating background is then found by:

$$S/N = \frac{\mu_{\text{on}}}{\sigma_{\text{off}}}, \quad (\text{E.1})$$

where μ_{on} is the average signal extracted from the “on” region, and σ_{off} is the standard deviation of the signal extracted from the “off” region. The approach of Equation E.1 is an alternative to looking for the optimal window for a fluctuating signal on top of a fluctuating background ($S/N = \frac{\mu_{\text{on}}}{\sigma_{\text{on}}}$), which, due to the inclusion of the signal deviations from the “on” region, is much less sensitive to the noise

fluctuations and has a strong dependence on the signal level, i.e. the Poisson fluctuations of the signal increases with amplitude.

In Figure E.2 the conflict between a large window size to contain the full signal, and a small window to minimise noise is evident, resulting in a limited region in which a high signal-to-noise can be achieved. In conclusion, an integration window width of 5 samples and a shift of 2 samples appeared to be optimal for a noise of 125 MHz, for both small and large amplitudes (Figures E.2b and E.2d respectively). This integration window is demonstrated in Figure E.1. As the *Charge Resolution* requirements are defined at an NSB of 125 MHz, these window parameters are adopted for the following investigations.

E.2.2 Comparison with *Cross Correlation*

As described previously in the thesis, the most appropriate performance criterion for a charge extraction technique used for a CTA camera is the *Charge Resolution*. Outlined in Section 7.3.1 are the names I have defined to distinguish between different *Charge Resolution* procedures, each using different datasets and/or procedures. In order to evaluate the performance of the *Cross Correlation* technique with respect to a simple integration window, their resulting *Charge Resolutions* were compared in investigations that explore the relevant parameter space.

The first comparison is shown in Figure E.3. It explores the comparative performance in the context of the measurements using the *Lab* dataset (i.e. using the real camera). A small performance improvement is observed with the cross-correlation technique for $Q_{\text{Exp}} > 10$ p.e..

In a comparison of the two extraction approaches when used in a simulation using the CHEC-S model, shown in Figure E.4, it is evident that the *Cross Correlation* approach performs worse than the *Window Integration*, especially at higher NSB.

Figure E.5 shows a similar comparison to the previous one, however the optical crosstalk of the simulation model was reduced to 20 %. The result is an improved performance when using the *Cross Correlation* technique at low NSB rate. However, at high NSB, the *Window Integrator* performs slightly better.

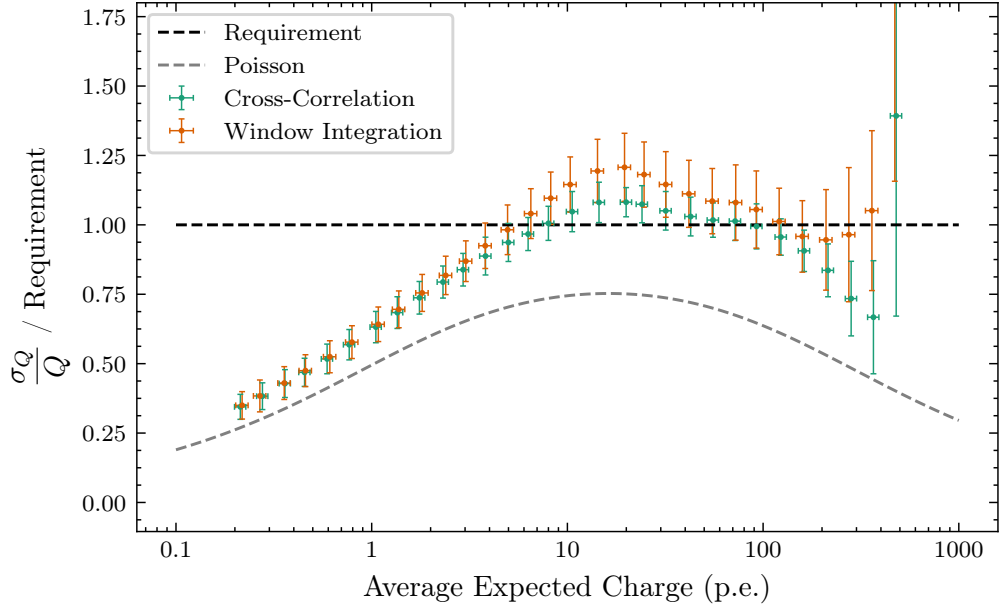


Figure E.3: *Charge Resolution* of the *Cross Correlation* charge extraction approach applied to uniformly illuminated lab data, compared to the *Charge Resolution* of the *Integration window* approach for the same dataset. The Y axis is limited to exclude the high values that arise from saturation.

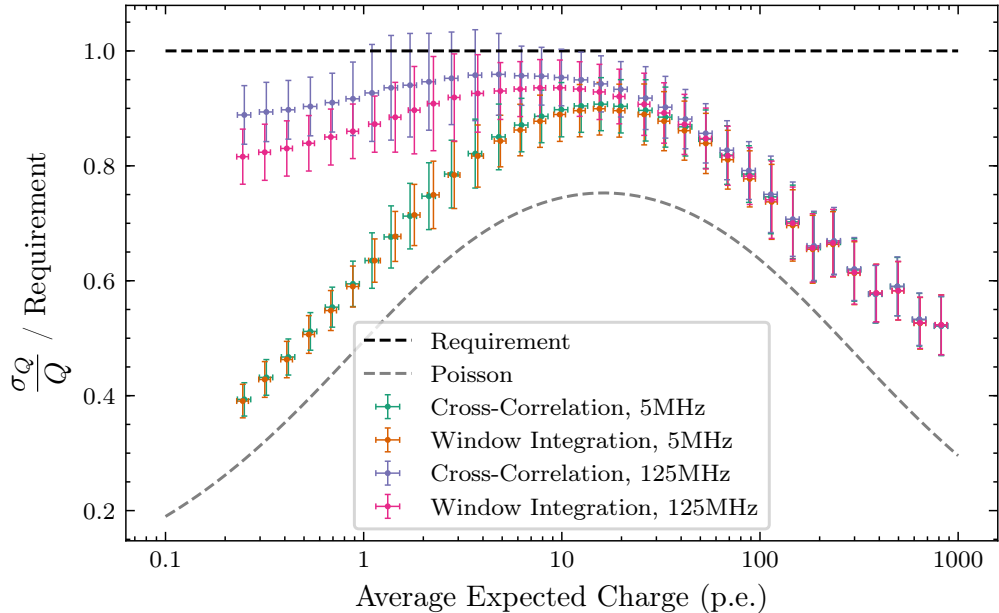


Figure E.4: *Charge Resolution* of the *Cross Correlation* charge extraction approach compared to the *Charge Resolution* of the integration window approach, for both 5 MHz and 125 MHz NSB noise. The dataset used is produced by Monte Carlo simulations of the camera uniformly illuminated, replicating the lab set-up (i.e. the *MCLab* procedure). The optical crosstalk of the photosensors in the simulation is 40 %.

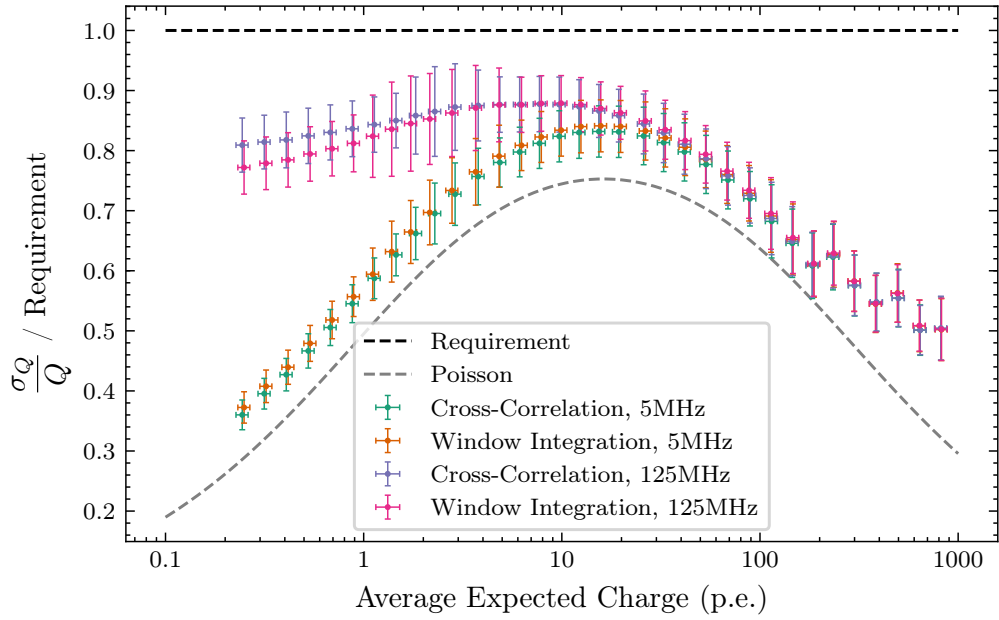


Figure E.5: Same as Figure E.4, but with a dataset containing an optical crosstalk value of 20 %.

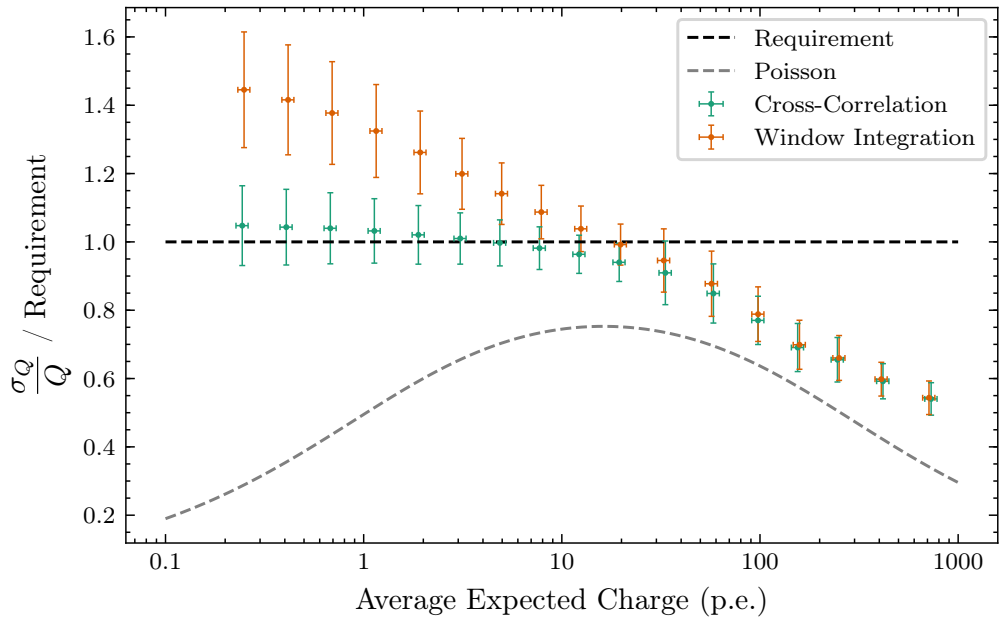


Figure E.6: Same as Figure E.4, but with a dataset containing a factor of 10 higher electronic noise.

Finally, in Figure E.6 a simulation of CHEC-S is used, but with a factor of 10 higher electronic noise. As a result, the *Cross Correlation* technique significantly improves the performance with respect to the *Window Integrator*.

E.2.3 Conclusion

The comparisons of *Charge Resolution* have confirmed our understanding of the *Cross Correlation* method:

- The *Cross Correlation* method amplifies anything correlated with reference pulse shape. This includes NSB and optical crosstalk factors. Therefore, when these are the dominant noise factors in the waveforms, the *Window Integrator* performs slightly better.
- When noise that is uncorrelated with the reference pulse shape is present in the waveform, such as a high amount of electronic noise, the *Cross Correlation* is an extremely useful tool to resolve the signal.

It would appear that with the current simulation model of CHEC-S, the major noise components are those correlated with the reference pulse shape. Therefore, not much improvement is available through the *Cross Correlation* technique. However, when the optical crosstalk of the SiPMs is lowered to 10 % (see Section 2.2.6), the other noise factors such as electronic noise could become a relatively significant contribution to the total noise (as occurs in Figure E.5). This would therefore justify the use of the *Cross Correlation* technique.

Despite the conclusion obtained from the simulations, there does appear to be an improvement when using the *Cross Correlation* method for measurements of the real camera (Figure E.3). The only likely source of uncorrelated noise at $Q_{\text{Exp}} > 10$ p.e. is from the residuals in the Transfer Function calibration. It would appear that the *Cross Correlation* method suppresses this additional noise component introduced by the calibration. As the Transfer Functions are not present in the simulations, this affect is not apparent in the *Charge Resolution* results obtained from them.

A further investigation into the actual parameter regions of Equation 3.2 which justify the use of the *Cross Correlation* approach is intended for the future.

References

- [1] J. V. Jelley. *Čerenkov radiation and its applications*. Pergamon Press, 1958. ISBN: 0080131271.
- [2] T. C. Weekes. *Very High Energy Gamma-Ray Astronomy*. Bristol and Philadelphia: Institute of Physics Publishing, 2003. ISBN: 0750306580.
- [3] A.M. Hillas. "Differences between gamma-ray and hadronic showers". In: *Space Science Reviews* 75.1-2 (Jan. 1996), pp. 17–30. ISSN: 0038-6308. DOI: 10.1007/BF00195021. URL: <http://link.springer.com/10.1007/BF00195021>.
- [4] Andrea De Franco. "Development of a Camera for Tera-electronVolt Gamma-ray Astronomy". DPhil. University of Oxford, 2016.
- [5] Aurelien Bouvier et al. "Photosensor characterization for the Cherenkov Telescope Array: silicon photomultiplier versus multi-anode photomultiplier tube". In: *SPIE Optical Engineering + Applications*. Ed. by Michael Fiederle et al. August. San Diego, California, United States, Sept. 2013, 88520K. ISBN: 9780819497024. DOI: 10.1117/12.2023778. arXiv: 1308.1390. URL: <http://dx.doi.org/10.1117/12.2023778>.
- [6] "CTA's expected baseline performance". [Online; accessed 26-09-2018]. URL: <https://www.cta-observatory.org/science/cta-performance>.
- [7] B.S. Acharya et al. "Introducing the CTA concept". In: *Astroparticle Physics* 43 (Mar. 2013), pp. 3–18. ISSN: 09276505. DOI: 10.1016/j.astropartphys.2013.01.007. URL: <http://linkinghub.elsevier.com/retrieve/pii/S0927650513000169>.
- [8] D. Marano et al. "Silicon Photomultipliers Electrical Model Extensive Analytical Analysis". In: *IEEE Transactions on Nuclear Science* 61.1 (Feb. 2014), pp. 23–34. ISSN: 0018-9499. DOI: 10.1109/TNS.2013.2283231. URL: <http://ieeexplore.ieee.org/document/6661445/>.
- [9] "Small-Sized Telescope". [Online; accessed 26-09-2018]. URL: <https://www.cta-observatory.org/project/technology/sst>.
- [10] E. Giro et al. "First optical validation of a Schwarzschild Couder telescope: the ASTRI SST-2M Cherenkov telescope". In: *Astronomy & Astrophysics* 608 (Dec. 2017), A86. ISSN: 0004-6361. DOI: 10.1051/0004-6361/201731602. arXiv: 1709.08418. URL: <http://dx.doi.org/10.1051/0004-6361/201731602>.
- [11] V. Vassiliev, S. Fegan, and P. Brousseau. "Wide field aplanatic two-mirror telescopes for ground-based γ -ray astronomy". In: *Astroparticle Physics* 28.1 (Sept. 2007), pp. 10–27. ISSN: 09276505. DOI: 10.1016/j.astropartphys.2007.04.002. arXiv: 0612718 [astro-ph]. URL: <http://dx.doi.org/10.1016/j.astropartphys.2007.04.002>.
- [12] The CTA Consortium. *Science with the Cherenkov Telescope Array*. WORLD SCIENTIFIC, Dec. 2018. ISBN: 978-981-327-008-4. DOI: 10.1142/10986. URL: <https://www.worldscientific.com/worldscibooks/10.1142/10986>.

- [13] Pierre Cristofari et al. “Supernova remnants in the very–high–energy sky: prospects for the Cherenkov Telescope Array”. In: *Proceedings of 35th International Cosmic Ray Conference — PoS(ICRC2017)*. Trieste, Italy: Sissa Medialab, Nov. 2017, p. 682. DOI: 10.22323/1.301.0682. arXiv: 1709.01900. URL: <https://pos.sissa.it/301/682>.
- [14] Ciro Bigongiari. “The Cherenkov Telescope Array”. In: *Nuclear and Particle Physics Proceedings* 279–281 (Oct. 2016), pp. 174–181. ISSN: 24056014. DOI: 10.1016/j.nuclphysbps.2016.10.025. arXiv: arXiv:1606.08190v1. URL: <https://linkinghub.elsevier.com/retrieve/pii/S2405601416302061>.
- [15] Cameron Rulten et al. “Simulating the optical performance of a small-sized telescope with secondary optics for the Cherenkov Telescope Array”. In: *Astroparticle Physics* 82 (Sept. 2016), pp. 36–48. ISSN: 09276505. DOI: 10.1016/j.astropartphys.2016.05.002. URL: <https://linkinghub.elsevier.com/retrieve/pii/S0927650516300652>.
- [16] J. J. Watson et al. “Inauguration and first light of the GCT-M prototype for the Cherenkov telescope array”. In: *AIP Conference Proceedings*. Vol. 1792. 2017, p. 080006. ISBN: 9780735414563. DOI: 10.1063/1.4969027. arXiv: 1610.01452. URL: <http://aip.scitation.org/doi/abs/10.1063/1.4969027>.
- [17] Hamamatsu. *Photomultiplier Tubes*. Technical Note, Accessed 20/09/2018. 2016, p. 129. URL: https://www.hamamatsu.com/resources/pdf/etd/PMT%7B%5C_%7DTPMZ0002E.pdf.
- [18] M L Knoetig et al. “FACT - Long-term stability and observations during strong Moon light”. In: *33rd International Cosmic Ray Conference (ICRC 2013)*. June. 2013, pp. 3–5. ISBN: 9788589064293. arXiv: arXiv:1307.6116v1. URL: <http://inspirehep.net/record/1244093/>.
- [19] Hamamatsu. *Photomultiplier Tubes: Basics and Applications*. Tech. rep. 2007. URL: https://www.hamamatsu.com/resources/pdf/etd/PMT%7B%5C_%7Dhandbook%7B%5C_%7Dv3aE.pdf.
- [20] Hamamatsu. *Flat panel type multianode PMT assembly H8500 series / H10966 series*. Technical Document, Accessed 20/09/2018. 2011. URL: https://www.hamamatsu.com/resources/pdf/etd/H8500%7B%5C_%7DH10966%7B%5C_%7DTPMH1327E.pdf.
- [21] D. Renker. “Geiger-mode avalanche photodiodes, history, properties and problems”. In: *Nuclear Instruments and Methods in Physics Research Section A: Accelerators, Spectrometers, Detectors and Associated Equipment* 567.1 (Nov. 2006), pp. 48–56. ISSN: 01689002. DOI: 10.1016/j.nima.2006.05.060. URL: <http://linkinghub.elsevier.com/retrieve/pii/S0168900206008680>.
- [22] A. Ghassemi, K. Sato, and K. Kobayashi. *MPPC*. Technical Note, Accessed 20/09/2018. 2017. URL: https://www.hamamatsu.com/resources/pdf/ssd/mppc%7B%5C_%7Dkapd9005e.pdf.
- [23] M. Heller et al. “An innovative silicon photomultiplier digitizing camera for gamma-ray astronomy”. In: *The European Physical Journal C* 77.1 (Jan. 2017), p. 47. ISSN: 1434-6044. DOI: 10.1140/epjc/s10052-017-4609-z. arXiv: 1607.03412. URL: <http://link.springer.com/10.1140/epjc/s10052-017-4609-z>.

- [24] Adrian Biland et al. “FACT - Status and Experience from Three Years Operation of the First SiPM Camera”. In: *Proceedings of The 34th International Cosmic Ray Conference — PoS(ICRC2015)*. Vol. 30-July-20. Trieste, Italy: Sissa Medialab, Aug. 2016, p. 1032. doi: 10.22323/1.236.1032. URL: <https://pos.sissa.it/236/1032>.
- [25] Hamamatsu. *S12642 DataSheet*. Data Sheet; Not publicly available. 2013.
- [26] SensL. *Introduction to SiPM*. Technical Note, Accessed 20/09/2018. 2011, pp. 1–16.
- [27] Ivan Rech et al. “Optical crosstalk in single photon avalanche diode arrays: a new complete model”. In: *Optics Express* 16.12 (June 2008), p. 8381. ISSN: 1094-4087. doi: 10.1364/OE.16.008381. URL: <https://www.osapublishing.org/oe/abstract.cfm?uri=oe-16-12-8381>.
- [28] S. Vinogradov. “Analytical models of probability distribution and excess noise factor of solid state photomultiplier signals with crosstalk”. In: *Nuclear Instruments and Methods in Physics Research Section A: Accelerators, Spectrometers, Detectors and Associated Equipment* 695 (Dec. 2012), pp. 247–251. ISSN: 01689002. doi: 10.1016/j.nima.2011.11.086. arXiv: 1109.2014. URL: <http://linkinghub.elsevier.com/retrieve/pii/S0168900211021565>.
- [29] M. Teich, Kuniaki Matsuo, and B. Saleh. “Excess noise factors for conventional and superlattice avalanche photodiodes and photomultiplier tubes”. In: *IEEE Journal of Quantum Electronics* 22.8 (Aug. 1986), pp. 1184–1193. ISSN: 0018-9197. doi: 10.1109/JQE.1986.1073137. URL: <http://ieeexplore.ieee.org/document/1073137/>.
- [30] W. J. Kindt, H. W. van Zeijl, and S. Middelhoe. “Optical Cross Talk in Geiger Mode Avalanche Photodiode Arrays: Modeling, Prevention and Measurement”. In: *28th European Solid-State Device Research Conference*. Bordeaux, France, 1998, pp. 192–195. URL: <http://ieeexplore.ieee.org/stamp/stamp.jsp?tp=%7B%5C%7Darnumber=1503521%7B%5C%7Disnumber=32252>.
- [31] R. Pagano et al. “Optimized silicon photomultipliers with optical trenches”. In: *2011 Proceedings of the European Solid-State Device Research Conference (ESSDERC)*. IEEE, Sept. 2011, pp. 183–186. ISBN: 978-1-4577-0707-0. doi: 10.1109/ESSDERC.2011.6044204. URL: <http://ieeexplore.ieee.org/document/6044204/>.
- [32] Hamamatsu. *MPPC : S14521-8648 (bare type) Specification Sheet*. Data Sheet; Not publicly available. 2018.
- [33] Hamamatsu. *MPPC : S14521-8649(resin type) Specification Sheet*. Data Sheet; Not publicly available. 2018.
- [34] J. Zorn et al. “Characterisation and testing of CHEC-M—A camera prototype for the small-sized telescopes of the Cherenkov telescope array”. In: *Nuclear Instruments and Methods in Physics Research Section A: Accelerators, Spectrometers, Detectors and Associated Equipment* 904 (Oct. 2018), pp. 44–63. ISSN: 01689002. doi: 10.1016/j.nima.2018.06.078. arXiv: 1806.11308. URL: <https://linkinghub.elsevier.com/retrieve/pii/S0168900218308143>.

- [35] Andrea De Franco. “The first GCT camera for the Cherenkov Telescope Array.” In: *Proceedings of The 34th International Cosmic Ray Conference — PoS(ICRC2015)*. Trieste, Italy: Sissa Medialab, Aug. 2016, p. 1015. doi: 10.22323/1.236.1015. URL: <https://pos.sissa.it/236/1015>.
- [36] Richard White. “CHEC: a Compact High Energy Camera for the Cherenkov Telescope Array”. In: *Journal of Instrumentation* 12.12 (Dec. 2017), pp. C12059–C12059. ISSN: 1748-0221. doi: 10.1088/1748-0221/12/12/C12059. arXiv: 1712.00354. URL: <http://stacks.iop.org/1748-0221/12/i=12/a=C12059?key=crossref.c5160d771b5f8af8a5917164c6d2c0ae>.
- [37] S. Funk et al. “TARGET: A digitizing and trigger ASIC for the Cherenkov telescope array”. In: *AIP Conference Proceedings*. Vol. 1792. 2017, p. 080012. ISBN: 9780735414563. doi: 10.1063/1.4969033. arXiv: 1610.01536. URL: <http://aip.scitation.org/doi/abs/10.1063/1.4969033>.
- [38] A. Albert et al. “TARGET 5: A new multi-channel digitizer with triggering capabilities for gamma-ray atmospheric Cherenkov telescopes”. In: *Astroparticle Physics* 92 (June 2017), pp. 49–61. ISSN: 09276505. doi: 10.1016/j.astropartphys.2017.05.003. arXiv: 1607.02443. URL: <https://linkinghub.elsevier.com/retrieve/pii/S0927650517301524>.
- [39] Anthony Brown et al. “Flasher and muon-based calibration of the GCT telescopes proposed for the Cherenkov Telescope Array”. In: *Proceedings of The 34th International Cosmic Ray Conference — PoS(ICRC2015)*. Vol. 30-July-20. Trieste, Italy: Sissa Medialab, Aug. 2016, p. 934. doi: 10.22323/1.236.0934. arXiv: 1509.00185. URL: <https://pos.sissa.it/236/934>.
- [40] Francesco Dazzi et al. *CTA Architecture*. Internal Document (V1.0). CTA Observatory, 2018.
- [41] “*Countries and Institutes in CTA Consortium*”. [Online; accessed 20-07-2018]. URL: <https://www.cta-observatory.org/about/cta-consortium/>.
- [42] “*Shareholders and Associate Members of CTAO gGmbH*”. [Online; accessed 20-07-2018]. URL: <https://www.cta-observatory.org/about/governance/>.
- [43] *CTA Requirements*. [Online; accessed 18-07-2018]. URL: <https://jama.cta-observatory.org>.
- [44] Alison Mitchell and Jim Hinton. *SYS-REQ/180326: Photoelectrons to Photons in Camera Performance Requirements*. Internal Document (Draft V1.0). CTA Observatory, 2018.
- [45] Stefan Ohm and Jim Hinton. *SCI-MC/121113: Impact of measurement errors on charge resolution and system performance*. Internal Document (V1.1). CTA Observatory, 2012.
- [46] Karl Kosack et al. *CTA High-Level Data Model Definitions*. Internal Document (Draft V0.3). CTA Observatory, 2017.
- [47] K. Bernlöhr et al. “Monte Carlo design studies for the Cherenkov Telescope Array”. In: *Astroparticle Physics* 43 (Mar. 2013), pp. 171–188. ISSN: 09276505. doi: 10.1016/j.astropartphys.2012.10.002. arXiv: 1210.3503 [astro-ph.IM]. URL: <http://dx.doi.org/10.1016/j.astropartphys.2012.10.002>.

- [48] Konrad Bernlöhr. “Simulation of imaging atmospheric Cherenkov telescopes with CORSIKA and sim_telarray”. In: *Astroparticle Physics* 30.3 (Oct. 2008), pp. 149–158. ISSN: 09276505. DOI: 10.1016/j.astropartphys.2008.07.009. arXiv: 0808.2253. URL: <http://linkinghub.elsevier.com/retrieve/pii/S0927650508000972>.
- [49] D Heck et al. *CORSIKA: A Monte Carlo Code to Simulate Extensive Air Showers*. Vol. FZKA 6019. FZKA-6019. FZKA, 1998, pp. 1–90. URL: <http://inspirehep.net/record/469835>.
- [50] Stéfan van der Walt, S. Chris Colbert, and Gaël Varoquaux. “The NumPy Array: A Structure for Efficient Numerical Computation”. In: *Computing in Science & Engineering* 13.2 (Mar. 2011), pp. 22–30. ISSN: 1521-9615. DOI: 10.1109/MCSE.2011.37. arXiv: 1102.1523. URL: <http://ieeexplore.ieee.org/document/5725236/>.
- [51] A. Balzer et al. “The H.E.S.S. central data acquisition system”. In: *Astroparticle Physics* 54 (Feb. 2014), pp. 67–80. ISSN: 09276505. DOI: 10.1016/j.astropartphys.2013.11.007. arXiv: arXiv:1311.3486v1. URL: <http://dx.doi.org/10.1016/j.astropartphys.2013.11.007>.
- [52] A.U. Abeysekara et al. “Data acquisition architecture and online processing system for the HAWC gamma-ray observatory”. In: *Nuclear Instruments and Methods in Physics Research Section A: Accelerators, Spectrometers, Detectors and Associated Equipment* 888.January (Apr. 2018), pp. 138–146. ISSN: 01689002. DOI: 10.1016/j.nima.2018.01.051. arXiv: 1709.03751. URL: <https://linkinghub.elsevier.com/retrieve/pii/S0168900218300688>.
- [53] E Gamma et al. *Design Patterns: Elements of Reusable Software*. Addison-Wesley professional computing series. Addison-Wesley, 1996, p. 395. ISBN: 0201633612. URL: <https://books.google.co.uk/books?id=vRfxugEACAAJ>.
- [54] R.D. Parsons and J.A. Hinton. “A Monte Carlo template based analysis for air-Cherenkov arrays”. In: *Astroparticle Physics* 56 (Apr. 2014), pp. 26–34. ISSN: 09276505. DOI: 10.1016/j.astropartphys.2014.03.002. arXiv: 1403.2993. URL: <http://dx.doi.org/10.1016/j.astropartphys.2014.03.002>.
- [55] Christoph Deil et al. “Gammapy - A prototype for the CTA science tools”. In: *Proceedings of 35th International Cosmic Ray Conference — PoS(ICRC2017)*. Trieste, Italy: Sissa Medialab, Aug. 2017, p. 766. DOI: 10.22323/1.301.0766. arXiv: 1709.01751. URL: <https://pos.sissa.it/301/766>.
- [56] D. Berge, S. Funk, and J. Hinton. “Background modelling in very-high-energy γ -ray astronomy”. In: *Astronomy & Astrophysics* 466.3 (May 2007), pp. 1219–1229. ISSN: 0004-6361. DOI: 10.1051/0004-6361:20066674. arXiv: 0610959 [astro-ph]. URL: <http://dx.doi.org/10.1051/0004-6361:20066674>.
- [57] J. Knöldlseder et al. “GammaLib and ctools”. In: *Astronomy & Astrophysics* 593 (Sept. 2016), A1. ISSN: 0004-6361. DOI: 10.1051/0004-6361/201628822. arXiv: 1606.00393. URL: <http://dx.doi.org/10.1051/0004-6361/201628822>.
- [58] K. Bechtol et al. “TARGET: A multi-channel digitizer chip for very-high-energy gamma-ray telescopes”. In: *Astroparticle Physics* 36.1 (Aug. 2012), pp. 156–165. ISSN: 09276505. DOI: 10.1016/j.astropartphys.2012.05.016. arXiv: 1105.1832. URL: <http://dx.doi.org/10.1016/j.astropartphys.2012.05.016>.

- [59] F. Aharonian et al. “Calibration of cameras of the H.E.S.S. detector”. In: *Astroparticle Physics* 22.2 (Nov. 2004), pp. 109–125. ISSN: 09276505. DOI: 10.1016/j.astropartphys.2004.06.006. arXiv: 0408145 [astro-ph]. URL: <http://linkinghub.elsevier.com/retrieve/pii/S0927650504001227>.
- [60] J. R. Taylor. *An introduction to error analysis : the study of uncertainties in physical measurements*. 2nd. Sausalito, Calif. : University Science Books, 1997, pp. 181–199. ISBN: 978-0935702101.
- [61] T. C. Weekes et al. “Observation of TeV gamma rays from the Crab nebula using the atmospheric Cerenkov imaging technique”. In: *The Astrophysical Journal* 342 (July 1989), p. 379. ISSN: 0004-637X. DOI: 10.1086/167599. URL: <http://adsabs.harvard.edu/doi/10.1086/167599>.
- [62] Idan Shilon et al. “Application of Deep Learning methods to analysis of Imaging Atmospheric Cherenkov Telescopes data”. In: March (2018). arXiv: 1803.10698. URL: <http://arxiv.org/abs/1803.10698>.
- [63] J. Holder. “Exploiting VERITAS Timing Information”. In: *29th International Cosmic Ray Conference (ICRC 2005)*. January. 2005, pp. 383–386. arXiv: 0507450 [astro-ph]. URL: <http://arxiv.org/abs/astro-ph/0507450>.
- [64] Peter Cogan. “Nanosecond Sampling of Atmospheric Cherenkov Radiation Applied to TeV Gamma-Ray Observations of Blazars with VERITAS”. Ph.D. University College Dublin, 2006.
- [65] P. Cogan and for the VERITAS Collaboration. “Analysis of Flash ADC Data With VERITAS”. In: *30th International Cosmic Ray Conference (ICRC 2007)*. Vol. 3. Merida, Yucatan, Mexico, 2007, pp. 1369–1372. arXiv: 0709.4208. URL: <http://arxiv.org/abs/0709.4208>.
- [66] Eric W. Weisstein. *"Cross-Correlation." From MathWorld—A Wolfram Web Resource*. [Online; accessed 20-07-2018]. URL: <http://mathworld.wolfram.com/Cross-Correlation.html>.
- [67] SciPy: Open source scientific tools for Python: `scipy.ndimage.correlate1d`. [Online; accessed 20-07-2018]. URL: <https://docs.scipy.org/doc/scipy/reference/generated/scipy.ndimage.correlate1d.html>.
- [68] J. Albert et al. “FADC signal reconstruction for the MAGIC telescope”. In: *Nuclear Instruments and Methods in Physics Research Section A: Accelerators, Spectrometers, Detectors and Associated Equipment* 594.3 (Sept. 2008), pp. 407–419. ISSN: 01689002. DOI: 10.1016/j.nima.2008.06.043. arXiv: 0612385 [astro-ph]. URL: <http://linkinghub.elsevier.com/retrieve/pii/S0168900208009091>.
- [69] Stefan Klepser et al. “Hardware and software architecture of the upgraded H.E.S.S. cameras”. In: *Proceedings of 35th International Cosmic Ray Conference — PoS(ICRC2017)*. Trieste, Italy: Sissa Medialab, Aug. 2017, p. 834. DOI: 10.22323/1.301.0834. arXiv: 1708.04550. URL: <https://pos.sissa.it/301/834>.

- [70] Raphaël Chalmé-Calvet et al. “Exploiting the time of arrival of Cherenkov photons at the 28 m H.E.S.S. telescope for background rejection: Methods and performance”. In: *Proceedings of The 34th International Cosmic Ray Conference — PoS(ICRC2015)*. Vol. 30-July-20. Trieste, Italy: Sissa Medialab, Aug. 2016, p. 842. DOI: 10.22323/1.236.0842. arXiv: 1509.03544. URL: <https://pos.sissa.it/236/842>.
- [71] D. Impiombato et al. “Procedures for the relative calibration of the SiPM gain on ASTRI SST-2M camera”. In: *Experimental Astronomy* 43.1 (Feb. 2017), pp. 1–17. ISSN: 0922-6435. DOI: 10.1007/s10686-016-9516-z. arXiv: 1612.02186. URL: <http://link.springer.com/10.1007/s10686-016-9516-z>.
- [72] AM Hillas. “Cerenkov light images of EAS produced by primary gamma”. In: *International Cosmic Ray Conference* (1985). URL: <http://adsabs.harvard.edu/abs/1985ICRC....3..445H>.
- [73] P. T. Reynolds et al. “Survey of candidate gamma-ray sources at TeV energies using a high-resolution Cerenkov imaging system - 1988-1991”. In: *The Astrophysical Journal* 404 (Feb. 1993), p. 206. ISSN: 0004-637X. DOI: 10.1086/172269. URL: <http://adsabs.harvard.edu/doi/10.1086/172269>.
- [74] A. Daum et al. “First results on the performance of the HEGRA IACT array”. In: *Astroparticle Physics* 8.1-2 (Dec. 1997), pp. 1–11. ISSN: 09276505. DOI: 10.1016/S0927-6505(97)00031-5. arXiv: 9704098 [astro-ph]. URL: <http://linkinghub.elsevier.com/retrieve/pii/S0927650597000315>.
- [75] John Hugh Dickinson. “Very High Energy Gamma-Rays from Binary Systems”. DPhil. Durham University, 2010.
- [76] Stefan Eschbach et al. “Studies towards an understanding of global array pointing for the Cherenkov Telescope Array”. In: *Proceedings of The 34th International Cosmic Ray Conference — PoS(ICRC2015)*. Trieste, Italy: Sissa Medialab, Aug. 2016, p. 1025. DOI: 10.22323/1.236.1025. URL: <https://pos.sissa.it/236/1025>.
- [77] R.W. Lessard et al. “A new analysis method for reconstructing the arrival direction of TeV gamma rays using a single imaging atmospheric Cherenkov telescope”. In: *Astroparticle Physics* 15.1 (Mar. 2001), pp. 1–18. ISSN: 09276505. DOI: 10.1016/S0927-6505(00)00133-X. arXiv: 0005468 [astro-ph]. URL: <http://linkinghub.elsevier.com/retrieve/pii/S092765050000133X>.
- [78] David J. Fegan. “gamma/hadron separation at TeV energies”. In: *Journal of Physics G: Nuclear and Particle Physics* 23.9 (Sept. 1997), pp. 1013–1060. ISSN: 0954-3899. DOI: 10.1088/0954-3899/23/9/004. URL: <http://stacks.iop.org/0954-3899/23/i=9/a=004?key=crossref.6d9048310a121dd1ec40ab2f50efd418>.
- [79] S Ohm, C. van Eldik, and K Egberts. “ γ /hadron separation in very-high-energy γ -ray astronomy using a multivariate analysis method”. In: *Astroparticle Physics* 31.5 (June 2009), pp. 383–391. ISSN: 09276505. DOI: 10.1016/j.astropartphys.2009.04.001. arXiv: arXiv:0904.1136v1. URL: <http://linkinghub.elsevier.com/retrieve/pii/S0927650509000589>.

-
- [80] A. Okumura. *The Prototype of Gamma-ray Cherenkov Telescope (GCT) of the Cherenkov Telescope Array (CTA)*. [Online Image; accessed 16-09-2018]. Dec. 2015. URL: <https://www.flickr.com/photos/akiraokumura/23472763315>.
 - [81] A. Okumura. *The Prototype of Gamma-ray Cherenkov Telescope (GCT) of the Cherenkov Telescope Array (CTA)*. [Online Image; accessed 16-09-2018]. Dec. 2015. URL: <https://www.flickr.com/photos/akiraokumura/23150523890>.
 - [82] M. Punch et al. “Detection of TeV photons from the active galaxy Markarian 421”. In: *Nature* 358.6386 (Aug. 1992), pp. 477–478. ISSN: 00280836. DOI: 10.1038/358477a0. URL: <http://www.nature.com/doifinder/10.1038/358477a0>.
 - [83] J. Quinn et al. “Detection of Gamma Rays with $E > 300$ GeV from Markarian 501”. In: *The Astrophysical Journal* 456.2 (Jan. 1996), pp. 83–86. ISSN: 0004637X. DOI: 10.1086/309878. URL: <http://stacks.iop.org/1538-4357/456/i=2/a=L83>.
 - [84] Markus Gaug et al. “Calibration strategies for the Cherenkov Telescope Array”. In: ed. by Alison B. Peck, Chris R. Benn, and Robert L. Seaman. July. Aug. 2014, p. 914919. ISBN: 9780819496171. DOI: 10.1117/12.2054536. URL: <http://proceedings.spiedigitallibrary.org/proceeding.aspx?doi=10.1117/12.2054536>.
 - [85] Thomas Armstrong et al. “Monte Carlo Studies of the Gamma-ray Cherenkov Telescope for the Cherenkov Telescope Array”. In: *Proceedings of The 34th International Cosmic Ray Conference — PoS(ICRC2015)*. Trieste, Italy: Sissa Medialab, Aug. 2016, p. 942. DOI: 10.22323/1.236.0942. arXiv: 1508.06088. URL: <https://pos.sissa.it/236/942>.
 - [86] Maria Concetta Maccarone. “ASTRI for the Cherenkov Telescope Array”. In: *Proceedings of 35th International Cosmic Ray Conference — PoS(ICRC2017)*. Trieste, Italy: Sissa Medialab, Aug. 2017, p. 855. DOI: 10.22323/1.301.0855. arXiv: 1709.03078. URL: <https://pos.sissa.it/301/855>.
 - [87] N Otte. “The Silicon Photomultiplier-A new device for High Energy Physics, Astroparticle Physics, Industrial and Medical Applications”. In: *International Symposium on Detector Development for Particle, Astroparticle and Synchrotron Radiation Experiments (SNIC 2006)*. April. 2006, pp. 1–9. URL: <http://www.slac.stanford.edu/econf/C0604032/papers/0018.pdf>.
 - [88] Simonetta Gentile, Ekaterina Kuznetsova, and Franco Meddi. “Photon detection efficiency of Geiger-mode avalanche photodiodes”. In: *International Linear Collider Workshop 2010, LCWS 2010 and ILC 2010*. June 2010. arXiv: 1006.3263. URL: <http://arxiv.org/abs/1006.3263>.